Opto-electronic, Electrical and Spectroscopic Studies of Some Two-Dimensional Materials

Thesis submitted for the degree of

Doctor of Philosophy (Science)

in

Physics (Experimental)

Submitted by

Didhiti Bhattacharya

Department of Physics

University of Calcutta

July, 2022

Dedicated to my Family

ACKNOWLEDGEMENT

It will not be enough to express my gratitude in words to all those people who helped me in this journey; I would like to give my many, many thanks to all of those. First of all, I would like to express my humble respect, special appreciation and thanks to my PhD supervisors Professor Samit Kumar Ray and Professor Rajib Kumar Mitra for proving me their tremendous academic support throughout. Their valuable guidance and discussions always gives me a new angle to deal the difficulties in my research problems and their moral support, optimism and constant encouragement are the source of inspiration for me. I am grateful to S.N. Bose National Centre for Basic Sciences for providing me all research facilities and healthy research environment since I joined this research centre and I am also thankful to DST, India for financial support.

I would like to convey my humble respect and sincere gratitude to Dr. Sayan Bayan for his valuable advices and guidance as senior. I express my profound thanks to all the members of Bio-Photonics lab (Nirnay da, Debasish da, Imadul da, Partha da, Saikat da, Shubhadip da, Riya and Sumana) at SNBNCBS for their support. I am really thankful to all the members of Micro-Science lab (Subhrajit da, Arup da, Sourabh da, Subhajit da, Tamal da and Shreyasi) at IIT KGP for cooperation. I thank my seniors Piya di, Shaptarshi da, Dipanwita madam, Sankar da, Dipika di, Subrata da, Akash da, Buddhadeb da for their affection and specially Dipanjan da and Arnab da for various help during writing my thesis. I am thankful to Shubhrasish, Biswajit, Subhadip, Rafiqul, Tania, Soumili, Koustuv, Amrit, Arundhati, Manjari, Sayantan, Sudip as friends for their unconditional help and company to me during all situations in my Ph.D time. I would like to express my sincere thanks to my all close friends for providing a wonderful and friendly environment in campus. I am thankful to many dear juniors for their various help and joyful company. I would like specially to thank my lab mate and friend Shubhrasish for his heartily assistance in my research and moral support in every moment. Completing this work would have been much more difficult without his supportive, forgiving, generous company.

I must thank Shakti da, Amit da, Joy da, Urmi di, Dipanyan da, Debargha da, Sourav da (Centre facility labs), Amit da (mechanical workshop) for their technical assistance during research works at SNBNCBS. I am thankful to all SNB staffs in different section for their supports. I thank Dr. Atindra Nath Pal for his valuable suggestions and fruitful collaborative

research works. I am grateful to Dr. Nitesh Kumar and Dr. Avijit Chowdhury for their various cooperation, helps and discussions.

I gratefully acknowledge Physics Department of Barasat Govt. College, for giving me perfect ambience and educational support during bachelor and master courses. I would like to express my profound gratitude to all of my teachers in my school and college days for their support, affection, encouragement and suggestions throughout my academic carrier. I must acknowledge and convey my sincere thanks to my school and college friends, I have learnt many important life lessons from them.

No words of appreciation could express my gratitude for my family, who has always been with me with me in all situations. Whatever I am today is because of their unconditional love, care, guidance, encouragement and moral support. To put in one line, the script of my success remains impossible without their huge sacrifices. My parents, sister, uncle, aunts are my strength and inspiration.

Lastly but definitely not the least, I owe a debt of gratitude to the almighty to sail the journey of my life and made this possible by being with me all the ups and downs.

Didhiti Bhattacharya

List of publications related to thesis work

1. Size-dependent optical properties of MoS_2 nanoparticles and their photo-catalytic applications

D Bhattacharya, S Mukherjee, RK Mitra, SK Ray Nanotechnology 31 (14), 145701

2. Flexible Biomechanical Energy Harvesters with Colossal Piezoelectric Output (~ 2.07 V/kPa) Based on Transition Metal Dichalcogenides-Poly(vinylidene fluoride) Nanocomposites

D Bhattacharya, S Bayan, RK Mitra, SK Ray ACS Appl. Electron. Mater. 2020, 2, 10, 3327–3335

3. 2D WS_2 Embedded PVDF Nanocomposites for Photosensitive Piezoelectric Nanogenerators with a Colossal Energy Conversion Efficiency ~ 25.6%

D Bhattacharya, S Bayan, RK Mitra, SK Ray Nanoscale, 2021, 13, 15819

4. Two-dimensional $Mo_xW_{1-x}S_2$ alloys for nanogenerators producing record piezo-output and coupled photodetectors for self-powered UV Sensor

D Bhattacharya, S Mukherjee, AN Pal, RK Mitra, SK Ray Adv. Optical Mater. **2022**, 2200353

5. Enhanced piezoelectric output performance from chemically synthesized TMDC heterostructure and flexible piezoelectric nanogenerator

D Bhattacharya, S Mukherjee, RK Mitra, SK Ray (Manuscript under preparation)

List of publications apart from thesis work

6. Self-powered flexible photodetectors based on Ag nanoparticle loaded g-C3N4 nanosheets and PVDF hybrids: Role of plasmonic and piezoelectric effects

S Bayan, **D Bhattacharya**, RK Mitra, SK Ray Nanotechnology 31 (2020) 365401 (10pp)

7. Two-dimensional graphitic carbon nitride nanosheets: a novel platform for flexible, robust and optically active triboelectric nanogenerators

S Bayan, **D Bhattacharya**, RK Mitra, SK Ray Nanoscale, 2020, 12, 21334

8. High Responsivity Gate Tunable UV-Visible Broadband Phototransistor Based on Graphene –WS_2 Mixed Dimensional (2D-0D) Heterostructure

S Mukherjee, **D Bhattacharya**, S Patra, S Paul, RK Mitra, P Mahadevan, AN Pal, SK Ray ACS Appl. Mater.Interfaces 2022,14,5775−5784

9. High performance Broadband Photodetection Based on Graphene–$MoS_{2x}Se_{2(1-x)}$ Alloy Engineered Phototransistors

S Mukherjee, **D Bhattacharya**, SK Ray, AN Pal (Accepted in ACS Appl. Mater.Interfaces 2022)

10. Plasmonic Functionalized TMDC based Superior Performance Broadband Graphene Phototransistors

S Mukherjee, **D Bhattacharya**, AN Pal, SK Ray (Manuscript under preparation)

Abstract

With increasing energy demands and environmental pollutions, it is very much necessary to develop and utilize clean renewable energy resources. As mechanical is an abundant resource of clean, green, sustainable energy and piezoelectric nanogenerators (PENG) devices can convert mechanical energy from surroundings into electrical energy, provide a potential method as a self-powered source. Among the various piezoelectric materials (quartz, ceramics, semiconductors, perovskites, two dimensional materials etc.) piezoelectric polymers such as PVDF (poly-vinylidene difluoride) and its copolymers have been used to manufacture PENGs for energy harvesting and self-powered sensors. To improve the performance of polymer based piezoelectric devices, incorporation of fillers (semiconductors, metal nanoparticles, perovskites etc.), chemical doping are interesting strategies. Coupling of piezoelectric and semiconducting properties or by fabricating the hybrid by combining piezoelectric and semiconducting materials have been used as basic building blocks for fabricating photosensitive piezoelectric nanogenerators, piezophototronic devices. Atomically thin, layered 2D materials (graphene, transition metal dichalcogenides (TMDC), hBN etc.) with intriguing electrical, optical, thermal, mechanical properties offer a broad spectrum of solutions in materials science and are promising candidates for energy application technology. The superior mechanical strength and flexibility of 2D materials perfectly fit the durability and adaptability requirement for wearable energy harvesting.

In this dissertation, 2D-TMDC nanosheets (MoS_2, WS_2) are exfoliated chemically and their spectroscopic, optoelectric, piezoelectric properties are studied and using those PENG devices are fabricated. This chemical exfoliation method enables to produce massive quantity crystalline, layered 2D-TMDCs in low cost and these PVDF-TMDC nanocomposites are used for fabricating self-powered, flexible piezoelectric nanogenerator without any need of external polling. The fabricated flexible, self-poled PVDF-MoS_2 nanogenerator device yields excellent piezoelectric output voltage under mechanical impact and strain with high energy conversion efficiency. It is reported that that two-dimensional semiconductor WS_2 nanosheets, with a broadband absorption spectrum, can serve as efficient filler into PVDF matrix to develop energy harvesting nanogenerators as well as self-powered optical sensors. The fabricated self-poled, photosensitive flexible PVDF-WS_2 nanogenerator device yields an enormously high piezoelectric output and record energy conversion efficiency with good

photoresponsivity at zero bias. TMDC nanosheets face significant challenges owing to the fact that chalcogen vacancies in such materials, lead to localized deep-level defect states (DLDs), which degrade their electronic and optoelectronics performances. Composition modulation (alloy formation) has been predicted to be a potential solution to suppress the deep-level defect states (DLDs) in TMDCs. The characteristics of a self-powered real time UV photodetection system based on impedance matching between piezoelectric nanogenerator and photodetector by using ternary TMDC ($Mo_xW_{1-x}S_2$) alloy is reported. To get the deeper understanding about piezoelectricity, piezoelectric characterizations of TMDC nanosheets and their heterostructures are examined through piezoelectric force microscopy (PFM). It is observed that the MoS_2-WSe_2 heterostructure exhibits highest piezoelectric coefficient among all due to formation of large band offset. The scalable, stain–sensitive TMDC heterostructure PENG device exhibits significantly high the output voltage in self-powered mode. All of these fabricated nanogenerator devices can harvest energy from different biomechanical impacts and regular human activities, establish the efficacy of TMDC based PENGs for the design and development of new generation smart and wearable electronic devices. Size dependent spectroscopic properties of synthesized MoS_2 NPs have been studied which is direct evidence of quantum confinement effect. It is demonstrated that that the different sized semiconducting MoS_2 NPs are promising candidate for fabrication of optoelectronic devices with a strong potential for the degradation of harmful chemicals in waste water under visible light irradiation.

In summary, these doctoral thesis works expand the basic understanding of optoelectronic, piezoelectric and spectroscopic properties of TMDC nanomaterials and the fabricated self-powered, energy harvesting PENG devices may promote its practical applications in the next generation self-powered sensor system and wearable electronics based IOT devices.

Contents:

Chapter 1: Introduction

Chapter 2: Experimental Techniques

Chapter 5: Two-dimensional $Mo_xW_{1-x}S_2$ alloys for nanogenerators producing record piezo-output and coupled photodetectors for self-powered UV Sensor

Chapter 6: Superior piezoelectric performance of chemically synthesized TMDC heterostructures for self-powered flexible piezoelectric nanogenerator

Chapter 7: Size dependent optical properties of MoS_2 nanoparticles and their photo-catalytic applications

Chapter 8: Conclusions and Future Scope of Study

Chapter: 1

Introduction

This chapter highlights the general introduction of the research work addressed in this dissertation. The motivation behind selecting this work and the self-powered energy harvesting devices using piezoelectric nanogenerators and the development of various sensor devices (photo, pressure, strain) by using the transition-metal dichalcogenides nanostructures are the main focus of this chapter. This chapter also deals with the related basic scientific knowledge and the review of past research works.

1.1 General Introduction:

During the last few decades with increasingly serious problems of the energy crisis and environmental pollution throughout the world, it is very necessary to develop renewable, clean energy resources which are pollution and maintenance free for growing development of human civilization. There are abundant natural resources of various clean and renewable energy sources which are sustainable and maintenance free, such as solar, thermal energy, water and wind flow energy. But the availability of such energy resources is not worldwide and in addition production cost is also high. Mechanical energy is a source of clean, sustainable energy resource that widely exists in the environment but is usually wasted in regular life. In this regard, piezoelectric and triboelectric nanogenerators are suitable for converting low frequency mechanical energy into electrical energy [1] and have the ability to harvest mechanical energy from regular human activities. The first piezoelectric nanogenerator (PENG) and the first triboelectric nanogenerator (TENG) were developed in 2006 [2],2012 [3], respectively, ushering in a new era of self-powered electrical energy generation. The understanding of photovoltaic, thermoelectric, piezoelectric, triboelectric, and other phenomenon, various technologies have been developed for energy harvesting from various resources. Also the innovations in materials design and research in device structure engineering and energy harvesting from them have substantially increased the device's performance. Piezoelectric materials have a wide range of applications in fabricating various sensors, actuators and various energy harvesting technologies. There are natural piezoelectric crystals (such as quartz), various perovskite materials (BTO, PZT etc.) [4–6], polymers [7](PVDF), semiconducting materials (ZnO, GaN, CdS etc.) [1,8] which can exhibit piezoelectricity. Coupling of piezoelectric and semiconducting properties (piezoelectric semiconducting nanosheets, nano-micro wires) [9,10] or by fabricating the hybrid by combining piezoelectric and semiconducting materials have been used as basic building blocks for fabricating innovative devices, such as photosensitive piezoelectric nanogenerators,

piezoelectric field-effect transistors, piezoelectric diodes, piezoelectric chemical sensors, and piezo-phototronic devices [11–15]. Furthermore, utilizing the piezoelectric-semiconductor properties, a new research field of piezotronics has been developed, which uses the effect of the piezoelectric potential created in the piezoelectric materials which controls the charge carrier transport characteristics [9,10,16] to fabricate various electronic devices, extending the potential applications in various microelectromechanical systems, human–computer interfacing, nanorobotics and sensors. A non-centro symmetric crystal structure naturally produces a piezoelectric effect when the material is strained. Under the effect of strain the positive and negative charge centres are displaced relatively, results a dipole moment. The addition of the dipole moments within this non-centro symmetric crystal creates a piezoelectric field, results a macroscopic potential drop along the straining direction inside the crystal and the generated potential is called the piezoelectric potential. The piezopotential can serve as driving force for the flow of electrons through the external load when it is subjected to external mechanical deformation, which is the fundamental working principle of a piezoelectric nanogenerator [2]. The energy harvesting self-powered systems are needed to be light weight and portable to power up electronic devices. They also need to be flexible and maintenance free for fabrication of next generation wearable and smart devices. For the rapid development of wearable electronics, portable gadgets, and the Internet of Things (IoT), much works have gone for evolving sustainable, mobile, and self-sufficient energy sources. Inorganic perovskites have high piezoelectric coefficients but are less selective for the applications in flexible nanogenerator domain due to their lack of bio-compatibility, durability, complex synthesis procedure and high toxicity. On the contrary, piezoelectric polymer and copolymers, are attractive for energy harvesting as they have high piezoelectric coefficient, chemical and thermal stability, bio-compatibility and light weight [7]. The piezo-characteristics of hybrid structures by introducing fillers such as, metal nanoparticles [17,18], perovskites [19,20], semiconductors [21,22] and two-dimensional materials [23–25] in polymer matrix have been studied widely because of easy fabrication process, compatibility and mechanical flexibility [18,26,27]. Furthermore, it has been found that hybrid devices are sensitive to various environmental conditions like temperature, light, pressure, chemicals etc. in self-powered mode [28–31] also.

The growing research interest in two-dimensional (2D) materials and substantial development on the studies onto their properties and applications accelerate the growth of research interest in energy harvesting devices based on these 2D materials. Atomically thin, layered structured 2D materials with highly intriguing electrical, optical, opto-electronic, thermal, mechanical

and chemical properties, such as graphene and graphene-based materials (graphene oxide, reduced graphene oxide or functional graphene based materials), transitional metal dichalcogenides (TMDCs), black phosphorus (BP) and transitional metal carbide, nitride, MXenes offer a broad spectrum in the direction of materials science [32–38] and are also promising candidates for energy application technology [39–41] also. For instance, the superior mechanical strength and flexibility of these two-dimensional materials perfectly fit the durability and adaptability requirement for self-powered, wearable, portable energy harvesting technology. The band structure engineering and charge carrier transport features arise from the quantum confinement effect in 2D materials provide appealing electrical and distinguished spectroscopic, optoelectrical performances. The tunable structural and physico-chemical properties of 2D materials lead to improvements of device performances such that these 2D materials have shown tremendous potential for fabrications of wearable energy harvesting and sensor devices also [42,43].

1.2 Transition Metal Dichalcogenides (TMDC):

Two-dimensional (2D) materials mainly exist in bulk form with weak interlayer attraction between each layers allows the exfoliation into atomically thin individual layers. The first explored 2D material is graphene, monolayer counterpart of graphite. Graphene is a unique example of an extremely high electrical and thermal conductor and exhibits high carrier mobility [44,45]. But, its semimetallic nature [46] of graphene prevents the applications in optoelectronics. In contrast that transition metal dichalcogenides (TMDC) exhibits encouraging light absorption- emission properties, covering ultraviolet-visible-near infrared wavelength range [47]. Besides that the electronic properties of TMDCs range from metallic to semiconducting [48], there are also TMDCs that exhibit interesting phenomenon like charge density waves and superconductivity.

1.2.1 Crystal Structure:

TMDCs are a class of materials with formula MX_2, where M is a transition metal element from group IV (Ti, Zr, Hf and so on), group V (Nb or Ta) or group VI (Mo, W and so on), and X is a chalcogen (S, Se or Te). These materials form layered structural unit X–M–X, where the chalcogen atoms in two hexagonal planes separated by a plane of metal atoms. Adjacent layers are held together by weak van der-Waals interaction to form the bulk crystal in a variety of polytypes [49]. Depending upon the variation of stacking orders and metal atom

coordination, the overall crystal symmetry of TMDCs can be hexagonal or rhombohedral, and the metal atoms have octahedral or trigonal prismatic coordination. The most stable unit cell has trigonal prismatic coordination with hexagonal symmetry, providing 2H semiconducting MX_2 phase, whereas, the metastable 1T phase has octahedral coordination with tetragonal symmetry. The very unlikely stable 3R phase possesses rhombohedral symmetry with three X-M-X units [50].

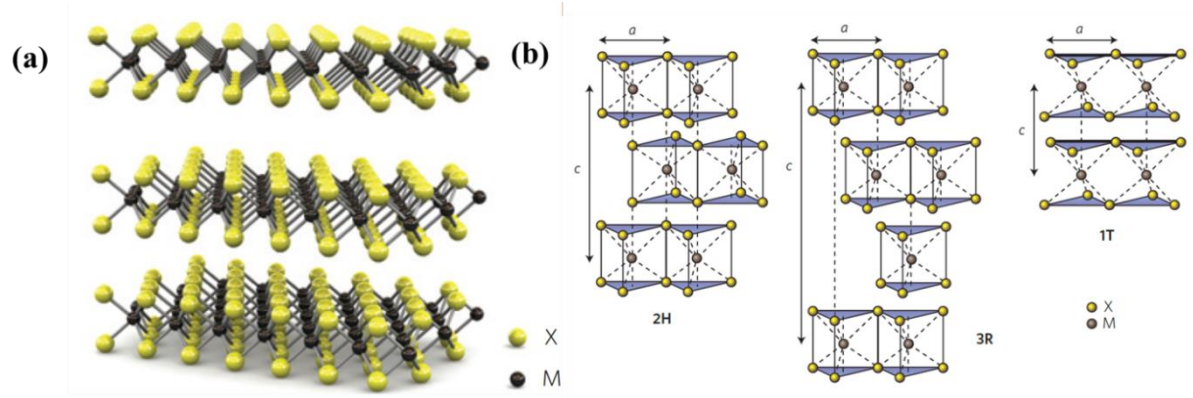

Figure 1.1 Structure of TMDC materials (a) Three-dimensional schematic representation of a MX_2 structure, with the chalcogen atoms (X) and the metal atoms (M), (b) Schematics of the structural polytypes: 2H (hexagonal symmetry, two layers per repeat unit, trigonal prismatic coordination), 3R (rhombohedral symmetry, three layers per repeat unit, trigonal prismatic coordination) and 1T (tetragonal symmetry, one layer per repeat unit, octahedral coordination). [Ref: 49, 50]

1.2.2 Electronic Band Structure:

Semiconducting TMDCs exhibit an indirect bandgap in the bulk and a direct gap in the monolayer. The direct bandgap is the prime reason for observing photoluminescence from monolayer MX_2, which have opened up the possibility of optoelectronic applications. The band structures of bulk and monolayer MX_2's are calculated from first principles, tight-binding approximations [51–53] and measured by using a variety of spectroscopic tools. At the Γ-point, the bandgap is indirect for the bulk material, but it is to be gradually shifted towards direct for the monolayer. The direct excitonic transitions at the K-point remain relatively unchanged with the variation of number of layers. Quantum confinement effect is the cause of the change in the band structure with layer number. It results in a change in the

hybridization between p_z-orbitals on chalcogen atoms and d orbitals on transition metal atom [54]. For example, the bulk indirect bandgap (~1.2 eV) of 2H-MoS_2 converts to a direct bandgap (~1.8 eV) in single-layer. Density functional theory (DFT) calculations predict that the conduction-band states at the K-point are mainly attributed to the localized *d*-orbitals on the Mo atoms which are relatively unaffected by interlayer coupling. However, the states near the Γ-point are due to combination of the antibonding p_z-orbitals of the S atoms and the d orbitals of Mo atoms, and have a strong interlayer coupling effect. Therefore, as the layer numbers change, the direct excitonic states near the K-point are relatively unchanged, but the transition at the Γ-point shift significantly indirect to direct transitions. All MoX_2 and WX_2 compounds are expected to exhibit a similar indirect- to direct-bandgap transformation with decreasing layer numbers [51].

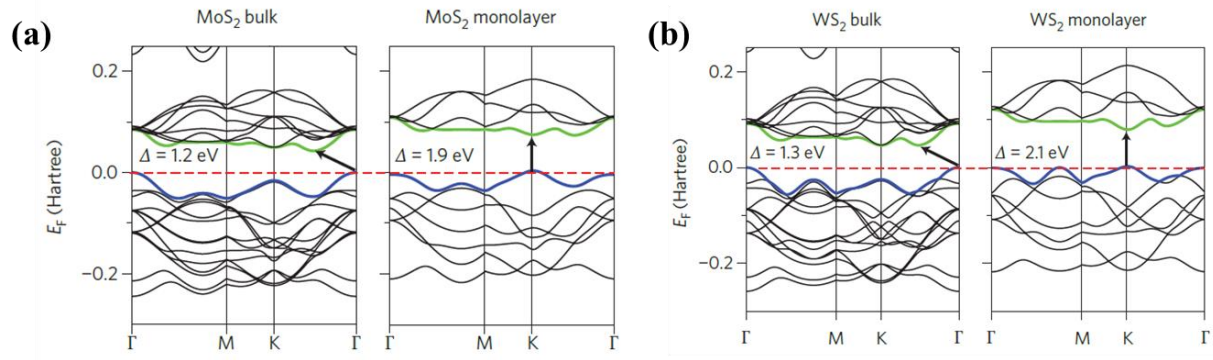

Figure 1.2 Band structures calculated from first-principles density functional theory (DFT) for bulk and monolayer (**a**) MoS_2 and (b) WS_2.[Ref: 51]

1.2.3 Optical Properties:

The optical properties of TMDCs are directly influenced by their electrical band structural properties. The change from indirect to direct bandgap and increase in bandgap energies are reflected in absorption and photoluminescence spectra [51,54,55]. The optical absorption spectrum of 2H-MX_2 exhibits prominent peaks corresponding to the exciton bands, arises due to the direct-gap transitions at the K-point of the Brillouin zone between the maxima of split-off valence bands and the minimum of the conduction band. Monolayer semiconducting 2H-MX_2 is a direct gap semiconductor, where the lowest energy interband transition occurs at the K point of the Brillouin zone and relaxation of excitons at the K point can result in emission of photons, so the monolayer semiconducting MX_2 exhibits sharp, intense photoluminescence spectra. The phonon dispersions of MX_2 have been extracted by *ab initio* calculations, and

can be correlated with experimentally obtained Raman spectra [56]. The main Raman peaks correspond to the in-plane E^1_{2g} and E_{1u} phonon modes, and the out-of-plane A_{1g} mode. These peak position shifts allow the variation of layer thicknesses which can be identified by Raman spectroscopy. The origins of the shifts have been identified as the influence of neighbouring layers on the effective restoring forces on atoms and the increase of dielectric screening of long-range Coulomb interactions [57].

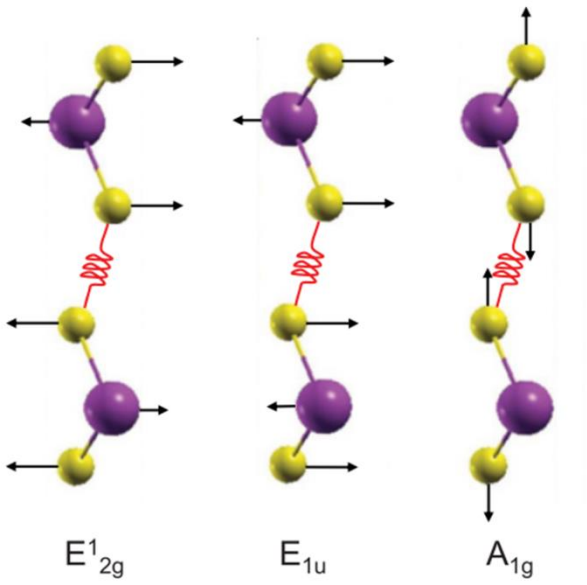

Figure 1.3 In-plane phonon modes E^1_{2g} and E_{1u}, and the out-of-plane phonon mode A_{1g}, for TMDCs, where transition metal atoms are denoted by violet and chalcogen atoms are denoted by yellow. [Ref: 57]

1.2.4 Optoelectric Properties:

For the TMDC semiconductors with broad absorption band, photons with energy greater than the bandgap energy can be readily absorbed. The absorbance and emission direct effect the photoconductivity [58]. The work functions and conduction- and valence-band edges of several TMDCs match with the work functions of commonly used electrode materials and the flexible nature with high Young's modulus of TMDC make those compatible to fabricate the flexible devices. Moreover, the ability to tune the bandgap of TMDCs with various intercalants such as metal ions and molecules may allow tunable optical absorbance which is suitable in photovoltaic and photodetector application purposes [59].

1.3 Synthesis of TMDCs:

For the reliable production of atomically thin layered 2D TMDCs there are the available methods for top-down exfoliation from bulk materials and for bottom-up synthesis. For the top-down approach micromechanical exfoliation, chemical exfoliations are well-known techniques to prepare TMDC nanosheets. In bottom-up approach, chemical vapour deposition (CVD) is the widely used to produce ultrathin layered 2D-TMDC nanomaterials.

1.3.1 Mechanical Exfoliation:

The micro-mechanical cleavage method is a famous traditional approach for exfoliation of layered bulk crystals to obtain layer 2D flakes [54,60]. Atomically thin flakes of TMDCs can be peeled from their bulk parent crystals by micromechanical cleavage using adhesive tape on target substrates. Nanoflakes produced by this mechanical exfoliation produce are highly pure and clean interface which is suitable to study their fundamental properties and high quality controlled device fabrication. But the yield of this method is low, not scalable and therefore there is no control over nanoflake's size and thickness.

1.3.2 Liquid Phase Exfoliation:

Liquid phase exfoliation method is extensively used to exfoliate layered nanosheet from bulk material and the exfoliated ultrathin layers are dispersed in particular solvent [61]. Here, the ultrasonic vibrations break the interlayer weak van der-Waals bond, but cannot break the covalent bonds of each layer and in this procedure the choice of solvent plays a crucial in exfoliation [62,63]. This method enables to produce massive quantity crystalline, layered 2D-TMDC nanosheets in low cost.

1.3.3 Chemical Vapour Deposition (CVD):

Chemical vapour deposition is a bottom-up synthesize procedure to prepare high quality ultrathin two dimensional layered flakes. In this process the given substrate is exposed to reactive precursor at specific conditions (temperature, pressure) and the precursor is decomposed or reacted to form ultrathin layer on the given substrate. This method allows for production of high crystalline, large scale layer of two dimensional TMDC material with tunable thickness and excellent electronic properties [64,65].

Instead of these commonly known procedures solvothermal/hydrothermal synthesise, ion-intercalation technique, atomic layer deposition (ALD), physical vapour deposition, pulsed laser deposition are also utilized [66,67] to produce TMDC layered materials.

1.4 Transition Metal Dichalcogenides (TMDC) Alloys:

1.4.1 Properties:

Transition metal dichalcogenides have attained great interest due to their improved mechanical, electrical and optoelectronic properties which has high impact towards practical applications. These can be utilized towards fabrication of novel nanoelectronic and optoelectronic devices. But the TMDC possess intrinsic deep level defects (chalcogen vacancy), which act as scattering centres to reduce charge carries mobility or act as trap states or recombination centres. These abundant mid-gap defect states significantly degrade the electric and optoelectric performances of the TMDC devices. Many approaches have been developed to reduce the deep level defects inside the semiconductors by introducing additional impurity by doping, strain engineering various other techniques. Introduction of foreign dopants suppress the deep-level defects inside the semiconductor through donor-acceptor level repulsion, but the solubility of the dopant and symmetry of the donor-acceptor level have grate impact of the efficacy of this method. The creation of passivated impurity states can modify the host band structure which makes the deep level shallower. But the intrinsic band structure of the host material changes significantly which can create additional problems. So it is highly desirable to develop new approach to reduce the deep level defect density with maintain the electronic properties of host material unchanged. Alloying is developed as a new approach for defect engineering in semiconductors as well as the bandgap of the alloys can be tuned by controlling the component concentration. Alloying is a way to supress the deep level defect states of the semiconductor with maintaining the basic properties of the semiconductor [68]. The alloying of the TMDC (MX_2) materials can be done either by replacing the transition metal (M) site or chalcogen (X) site. Common semiconductor alloys exhibit positive formation energy of enthalpy, whereas the TMDC semiconductor alloys exhibit negative enthalpy value, indicating higher atomic ordering [69]. This atomic ordering plays crucial role in determining the alloys properties. Density functional calculations (DFT) exhibit the stabilities and electronic properties of the TMDC alloys ($Mo_xW_{1-x}S_2$, $Mo(S_xSe_{1-x})_2$) and indicate that the alloy formation is favourable at room

temperature [70–72]. These materials can be synthesized by chemical vapour deposition, solvothermal method or can be exfoliated in layered structure from bulk crystals. Improved electric, optoelectric and catalytic performances [73–76] are obtained from the ternary alloys than there binary counterparts due to reduced density of defect states and the internal strain induced local lattice structure distortion as well as band structure modulation.

1.4.2 Synthesis of two-dimensional layered TMDC alloy:

Variable stoichiometric TMDC ternary alloy materials can be synthesized by different approaches, among them chemical vapour transport (CVT), chemical vapour deposition (CVD), physical vapour deposition, pulsed laser deposition, molecular beam epitaxy are very well known [75–77]. Besides that micromechanical exfoliation from bulk crystal, liquid phase exfoliation of bulk crystal, low temperature solvothermal synthesis, thermolysis etc. are also used for production of layered two dimensional TMDC alloys [73,78].

1.5 TMDC Heterostructures:

1.5.1 Properties:

Two dimensional transition metal dichalcogenides have attracted great attentions due to their unique structure, exciting electrical, optical properties and extraordinary chemical, thermal stabilities ensuring them to be recognized as emerging candidates for next generation high performance electric, opto-electric and smart generation devices. Benefiting from these exciting properties, the 2D TMDCs have demonstrated their potential in electronics, optoelectronics, valleytronics, spintronics, catalysis etc. But some disadvantages of individual TMDC crystals restrict their applications. The ultrathin layer of TMDC limits the absorbance which restricts the performance of optoelectric devices. Their short lifetime causes difficulty to control the excitonic dynamics [79,80]. The van der Waals TMDC heterostructures attain high research interest in spectroscopy, optoelectronics, photocatalysis and various electronic device application purposes as they can overcome shortcoming arises from individual TMDCs. The stacking of individual TMDC layers by van der Waals interaction enables the formation of atomically sharp interfaces and provides the way to study the heterostructure junctional properties [81]. According to the band alignment of two-dimensional layered TMDCs, mainly three types of heterostructure formation can be possible (i) type-I (symmetric) alignment is mainly utilized in mainly optical devices, such as light-emitting

diodes (LED), lasers as they can provide a way to spatially confine the electrons and holes for efficient recombination, (ii) type-II (staggered) alignment is useful in unipolar device fabrication as they allow band offsets (either in conduction or valance or both side), which allow extremely strong quantum confinement effect, (iii) type-III (broken) heterostructure is useful to fabricate the tunnel field effect transistor for enhancing the tunnel current density and infrared intersubband superlattice lattice lasers. Type-II & III heterostructures are useful to engineer conduction to valance band transition energy. Type-II band alignment is very well-known in TMDC heterostructure (MoS_2-WSe_2, MoS_2-WS_2, WS_2-WSe_2) which can reduce the overlap between electrons and holes wave functions by slowing down the charge carrier recombination [82]. The formation of long lived excitons is an efficient way to enhance the performances of various optoelectronic (photodetector, photovoltaic) devices. So the crystalline TMDC heterostructures can be employed to fabricate high performance low power consuming optoelectronic devices, field-effect transistors, spintronics and various sensor devices and also exhibits enhanced catalytic activities [83–85].

1.5.2 Synthesis of two-dimensional TMDC heterostructures:

To fabricate the TMDC heterostructure, several techniques are reported, such as dry transfer technique based on micromechanical exfoliation, chemical vapour deposition (CVD), atomic layer deposition (ALD), liquid phase exfoliation etc. In this dry transfer technique micromechanically exfoliated one TMDC layer can be attached on top of other TMDC layer by using dry transfer technique (by using optical microscope) to get the desired heterostructure [86]. The yield of this method is very low due to small size, variation of thickness but highly clean interface can be obtained in this procedure. For scalable, uniform and reproducible synthesis of 2D TMDC heterostructure, single step or two step CVD technique [85,87] is employed. Depending upon the precursor material, growth condition (temperature, pressure, carrier gas flow), controlling the growth rate different types (lateral, vertical) of heterostructure fabrication is possible. As low cost and large area with reproducibility are required for practical application purposes, in this regard liquid exfoliation (from bulk crystal) technique is very much used as it is simple, efficient economically effective for large scale TMDC heterostructure synthesis [88].

1.6 TMDC Quantum Dots:

1.6.1 Properties:

Two-dimensional transition metal dichalcogenides are an emerging class of materials having extraordinary electric, optoelectronic, thermal, catalytic properties. When the lateral sizes of two dimensional materials are reduced below their Bohr radius then the two dimensional materials are transformed into zero dimensional (0D) materials. These 0D materials exhibit new characteristics or improved properties than their two dimensional counterparts due to arising of edge sites and quantum confinement effects [89–91]. At the same time, theses 0D materials (quantum dots) still preserve their inherent properties of 2D parents. This new class of 0D materials offer larger surface to volume ratio, more provision for functionalization, tunable physio-chemical properties. To obtain the quantum dots (QDs) of TMDCs (MX_2), it is necessary to break the in-plane covalent (X-M-X) bond, so that abundant edge atoms (M or X) are produced. Due to the presence of edge states, the 0D -TMDCs are promising candidate for catalytic applications. TMDC QD's can be dispersed in suitable solvents and exhibits strong emissive properties which can be used for bio-imaging, optoelectronic applications. TMDC QD's exhibit tunable band gap due to quantum confinement effect, they can also exhibit also wider direct bandgap and improved quantum yield than the 2D layered counterparts [91]. In addition to the size dependent quantum confinement effect the bandgap is strongly influenced by defects, functional groups and additional dopant during synthesize time. The size variable TMDC quantum dots demonstrate potentials in optical sensing, photovoltaics, catalytic, bio-imaging, energy storage and conversion also.

1.6.2 Synthesis of TMDC QDs:

TMDC quantum dots can be synthesized from bulk material by various chemical, electrochemical and physical processes. These can be synthesized by chemical etching, ion-intercalation, hydrothermal or solvothermal cutting, ultrasonication treatment, ball milling etc. [92–94]. Among them ultrasonication assisted with grinding, hydrothermal are most commonly used techniques for mass production of TMDC QDs.

1.7 Motivation of the thesis:

Due to rapid development of science and technology portable, wearable and smart devices attain high research interests. But the power supply of these devices limits their size and

restricted capacity of energy storage affects their operational applications. The conception of self-powering is an attractive avenue for continuous power supply for various electronic devices. Piezoelectric nanogenerator can convert mechanical energy (from various surrounding resources) to electrical energy, provide a potential method for designing self-powered sources. Various inorganic materials (quartz, PZT, perovskites) are widely used as piezoelectric nanogenerators (PENG) for energy harvesting and self-powered sensors. But environmental toxicity and complicated fabrication procedure are main disadvantages of them for the versatile use of PENG devices. Compared with inorganic piezoelectric materials piezoelectric polymers (PVDF and co-polymers) are excellent for fabrication of PENG for their flexibility, light weight, easy synthesize procedure, long term stability. Not only that these polymers can be easily functionalized with semiconductors, oxides and metal nanoparticles which can improve its piezoelectric activities and not only that these nanocomposites can be used self-powered PENG without any traditional polling treatment. Incorporating chemically exfoliated two-dimensional transition metal dichalcogenides (MoS_2, WS_2 nanosheets) as filler within PVDF polymer is treated as an efficient way for the development of self-powered piezoelectric energy harvesters. Besides that the semiconducting property and optical activity of TMDC's can be coupled with piezoelectricity so that photosensitive nanogenerators and photo-piezotronics can be demonstrated. 2D-TMDCs have attracted great interest due to their intrinsic optoelectric and piezoelectric properties, but the still now the research is limited with mechanically exfoliated or CVD grown materials. We have extensively studied the piezoelectric properties of chemically exfoliated TMDC nanosheets and TMDC heterostructures. It is observed that improved piezoelectric performance is obtained from TMDC heterostructures than the individual TMDC. TMDC heterostructure based self-polled, low cost PENGs exhibit strain sensitivity and can harvest biomechanical energy also. Besides the wide application of TMDC nanosheets, face significant challenges owing to the fact that chalcogen vacancies in such materials, lead to localized deep-level defect states (DLDs), which degrade their electronic and optoelectronics properties. Composition modulation has been predicted to be a potential solution to suppress the DLDs, and theoretical studies have predicted that ternary alloys of TMDCs are thermodynamically more favourable than their binary counterparts. Although TMDC ternary alloys exhibit superior electrical, optoelectronic and catalytic performances than binary counterparts but they are relatively less studied. We have synthesized TMDC ternary alloy hydrothermally and it is observed the improved optoelectric performance is obtained from the ternary alloy than the binary TMDC nanosheets. It is reported the

characteristics of a self-powered real time UV photodetection system based on impedance matched piezoelectric nanogenerator and photodetector by using ternary TMDC ($Mo_xW_{1-x}S_2$) alloys. The self-powered system is capable of real time UV radiation monitoring in human body and may stimulate its practical application in the next generation photodetection system, sensor and wearable electronics based IOT devices. This self-powered, light-weight, highly flexible and multi-functional PENG devices have opened up a new avenue for diverse research fields, particularly in biomechanical energy harvesting, human-machine interface control and enabling sensing technology.

1.8 Aim and objectives:

The present dissertation aims to investigate the optoelectronic, piezoelectric and spectroscopic properties of TMDC nanostructures for energy harvesting, flexible, low cost, large scale piezoelectric devices, photo-sensitive devices with a focus on the following objectives:

1.1 Synthesis and characterization of TMDC nanostructures

(i) Synthesis of semiconducting MoS_2, WS_2 nanosheets/nanoparticles and studying their size dependent properties.

(ii) Synthesis of ternary TMDC alloy ($Mo_xW_{1-x}S_2$) nanosheets and studying their characterizations.

(iii) Synthesis and characteristics of various TMDC hybrid heterostructures (MoS_2-WS_2, WS_2-WSe_2, MoS_2-WSe_2).

1.2 Fabrication of self-polled, flexible, large scale energy harvesting PVDF-TMDC composed piezoelectric nanogenerators.

1.3 Fabrication of UV photodetector, piezoelectric nanogenerators and photodetector coupled piezoelectric nanogenerator-self-powered UV sensors by using ternary TMDC ($Mo_xW_{1-x}S_2$) alloy nanosheets.

1.4 Fabrication of flexible, stain sensitive devices and self-polled piezoelectric nanogenerator on PET substrates by using TMDC heterostructures (MoS_2-WSe_2).

1.9 Organizations of the thesis:

The entire thesis has been divided into eight chapters. A brief outline of the different chapters of the thesis has been given below:

Chapter 1: Introduction

This chapter presents the importance of renewable energy resources which are self-powered, low cost and maintenance free, specially focusing on piezoelectric energy harvesting devices by using transition metal dichalcogenides (TMDCs). Previous studies indicate that there are enough scope for the systemic investigation of two-dimensional layered TMDCs and studying self-powered energy harvesting PENGs. The present dissertation contains seven chapters with an aim to study some of these issues.

Chapter 2: Experimental Techniques

This chapter describes the synthesis technique for various TMDC nanostructures and different characterization tools for characterization to investigate different properties. The experimental techniques for fabrication of devices are also described in this chapter.

Chapter 3: Flexible bio-mechanical energy harvesters with colossal piezoelectric output based on PVDF-MoS_2 nanocomposites

This chapter demonstrates an extraordinarily high piezoelectric output from a composite nanogenerator fabricated by combining chemically exfoliated MoS_2 nanosheets with PVDF polymer. This self-poled, flexible, strain sensitive highly stable piezoelectric nanogenerator (PENG) exhibits superior mechanical to electrical conversion efficiency and able to charge up various electronic devices. This PENG can harvest energy from different biomechanical activities to establish the efficacy of TMDC MoS_2 based nanocomposites for the design and development of new generation smart and wearable electronic devices.

Chapter 4: Two dimensional WS_2 embedded PVDF nanocomposites for photosensitive piezoelectric nanogenerators

This chapter demonstrates the fabrication of photosensitive piezoelectric nanogenerator where chemically exfoliated 2H-WS_2 nanosheets are embedded in PVDF polymer matrix.

Chemically exfoliated WS_2 nanosheets have broad absorbance band which is responsible for photosensitivity of this nanogenerator and also exhibits enhanced energy harvesting ability under illuminated condition. Besides biomechanical energy harvesting, this PENG exhibits record energy conversion efficiency with a good photoresponsivity at zero bias under application of strain.

Chapter 5: Two-dimensional $Mo_xW_{1-x}S_2$ alloys for nanogenerators coupled photodetectors for self-powered UV Sensor

This chapter explains the demonstration of a self-powered real time UV photodetection system based on impedance matched piezoelectric nanogenerator and photodetector using ternary TMDC ($Mo_xW_{1-x}S_2$) alloys. The optimized $Mo_{0.5}W_{0.5}S_2$ ternary alloy nanosheets synthesized using a simple hydrothermal method have been used to fabricate UV photodetectors, which exhibit outstanding photodetection ability under 365 nm illumination. The piezoelectric nanogenerator fabricated using the ternary $Mo_{0.5}W_{0.5}S_2$ alloy nanosheets in PVDF matrix exhibits record performance. By coupling the above two individual devices, we have demonstrated a self-powered UV photodetection system, which produces a large voltage responsivity indicating the ability to detect UV radiation even at a low intensity. The self-powered system is capable of real time UV radiation monitoring in human body and may stimulate its practical application in the next generation photodetection system in the sensor and wearable electronics based IOT devices.

Chapter 6: Superior piezoelectric performance of chemically synthesized TMDC heterostructures for self-powered flexible piezoelectric nanogenerator

This chapter presents the characteristics of chemically synthesized TMDC heterostructures and it is observed that this TMDC heterostructure based piezoelectric devices overcome the drawbacks of mechanically exfoliated low yield PENG devices. The strain sensitive piezoelectric properties and biomechanical energy abilities are also investigated. This self-powered, atomically thin, highly flexible and multi-functional PENG device may open up a new avenue for diverse research fields, particularly in biomechanical energy harvesting, human-machine interface control and enabling sensing technology.

Chapter 7: Size dependent optical properties of MoS_2 nanoparticles and their photo-catalytic applications

This chapter reports the synthesis of variable sized semiconducting MoS_2 nanoparticles by simple chemical exfoliation technique. Size dependent spectroscopic properties of these synthesized MoS_2 NPs have been studied using UV-Vis absorption, photoluminescence (PL), Raman and time resolved emission spectroscopy techniques. The effect of size on quantum confinement has also been studied. This highly luminescent MoS_2 NP can act as a photo-catalyst in presence of visible light for degradation of brilliant green dye. This study systematically shows that the different sized semiconducting MoS_2 NPs are promising candidate for optoelectronic devices with a strong potential for the degradation of harmful chemicals in waste water under visible light irradiation.

Chapter 8: Conclusions and Future Scope of Study

This chapter addresses the overall conclusion of research work along with future scope of this work.

1.10 References:

1. Y. Hu, Y. Zhang, C. Xu, G. Zhu and Z. L. Wang, Nano Lett., 2010, **10**, 5025–5031.
2. Z. L. Wang and J. Song, Science (80-.)., 2006, **312**, 242–246.
3. F. R. Fan, L. Lin, G. Zhu, W. Wu, R. Zhang and Z. L. Wang, Nano Lett., 2012, **12**, 3109–3114.
4. Z. H. Lin, Y. Yang, J. M. Wu, Y. Liu, F. Zhang and Z. L. Wang, J. Phys. Chem. Lett., 2012, **3**, 3599–3604.
5. J. H. Jung, M. Lee, J. Il Hong, Y. Ding, C. Y. Chen, L. J. Chou and Z. L. Wang, ACS Nano, 2011, **5**, 10041–10046.
6. E. J. Lee, T. Y. Kim, S. W. Kim, S. Jeong, Y. Choi and S. Y. Lee, Energy Environ. Sci., 2018, **11**, 1425–1430.
7. C. Chang, V. H. Tran, J. Wang, Y. K. Fuh and L. Lin, Nano Lett., 2010, **10**, 726–731.
8. C. H. Wang, W. S. Liao, Z. H. Lin, N. J. Ku, Y. C. Li, Y. C. Chen, Z. L. Wang and C. P. Liu, Adv. Energy Mater., 2014, **4**, 1–7.
9. Y. Duan, M. Cong, D. Jiang, W. Zhang, X. Yang, C. Shan, X. Zhou, M. li and Q. Li, Adv. Mater. Interfaces, 2019, 6.
10. Q. Yang, X. Guo, W. Wang, Y. Zhang, S. Xu, D. H. Lien and Z. L. Wang, ACS Nano,

2010, **4**, 6285–6291.

11. R. Wang, F. Zhou, L. Lv, S. Zhou, Y. Yu, F. Zhuge, H. Li, L. Gan and T. Zhai, CCS Chem., 2019, **1**, 268–277.
12. D. You, C. Xu, W. Zhang, J. Zhao, F. Qin and Z. Shi, Nano Energy, 2019, **62**, 310–318.
13. M. H. You, X. X. Wang, X. Yan, J. Zhang, W. Z. Song, M. Yu, Z. Y. Fan, S. Ramakrishna and Y. Z. Long, J. Mater. Chem. A, 2018, **6**, 3500–3509.
14. Y. Ai, Z. Lou, S. Chen, D. Chen, Z. M. Wang, K. Jiang and G. Shen, Nano Energy, 2017, **35**, 121–127.
15. L. Lv, F. Zhuge, F. Xie, X. Xiong, Q. Zhang, N. Zhang, Y. Huang and T. Zhai, Nat. Commun., 2019, **10**, 1–10.
16. Y. Purusothaman, N. R. Alluri, A. Chandrasekhar and S. J. Kim, J. Mater. Chem. C, 2017, **5**, 415–426.
17. S. K. Ghosh and D. Mandal, Nano Energy, 2018, **53**, 245–257.
18. L. Zhu, J. Phys. Chem. Lett., 2014, **5**, 3677–3687.
19. S. Mondal, T. Paul, S. Maiti, B. K. Das and K. K. Chattopadhyay, Nano Energy, 2020, **74**, 104870.
20. R. Ding, X. Zhang, G. Chen, H. Wang, R. Kishor, J. Xiao, F. Gao, K. Zeng, X. Chen, X. W. Sun and Y. Zheng, Nano Energy, 2017, **37**, 126–135.
21. Y. Mao, P. Zhao, G. McConohy, H. Yang, Y. Tong and X. Wang, Adv. Energy Mater., 2014, **4**, 1–7.
22. S. Bayan, D. Bhattacharya, R. K. Mitra, S. K. Ray and S. K. Ray, Nanotechnology, 2020, **31**, 365401.
23. P. Yadav, T. D. Raju and S. Badhulika, ACS Appl. Electron. Mater., 2020, **2**, 1970–1980.
24. D. Bhattacharya, S. Bayan, R. K. Mitra and S. K. Ray, ACS Appl. Electron. Mater., 2020, **2**, 3327–3335.
25. D. Bhattacharya, S. Bayan, R. K. Mitra and S. K. Ray, Nanoscale, 2021, **13**, 15819–15829.
26. W. Han, L. Zhang, H. He, H. Liu, L. Xing and X. Xue, Nanotechnology, 2018, **29**, 255501.
27. M. Pusty, L. Sinha and P. M. Shirage, New J. Chem., 2019, **43**, 284–294.
28. S. K. Karan, R. Bera, S. Paria, A. K. Das, S. Maiti, A. Maitra and B. B. Khatua, Adv. Energy Mater., 2016, **6**, 1–12.

29. T. Huang, S. Yang, P. He, J. Sun, S. Zhang, D. Li, Y. Meng, J. Zhou, H. Tang, J. Liang, G. Ding and X. Xie, ACS Appl. Mater. Interfaces, 2018, **10**, 30732–30740.
30. K. Shi, B. Sun, X. Huang and P. Jiang, Nano Energy, 2018, **52**, 153–162.
31. S. Siddiqui, H. B. Lee, D. Il Kim, L. T. Duy, A. Hanif and N. E. Lee, Adv. Energy Mater., 2018, **8**, 1–11.
32. O. Lopez-Sanchez, D. Lembke, M. Kayci, A. Radenovic and A. Kis, Nat. Nanotechnol., 2013, **8**, 497–501.
33. D. Xiang, C. Han, J. Wu, S. Zhong, Y. Liu, J. Lin, X. A. Zhang, W. Ping Hu, B. Özyilmaz, A. H. C. Neto, A. T. S. Wee and W. Chen, Nat. Commun., 2015, **6**, 1–8.
34. W. Zhu, T. Low, Y. H. Lee, H. Wang, D. B. Farmer, J. Kong, F. Xia and P. Avouris, Nat. Commun., 2014, **5**, 1–8.
35. K. Kang, S. Xie, L. Huang, Y. Han, P. Y. Huang, K. F. Mak, C. J. Kim, D. Muller and J. Park, Nature, 2015, **520**, 656–660.
36. Z. Sun, A. Martinez and F. Wang, Nat. Photonics, 2016, **10**, 227–238.
37. K. F. Mak and J. Shan, Nat. Photonics, 2016, **10**, 216–226.
38. W. J. Yu, Y. Liu, H. Zhou, A. Yin, Z. Li, Y. Huang and X. Duan, Nat. Nanotechnol., 2013, **8**, 952–958.
39. D. W. Park, A. A. Schendel, S. Mikael, S. K. Brodnick, T. J. Richner, J. P. Ness, M. R. Hayat, F. Atry, S. T. Frye, R. Pashaie, S. Thongpang, Z. Ma and J. C. Williams, Nat. Commun., , DOI:10.1038/ncomms6258.
40. S. Das, D. Pandey, J. Thomas and T. Roy, Adv. Mater., 2019, **31**, 1–35.
41. Y. Pang, Z. Yang, Y. Yang and T. L. Ren, Small, 2020, **16**, 1–26.
42. D. Akinwande, N. Petrone and J. Hone, Nat. Commun., 2014, **5**, 1–12.
43. J. Zang, S. Ryu, N. Pugno, Q. Wang, Q. Tu, M. J. Buehler and X. Zhao, Nat. Mater., 2013, **12**, 321–325.
44. A. A. Balandin, S. Ghosh, W. Bao, I. Calizo, D. Teweldebrhan, F. Miao and C. N. Lau, Nano Lett., 2008, **8**, 902–907.
45. A. S. Mayorov, R. V. Gorbachev, S. V. Morozov, L. Britnell, R. Jalil, L. A. Ponomarenko, P. Blake, K. S. Novoselov, K. Watanabe, T. Taniguchi and A. K. Geim, Nano Lett., 2011, **11**, 2396–2399.
46. A. H. Castro Neto, F. Guinea, N. M. R. Peres, K. S. Novoselov and A. K. Geim, Rev. Mod. Phys., 2009, **81**, 109–162.
47. L. F. Mattheiss, Phys. Rev. B, 1973, **8**, 3719–3740.
48. J. A. Wilson and A. D. Yoffe, Adv. Phys., 1969, **18**, 193–335.

49. B. Radisavljevic, A. Radenovic, J. Brivio, V. Giacometti and A. Kis, Nat. Nanotechnol., 2011, **6**, 147–150.
50. Y. Ding, Y. Wang, J. Ni, L. Shi, S. Shi and W. Tang, Phys. B Condens. Matter, 2011, **406**, 2254–2260.
51. A. Kuc, N. Zibouche and T. Heine, Phys. Rev. B - Condens. Matter Mater. Phys., 2011, **83**, 1–4.
52. T. Li and G. Galli, J. Phys. Chem. C, 2007, **111**, 16192–16196.
53. S. Lebègue and O. Eriksson, Phys. Rev. B - Condens. Matter Mater. Phys., 2009, **79**, 4–7.
54. A. Splendiani, L. Sun, Y. Zhang, T. Li, J. Kim, C. Y. Chim, G. Galli and F. Wang, Nano Lett., 2010, **10**, 1271–1275.
55. K. F. Mak, C. Lee, J. Hone, J. Shan and T. F. Heinz, Phys. Rev. Lett., 2010, **105**, 2–5.
56. C. Lee, H. Yan, L. E. Brus, T. F. Heinz, J. Hone and S. Ryu, ACS Nano, 2010, **4**, 2695–2700.
57. A. Molina-Sánchez and L. Wirtz, Phys. Rev. B - Condens. Matter Mater. Phys., 2011, **84**, 1–8.
58. H. S. Lee, S. W. Min, Y. G. Chang, M. K. Park, T. Nam, H. Kim, J. H. Kim, S. Ryu and S. Im, Nano Lett., 2012, **12**, 3695–3700.
59. Y. Li, L. Li, S. Li, J. Sun, Y. Fang and T. Deng, ACS Omega, 2022, **7**, 13615–13621.
60. K. S. Novoselov, A. K. Geim, S. V. Morozov, D. Jiang, M. I. Katsnelson, I. V. Grigorieva, S. V. Dubonos and A. A. Firsov, Nature, 2005, **438**, 197–200.
61. G. Cunningham, M. Lotya, C. S. Cucinotta, S. Sanvito, S. D. Bergin, R. Menzel, M. S. P. Shaffer and J. N. Coleman, ACS Nano, 2012, **6**, 3468–3480.
62. J. N. Coleman, M. Lotya, A. O'Neill, S. D. Bergin, P. J. King, U. Khan, K. Young, A. Gaucher, S. De, R. J. Smith, I. V. Shvets, S. K. Arora, G. Stanton, H. Y. Kim, K. Lee, G. T. Kim, G. S. Duesberg, T. Hallam, J. J. Boland, J. J. Wang, J. F. Donegan, J. C. Grunlan, G. Moriarty, A. Shmeliov, R. J. Nicholls, J. M. Perkins, E. M. Grieveson, K. Theuwissen, D. W. McComb, P. D. Nellist and V. Nicolosi, Science (80-.)., 2011, **331**, 568–571.
63. P. May, U. Khan, J. M. Hughes and J. N. Coleman, J. Phys. Chem. C, 2012, **116**, 24390–24391.
64. K. K. Liu, W. Zhang, Y. H. Lee, Y. C. Lin, M. T. Chang, C. Y. Su, C. S. Chang, H. Li, Y. Shi, H. Zhang, C. S. Lai and L. J. Li, Nano Lett., 2012, **12**, 1538–1544.
65. S. Balendhran, J. Z. Ou, M. Bhaskaran, S. Sriram, S. Ippolito, Z. Vasic, E. Kats, S.

Bhargava, S. Zhuiykov and K. Kalantar-Zadeh, Nanoscale, 2012, **4**, 461–466.

66. Y. Peng, Z. Meng, C. Zhong, J. Lu, W. Yu, Z. Yang and Y. Qian, J. Solid State Chem., 2001, **159**, 170–173.
67. Y. Peng, Z. Meng, C. Zhong, J. Lu, W. Yu, Y. Jia and Y. Qian, Chem. Lett., 2001, 772–773.
68. V. Popescu and A. Zunger, Phys. Rev. Lett., 2010, **104**, 1–4.
69. J. H. Yang and B. I. Yakobson, Chem. Mater., 2018, **30**, 1547–1555.
70. B. Huang, M. Yoon, B. G. Sumpter, S. H. Wei and F. Liu, Phys. Rev. Lett., 2015, **115**, 1–5.
71. J. Xi, T. Zhao, D. Wang and Z. Shuai, J. Phys. Chem. Lett., 2014, **5**, 285–291.
72. J. Kang, S. Tongay, J. Li and J. Wu, J. Appl. Phys., , DOI:10.1063/1.4799126.
73. Y. R. Lim, J. K. Han, Y. Yoon, J. B. Lee, C. Jeon, M. Choi, H. Chang, N. Park, J. H. Kim, Z. Lee, W. Song, S. Myung, S. S. Lee, K. S. An, J. H. Ahn and J. Lim, Adv. Mater., 2019, **31**, 1–14.
74. K. Hou, Z. Huang, S. Liu, G. Liao, H. Qiao, H. Li and X. Qi, Nanoscale Adv., 2020, **2**, 2185–2191.
75. S. G. Yi, S. H. Kim, S. Park, D. Oh, H. Y. Choi, N. Lee, Y. J. Choi and K. H. Yoo, ACS Appl. Mater. Interfaces, 2016, **8**, 33811–33820.
76. Z. Zheng, J. Yao and G. Yang, ACS Appl. Mater. Interfaces, 2017, **9**, 14920–14928.
77. J. G. Song, G. H. Ryu, S. J. Lee, S. Sim, C. W. Lee, T. Choi, H. Jung, Y. Kim, Z. Lee, J. M. Myoung, C. Dussarrat, C. Lansalot-Matras, J. Park, H. Choi and H. Kim, Nat. Commun., 2015, **6**, 1–10.
78. K. Yang, X. Wang, H. Li, B. Chen, X. Zhang, S. Li, N. Wang, H. Zhang, X. Huang and W. Huang, Nanoscale, 2017, **9**, 5102–5109.
79. D. Kozawa, A. Carvalho, I. Verzhbitskiy, F. Giustiniano, Y. Miyauchi, S. Mouri, A. H. Castro Neto, K. Matsuda and G. Eda, Nano Lett., 2016, **16**, 4087–4093.
80. J. Chen, W. Zhou, W. Tang, B. Tian, X. Zhao, H. Xu, Y. Liu, D. Geng, S. J. R. Tan, W. Fu and K. P. Loh, Chem. Mater., 2016, **28**, 7194–7197.
81. B. Amin, T. P. Kaloni, G. Schreckenbach and M. S. Freund, Appl. Phys. Lett., 2016, **108**, 2–6.
82. V. O. Özçelik, J. G. Azadani, C. Yang, S. J. Koester and T. Low, Phys. Rev. B, 2016, **94**, 035125.
83. M. D. Sharma, C. Mahala and M. Basu, Inorg. Chem., 2020, **59**, 4377–4388.
84. I. W. P. Chen, Y. M. Lai and W. S. Liao, Nanomaterials, 2021, **11**, 2436.

85. C. K. Kanade, H. Seok, V. K. Kanade, K. Aydin, H. U. Kim, S. B. Mitta, W. J. Yoo and T. Kim, ACS Appl. Mater. Interfaces, 2021, **13**, 8710–8717.
86. Q. Li, L. Tang, C. Zhang, D. Wang, Q. J. Chen, Y. X. Feng, L. M. Tang and K. Q. Chen, Appl. Phys. Lett., 2017, **111**, 171602.
87. K. Chen, X. Wan, W. Xie, J. Wen, Z. Kang, X. Zeng, H. Chen and J. Xu, Adv. Mater., 2015, **27**, 6431–6437.
88. G. J. Lai, L. M. Lyu, Y. S. Huang, G. C. Lee, M. P. Lu, T. P. Perng, M. Y. Lu and L. J. Chen, Nano Energy, 2021, **81**, 105608.
89. T. P. Nguyen, W. Sohn, J. H. Oh, H. W. Jang and S. Y. Kim, J. Phys. Chem. C, 2016, **120**, 10078–10085.
90. L. Lin, Y. Xu, S. Zhang, I. M. Ross, A. C. M. Ong and D. A. Allwood, ACS Nano, 2013, **7**, 8214–8223.
91. A. D. Yoffe, Adv. Phys., 1993, **42**, 173–266.
92. S. Mukherjee, S. Biswas, A. Ghorai, A. Midya, S. Das and S. K. Ray, J. Phys. Chem. C, 2018, **122**, 12502–12511.
93. S. Mukherjee, R. Maiti, A. Midya, S. Das and S. K. Ray, ACS Photonics, 2015, **2**, 760–768.
94. S. Sharma, J. Singh, S. Bhagat, M. Singh and S. Sharma, Mater. Res. Express, 2018, **5**, 045047.

Chapter: 2

Experimental Techniques

This chapter elaborates the details of the various experimental techniques employed for the synthesis of different nanostructures of TMDC materials, along with the different characterization techniques employed to study the nanostructures. This chapter also highlights the fabrication techniques of nano-devices which are used for this dissertation.

2.1 Introduction:

This chapter provides an overview on the synthesis, fabrication, characterization and experimental techniques that have been employed in the course of present thesis work. For the successful fabrication of two dimensional material based piezoelectric nanogenerators and sensor devices for the development of the future smart technology, it is very crucial to synthesis high quality layered nanosheets of two dimensional materials. Hence, detailed characterizations are also necessary to examine and optimize the respective optical and piezoelectric parameters of the synthesized nanomaterials.

For the works presented in this thesis, the layered two- dimensional materials (TMDCs) are synthesized by chemical exfoliation techniques. The crystal structures, chemical compositions, surface profile and detailed morphologies are studied by X-ray diffraction (XRD), scanning electron microscopy (SEM) along with X-ray energy dispersive spectroscopy (EDAX), transmission electron microscopy (TEM), atomic force microscopy (AFM) techniques. The spectroscopic and optical characterizations are studied by using UV-Vis absorption spectroscopy, Fourier transformed infrared spectroscopy (FTIR), photoluminescence spectroscopy (PL) and raman spectroscopy techniques. For fabrication of photodetector the electrodes are made by photolithography technique by using laser writer lithography (LW405-MICROTECH) followed by Ti/Au deposition by e-beam deposition. For the fabrication of piezoelectric nanogenerator on flexible substrate, the electrodes are made by depositing Ti/Au by e-beam evaporation through a wire shadow mask. The output voltages from the piezoelectric nanogenerators are recorded by using a digital oscilloscope (SMO702 (scientific)). The optoelectronic-characteristics of the photodetectors are measured by a probe station equipped with a Keithley 2450 source meter. Thorlab LED (365 nm) is employed for optical illumination source and to calibrate the illumination power spectrometer coupled with integrating sphere (Flame-Ocean optics) is used. The piezoelectric characterizations are performed by piezoelectric force microscopy (PFM) and electrical measurements are done by a Keithley 2450 source meter and external mechanical strain are employed through a linear stage.

2.2 Synthesis Technique:

2.2.1 Hydrothermal Method:

Hydrothermal synthesis is one of the most commonly used method for preparation of nanomaterials. It is basically a solution reaction based process. The chemical reactions are occurred in a sealed container and the solution is heated above the ambient temperature and kept in higher than atmospheric pressure. In this process, the crystal growth is normally performed in an apparatus consists of a steel pressure vessel, which is called autoclave and a teflon chamber is kept inside the autoclave. The autoclave is usually thick walled steel cylinder which must stand with high temperature and pressure for a prolonged time. The autoclave must be inert with respect to solvent. The closer is an important part of the autoclave. The precursor dispersed in solution is poured in the teflon chamber in such a way that it should not be more than 70% of the volume of the chamber. The autoclave system is heated to certain temperature and after heating it is should come down to the room temperature and the resulting material is stored at the bottom of the teflon chamber and this is schematically depicted in Figure 2.1. During the hydrothermal synthesis procedure the growth and nucleation of the material depends on pressure and temperature [1]. Hydrothermal synthesis method offers many advantages for nanomaterials growth such as relatively mild operating condition (reaction temperature < 300^{O}c) and minimum loss of materials.

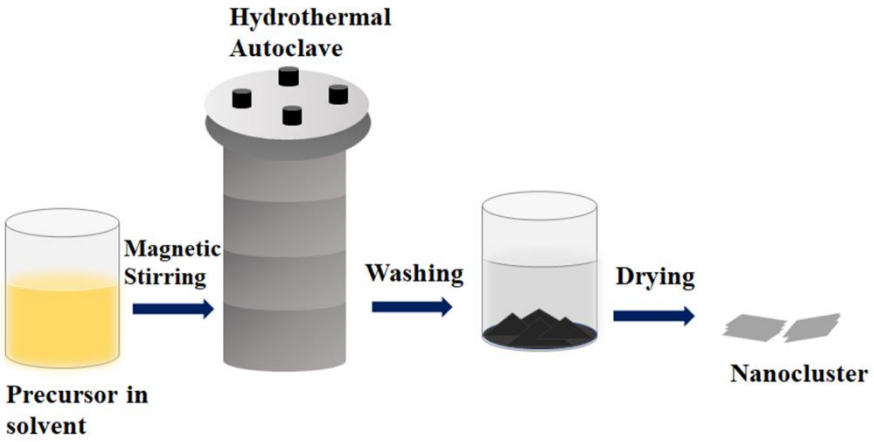

Figure 2.1 Schematic of hydrothermal synthesis technique.

2.2.2 Liquid Phase Exfoliation Technique:

Liquid phase exfoliation (LPE) is one of the most versatile exfoliation techniques for large scale production of layered nanomaterials. It involves the production of few layered nanosheets by applying high shear or ultrasound to materials in appropriate solvent. The weak interlayer interactions between adjacent sheets need to overcome by imparting energy during exfoliation process, when the material is exposed to ultrasound resulting hydrodynamic force breaks the van-der Waals force. By choosing suitable solvent, interactions at the liquid-nanosheet interface reduce the net exfoliation energy and stabilize the nanosheets dispersion in solvent [2]. This process is schematically depicted in Figure 2.2. The resulting dispersions can be very easily processed into nanostructured device by a range of methods, such as dip coating, spin coating, spray deposition, inkjet printing etc.

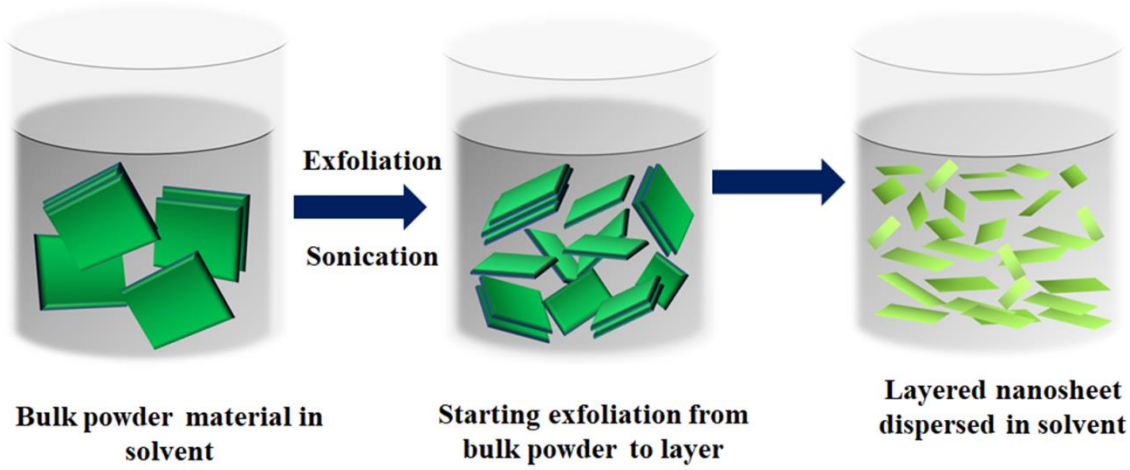

Figure 2.2 Schematic of liquid phase exfoliation synthesis technique.

2.3 Structural Characterizations:

2.3.1 X-ray Diffraction:

The XRD technique, a non-destructive technique is used to investigate the crystalline material structure, including atomic arrangement, crystallite size and defects. Here a beam of X-rays is incident on the sample and is diffracted by the atomic planes. By measuring the

angles and intensities of these diffracted beams, one can determine the atomic arrangement, phase, crystallinity, thickness of films and other various information (strain, orientations, imperfections), i.e. the overall atomic arrangements.

Figure 2.3 presents a schematic of the XRD technique. The X-ray diffractometer consists of X-ray tube (source of X-ray), incident beam optics (before it hits the sample), and goniometer (platform that holds the sample stage and detector) with sample holder, receiving optics (beam from the sample) and detector (which measure the intensity of X-ray scattered by the sample). A crystal can be considered as a regular array of atoms, which can elastically scatter electromagnetic waves like x-rays. The scattered beams form secondary waves which can interfere constructively at certain directions according to the Bragg's condition:

$$2d\sin\theta = n\lambda \qquad (2.1)$$

Here d is the spacing between the atomic planes, θ is the incident angle, *n* is any integer and λ is the wavelength of the X-ray beam. Therefore, for a certain lattice structure (that corresponds to *d*), the diffraction spots appear only at certain angles of incidence. Diffraction occurs only when the Bragg's law is satisfied for constructive interface (X-rays) from planes with spacing d and the corresponding intensities along with angle of the reflected beam with respect to the direction of the incident beam (2θ) are noted [3].

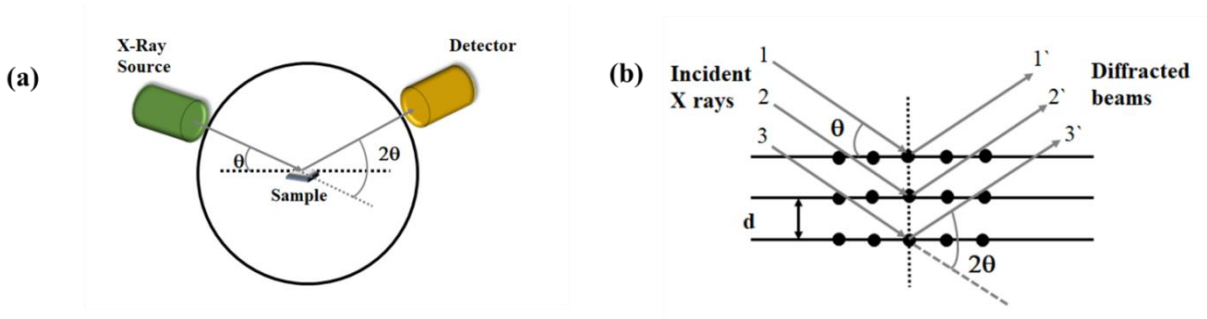

Figure 2.3 Schematic diagram of (a) X-ray diffraction and (b) X-ray diffractometer.

2.3.2 Atomic Force Microscopy (AFM):

The atomic force microscopy is a kind of scanning probe microscope in which topographical image of the sample surface can be achieved based on interaction between a tip and sample surface. A typical AFM consists of a cantilever with a tip (probe) at the free end, a laser, four quadrant photodetector and a scanner and is schematically depicted in Figure 2.4. When the tip comes very close to the sample surface, the attractive and repulsive forces due to

interactions between the tip and sample surface causes the bending of the cantilever. The up-down and side to side motion of the AFM tip as it scans along the surface is monitored through as a laser beam reflected off the cantilever. The reflected beam is tracked by the position sensitive photodetector that picks up the vertical and lateral motion of the probe. By calibrating the deflection sensitivity, the surface thickness of the sample can be estimated and the created image is topographical illustration of the sample surface [4]. Mainly three operational modes are used in AFM, (i) Contact mode, where the tip is able to move over the sample surface with a specific height or under a constant force and the movement of the tip is strongly influenced by frictional and adhesive force between the tip and sample. In (ii) Tapping mode the tip oscillates (nearby its resonance frequency) with sufficient amplitude from the sample surface such that the tip-sample interaction is conserved during the scanning. For (iii) Non-contact mode the tip does not touch the sample, it oscillates above the sample surface during the scanning period [5].

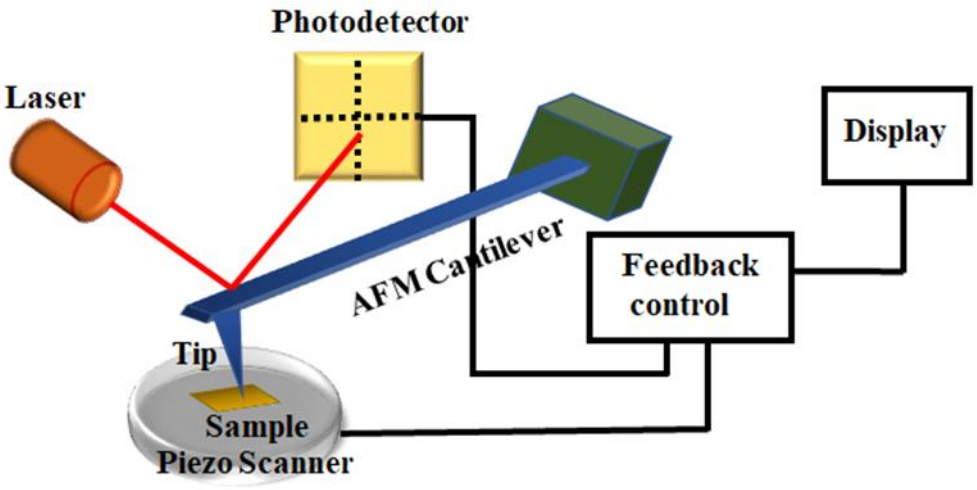

Figure 2.4 Schematic diagram of atomic force microscopy (AFM).

2.3.3 Scanning Electron Microscopy (SEM)

A scanning electron microscope (SEM) is used to characterize the surface topography and morphology of samples by scanning it with a focused beam of electrons. The electrons in the beam interact with the sample, producing various signals which provide the information

about the surface morphology and composition [6]. The advantage of this tool over the conventional optical microscopy lies in its high resolution (~1 nm), owing to the much shorter de Broglie wavelength of electrons. SEM consists of an electron gun which produce high energy electron beam, a magnetic condensing lens is used to condense the electron beam and a scanning coil is arranged in between magnetic condensing lens and sample. The electron detector is used to collect the secondary electrons which can be converted into electrical signals. When the accelerated primary electrons from the electron gun strike on the sample through the condensing lens and scanning coil, it produces secondary electrons which are collected by electron detector and the total set-up is schematically shown in Figure 2.5. The electron beam is scanned in a raster pattern, and the position of the beam is combined with the intensity of the detected signal to produce an image. The signal intensity depends on the number of the emitted secondary electrons. The secondary electron (SE) beams are emitted from very close to the sample surface, produce very high resolution image of sample surface. On the other hand back scattered electron (BSE) beams are reflected from the surface by elastic scattering, they emerge from the deeper locations within the sample. For this reason the BSE are used in analytical SEM, along with the spectra made from the characteristic X-rays, because the intensity of the BSE signal is strongly related to atomic number of the sample, which is rigorously used to study the elemental composition of the sample.

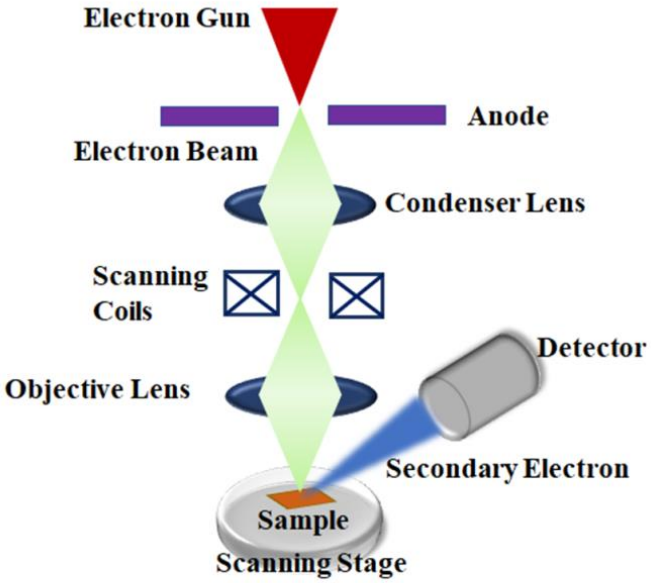

Figure 2.5 Schematic diagram of scanning electron microscopy (SEM).

2.3.4 Transmission Electron Microscopy (TEM):

Transmission electron microscopy (TEM) is a very powerful tool in material science, where a high energy electron beam shone through sample, and the interaction between the electrons and the sample can be used to observe the crystal structure of the sample and morphology with elemental analysis. TEM can be used to study the crystal grain boundaries, structural dislocations, defects in materials and can be used to analyse the quantity, size and shape of low dimensional objects (quantum dots, nanosheets, nanowires) [7].It consists of electron gun as source of high energy electrons, magnetic condensing lens is used to condense electrons and to adjust the portion of the electron falls on specimen. The sample is placed between the condensing lens and objective lens. The magnetic object lens is used to block the high angle diffracted beam and aperture is used to eliminate the diffracted beam and in turn increases the contrast of the image. The magnetic projector lens is placed above the fluorescent screen in order to achieve higher magnification. The image can be recorded by using fluorescent screen or CCD (charged coupled device). When an electron beam passes through a thin specimen, and the transmitted electrons are produced, sophisticated systems of electromagnetic lens focus the transmitted electrons by objective lens and produce the image and diffraction pattern and elemental analysis can be done depending on the mode of operation and simplified ray diagram is shown in Figure 2.6.

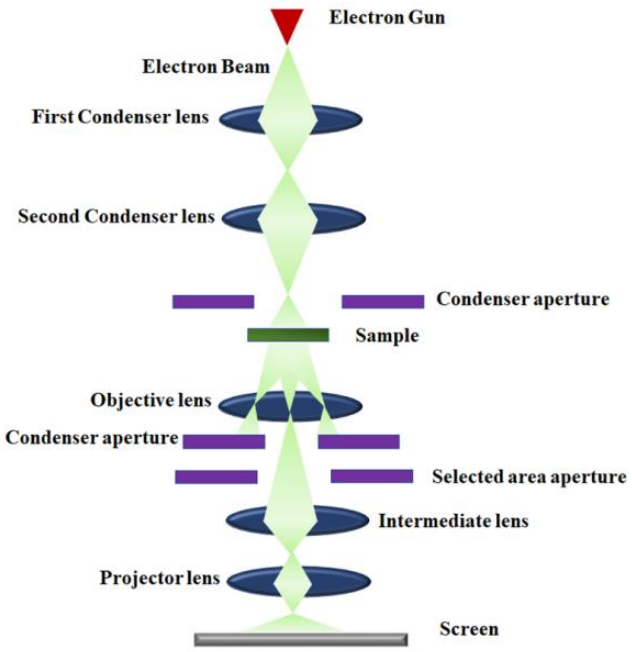

Figure 2.6 Simplified schematic diagram of transmission electron microscopy (TEM).

Lastly, although this technique facilitates the inspection of the finer details of the sample even down to atomic level, the facts like extensive sample preparation, relatively small field of view, and potential of damaging the sample (especially biological samples) limit its wide range application.

2.4 Spectroscopic Characterizations:

2.4.1 UV-Vis Absorption Spectroscopy:

UV-Vis spectroscopy is one of the most common and fundamental electronic spectroscopic technique that records the transmitted or reflected light from the material and presents information about the absorption signals due to the electronic transitions [8]. The electronic spectra of materials can be obtained due to the absorption of ultraviolet and visible regions of electromagnetic spectrum. It is also an excellent technique to determine the band gap energy of semiconducting material. This UV-Vis spectrometer can operate in two modes (i) transmission and (ii) reflection mode. UV-Vis spectrometer consists of light source, monochromator system, sample holder system, detector and amplifier with recording electronic device and is schematically shown in Figure 2.7. UV-Vis spectroscopy obeys the Lambert-Beer law, when a beam of monochromatic light is passed through a sample (absorbing materials), the intensity of the transmitted radiation is decreased after passing through the sample. Lambert-Beer law

$$A = log_{10}\left(\frac{I_0}{I}\right) = \in Cl \qquad (2.2)$$

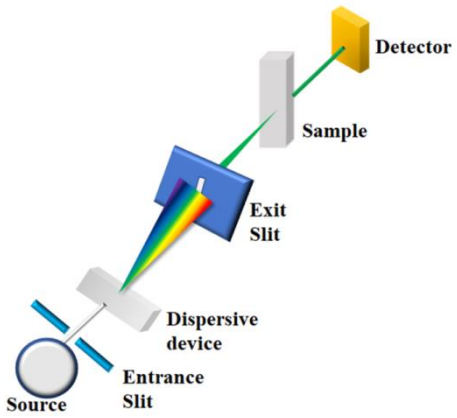

Figure 2.7 Schematic diagram of UV-Visible absorbance spectrophotometer.

Where A is absorbance, I_o is the intensity of incident radiation, I is the intensity of transmitted radiation after passing through the sample, ∈ is molar absorptivity or extinction coefficient, c is the concentration of the absorbing species and l is the path length of the sample. In the present work, UV-visible absorption spectra were recorded at room temperature using a Shimadzu spectrometer, UV-2600 and taking the solutions in a 1 cm quartz cuvette.

2.4.2 Fourier Transformed Infrared Spectroscopy (FTIR):

Fourier Transform Infrared spectroscopy (FTIR) is a powerful tool for identifying the chemical bonds present in a molecule by producing an infrared absorption spectrum [9]. When the sample selectively absorbs specific wavelength (infrared) causes the change of dipole moment, consequently the vibrational energy level of molecules transfer from ground state to excited state and the absorption peak is related to the number of vibrational degrees of freedom of molecule. The position (in frequency) of the absorption peak is determined by the vibrational energy gap and the intensity of absorption peak is related with the change of dipole moments and the possibility of the transition energy levels. FTIR spectrometer consists of IR radiation source, monochromator device (to separate or disperse a broad spectrum into individual narrow IR frequencies), sample and reference cells and detector system with display unit. The two beam Michelson interferometer, the fundamental part of the FTIR, is schematically shown in Figure 2.8.

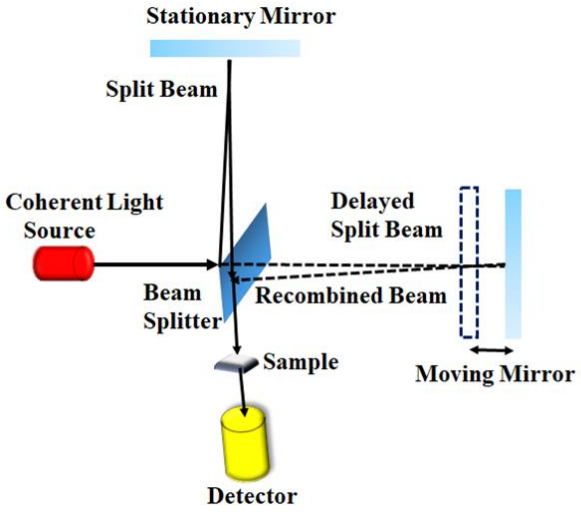

Figure 2.8 Schematic diagram of interferometer of Fourier transform infrared spectrometer.

As shown in the diagram, the collimated IR beam is partially reflected by and transmitted through the beam splitter (a half silvered mirror) and moves to the stationary and moving mirrors, respectively. Now the transmitted beam from the fixed mirror and reflected beam from the moving mirror may interfere (either constructively or destructively) at the back side of the beam splitter depending on the wavelengths of the lights and the optical path difference introduced by the moving mirror.

2.4.3 Raman Spectroscopy:

Raman spectroscopy is a very powerful non-destructive tool to characterize the vibrational spectroscopy of materials. When monochromatic light is incident upon a sample most of the portion is scattered elastically which is called Rayleigh scattering and a small portion is scattered inelastically and it is known as Raman scattering (consists of stokes and anti-stokes lines) [10]. The Raman spectrometer consists of three main components-(i) laser as a source of monochromatic illumination, (ii) objective with sample holder, (iii) detector system with a display unit and is schematically depicted in Figure 2.9.

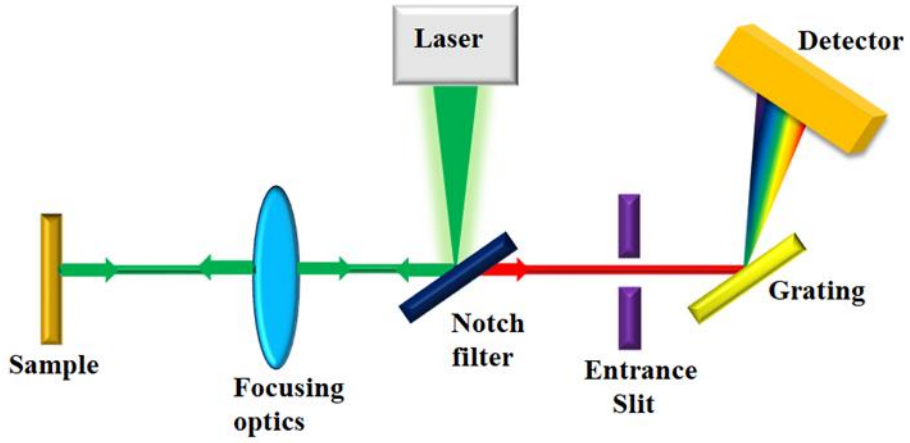

Figure 2.9 Schematic ray diagram of Raman spectrometer.

For a material to exhibit Raman shift, there must be a change in its electric dipolar polarizability with respect to vibrational coordinate. When the photon excites the sample, the excitation puts the sample into a virtual energy state for a short time before the emission of photon. The intensity of the Raman scattering is proportional to its polarizability change.

Therefore the Raman spectrum (scattering intensity as a function of frequency shifts) depends on the roto-vibronic states of that material. The spectrum is measured with respect to the laser line as reference and hence the peaks are measured as a shift from the laser line. The peak positions are determined by the vibrational energies associated with the bonds of the exposed sample [11].

.

2.4.4 Photoluminescence Spectroscopy:

Photoluminescence is a process in which a sample absorbs photons (electromagnetic radiation) of definite energy and then re-emits photons with lower energies. By absorbing photon the sample is switched to excited state of higher energy for short time (~ns) and reemits photon of lower energy [12]. Photoluminescence spectroscopy gives idea about energy band gap, vacancy states, defect levels of materials. It consists of monochromatic light source to excite the sample, focusing object with suitable sample compartment, detection unit for emission signal with a display unit and it is schematically depicted in Figure 2.10. If the incident photon energy ($E= hc/\lambda$) is greater than the band gap of that particular material (semiconductor), then by absorbing the illumination the electrons from the valence band go to the conduction band by crossing the forbidden energy gap and falls back down to the valence band or nearby acceptor states. Similarly, electrons can also fall from the various impurity states near to the conduction band. As electrons fall down, the energy associated is emitted as luminescent photons which are emitted from the material. The process of photon excitation followed by photon emission it is called photoluminescence.

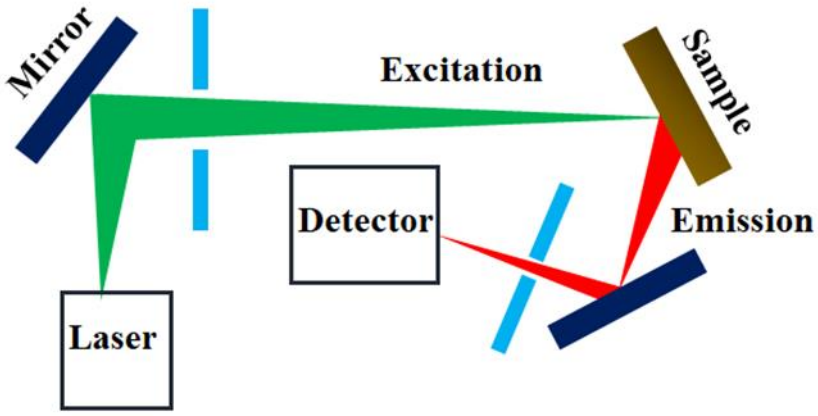

Figure 2.10 Schematic diagram of Photoluminescence spectrometer.

2.4.5 Time-resolve photoluminescence study:

The lifetime of generated carriers have been investigated by employing the time-correlated single photon counting spectroscopy (TCSPSC) set up. There are mainly two methods to measure the lifetime, time domain and frequency domain technique. In time domain methods the sample is excited with a pulse of light and the pulse width is made as short as possible, preferably much shorter than the decay time of the sample. The TCSPC instrument consists of high repetition rate laser light source, grating monochromator, high speed microchannel plate (MCP) photomultiplier tube (PMT) [13] and the simplified schematic is shown in Figure 2.11. When the sample is excited by sharp pulse of light results a population density in the excited state and the excited state population decays in a particular fashion. Emission is a random event, each excited carrier has the same probability of emitting in a given period of time. This results an exponential decay of excited state population and from that the decay time can be calculated. Here we have used Edinburgh Instruments with a pulsed diode laser as the excitation source for time-resolved photoluminescence study.

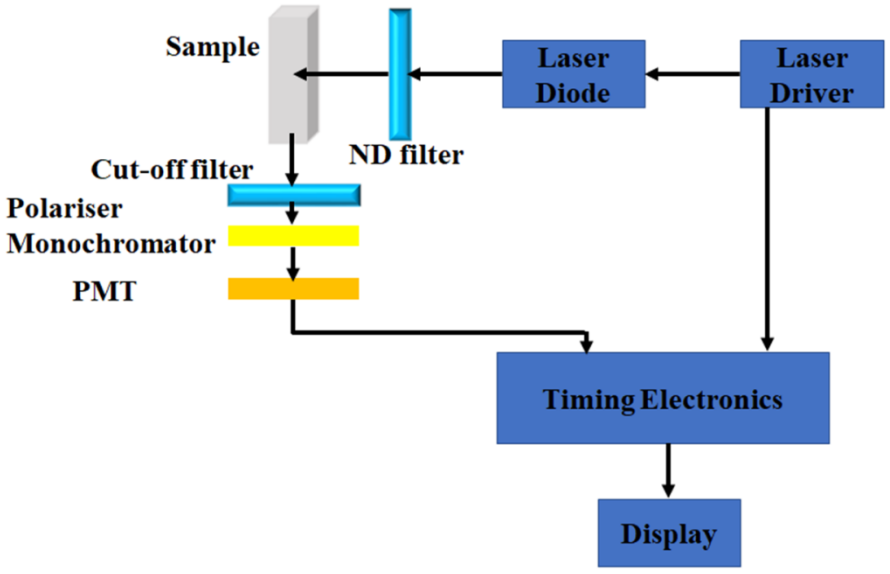

Figure 2.11 Schematic diagram of time resolved photoluminescence spectrometer.

2.5 Fabrication technique:

2.5.1 Lithography:

To manufacture integrated circuits, photolithography or optical lithography is used to create finely pattern thin films of suitable material on substrates such as silicon wafers by using light, followed by etching and deposition for protection. It is employed to fabricate micro and nanostructures in a photoresist thin film through light expose of chosen pattern. There are several steps involved in the photolithography process. Patterns are generated by selectively exposing a light sensitive substrate (photoresist) coated wafer to photo irradiation through a pattered mask, and by subsequently removing the unexposed area of the film through dissolution in appropriate solvent (photoresist developer). Photoresist solution is first spin coated onto the entire surface of the substrate and pre-bake is applied to remove the residual solvent, typically at 100 or 110^{o}C on a hotplate. Next a photomask with the desired feature is placed over the photoresist. Then the photoresist will be exposed to UV radiation through mask. After expose, the exposed wafer undergoes a development process whereby the masked/ unmasked portions of the photoresists are dissolved by chemical developer (solvent). This process yields either positive or negative resistance depending on the radiation and the nature of the resists. Positive photoresist is a type of photoresist where the exposed portion is soluble to developer solution while the unexposed resist remaining on the substrate while negative photoresist is vice-versa, the exposed portion is insoluble to the developer solution while the unexposed resist is dissolved away by the developer. The schematic representation of the step by step process flow of photolithography is represented in Figure 2.12(a).

2.5.2 Electron Beam Deposition:

Electron beam or electron beam vapour deposition is a form of physical vapour deposition in which a target material used as a coating is irradiated with an electron beam from a charged tungsten filament to vaporize it, and then converted into a gas state for vapour deposition on the material to be coated. This device consists of two main sections; an electron source, which is housed in the vacuum evaporation device, and generates electrons, accelerates them as an electron beam, and deflects them, and a crucible (hearth) section that holds the evaporant material. Here the material to be deposited is kept in a water cooled graphite crucible which is placed inside an evacuated chamber. A beam of electron generated by a hot

tungsten filament by thermionic emission is guided and focused onto the material with the help of deflecting and focusing magnets. The focused e-beam heats the sample to its boiling point. The vapour of the material moves towards the substrate which is loaded on a sample holder and gets condensed all over its surface. The sample holder is mounted on a rotation motor, which rotates during the deposition, in order to obtain a uniform deposition and is schematically depicted in Figure 2.12(b).

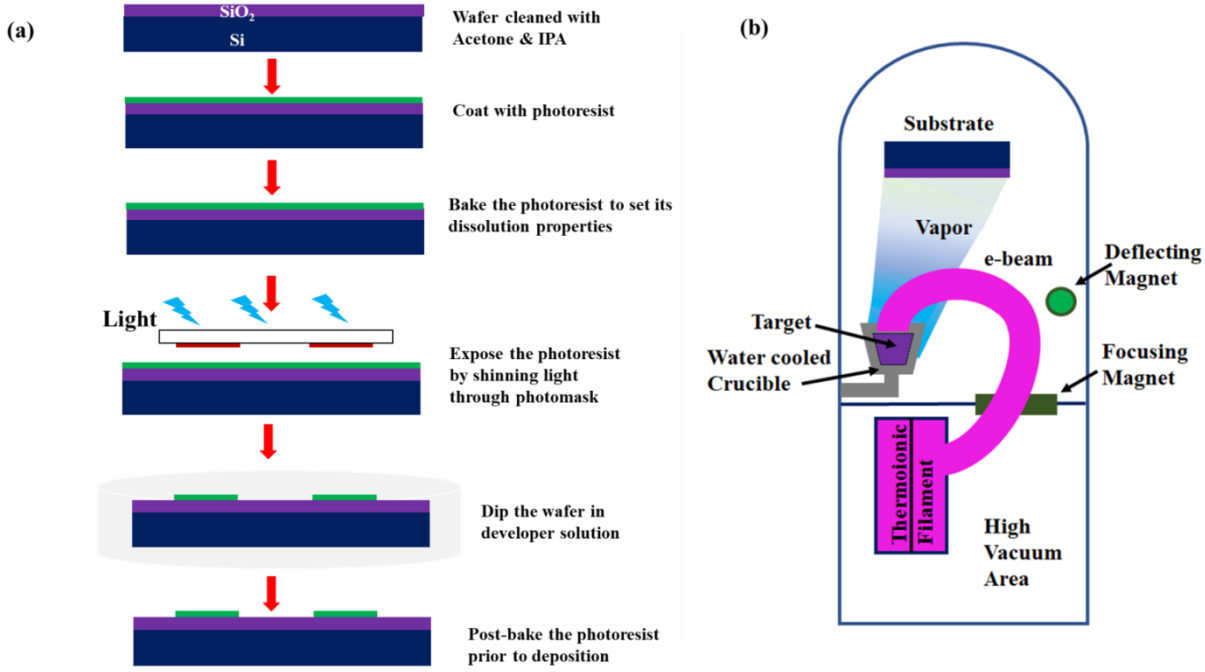

Figure 2.12 (a) Schematic of step-by-step photolithography procedure, (b) simplified schematic e-beam evaporator.

2.6 References:

1. H. Hayashi and Y. Hakuta, Materials (Basel)., 2010, **3**, 3794–3817.
2. V. Nicolosi, M. Chhowalla, M. G. Kanatzidis, M. S. Strano and J. N. Coleman, Science (80-.)., 2013, **340**, 72–75.
3. M. A. Moram and M. E. Vickers, Reports Prog. Phys., , DOI:10.1088/0034-4885/72/3/036502.
4. R. Splinter, Handb. Phys. Med. Biol., 2010, **56**, 5-1-5–9.
5. K. W. Shinato, F. Huang and Y. Jin, Corros. Rev., 2020, **38**, 423–432.

6. D. McMullan, Scanning, 1995, **17**, 175–185.
7. P. J. Goodhew, J. Humphreys and J. Humphreys, Electron Microsc. Anal., , DOI:10.1201/9781482289343.
8. C. B. Boss and K. J. Fredeen, North, 1997, 2–12.
9. C. N. Banwell, Fundamentals of Molecular Spectroscopy, 1983, 1–266.
10. J. R. Ferraro, K. Nakamoto and C. W. Brown, Introductory Raman Spectroscopy: Second Edition, 2003.
11. H. G. M. Edwards, Modern Raman spectroscopy—a practical approach.Ewen Smith and Geoffrey Dent. John Wiley and Sons Ltd, Chichester, 2005. Pp. 210. ISBN 0 471 49668 5 (cloth, hb); 0 471 49794 0 (pbk), 2005, vol. 36.
12. J. R. Albani, Fluorescence Spectroscopy Principles, 2007.
13. S. K. Chakraborty, On disturbances produced in an elastic medium by twists applied on the inner surface of a spherical cavity, 1956, vol. 33.

Chapter: 3

Flexible bio-mechanical energy harvesters with colossal piezoelectric output based on PVDF-MoS_2 nanocomposites

A simple and scalable technique is reported to demonstrate self-poled, flexible and superior-performance piezoelectric nanogenerators by using chemically exfoliated layered MoS_2 nanosheets embedded in poly (vinylidene fluoride) PVDF polymers. These self-poled nanogenerators can produce an open-circuit voltage up to ~ 22 V, even with an application of a very low mechanical compression (~10.6 kPa) leading to an unprecedented piezoelectric output (2.07 V/kPa) using a two-dimensional material. On the other hand, in bending condition (~0.11% strain), the nanogenerator device generates ~ 2.5 V with a piezoelectric energy conversion efficiency of ~ 17.8%, which is capable to drive multiple commercial light emitting devices. The fabricated flexible self-poled MoS_2-PVDF nanogenerators have been used to harvest biomechanical energy from simple human activities (finger tapping, variation in movements of finger and wrist etc.) which offers an excellent power density of ~88.5 $\mu W/cm^2$ upon finger tapping (~3.1 kPa) and display a significant enhancement of performance over control PVDF devices. Our results open up the feasibility of using chemically exfoliated two-dimensional transition metal di-chalcogenides for the design and development of high-efficiency, portable energy harvesting devices.

3.1 Introduction:

In addition to the various renewable energy resources (solar, thermal, wind etc.), energy harvesting by using mechanical impacts (bending, pressing, twisting etc.) and human bio-mechanical activities now a day have attracted enormous interests for driving portable electronic devices, sensors and wearable smart electronics. In this regard, piezoelectric and triboelectric devices have attracted increasing attention for the conversion of mechanical to electrical energy. Various approaches have already been reported for designing portable, scalable, mechanically durable self-powered flexible devices based on piezoelectric nanomaterials which offer good mechanical to electrical energy conversion efficiency [1-6]. The first piezoelectric nanogenerator based on zinc oxide nanowire arrays was proposed by Wang et al. [7,8]. Since then substantial researches have been reported on piezoelectric-nanogenerator (PENG) by using well-known piezoelectric materials, such as ZnO, GaN, PZT along with both organic and inorganic materials including halide perovskites [8-16]. Among organic materials, polyvinylidene-fluoride (PVDF), a commonly known polymer, has been found to be potentially attractive for flexible, large area and cost-effective nanogenerator devices due to its high piezoelectric coefficient, light weight, large thermal expansion coefficient and bio-compatibility [3,17-22]. PVDF polymers usually exhibit different configurations e.g. α-phase (TGTG conformation), β-phase (TTTT-conformation) and γ-phase (T_3GT_3G conformation).

Among them, α-phase is piezo-electrically inactive and γ–phase shows weak piezo behavior, whereas β-phase is the most electroactive one exhibiting the highest piezoelectric coefficient due to parallel stacking of (-CH_2-/-CF_2-) dipoles [2,3,23]. For the nucleation of electroactive β-phase, various techniques have been used such as mechanical stretching, application of high pressure, high temperature annealing, electrospinning, poling, casting etc. Several groups have reported the increased nucleation of piezoelectric active β-phase by incorporating nanofillers e.g. metal nanoparticles [3], perovskite materials [1,24-26], semiconducting nanosheets [27-30], carbon nanotubes [31-33] , bio- materials [34] etc. within the PVDF matrix. It has further been concluded that piezoelectric performance can be significantly enhanced in PVDF-graphene nanocomposites [35,36] using graphene-oxide as a nanofiller in PVDF matrix [37-45]. In addition to graphene, two dimensional transition metal di-chalcogenides (TMDCs) have also been found to be attractive filler materials due to their mechanical flexibility (high Young's modulus), chemical and thermal stability and superior electrical properties. Theoretical predictions and experimental results reveal that the TMDC materials exhibit piezoelectric response in monolayer and odd layered structures because of their broken inversion symmetry, which is not observed in their bulk counterpart [46,47].

For energy harvesting from bio-mechanical and regular human activities, a very high mechanical to electrical energy conversion efficiency is essential since the piezoelectric output per unit pressure is an appropriate figure of merit instead of mentioning the absolute output used in literatures for varying mechanical impacts (up to hundreds of MPa), making the comparison of sensitivity extremely difficult. In this study, we have reported an extraordinarily high piezoelectric output (~2.07 V/kPa) from this composite nanogenerator fabricated by combining chemically exfoliated MoS_2 nanosheets as filler in PVDF polymer. In contrast of the fabrication of PVDF-MoS_2 through electrospinning method [48], we have demonstrated a simple cost effective technique to fabricate self-poled PVDF-MoS_2 nanocomposites, hitherto unreported. Fabricated flexible, self-poled nanogenerator devices yield a piezoelectric output voltage of as high as 22.0 V under an impact of 10.6 kPa and that of 2.5 V by mechanical bending causing an external strain of ~ 0.11%. For demonstration, the nanogenerator can be utilized to charge a capacitor to drive multiple commercial light emitting diodes. Fabricated flexible devices, with the highest piezoelectric output of ~ 2.07 V/kPa by using a two dimensional material, could harvest energy from different biomechanical activities to establish the efficacy of TMDC MoS_2 based nanocomposites for the design and development of new generation smart and wearable electronic devices.

3.2 Experimental Section:

3.2.1 Materials and Methods:

All the chemicals (MoS_2 powder, PVDF powder) and solvents (DMF) were purchased from Sigma-Aldrich and used without further purification.

3.2.2 Synthesis:

Bulk MoS_2 powder (Sigma Aldrich), dissolved in a DMF solution (1mg/ml), was bath sonicated for 8 hrs. Thereafter the suspension was centrifuged at 2000 rpm for 10 min to remove the bulk precipitate and the supernatant solution was centrifuged at 6000 rpm for 15 min to obtain a solution of MoS_2 nanosheets dispersed in DMF and these MoS_2 nanosheets were used for further experiments. PVDF powder (Sigma Aldrich), dissolved in a DMF solvent, was also sonicated for 2 hrs. to obtain a homogeneous solution of PVDF precursor. This was used to fabricate bare PVDF based nanogenerator as the control device. For the preparation of PVDF-MoS_2 nanocomposites, a definite quantity of PVDF powder was mixed with chemically exfoliated MoS_2 nanosheets (dispersed in DMF) with mass ratio varying from 0.15 to 0.25 % followed by sonication to prepare a uniform homogeneous solution and it is schematically shown in below (Scheme:3.1).

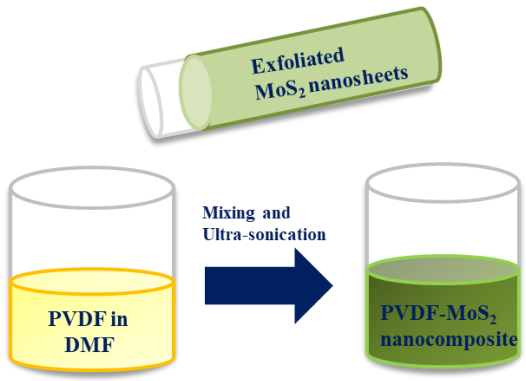

Scheme:3.1 Schematic synthesis of PVDF-MoS_2 nanocomposite.

3.2.3 Device fabrication:

A homogeneous mixture of PVDF and MoS_2 nanosheets was spin coated (at 1000 rpm, 10 sec) on indium tin oxide (ITO) coated flexible poly (ethylene terephthalate) (PET) substrates. Another ITO coated PET substrate was brought into contact so that the nanocomposite film was sandwiched between two ITO layers, acting as top and bottom electrodes, (Scheme:3.2). In order to increase the fraction of electroactive β–phase in PVDF, the composite system was then annealed at 80°C under ambient conditions. The size of a typical PVDF-MoS_2 nanocomposite device was ~ 1.0×1.0 cm^2. The same fabrication procedure was followed to prepare a control sample with bare PVDF film sandwiched between two ITO coated PET substrates. All the fabricated nanogenerator devices could be bent by fingers in a reversible way indicating their good mechanical flexibility, which is essential for their applications in embedded and wearable electronics.

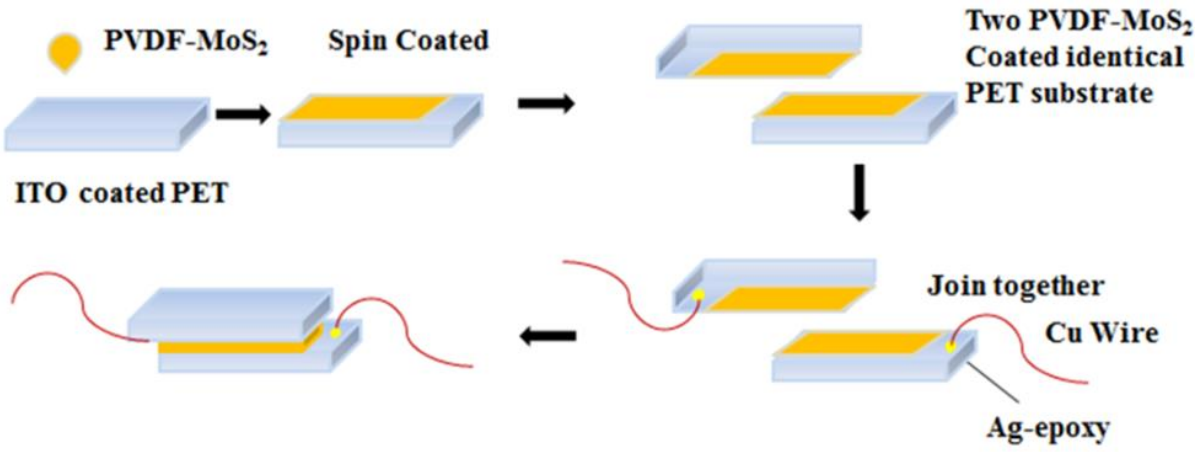

Scheme:3.2 Schematic fabrication steps of PVDF-MoS_2 nanocomposite flexible piezoelectric nanogenerator.

3.2.4 Characterizations:

The phase and crystallinity of PVDF and PVDF–MoS_2 composites were investigated by X-ray diffraction (PANalytical X-PERT PRO) using Cu-Kα radiation (1.54A°). Fourier transform infrared (FTIR) spectroscopy was carried out using a JASCO FTIR-6300 spectrometer. Surface profiles of the device structure and the elemental composition of these nanocomposites were examined using a field-emission scanning electron microscope (FE-

SEM) with an electron energy ~20 keV and equipped with an energy-dispersive X-ray (EDAX) spectrometer. The morphology of chemically exfoliated MoS_2 nanosheets was investigated using a high-resolution transmission electron microscope (HRTEM, FEI-TECNAI G2 20ST, energy ~200 keV). Absorption spectrum of chemically exfoliated MoS_2 nanosheet was measured using a UV-Vis spectrometer (Shimadzu -UV-Vis 2600 Spectrophotometer) and Raman spectrum was recorded with a spectrometer (LabRam HR Evolution; HORIBA France SAS-532nm laser). A Keithley 2450 source meter and a digital oscilloscope (SMO702 (scientific)) were used for the electrical measurements.

3.3 Results and discussions:

3.3.1 Structural and Spectroscopic Studies of MoS_2 nanosheets:

A typical transmission electron micrograph of exfoliated MoS_2 nanosheets is presented in Figure 3.1(a), indicates the formation of nanosheet. The HRTEM micrograph shown in Figure 3.1(b) reveals an interlayer spacing of ~ 0.27 nm, which corresponds to the (100) plane of semiconducting 2H -MoS_2 . The selected area electron diffraction (SAED) pattern (Figure 3.1(c)) indicates the hexagonal crystal structure. The AFM image (Figure 3.1(d)) shows the exfoliation of a few layers (~ 2-3) of two-dimensional material.

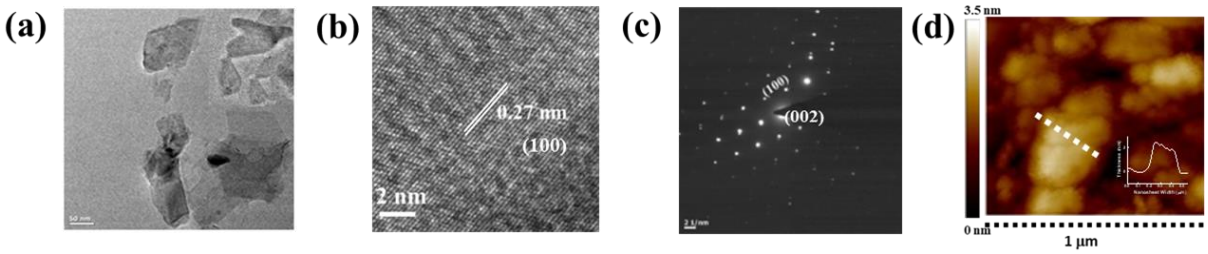

Figure 3.1 (a) Representative TEM image of chemically exfoliated MoS_2 nanosheets. (b) HRTEM shows an inter-planar spacing of 2H-MoS_2 (100) phase. (c) Selected Area Electron Diffraction (SAED) pattern of MoS_2 nanosheets. (d) AFM image of chemically exfoliated MoS_2 nanosheets and inset shows the height profile.

In the absorbance spectrum characteristic peaks are observed at 675 nm and 615 nm marked as exciton A, B respectively in Figure 3.2(a). In Raman spectrum two characteristics modes of vibration A_{1g} and E^1_{2g} of MoS_2 assigned to the out-of-plane and in-plane vibrations of the Mo and S atoms, respectively, are shown in Figure 3.2(b). The characteristic peaks for A_{1g} and E^1_{2g} vibrations are occurred at 405 and 382 cm^{-1} respectively, for the exfoliated MoS_2 nanosheets. Both the absorbance and Raman spectrum agrees with formation of few layered exfoliated MoS_2 nanosheets. From the XRD diffraction pattern (Figure 3.2(c)) peak at 14.4^o indicates the formation of (002) plane of MoS_2 nanosheet which indicates the good crystallinity of exfoliated MoS_2 nanosheets.

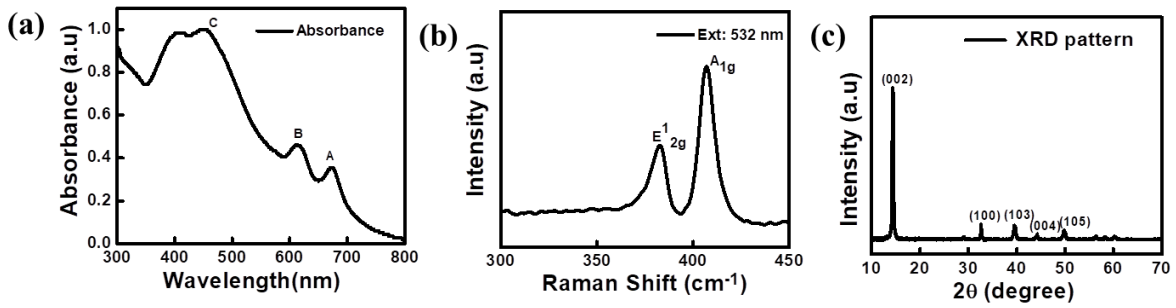

Figure 3.2 (a) Absorbance spectra (b) Raman spectra (c) XRD pattern of exfoliated MoS_2 nanosheets.

3.3.2 Structural Studies on PVDF-MoS_2 nanocomposite:

SEM micrographs of control (untreated) PVDF and PVDF-MoS_2 nanocomposite presented in Figure 3.3(a) & (b) indicate that MoS_2 nanosheets are distributed within the PVDF matrix. A magnified FESEM image in Figure 3.3(c) suggests that embedded MoS_2 nanosheets are dispersed randomly.

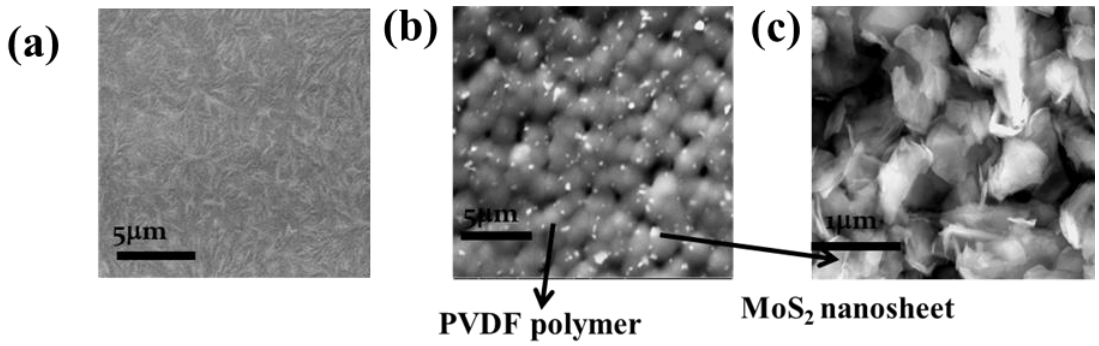

Figure 3.3 SEM images of (a) control PVDF (b) PVDF-MoS_2 nanocomposite and (c) Magnified view of PVDF-MoS_2 nanocomposites shows embedded MoS_2 nanosheets within PVDF.

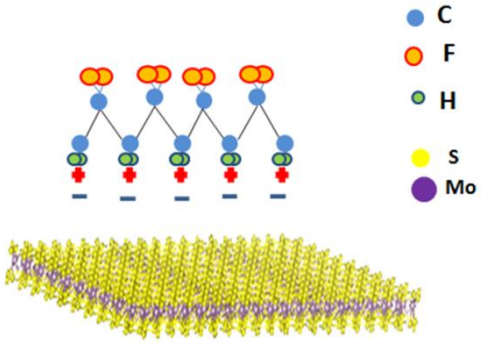

Scheme:3.3 Schematic mechanism of attachment of PVDF with MoS_2 nanosheets due to van-der-Waals interactions.

It is known that PVDF is a semi-crystalline polymer which exhibits five crystalline phases, namely α, β, γ, δ, ε phases differ in lattice types and chain formation ability.[1,39]. X-ray diffraction (XRD) pattern in Figure 3.4(a) of control (untreated) PVDF shows prominent peaks at 18.3°, 19.9°, 26.6°, which are evidences of formation for α–phase [39]. On the other hand, PVDF-MoS_2 nanocomposite exhibits two dominant diffraction peaks, one is related with 2H-MoS_2 (002) plane at 14.4° and the other broad peak is ascribed due to PVDF. By deconvolution of this broad diffraction peak, prominent α–phase feature at 18.3° and a dominant β–phase peak at 20.5° are observed, as shown in the inset of Figure 3.4(a). Thus XRD results confirm the formation of crystalline β–phase in PVDF, which is essential to

attain spontaneous polarization which leads to the piezoelectric characteristics [49]. It is be noted that the commonly observed α–phase does not exhibit any piezoelectric behavior, because of the anti-parallel stacking of (-CH_2-/-CF_2-) dipoles [2]. Fourier transform infrared (FTIR) spectra of control PVDF (untreated) exhibits absorption peaks at 614, 763 and 795 cm^{-1} (Figure 3.4(b)), which can be related to the mixed CF_2 bending, C-C-C skeletal vibration and in-plane bending/rocking vibrational modes, for α–phase [49] respectively. Two additional peaks occurred at 532 cm^{-1} and 975 cm^{-1} and these peaks are attributed due to the formation of α–phase [50]. In both control PVDF and PVDF-MoS_2 nanocomposites, the characteristics peaks of β-phases are observed at 510 and 1074 cm^{-1} [50,51], while the evidence of γ-phase is observed at 482, 1176 and 1234 cm^{-1} peaks [3,51]. Apart from these, the peak obtained at 1404 cm^{-1} is considered to be the combined contribution of both the β and γ–phases [50]. For PVDF-MoS_2 nanocomposites, two new absorption peaks are observed prominently at 840 and 1275 cm^{-1}, which are attributed to CH_2 rocking /CF_2 asymmetrical stretching and C-F stretching vibrations, respectively exhibiting the evidence of the formation of crystalline β–phase [52]. Moreover, the peaks corresponding to the α–phase features at 532, 614, 763, 795 and 975 cm^{-1} are almost diminished intensity. From FTIR absorption measurements, the fraction of electroactive β–phase in the PVDF-MoS_2 nanocomposite is estimated to be 0.815, this high value necessary for enhancing the piezo responses. Thus both XRD and FTIR studies it can be established that the presence of MoS_2 nanosheets filler leads to the nucleation of piezoelectric β–phase [49] in PVDF-MoS_2 nanocomposite. It may be noted that the negatively charged MoS_2 surface (difference in electronegativity between S and Mo atoms)can interact with the CH_2 (positive site) of H-C-F polymer dipoles, which can enhance the Van-der-Waals (electrostatic) interactions between 2D MoS_2 nanosheets and PVDF chains, engender a "super-2D-confinement" [49]. It results in the enhancement of electroactive β-phase in the nanocomposites. Such modulation in crystallization is consistent with the surface charge induced crystallization phenomenon which are reported for various fillers such as $BaTiO_3$, clays, ionic salts, carbon nanotubes etc. in a PDVF matrix [27,53-56]. The presence of electrostatic interactions between n-type MoS_2 nanosheets and the polymer chain leads to the alignment of dipoles and helps for the nucleation of β–phase and is shown in Scheme:3.3. Due to presence of MoS_2, under application of an external force changes the dipolar distribution within the composite by inducing PVDF the dipoles to align along the direction of the mechanical force, which result the enhancement of piezo-response.

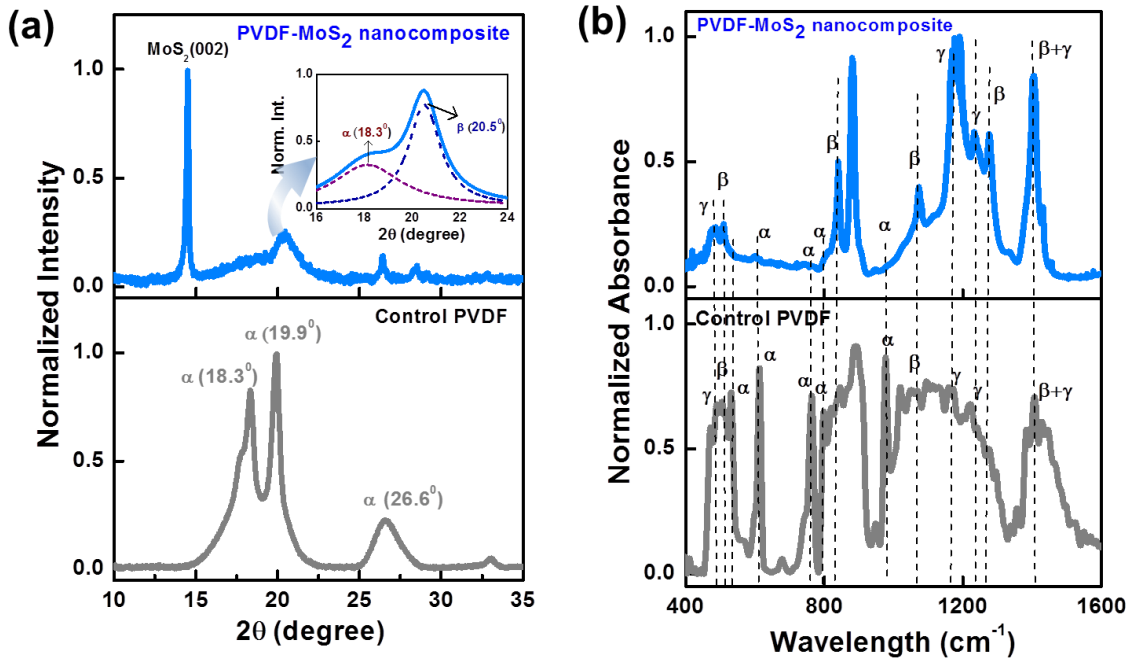

Figure 3.4 (a) X-ray diffraction pattern and (b) FTIR absorption spectra of control PVDF (bottom panels) and PVDF-MoS_2 nanocomposite (top panels). The inset in the top panel of Figure (a) reveals the formation of an electroactive β–phase within PVDF-MoS_2 nanocomposites.

3.3.3 Piezoelectric Studies:

A typical cross-sectional SEM image of the nanogenerator device structure in Figure 3.5(a) depicts that a nanocomposite film is ~100 μm thick (including the two ITO-PET electrode the device is ~300 μm thick) is sandwiched between two ITO -PET substrates. Under application an instantaneous external mechanical forces on the fabricated device, a pulsed type voltage waveform is obtained. In absence of an external applied force, there is no electrical output voltage due to net zero dipole moment. By application of vertical compression, the distribution of dipoles within the nanocomposite is altered leading to generation of a piezoelectric potential, which is schematically displayed in Figure 3.5(b). Positive and negative charges are accumulated on the two electrodes to screen the developed piezoelectric potential, which results generation of a positive voltage signal from the piezoelectric nanogenerator device corresponding to the first positive peak shown in Figure 3.5(c). When the vertical compression is released, the dipolar alignment inside the nanocomposite is deformed and consequently the developed piezo-potential across the electrodes diminishes.

These accumulated charges are transported back in the reverse direction and a negative pulse is observed and also is depicted in Figure 3.5(c). Piezoelectric output voltages from the control PVDF (Figure 3.5(d) & (e)) and self-poled PVDF-MoS_2 (Figure 3.5(f) & (g)) piezoelectric devices have been measured under application of vertical periodic compression and release process using finger tapping and mechanical impact. The finger tapping and external mechanical impacts are measured to be ~0.08N, 0.3N, and the effective impact areas of the devices being 0.26 cm^2 and 0.28 cm^2, respectively. The calculation of mechanical pressure induced by falling object (here pressure imparting by variable weight mass) is based on the physical model combining the gravity term and interval between pulse term. It is based on the simple classical mechanical kinetic energy and momentum theorem

$$mgh = \frac{1}{2}mv^2 \qquad (3.1) \qquad v = \sqrt{2gh}$$

$$F = \frac{mv}{\Delta t} + mg \qquad (3.2)$$

$$P = \frac{F}{A} \qquad (3.3)$$

Where m is the mass of the falling object, h is initial distance between the impacting mass and the PENG, v is maximum falling velocity of the object. And A is the effective contact area between the impacting mass and the PENG, g is the gravitational acceleration.

Output voltages of piezoelectric nanogenerator (PENG) devices measured by simple finger tapping are depicted in Figure 3.5(d) & (f). It is observed that the PVDF-MoS_2 PENG device exhibits an output voltage 4.5 V with a sensitivity ~1.45 V/kPa, a highly enhanced (~67 times) piezoelectric performance over the control PVDF device one. Furthermore, a much higher piezoelectric output voltage (22 V) is obtained upon applying the devices to a higher mechanical impact (~10.6 kPa), as depicted in Figure 3.5(e) and (g) for control and nanocomposite devices, respectively. The sensitivity of the PENG is defined as, $Sensitivity\ (S) = \frac{V_{out}}{F}$, Where V_{out} is the obtained piezoelectric output voltage and F is the magnitude of impact on the nanogenerator. The generation of a high piezo-voltage (with a sensitivity ~2.07 V/kPa) in the nanocomposite device using mechanical impact, is unprecedented and numerically much higher than those reported earlier by using any two dimensional materials (Table-3.1). The use of MoS_2 as a nano-filler within PVDF results in a net increase in the dipole moment along the stress induced direction and thereby enhances the potential difference across the electrodes, which causes an upsurge in the output voltage [49].

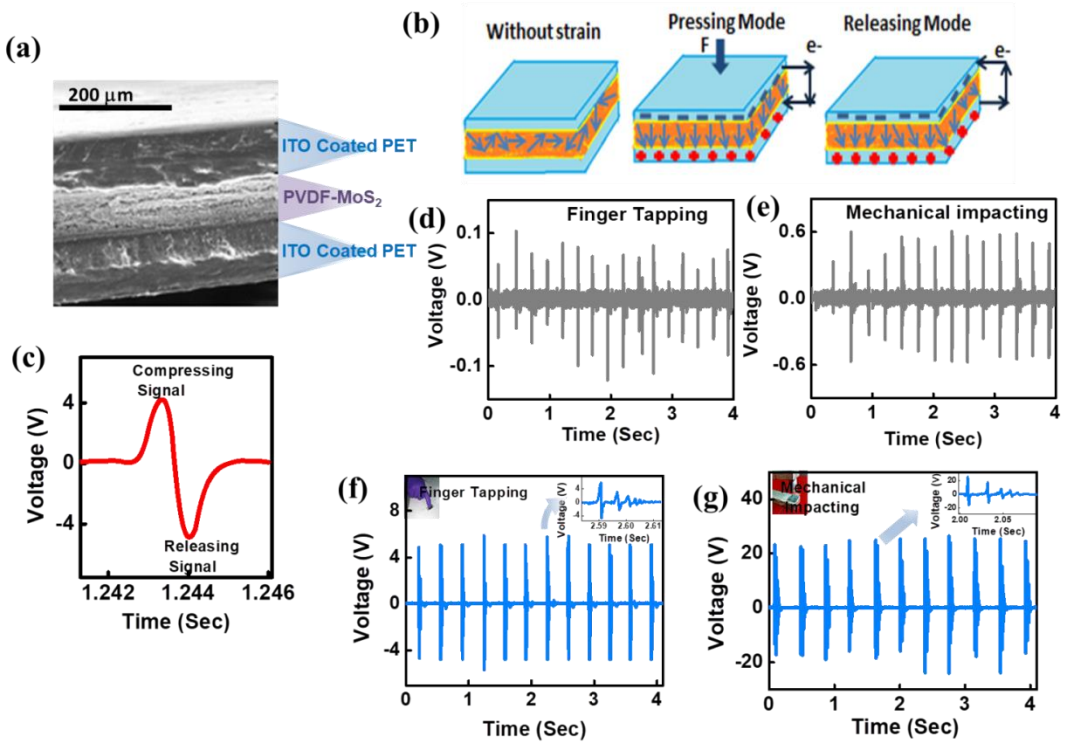

Figure 3.5 (a) Cross-sectional SEM image of the PENG device by using PVDF-MoS_2 nanocomposite. (b) Schematic representation of operation of a self-poled PENG nanogenerator. (c) Typical output waveforms from the PENG during press and release. Piezoelectric output voltages for control PVDF nanogenerator by (d) Finger tapping and (e) Mechanical impact (~10.6 kPa). Corresponding output voltages from the device using PVDF-MoS_2 nanocomposite by (f) Finger tapping and (g) Mechanical impact (~10.6 kPa), with their insets representing magnified views of voltage waveforms.

Along with the intense piezo-voltage, a secondary output (as a consequence of the damped piezoelectric signal) arising from the elastic restoring force between the composite film and PET substrates can be recorded (inset of Figure 3.5(f) and (g)). Observation of such damped piezoelectric output voltages is in agreement with earlier reports using $FAPbBr_3$NPs - PVDF composite films [1] and $FAPbBr_3$ nanoparticles–PDMS composites encapsulated between two electrodes [57].

To investigate the effect of filler MoS_2 nanosheet concentration on the performance of the piezoelectric nanogenerators, devices have been fabricated with different wt.% of MoS_2 as

nano-fillers in PVDF matrix. The piezoelectric output voltage increases with increasing the filler concentration and reaches a saturation voltage value for a filler concentration of ~0.20%, as depicted in Figure 3.6(a) and (b). The increase in the effective dielectric permittivity with concentration of MoS_2 nanosheets leads to an enhanced polarization within the composite, which is the prime reason for the generation of the observed enhanced high piezoelectric outputs [1,2]. The increment in filler concentration above a certain value (~0.20%) affects the viscosity of the nanocomposite in which results the formation of a non-uniform film. We therefore keep the filler concentration optimized at 0.2% in the nanogenerator devices for the rest of the investigation.

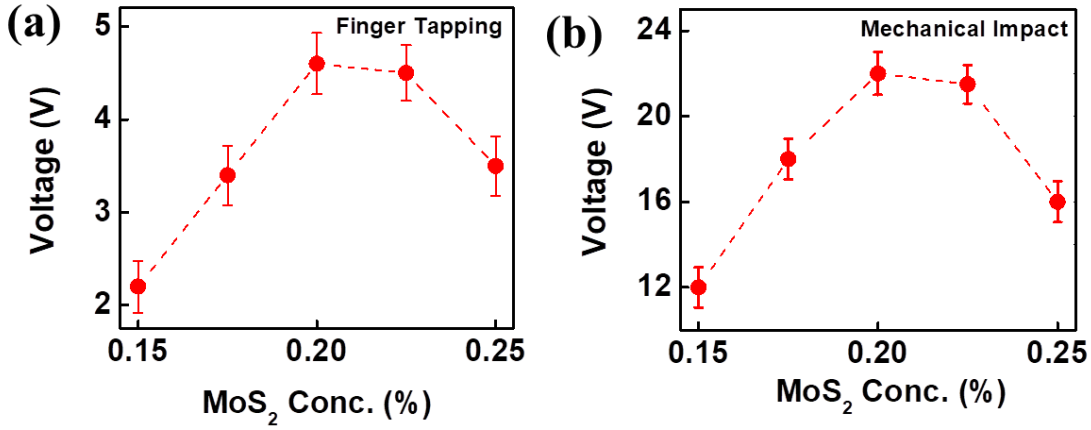

Figure 3.6 Piezoelectric output voltage with varying filler concentration by (a) Finger tapping and (b) Mechanical impact (~10.6 kPa) onto the PVDF-MoS_2 PENG.

The ITO contacts form an almost perfect Ohmic contact with electrically n-type MoS_2, which is helpful for charge transfer between ITO-MoS_2 layers (Figure 3.7(a)). Besides that the thickness of the nanocomposite film can be controlled by varying the spin-coating time, speed, so the effect of film thickness on piezoelectric output voltages is studied. From this study the optimized film thickness (~100 μm) has been used for further study (Figure 3.7(b) and (c)).

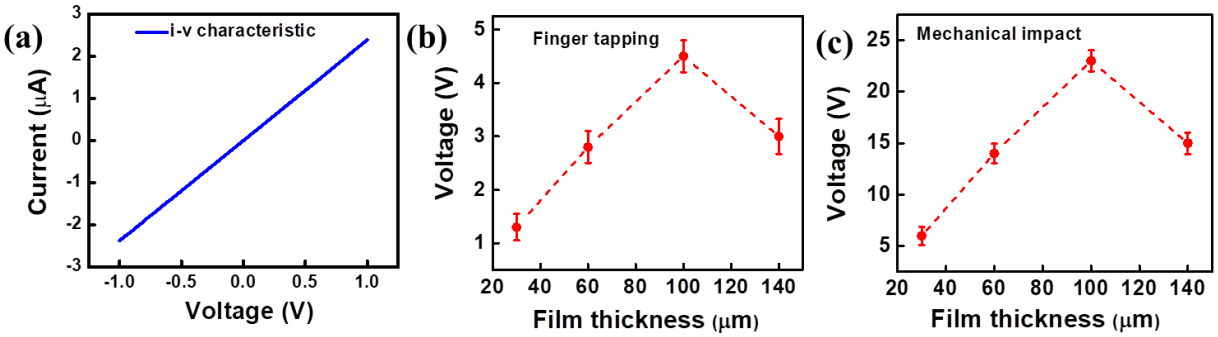

Figure 3.7 (a) I-V characteristics of the PVDF-MoS_2 PENG device. The variation of piezo-electric output voltage with variable film thickness due to (b) Finger tapping, (c) Mechanical impact.

We have also measured the piezoelectric output voltage and generated power from PVDF-MoS_2 nanogenerator across a varying load resistance (500 kΩ – 100 MΩ) using simple finger tapping with a very low mechanical impact (~3.1 kPa). While the piezo-output voltage of the self-poled nanogenerator device is found to increase as a function of load resistance, a maximum power density ~88.5 μW/cm^2 is obtained under a load resistance of ~ 1 MΩ, as depicted in Figure 3.8(a). As the load resistance is increased further the power density decreases due to reduction of output current. We have compared our performance with other reported results using 2D filler based PVDF piezoelectric nanogenerators (PENGs) in Table-3.1. We have observed that the performance of the present PVDF-MoS_2 based device is much superior as compared to similar types of PENGs. The fabricated PENG devices are found to be extremely sensitive to the minute external impact and have been tested by using varying mechanical force (different weights from a fixed height), as schematically shown in Figure 3.8(b). The open circuit output voltage is found to be increased with increasing weight and depicted in Figure 3.8(c), which indicates that the fabricated PENGs are also promising devices for pressure sensing purposes [38,58,59]. During the detection of very low pressure due to the impact of a small mass, the sensitivity of the PVDF-MoS_2 PENG has been found to be ~0.117 V/ Pa. Hence, this PENG can distinguish small change in mechanical impact precisely and it is suitable for the detection of low impact forces.

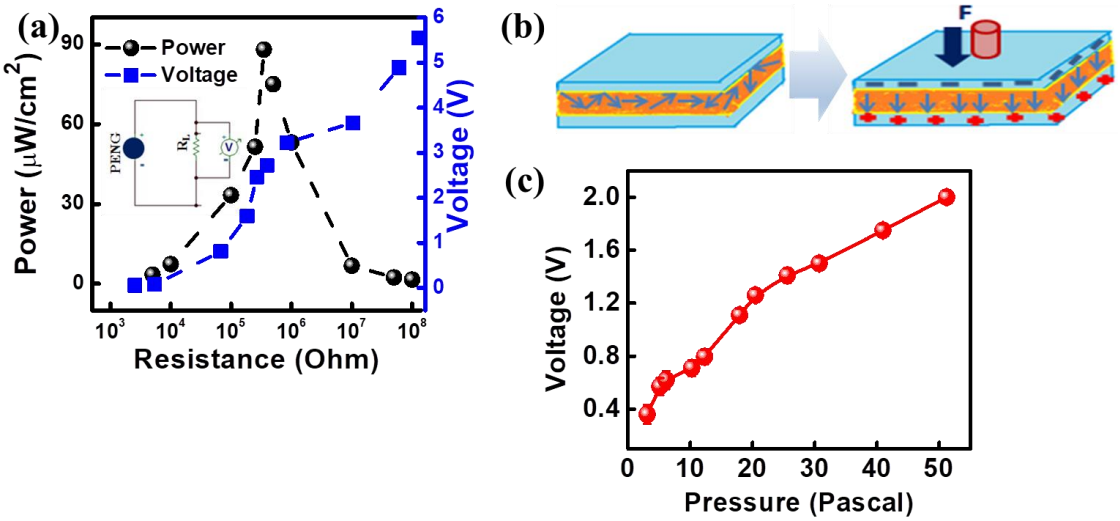

Figure 3.8 (a) Piezoelectric output power density and voltage from the PVDF-MoS_2 PENG with finger tapping for varying load resistance and inset shows the corresponding circuit diagram. (b) Schematic representation of applying a mechanical force & pressure using variable weight and (c) Variation of output voltage with pressure on PVDF-MoS_2 nanogenerators.

Similar to tapping, bending of the flexible PVDF-MoS_2 PENG devices also found to produce output voltage, which is 25 times higher than that of the control PVDF device under the same bending (applied strain) condition. The representative figures are provided in Figure 3.9(a) and (b) under an external mechanical strain of ~0.11%.

In this experiment, the mechanical strain (ε) in bent condition has been generated by a home-made bending set up. The strain on the film was calculated by considering the film thickness and the effective bending radius by following the relation $\varepsilon = \frac{h_s}{2R_o}$ where h_s is the thickness of the PENG device and R_o is the bending radius

$$R_o = \frac{L}{2\pi\sqrt{\frac{dL}{L} - \frac{\pi h_S^2}{12L^2}}} \qquad (3.4)$$

Where L is the undeformed original length, dL is the change of length due to bending.

Thus the fabricated light-weighted, flexible PENGs can be used as an energy harvesting wearable sensors, which are suitable of monitoring various human physiological signals, as they produce output voltages upon movement of different parts of human body (Figure 3.9(c) & (d)). The sensitivity of energy harvesting from the flexible PENG upon simple human activities is comparable with the previously reported results [35,44,55] by using PVDF based nanocomposites, making those attractive for wearable electronics applications.

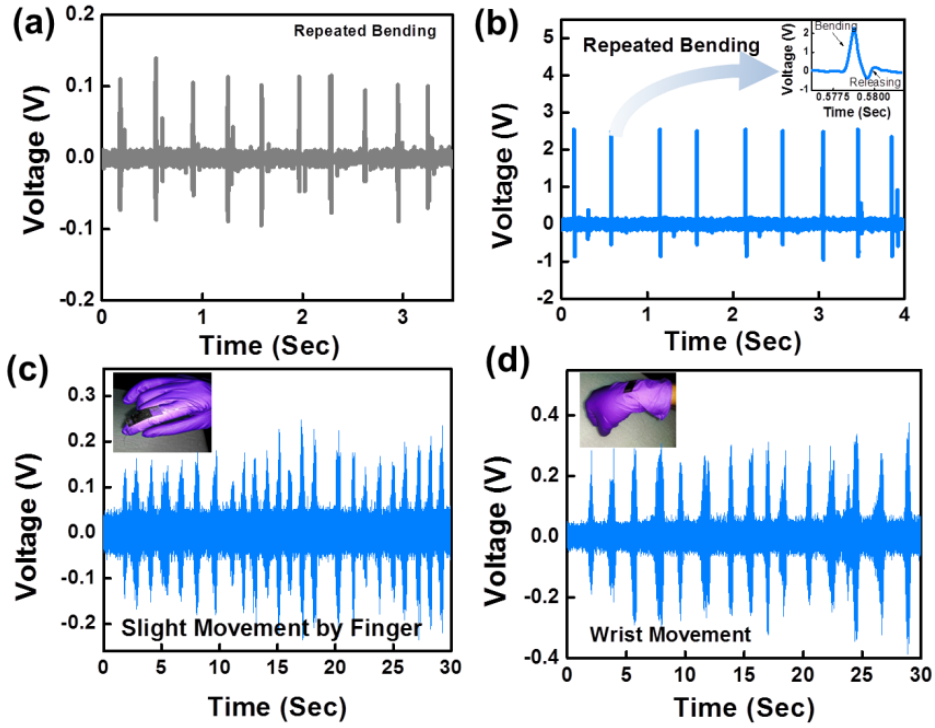

Figure 3.9 PVDF-MoS_2 PENG piezo-output waveforms due to repeated bending from (a) Control PVDF and (b) PVDF-MoS_2 PENG devices with application of mechanical strain of ~ 0.11%. Inset in Figure (b) presents a magnified view of the voltage profile. Piezoelectric output voltage due to bio-mechanical activities from the PVDF-MoS_2 PENG due to (c) Movement of a finger and (d) Movement of wrist.

The piezoelectric performance of PENG devices has also been investigated by connecting these in parallel as well as in series configurations. When two PENG devices with an individual output voltage of~ 10 V (under ~5 kPa mechanical stress) are connected in series, the peak output voltage is increased to ~20 V (Figure 3.10), nearly equal to the sum of two peak voltages from each nanogenerator. It reveals that PVDF-MoS_2 integrated PENG devices

follow the general rules of cell connections in agreement with the previously reported PVDF-based PENGs [60].

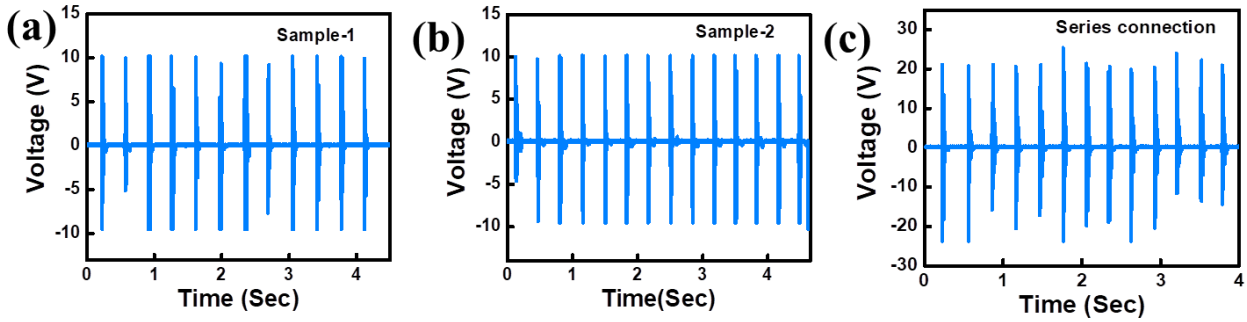

Figure 3.10 Piezoelectric output voltage from PVDF-MoS_2 devices for (a) sample-1 (b) sample-2 and (c) samples are in series connection.

We have used the PENG device to charge up a capacitor through a full-wave bridge rectifier circuit, shown in Figure 3.11(a) under bending and released conditions. Under the bending condition, the nanocomposite PENG is able to charge a commercial 1.2 µF capacitor up to 3.5 V within 70 s, as shown in Figure 3.11(b) and the charging efficiency is observed to be higher than other previously reported results [1,3]. The inset of Figure 3.11(b) presents the charging characteristics of different capacitors. We have estimated the stored electrostatic energy within the capacitor by using the relation $E_{stored} = \frac{CV^2}{2}$, where C is the capacitance and V is the charging voltage across the capacitor under the steady state condition for a definite time. The stored energy across this capacitor is found to be 7.35 µJ, which can be considered to be quite higher than for two-dimensional-PVDF based PENG devices [38,59]. The energy conversion efficiency (η) of the PVDF-MoS_2 composite nanogenerator can be estimated from the ratio, $\eta = \frac{E_e}{E_s}$ where E_s is the mechanical strain energy and E_e is the average energy stored in the capacitor. The mechanical strain energy can be expressed as $E_s = \frac{YAL\sigma^2}{2}$, where A is the effective area (1.0×1.0 cm^2), L is the thickness of composite~ (~300 µm), σ is resultant strain ~ 0.11% and Y is the Young's modulus of the composite. The Young's modulus of the composite has been estimated to be 2.126 GPa by using the rule of

mixtures (270 GPa for MoS_2 and 2.17 GPa for PVDF) [61,62] and Young's modulus of the nanocomposite is estimated as,

$$E_c = fE_f + (1 - f)E_m \qquad (3.5)$$

Whereas f is filler fraction, E_f is Young's modulus of filler, E_m is the Young's modulus of matrix. The estimated stored mechanical energy is estimated to be 4.108×10^{-5} J and the energy conversion efficiency of the nanogenerator is ~ 17.8%. The efficiency value is comparable to or much higher than the other reported PVDF matrix based nanogenerators using these two-dimensional materials [2,38]**.** The capacitor charged by the nanogenerator can be used to drive commercial LEDs (different colours-red, yellow, green) having output power ~ 110 mW (max.) each and a forward current of ~ 25 mA (max.), as presented in the Figure 3.11(c), demonstrating their efficacy for practical application purposes. Finally the stability of the flexible nanogenerator has been verified upon by recording the output voltage from the device after keeping it in the ambient laboratory condition for a long time (~ eight weeks). Figure 3.11(d) exhibits that no significant reduction in the output voltage (under 10.6 kPa mechanical impact) is observed for an eight week old device, as compared to the freshly prepared one. The superior stability and fatigue-free performance (on repeated bending cycles) of PVDF-MoS_2 PENGs without any significant change in output voltage have demonstrated its potential as an effective energy harvesting device that can be useful for real life practical applications.

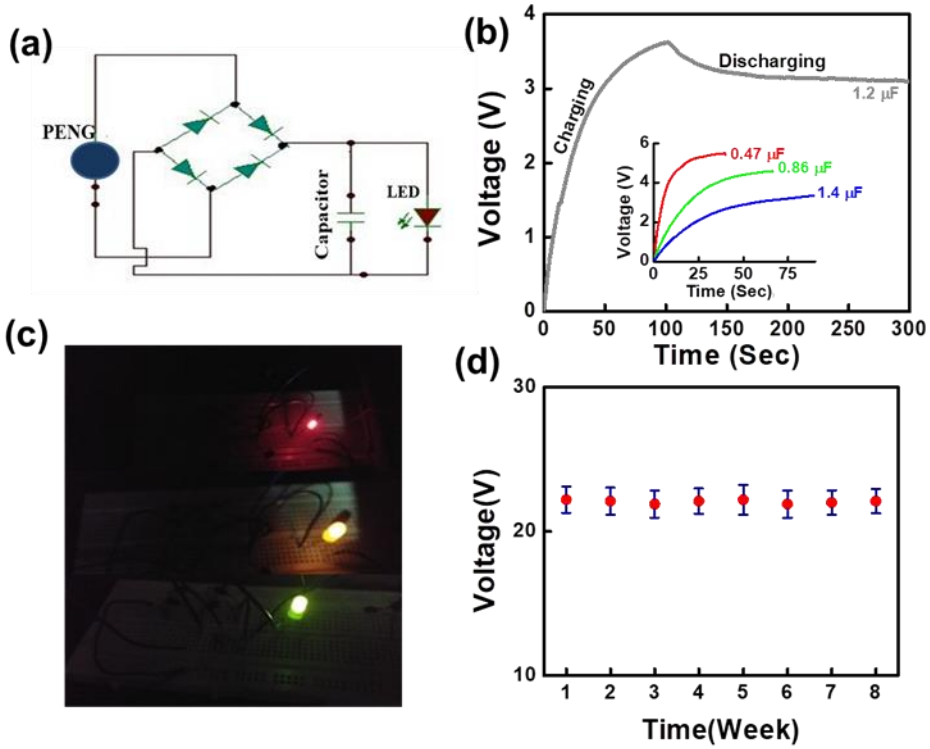

Figure 3.11 (a) Circuit diagram for charging a capacitor for driving commercial LEDs. (b) Charging and discharging of a typical capacitor of capacitance 1.2 μF, the inset represents the charging characteristics of different capacitors. (c) Glowing of different colour multiple LEDs and (d) Stability of output voltage of PVDF-MoS_2 PENG nanocomposite device as a function of time under a mechanical impact of 10.6 kPa.

Table-3.1 Comparison of output performance of composite piezoelectric nanogenerators using 2D materials / halide perovskites and PVDF

System	**Poling and not polling**	**Configuration of the device**	**Nature & magnitude of mechanical impact force/pressure**	**Piezo-output /Output Power density**	**Efficiency**	**Type of body movement and output voltage**	**Ref**
PVDF-TrFE and GO	Electrical poling 300 kV/cm	Au/PVDF-TrFE-GO/ITO-PET	Pressure ~ 320 kPa	0.0134V/kPa 4.41 μW/cm^2			45
Graphene-AgNP-PVDF	Self-poled	Electrode/PVDF-G-Ag/Electrode	Pressure ~ 5.2 kPa	0.0192 V/kPa 0.75 nW/cm^2	15%		38
PVDF-AlO-rGO	Self-poled	Al// PVDF-AlO-rGO/Al with PDMS encapsulation	Pressure ~ 31.19 kPa	1.15 V/kPa 3.63 μW/ cm^2	12.47 %		2
PVDF-GO	Self-poled	Cu/PVDF-GO/Cu with PDMS encapsulation	Force ~12 N	0.175 V/N		Finger bending 0.06V	44
RGO-P(VDF-TrFE)-PMN-PT	Electrical poling~ 50 kV/cm	Al foil/ RGO-P(VDF-TrFE)-PMN-PT/ITO-PET	Force ~2 N	2.5 V/N 6.5 μW/cm^2			43
PVDF/Nafion/GQD	Solution casting and pressure crystallization	Al/ PVDF-Nafion-GQD/Al	Force ~ 60 N	0.066 V/N			36
PVDF/Graphene coating on Fabrics	Electromagnetic punch	Al/ PVDF-Graphene coated Fabric/Al	Force~ 0.45N	34 V/N		Running~1.0 V	35

Ce3+-doped PVDF/Graphene	Electrospinning 1.2 kV/cm	Electrode/PVDF-Ce-G/Electrode	Pressure ~6.6 kPa	1.66 V/kPa 0.052 μW/cm^2			59
Graphene -PVDF-BaTiO3	Electrical poling ~150 kV/cm	PET-ITO/ G-PVDF-BTO/Au-PET	Force~ 10 N	0.7 V/N 0.72 μW/cm^2			42
RGO- PVDF-TrFE-$BaTiO_3$	Electrical poling ~50 kV/ cm	PDMS-Au/ RGO-PVDF-TrFE-$BaTiO_3$/Cu-PET	Force~ 2 N	2.5 V/N 0.6 μW/cm^2			41
PVDF-GO	Electrospinning 1.041 kV/cm	Cu-Ni polyester fabric/PVDF NF-GO/ Cu-Ni polyester fabric	Finger Pressure ~ 8.8 kPa	0.79 V/kPa 0.62 μW/cm^2		Wrist movement 0.05 V	55
MoS_2-PVDF	Electrospinning 0.833 kV/cm	Electrode/ MoS_2-PVDF /Electrode	Pressure ~ 8.8 kPa	1.59 V/kPa 16 nW/cm^2			48
Functionalized GO-PVDF fiber	Electrospinning 1.33 kV/cm	Al foil-Cu wire/ Functionalized GO-PVDF fiber/ Al foil-Cu wire	Pressure ~ 8.61×10^4 kPa	7.2×10^{-3} V/kPa 48.3 μW/cm^2			40
PVDF-$MASnI_3$	Electric polling 50 kV/cm	ITO-PET/PDMS/ PVDF-$MASnI_3$/Au-PI	Pressure ~500 kPa	7.6×10^{-3} V/kPa 21.6 μW/cm^2			24
PVDF-$MAPbI_3$	Electrical polling 80 kV/cm	Au-PI/PDMS/ PVDF-$MAPbI_3$/PDMS/ITO-PET	Force ~ 50N	0.91 V/N			25
PVDF-$FAPbBr_3$	Electrical Polling 50 kV/cm	Au-Cr PET/ PVDF-$FAPbBr_3$ NP/ Au-Cr PET	Pressure ~500 kPa	0.06 V/kPa	0.55%		1
PVDF- $CsPbBr_3$	Self-poled	Electrode/ PVDF-$CsPbBr_3$/Electrode	Pressure ~10^5kPa	1.2×10^{-3} V/kPa			26
PVDF-MoS_2	Self-poled	**ITO-PET/PVDF-MOS_2/ ITO-PET**	**Pressure ~~ 10.6 kPa**	**2.07 V/kPa (73.33 V/N) 88.5 μW/cm^2**	17.8%	Finger bending 0.15 V Wrist movement 0.3 V	This study

3.4 Summary:

Mechanically flexible, self-poled PVDF-MoS_2 PENGs have been fabricated by using chemically exfoliated two-dimensional MoS_2 nanosheets and PVDF polymers. The exfoliated MoS_2 enhances the fraction of electroactive, piezoelectric β-phase at an optimized filler concentration of ~0.20 %, results a drastic enhancement in the nanogenerator performance over the bare PVDF based devices. Fabricated PVDF-MoS_2 nanogenerators exhibit a record piezoelectric output of ~ 2.07 V/kPa (22 V at 10.6 kPa) and superior power density (~88.5 μW/cm^2) which are comparable or higher than the otherwise reported 2D materials based nanocomposite systems. This hybrid nanogenerator is also able to generate piezoelectric output under a very low mechanical strain (~2.5 volt for 0.11% strain) and is very sensitive (~ 4.5 V) towards human finger touch, which paves a promising application of energy harvesting by utilizing everyday biomechanical activities. Besides that the fabricated PENG is flexible and it needs low cost fabrication process, (here we have avoided costly physical

vapor deposition process) and completely eco-friendly. The experimental evidence of charging of a capacitor and the glowing of light sources without any external power supply led us to predict that the appropriate design of this PENG can explore its application to power up different portable electronic gadgets, which can be used in our everyday life. This PENG offers very good piezoelectric characteristics associated with high strain sensitivity that enable us to detect very minute external impact and can also harvest energy from biomechanical activities suggesting their use as a motion sensor, detection, wearable electronic devices and health monitoring purposes. The reported results of the present investigation with distinctive features exhibiting superior piezo-voltage, high strain sensitivity, energy harvesting from bio-mechanical motion and excellent durability make the flexible nanocomposite PENGs attractive for future wearable, stretchable and portable electronic devices.

3.5 References:

1. R. Ding, X. Zhang, G. Chen, H. Wang, R. Kishor, J. Xiao, F. Gao, K. Zeng, X. Chen and X. W. Sun, Nano Energy, 2017, **37**, 126-135.
2. S. K. Karan, R. Bera, S. Paria, A. K. Das, S. Maiti, A. Maitra and B. B. Khatua, Adv. Energy Materials, 2016, **6**, 1601016.
3. S. K. Ghosh and D. Mandal, Nano Energy, 2018, **53**, 245-257.
4. S. K. Ghosh, T. K. Sinha, B. Mahanty and D. Mandal, Energy Technol., 2015, **3**, 1190-1197.
5. Q. Zheng, H. Zhang, H. Mi, Z. Cai, Z. Ma and S. Gong, Nano Energy, 2016, **26**, 504-512.
6. M. Pusty, L. Sinha and P. M. Shirage, New J. Chem., 2019, **43**, 284-294.
7. Z. L. Wang and J. Song, Science, 2006, **312**, 242-246.
8. G. Zhu, R. Yang, S. Wang and Z. L. Wang, Nano Lett., 2010, **10**, 3151-3155.
9. J. H. Jung, M. Lee, J.-I. Hong, Y. Ding, C.-Y. Chen, L.-J. Chou and Z. L. Wang, ACS Nano, 2011, **5**, 10041-10046.
10. Y. Hu, Y. Zhang, C. Xu, G. Zhu and Z. L. Wang, Nano Lett., 2010, **10**, 5025-5031.

11. Z.-H. Lin, Y. Yang, J. M. Wu, Y. Liu, F. Zhang and Z. L. Wang, J. Phys. Chem. Lett., 2012, **3**, 3599-3604.
12. B. K. Yun, Y. K. Park, M. Lee, N. Lee, W. Jo, S. Lee and J. H. Jung, Nanoscale Res. Lett., 2014, **9**, 4.
13. E. J. Lee, T. Y. Kim, S.-W. Kim, S. Jeong, Y. Choi and S. Y. Lee, Ener. & Envir. Sci., 2018, **11**, 1425-1430.
14. C. H. Wang, W. S. Liao, Z. H. Lin, N. J. Ku, Y. C. Li, Y. C. Chen, Z. L. Wang and C. P. Liu, Adv. Energy Mater, 2014, **4**, 1400392.
15. K. Y. Lee, B. Kumar, J.-S. Seo, K.-H. Kim, J. I. Sohn, S. N. Cha, D. Choi, Z. L. Wang and S.-W. Kim, Nano Lett., 2012, **12**, 1959-1964.
16. Y. Hao, Y. Hou, J. Fu, X. Yu, X. Gao, M. Zheng and M. Zhu, Nanoscale, 2020, **12**, 13001-13009.
17. A. J. Lovinger, Science, 1983, **220**, 1115-1121.
18. W. Zeng, X.-M. Tao, S. Chen, S. Shang, H. L. W. Chan and S. H. Choy, Energy Environ. Sci., 2013, **6**, 2631-2638.
19. M. Kashfi, P. Fakhri, B. Amini, N. Yavari, B. Rashidi, L. Kong and R. Bagherzadeh, J. Indus.Textiles, 2020, 1528083720926493.
20. S. Azmi, S.-M. Hosseini Varkiani, M. Latifi and R. Bagherzadeh, J. Indus.Textiles, 2020, 1528083720928822.
21. M. S. Sorayani Bafqi, R. Bagherzadeh and M. Latifi, J. Indus.Textiles, 2017, **47**, 535-550.
22. G. Zandesh, A. Gheibi, M. Sorayani Bafqi, R. Bagherzadeh, M. Ghoorchian and M. Latifi, J. Indus.Textiles, 2017, **47**, 348-362.
23. M. S. Sorayani Bafqi, M. Latifi, A.-H. Sadeghi and R. Bagherzadeh, J. Indus.Textiles, 2020, 1528083720915835.
24. S. Ippili, V. Jella, J.-H. Eom, J. Kim, S. Hong, J.-S. Choi, V.-D. Tran, N. Van Hieu, Y.-J. Kim and H.-J. Kim, Nano Energy, 2019, **57**, 911-923.
25. V. Jella, S. Ippili, J.-H. Eom, J. Choi and S.-G. Yoon, Nano Energy, 2018, **53**, 46-56.
26. S. Mondal, T. Paul, S. Maiti, B. K. Das and K. K. Chattopadhyay, Nano Energy, 2020, 104870.
27. J. Ma, Q. Zhang, K. Lin, L. Zhou and Z. Ni, Mater. Res. Express, 2018, **5**, 035057.
28. M. Lee, C. Y. Chen, S. Wang, S. N. Cha, Y. J. Park, J. M. Kim, L. J. Chou and Z. L. Wang, Adv. Mater., 2012, **24**, 1759-1764.

29. S. Bayan, D. Bhattacharya, R. K. Mitra and S. K. Ray, Nanotechnology, 2020, **31**, 365401.
30. P. Fakhri, B. Amini, R. Bagherzadeh, M. Kashfi, M. Latifi, N. Yavari, S. A. Kani and L. Kong, RSC Adv., 2019, **9**, 10117-10123.
31. Y. Ahn, J. Y. Lim, S. M. Hong, J. Lee, J. Ha, H. J. Choi and Y. Seo, J. Phys. Chem. C, 2013, **117**, 11791-11799.
32. A. Wang, M. Hu, L. Zhou and X. Qiang, Nanomaterials, 2018, **8**, 1021.
33. H. Yu, T. Huang, M. Lu, M. Mao, Q. Zhang and H. Wang, Nanotechnology, 2013, **24**, 405401.
34. A. Gaur, S. Tiwari, C. Kumar and P. Maiti, Nanoscale Adv., 2019, **1**, 3200-3211.
35. T. Huang, S. Yang, P. He, J. Sun, S. Zhang, D. Li, Y. Meng, J. Zhou, H. Tang and J. Liang, ACS Appl. Mater. Inter, 2018, **10**, 30732-30740.
36. C. Xu, L. Jin, L. Zhang, C. Wang, X. Huang, X. He, Y. Xu, R. Huang, C. Zhang and W. Yang, Composites Sci. and Tech., 2018, **164**, 282-289.
37. Y. Ai, Z. Lou, S. Chen, D. Chen, Z. M. Wang, K. Jiang and G. Shen, Nano Energy, 2017, **35**, 121-127.
38. T. K. Sinha, S. K. Ghosh, R. Maiti, S. Jana, B. Adhikari, D. Mandal and S. K. Ray, ACS Appl. Matter. Interfaces, 2016, **8**, 14986-14993.
39. S. K. Karan, D. Mandal and B. B. Khatua, Nanoscale, 2015, **7**, 10655-10666.
40. S. Tiwari, A. Gaur, C. Kumar and P. Maiti, Sustainable Energy Fuels, 2020, **4**, 2469-2479.
41. U. Yaqoob and G.-S. Chung, Mater. Struct, 2017, **26**, 095060.
42. U. Yaqoob, A. I. Uddin and G.-S. Chung, Appl. Surf. Sci. , 2017, **405**, 420-426.
43. U. Yaqoob, A. I. Uddin and G.-S. Chung, Compos: Part B: Eng., 2018, **136**, 92-100.
44. M. Kim, V. K. Kaliannagounder, A. R. Unnithan, C. H. Park, C. S. Kim and A. Ramachandra Kurup Sasikala, Appl.sci., 2020, **10**, 3493.
45. V. Bhavanasi, V. Kumar, K. Parida, J. Wang and P. S. Lee, ACS Appl. Mater. Interfaces., 2016, **8**, 521-529.
46. W. Wu, L. Wang, Y. Li, F. Zhang, L. Lin, S. Niu, D. Chenet, X. Zhang, Y. Hao and T. F. Heinz, Nature, 2014, **514**, 470-474.
47. S. A. Han, T. H. Kim, S. K. Kim, K. H. Lee, H. J. Park, J. H. Lee and S. W. Kim, Adv. Mater., 2018, **30**, 1800342.

48. K. Maity, B. Mahanty, T. K. Sinha, S. Garain, A. Biswas, S. K. Ghosh, S. Manna, S. K. Ray and D. Mandal, Energy Technol., 2017, **5**, 234-243.
49. K. Cai, X. Han, Y. Zhao, R. Zong, F. Zeng and D. Guo, ACS Sustainable Chem. Eng, 2018, **6**, 5043-5052.
50. X. Cai, T. Lei, D. Sun and L. Lin, RSC Adv., 2017, **7**, 15382-15389.
51. N. R. Alluri, A. Chandrasekhar, J. H. Jeong and S.-J. Kim, J. Mater. Chem. C, 2017, **5**, 4833-4844.
52. P. Sahatiya, S. Kannan and S. Badhulika, Applied Materials Today, 2018, **13**, 91-99.
53. Y. Zhang, L. Ye, B. Zhang, Y. Chen, W. Zhao, G. Yang, J. Wang and H. Zhang, J. Membrane. Sci, 2019, **579**, 22-32.
54. Y. Zhao, Q. Liao, G. Zhang, Z. Zhang, Q. Liang, X. Liao and Y. Zhang, Nano Energy, 2015, **11**, 719-727.
55. K. Roy, S. K. Ghosh, A. Sultana, S. Garain, M. Xie, C. R. Bowen, K. Henkel, D. Schmeiβer and D. Mandal, ACS Appl. Nano Mater., 2019, **2**, 2013-2025.
56. Y. Xin, X. Qi, H. Tian, C. Guo, X. Li, J. Lin and C. Wang, Materials Lett., 2016, **164**, 136-139.
57. R. Ding, H. Liu, X. Zhang, J. Xiao, R. Kishor, H. Sun, B. Zhu, G. Chen, F. Gao and X. Feng, Adv. Funct. Mater, 2016, **26**, 7708-7716.
58. C. Zhang, Y. Fan, H. Li, Y. Li, L. Zhang, S. Cao, S. Kuang, Y. Zhao, A. Chen and G. Zhu, ACS Nano, 2018, **12**, 4803-4811.
59. S. Garain, S. Jana, T. K. Sinha and D. Mandal, ACS Appl. Mater. Inter., 2016, **8**, 4532-4540.
60. Y. Mao, P. Zhao, G. McConohy, H. Yang, Y. Tong and X. Wang, Adv. Energy Mater, 2014, **4**, 1301624.
61. S. Bertolazzi, J. Brivio and A. Kis, ACS Nano, 2011, **5**, 9703-9709.
62. H. S. Kim, D. W. Lee, D. H. Kim, D. S. Kong, J. Choi, M. Lee, G. Murillo and J. H. Jung, Nanomaterials, 2018, **8**, 777.

Chapter: 4

Two dimensional WS_2 embedded PVDF nanocomposites for photosensitive piezoelectric nanogenerators

Benefited with the advantage of low cost, light weight and mechanical flexibility, piezoelectric nanogenerators have potential for applications in renewable energy harvesting from various unexplored sources. Here we report the demonstration of record efficiency flexible piezoelectric nanogenerators (PENG) using composites of polyvinylidene fluoride (PVDF) and chemically exfoliated tungsten disulfide (WS_2) nanosheets, which are found to be strongly photosensitive making them attractive for self-powered optical devices. The presence of two-dimensional (2D) WS_2 nanosheets in PVDF matrix plays a dual role in enhancing the nucleation of electroactive b-phase as well as induces a strong photosensitivity in the nanocomposite. The PVDF-WS_2 composed flexible device is able to produce an enormously high output voltage~116V (for an impact of 105 kPa) and a piezoelectric energy conversion efficiency ~25.6%, which is the highest among the reported values on PVDF-2D materials based piezoelectric nanogenerators. This self-poled piezo-phototronic device exhibits strain-dependent photocurrent at zero bias and displays a responsivity of 6.98×10^{-3} A/W at 0.75% strain under the illumination of 410 nm. The fabricated PENG is also able to harvest energy from routine human activities (finger tapping, writing on a paper, mouse click etc.) and movement of human body parts. The results open up a new horizon in piezo-phototronic materials through the realization of photosensitive multifunctional PENGs, which can be scaled up for fabricating compact, high performance, portable and self-powered wearable electronic devices for smart sensor applications.

4.1 Introduction:

Due to day by day the increasing demand of sensors and IOT based applications, miniaturized nanogenerator (piezoelectric, triboelectric, thermoelectric etc.) devices for driving low power systems are studied with immense interests. The advantage of such nanogenerator devices is that they can easily convert mechanical, optical, thermal energy into electrical energy and abundant resources of them are also available and apart from that, human regular activities are also huge resources of bio-mechanical energy. Amongst the different types of energy harvesting devices, piezoelectric nanogenerators are very promising in energy harvesting due to their efficacy towards portable and wearable electronic devices. Following the first demonstration of ZnO nanowire array based piezoelectric nanogenerator by Wang et al. [1] several famous piezoelectric materials such as, GaN, PZT, $BaTiO_3$, $NaNbO_3$, $LiNbO_3$ etc. have studied [2-9]. Amongst those, inorganic perovskites have high piezoelectric coefficients and exhibit higher piezoelectric performances but those are less selective for

applications in flexible piezoelectric nanogenerator domain due to the lack of durability, bio-compatibility complex synthesis procedure and high toxicity with high production cost. Some other materials with high piezo-coefficients have complicated structures but due to high fabrication cost they are not suitable for commercial applications. On contrary, piezoelectric polymer and copolymers (such as poly-vinylidene fluoride (PVDF)), are attractive for energy harvesting as they possess high piezoelectric coefficient, thermal, mechanical and chemical stability, bio-compatibility and light weight [9-12]. PVDF, the semi crystalline polar polymer generally exhibits active crystalline phases (α, β, γ , δ (polar version of α)) depending on their structural chain configurations [10,13]. Amongst them α–phase (TGTG conformation) is not electroactive and γ–phase (T_3GT_3G conformation) has very low piezoelectric coefficient, whereas β-phase (TTTT conformation) possesses the highest dipole moment per unit volume and is most desirable for piezoelectricity. But commercially available PVDF polymer is mostly found in α–phase, hence are not suitable for piezoelectric nanogenerator fabrication purpose. Previous researches have revealed that the presence of β-phase has massive effect on the piezoelectricity of PVDF [11,14-16]. Presence of β–phase can be achieved through preferential alignment of $–CH_2/-CF_2$ dipoles in the direction normal to the chain axis of PVDF and several techniques such as, mechanical stretching, electrospinning, electrical polling, high temperature annealing have been performed for achieving β-phase [17-20] in PVDF.

Recent studies have reported that incorporation of fillers in PVDF matrix is another effective technique for achieving β-phase. The piezo-characteristics of hybrid nanocomposites by introducing fillers such as, metal nanoparticles, perovskites, semiconductors and two dimensional materials in PVDF matrix have been studied widely because of their easy fabrication technique, compatibility and mechanical flexibility [10,11,14, 1-26]. Further, it has been found that these devices are also sensitive to various environmental conditions like light, temperature, pressure etc. [16,17,27-33]. In this regard, the introduction of optically active fillers within the PVDF is extremely interesting as it can make the hybrid system suitable for next generation photo-piezotronic devices [13,34-37] fabrication purposes. To date, most of the aforementioned devices demonstrating piezotronic and photo-piezotronic effects have been realized by coupling of semiconducting and piezoelectric properties of piezoelectric films. Here we have reported the piezoelectric and photosensing properties of two dimensional (2D) transition metal dichalcogenides incorporated PVDF nanocomposites on flexible substrates. We have demonstrated that two-dimensional semiconductor tungsten

disulphide (WS_2) nanosheets, with a broadband absorption spectrum, can serve as efficient filler into PVDF matrix to develop nanogenerators as well as self-powered optical sensors. Chemically exfoliated WS_2 nanosheets in DMF solvent have good dispersity in PVDF matrix forming homogeneous, uniformly distributed PVDF-WS_2 nanocomposite. Therefore the crystallinity and optical properties of WS_2 remain unchanged within PVDF matrix. Uniform distribution of WS_2 nanosheets in PVDF matrix and their good interfacial property within the nanocomposite result in superior piezoelectric response. The fabricated self-poled, flexible PVDF-WS_2 nanogenerator device yields an enormously high piezoelectric output voltage ~116.0 V under an impact of only 105 kPa and ~4 V by external mechanical bending induced strain of ~ 0.75%. The device exhibits a record energy conversion efficiency of ~ 25.6% using 2D materials with a photoresponsivity ~ 6.98×10^{-3} A/W at zero bias at 0.75% strain.

4.2 Experimental Section:

4.2.1 Materials and Methods:

All the chemicals (WS_2 powder, LiBr, PVDF powder) and solvents (hexane, DMF) were purchased from Sigma-Aldrich and used without further purification.

4.2.2 Synthesis:

WS_2 nanosheets were chemically exfoliated by using Li-intercalation technique. Bulk WS_2 powder 2.5 gm with anhydrous LiBr at 1:1 molar ratio were dispersed in 20 ml hexane solution. This solution was sonicated for 4 hrs. by using bath sonicator. After sonication the resulting black dispersion was centrifuged at 4000 rpm for 10 mins to remove hexane and untreated Li ions. The wet sediments were washed by dispersing in DMF by shaking followed by centrifugation. By repeating this procedure twice the wet sediment of WS_2 was completely transferred in DMF solvent. The final exfoliation was done in DMF by bath sonication for 1hr. Then the resulting solution was centrifuged at 5000 rpm for 10min and greenish colour exfoliated WS_2 nanosheets were obtained and used for further studies.
Commercially available PVDF powder (0.25 g) was added with chemically exfoliated WS_2 nanosheets dispersed in DMF, PVDF-WS_2 nanocomposites for different filler ratios (0.037%, 0.075%, 0.125%, 0.187% and 0.262%) were prepared. To get a homogeneous mixture of PVDF-WS_2 the solution was sonicated for 4 hrs. This mixture was then used for further measurements and device fabrication purpose. To synthesize control PVDF based

nanogenerator, bare PVDF powder was added into DMF solvent in absence of WS_2 nanosheets using a similar procedure.

4.2.3 Device fabrication:

The homogeneous solution of PVDF-WS_2 nanocomposite was spin-coated at 1000 rpm for 10 sec on an ITO coated PET substrate. Aluminum (Al) foil was attached on the top of the spin coated films so that the PVDF- WS_2 composite was sandwiched between the top Al electrode and ITO coated PET substrate (bottom electrode). Thereafter, the device was kept for drying at 60^{o}C for 1.5 hrs. to obtain the final device configuration (Al/PVDF-WS_2/ITO-PET) (Scheme:4.1).

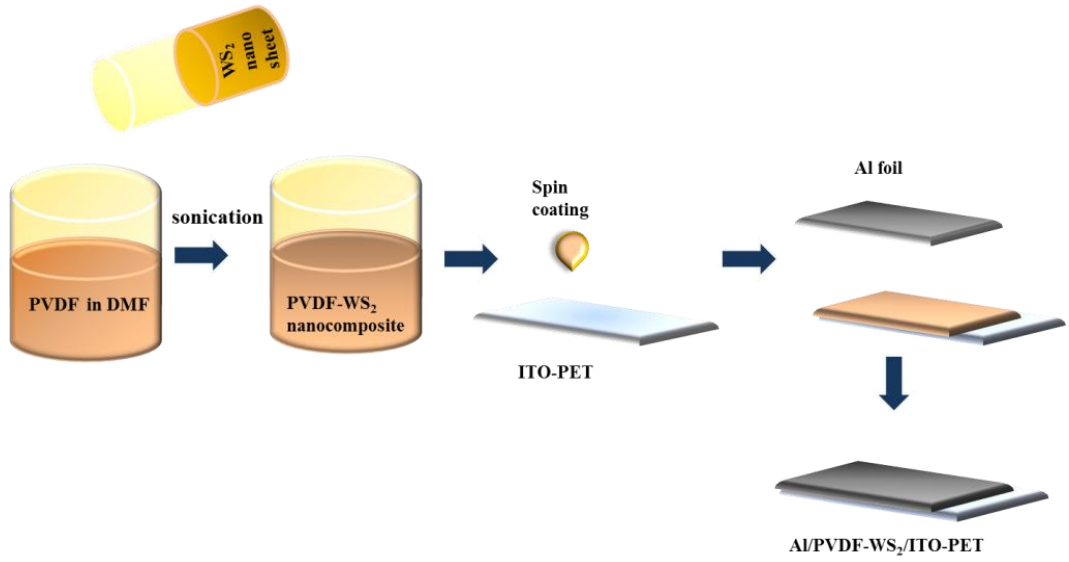

Scheme:4.1 Schematic fabrication process of PVDF-WS_2 composed piezoelectric nanogenerator device.

4.2.4 Characterizations:

The phase and crystallinity of control PVDF and PVDF–WS_2 nanocomposites were investigated by X-ray diffraction (RIGAKU MiniFlex with Cu-Kα, 1.54Å). Fourier transform infrared (FTIR) spectroscopy was carried out using a JASCO FTIR-6300 spectrometer. Surface profiles of the nanocomposites and device structure were examined using a field-

emission scanning electron microscope (FESEM) equipped with an energy-dispersive X-ray (EDAX) spectrometer, with an electron energy of 20 keV. The morphology of chemically exfoliated WS_2 nanosheets was investigated using a high-resolution transmission electron microscope (FEI-TECNAI G2 20ST, energy 200 keV) and atomic force microscopy (di INNOVA). Absorption spectrum of chemically exfoliated WS_2 nanosheet was measured using a UV-Vis spectrometer (Shimadzu -UV-Vis 2600 Spectrophotometer) and Raman spectrum was recorded with a spectrometer (LabRam HR Evolution; HORIBA France SAS-532nm laser). A Keithley 2450 source meter and a digital oscilloscope (SMO702 (scientific)) were used for the electrical measurements.

4.3 Results and Discussions:

4.3.1 Structural and Spectroscopic Studies of WS_2 nanosheets:

Figure 4.1(a) shows the TEM image of the exfoliated WS_2 nanosheets. HRTEM in Figure 4.1(b) shows the lattice fringe pattern with an inter-planar spacing of 0.27 nm for the (100) plane and 0.62 nm for (002) plane of the 2H-WS_2 nanosheets. The Selected area electron diffraction (SAED) pattern of WS_2 flakes in Figure 4.1(c) indicates the hexagonal atomic arrangement of 2H-WS_2 nanosheets. The AFM image in Figure 4.1(d) indicates that the exfoliated WS_2 nanosheets are few layered in thickness.

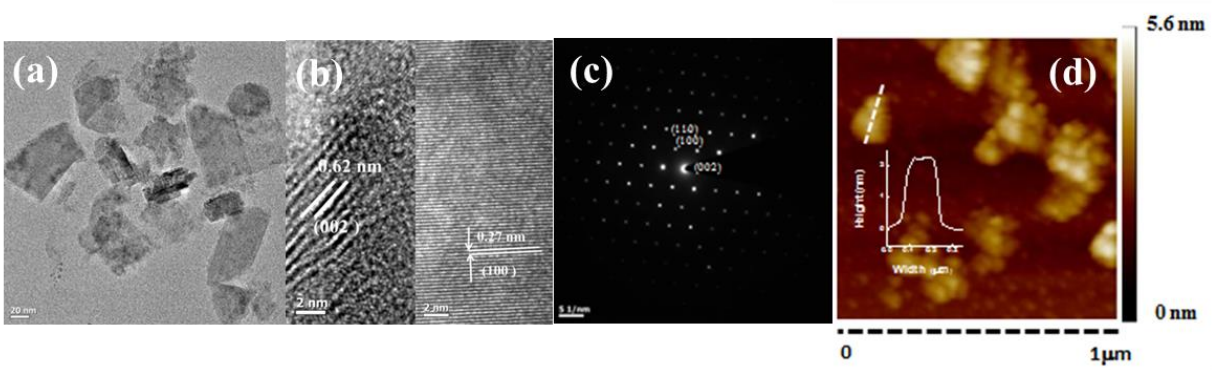

Figure 4.1 (a) TEM image of exfoliated WS_2 nanosheets. HRTEM image of WS_2 nanosheet indicating (b) Inter planer (100) spacing of 0.27 nm, (002) of 0.62 nm and (c) Selected area electron diffraction (SAED) pattern showing the crystallinity and hexagonal atomic orientation of WS_2 nanosheets. (d) AFM image of WS_2 nanosheets and the high profile of a sheet.

From the absorbance spectrum characteristic peaks are observed at 628 nm, 523 nm, 452 nm and 409 nm marked as A, B, C and D, respectively [38] in Figure 4.2(a). In Raman spectrum two characteristics modes of vibration A_{1g} and E^1_{2g} of WS_2 assigned to the out-of-plane and in-plane vibrations of the W and S atoms, respectively, are shown in Figure 4.2(b). The characteristic peaks for A_{1g} and E^1_{2g} vibrations are observed at 417.4 and 352.8 cm^{-1} respectively, for the exfoliated WS_2. Both the absorbance and Raman spectrum agrees with formation of few layered exfoliated WS_2 nanosheets. The XRD diffraction pattern (Figure 4.2(c)), peak at 14.4^o indicates the formation of (002) plane of WS_2 nanosheet which indicates the good crystallinity of exfoliated WS_2 nanosheets.

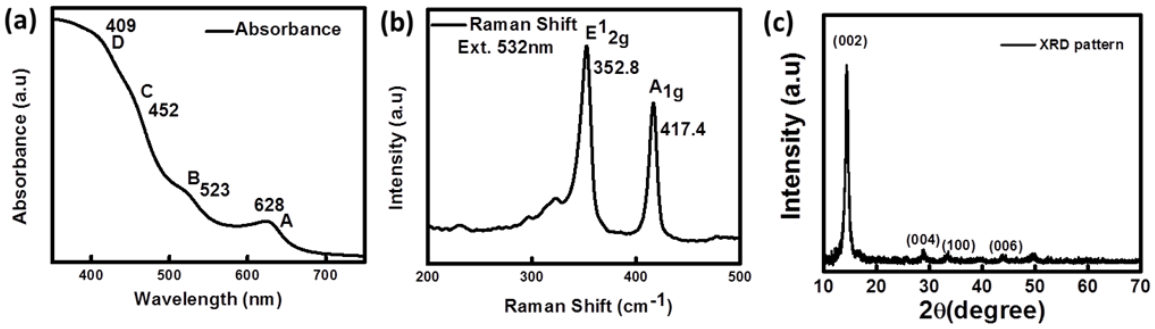

Figure 4.2 (a) Absorption spectrum (b) Raman spectrum and (c) XRD pattern of synthesized WS_2 nanosheets.

4.3.2 Structural Studies of PVDF-WS_2 nanocomposite:

Scanning electron micrographs (SEM) showing the morphology of PVDF and PVDF-WS_2 nanocomposites are depicted in Figure 4.3(a) & (b) respectively. The surface of control PVDF (without any WS_2) nanosheets is presented in Figure 4.3(a), which is relatively smoother as compared to that of the nanocomposite and depicted in Figure 4.3(b), and nanosheets are found to be well dispersed within PVDF matrix. From the cross-sectional SEM image, are presented in Figure 4.3(c), the thickness of the PVDF-WS_2 nanocomposite film is estimated to be~ 40 ±3 μm and that of the composed device including the electrodes is ~ 150 ±5 μm.

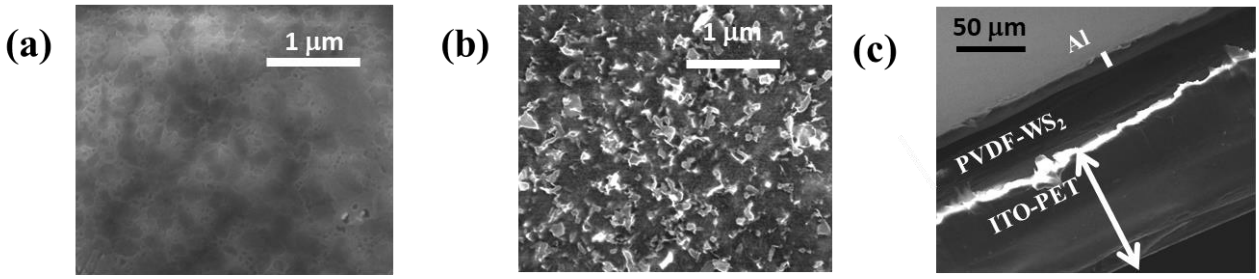

Figure 4.3 Typical SEM images of (a) control PVDF and (b) PVDF-WS_2 nanocomposite. (c) Cross-sectional view of a PVDF-WS_2 nanogenerator device.

The PVDF-WS_2 nanocomposites with a higher fraction of β-phase are necessary because of their improved piezoelectric response. Here, XRD and FTIR analyses have been carried out to investigate the influence of WS_2 nanosheets as filler on the crystalline structures of PVDF Figure 4.4(a) exhibits the XRD pattern of control PVDF and PVDF-WS_2 nanocomposites. For control PVDF, the characteristic nonpolar α-phase peaks are occurred at 17.6^o (100), 18.3^o (202) and 19.9^o (110) [13,39,40]. On the other hand, PVDF-WS_2 exhibits a characteristic sharp peak at 14.4^o demonstrating the crystalline phase of WS_2 (002) [41,42]. In PVDF-WS_2 nanocomposite, the dominant XRD peak is observed at 20.5^o (200), emanates from the electroactive crystalline β-phase of PVDF [21,27], which appears for all filler concentrations. We have observed that the diffraction peak intensities for α-phase at 17.6^o, 18.3^o, 19.9^o diminish gradually with increasing filler concentration. The dominance of β-phase peak and diminishing nature of α-phase peak of PVDF-WS_2 nanocomposite indicate the WS_2 mediated reorientation of functional groups in PVDF. To validate this premise by studying the existence of functional groups, FTIR measurements have been carried out (Figure 4.4(b)). For control PVDF, the vibrational bands appearing at 614, 763, 794 and 975 cm^{-1} are attributed due to the non-polar α-phase [21,43] and they are related to the mixed CF_2 bending, CCC skeletal vibration, the in plane bending or rocking vibration and CH_2 rocking vibration, respectively [21]. On the other hand, the bands appearing at 510 and 1074 cm^{-1} correspond to the β-phase and features observed at 1234 and 1177 cm^{-1} [43] are the signatures of the presence of γ-phases. Absorption peaks have observed at 1401 cm^{-1} ,considered to be the contribution from both β and γ -phases [43]. And also the appearance of two new sharp peaks at 839 and 1274 cm^{-1} in the FTIR spectra of the PVDF-WS_2 nanocomposites are the signatures of the

presence of intense electroactive β-phase [16,17,43] and the peak at 839 cm^{-1} is due to mixed CF_2 asymmetric stretching and CF_2 rocking vibration and the peak at 1274 cm^{-1} is related with C-F stretching vibrations. The vibrational band at 1074 cm^{-1} is related to the linear dependency on the thickness of film and independent on its crystallinity. The nucleation of the electroactive β–phase and the reduction of non-polar α-phase take place due to the addition of WS_2 in PVDF matrix, as presented in Figure 4.4(c). The relative fraction of β-phase, F(β) present in the samples can be calculated by using

$$F(\beta) = \frac{A_\beta}{\left(\frac{K_\beta}{K_\alpha}\right)A_\alpha + A_\beta} \quad (4.1)$$

whereA_α and A_β are the absorbance (as measured using FTIR spectroscopy) of the bands at 763 and 839 cm^{-1} corresponding to the formation of α- and β-phases, respectively, K_α and K_β are the absorption coefficients at the respective wave number, which are 6.1×10^4 and 7.7×10^4 cm^2/mol [10, 44]. From the above estimation, the electroactive β-phase fraction which is mainly responsible for piezoelectric response is plotted as a function of WS_2 concentration in Figure 4.4(c). It is observed that F(β) increases initially with increasing WS_2 content and attains a highest value of ~ 85% for 0.187% WS_2 filler loading beyond which it decreases. Such a decrease in F(β) beyond a critical loading could be explained by taking into consideration of the possibility agglomeration of WS_2 nanosheets within the PVDF polymer matrix, as the filler loading concentration beyond 0.187% may lower the surface charge interaction of WS_2 with PVDF. From the XRD pattern, the ratio of the intensity of the peaks at 20.5^o and 18.3^o, $\frac{I_{20.5}}{I_{18.3}}$ has been calculated, which provides a qualitative estimation about the relative content of β-phase and α-phase [45], as shown in Figure 4.4(c). It is observed that this ratio attains its highest value at 0.187% filler content, in corroboration with the FTIR results [10,21,44, 45].

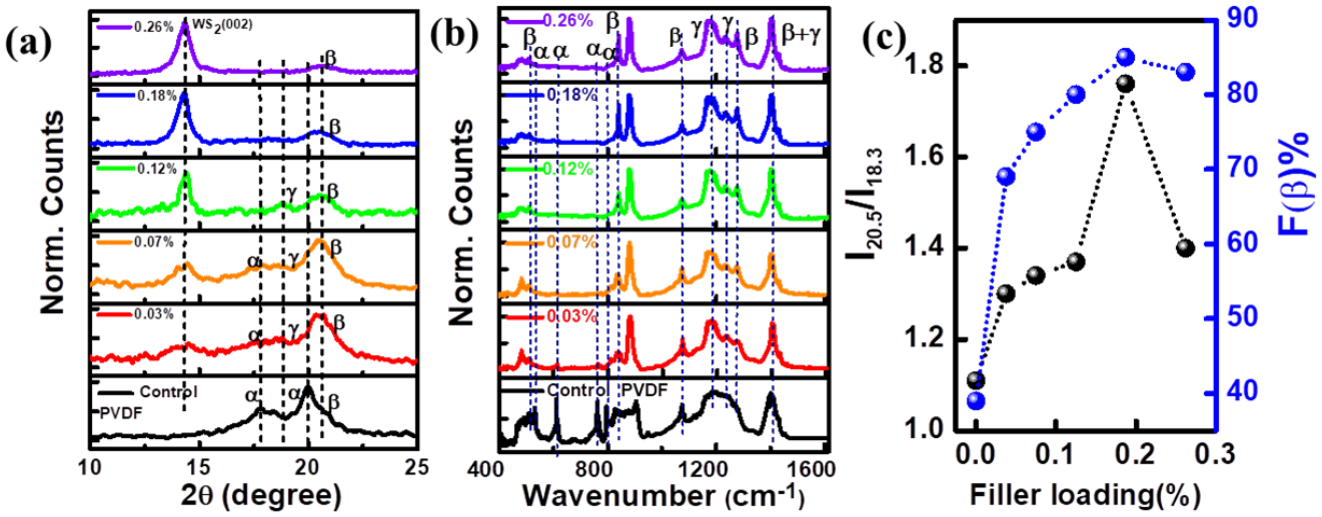

Figure 4.4 (a) X-ray diffraction patterns and (b) Fourier transform infrared spectra of control PVDF and PVDF-WS_2 nanocomposite films at various WS_2 filler loading fraction. (c) Variation of intensity ratio $\frac{I_{20.5}}{I_{18.3}}$ from XRD pattern and relative β-phase content from FTIR spectra as a function of WS_2 filler content.

4.3.3 Piezoelectric Studies:

The working mechanism of this piezoelectric nanogenerator (PENG) can be explained in terms of the combined effect of the PVDF dipoles and the surface charges of WS_2 nanosheets. The opposite polarity surface charges on WS_2 interact with the dipoles (-CF_2-/-CH_2-) of PVDF, which results the development of charge density within the nanocomposite, leading to the formation of piezoelectric active β–phase through the surface charge induced electrostatic interactions [46,47] and it is schematically presented in Figure 4.5(a). The (-CH_2/-CF_2) bond stretching vibration, dipole-dipole interaction between WS_2 nanosheets and PVDF and the stress induced polarization are the main reasons behind the conversion form nonpolar α-phase to electroactive β-phase [13] within the nanocomposite. WS_2 nanosheets act here as a nucleating agent to form the polar crystalline β-phase in PVDF-WS_2 nanocomposite. The working mechanism of this PVDF-WS_2 composite PENG is schematically displayed in Figure 4.5(b) where the attraction between the surface charge of WS_2 nanosheets and the dipoles of PVDF is highlighted. In the absence of any external mechanical impact all the dipoles within the hybrid nanocomposite film are oriented randomly, results a zero net dipole

moment (Figure 4.5(b) (i)). Application of an external mechanical force aligns the dipoles in the direction of the applied force through stress induced polarization. When the piezoelectric nanogenerator PENG is subjected to a vertical compressive stress, the crystal structure of the nanocomposite gets deformed, i.e., the dipolar distribution within the nanocomposite is altered, which consequently produces positive and negative potential across the two electrodes (Figure 4.5(b) (ii)). The potential difference between the top and the bottom electrodes generate a piezoelectric potential which drives the flow of electrons from one electrode to the other through an external circuit. As the compressive strain is released, the piezoelectric potential vanishes immediately (Figure 4.5(b) (iii)) and to compensate that, the electrons accumulated near the electrode flow back to the other one through the external circuit, leading to an electric signal in the opposite direction. So an alternating voltage signal is obtained during this continuous vertical compression and release. Piezoelectric outputs from the PVDF-WS_2 composite nanogenerator, as obtained under vertical repetitive compression and release of manual human finger tapping (~3.1 kPa pressure) are presented in Figure 4.5(c).

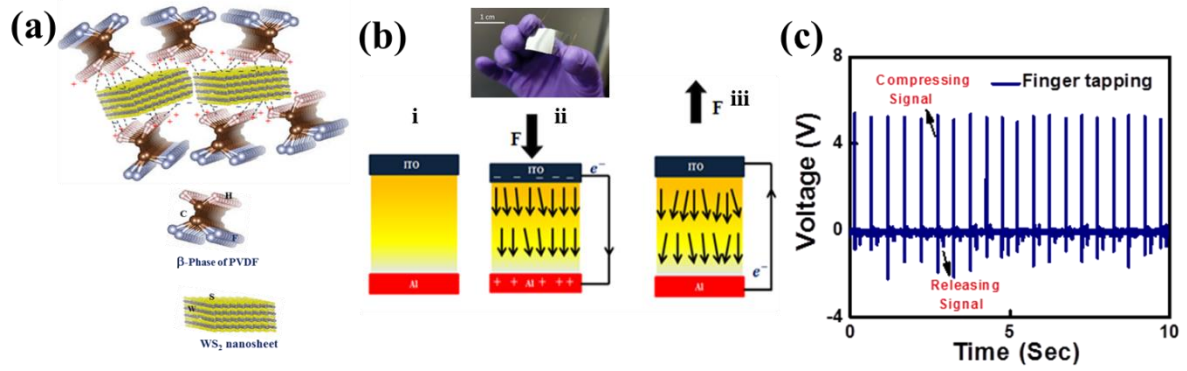

Figure 4.5 Schematic mechanisms of (a) Interactions between WS_2 and PVDF within PVDF-WS_2 nanocomposite and (b) Operation of a piezo-electric nanogenerator and the device image is showing in inset. (c) Open-circuit output voltage from PVDF-WS_2 PENG for 0.187% filler loading for repeated finger tapping.

Polarity switching tests have been performed to verify whether the output voltage originates owing to the piezoelectric phenomenon or not. As expected, we have observed output voltages with opposite sign from the PENG when they are connected in reverse configuration, confirming that the piezoelectric signals are reversible in nature and are presented in Figure 4.6(a) & (b). To study the effect of the filler concentration on the

piezoelectric response, we have studied nanogenerators with different WS_2 nanosheets concentrations (0.037%, 0.07%, 0.12%, 0.18% and 0.26%). The mechanical energy-harvesting ability of these self-poled devices are examined without any electrical poling treatment. The piezo-response from all the nanogenerators are analyzed by applying repeated finger tapping with identical frequency (2 Hz) and the open circuit piezoelectric output voltages are recorded. From Figure 4.6(c) it is observed that the open-circuit piezoelectric voltage from the PVDF-WS_2 PENG increases initially with increasing WS_2 filler loading and the PENG device with 0.187% WS_2 filler concentration produces the highest piezoelectric open circuit output voltage of ~5.3 V. So from this above result it can be claimed that the best performance is delivered by the device with 0.187% filler concentration, in corroboration with the XRD and FTIR results [10,13]. The nanogenerator has been subjected to varying external mechanical forces (7.55, 9.05 and 11.33 kPa at 2Hz) and it is observed that the generated piezopotential increases with increasing external mechanical impact, as depicted in Figure 4.6(d). The increase of piezopotential can be ascribed to the preferential orientation of the electric dipoles within the nanocomposite in a particular direction due to the external stress induced effect [48].

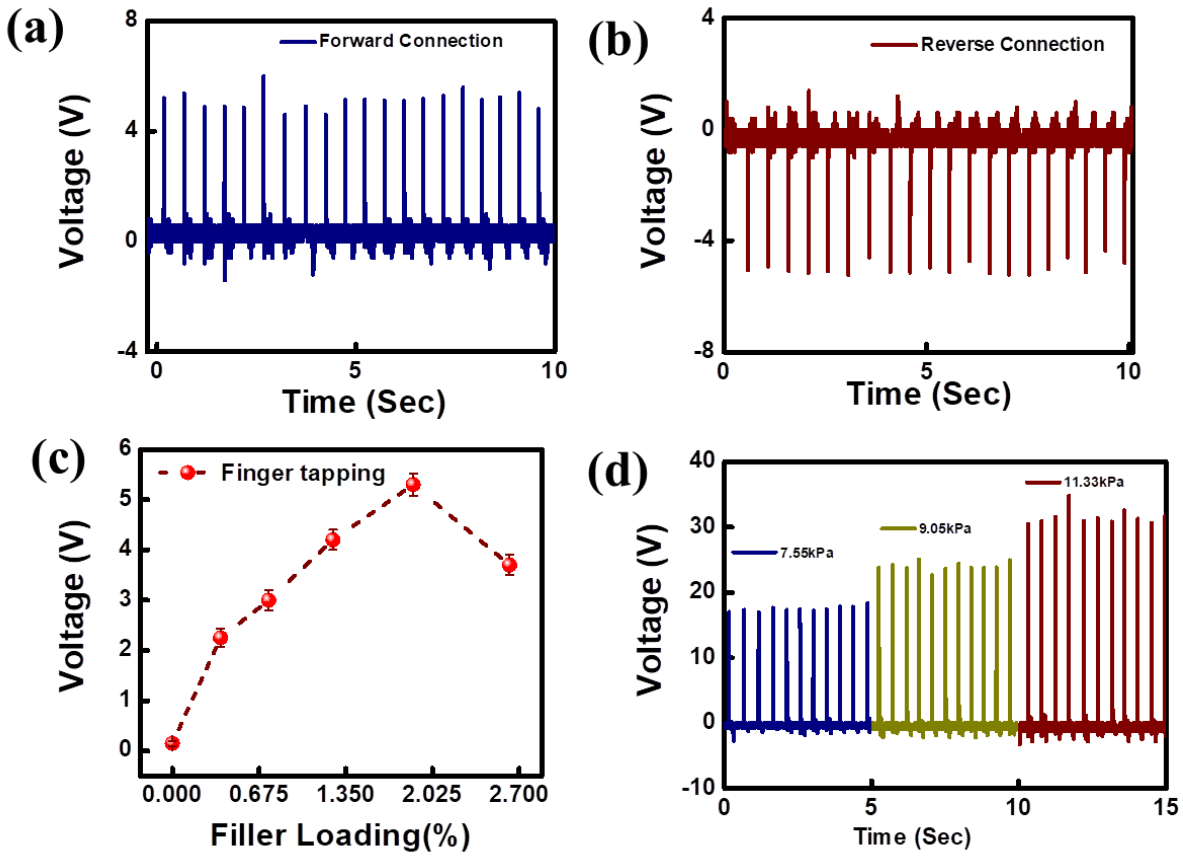

Figure 4.6 Open-circuit piezoelectric output voltages from PVDF-WS_2 PENG in (a) forward (b) reverse connection. (c) Variation of open circuit output voltage due to variation of filler loading fraction. (d) Variation of open circuit output voltage with variation of mechanical impact.

Under application of periodic applied stress (~ 105 kPa), very high output voltage is obtained from this self-powered nanogenerator ~116 V in open circuit condition, which is depicted in Figure 4.7(a). The output performance of this PENG is found to be superior to other reported PVDF-2D and perovskite based devices and is presented in Table-4.1. In this PVDF-WS_2 self-powered system, the polymer PVDF matrix interacts with filler WS_2 by electrostatic dipole-dipole interaction. This interfacial interaction affects the motion of PVDF, resulting in the formation of piezoelectric β-phase [10]. This similar mechanism is responsible for other well-known semiconductors (ZnO, TiO_2 etc.) and perovskite ($CsPbBr_3$, $MAPbI_3$, $FAPbBr_3$, $BaTiO_3$) – PVDF nanocomposites [10,13,14,34]. In this study, we have used chemically exfoliated two dimensional WS_2 nanosheets as filler within the PVDF matrix, the intrinsic polar WS_2 surface can easily interact with CF_2 or CH_2 groups of PVDF and initiate the nucleation of β-

phase. As a result of this, the PVDF-WS_2 nanocomposite exhibits a higher value of β-phase fraction (F(β)) which leads to a higher piezoelectric output voltage. On contrary, many fillers having high intrinsic conductivity (graphene, some perovskites etc.) cause unwanted carrier recombination with polymer matrix and results a higher leakage current within this nanocomposite, which deteriorate the piezoelectric performance of the nanogenerator [13]. In addition to that, the semiconducting nature of WS_2 may enhance the local electric field to generate more induced charges, resulting in a stronger coulomb force which is helpful for conversion into a higher fraction of β-phase. Besides, the good dispersity of chemically exfoliated WS_2 (in DMF solvent) within the PVDF matrix offers homogeneity and leads to a uniform distribution of WS_2 throughout the nanocomposite without much agglomeration. This aggregation-free filler-matrix nanocomposite is very much important for enhanced nanogenerator performance. The uniform distribution of WS_2 nanosheet within the PVDF matrix accelerates the nucleation of the piezoelectric polar β–phase in PVDF-WS_2 nanocomposite. Consequently the piezoelectric performance of PVDF-WS_2 based PENG gets enhanced and is found to be superior to the other reported similar systems.

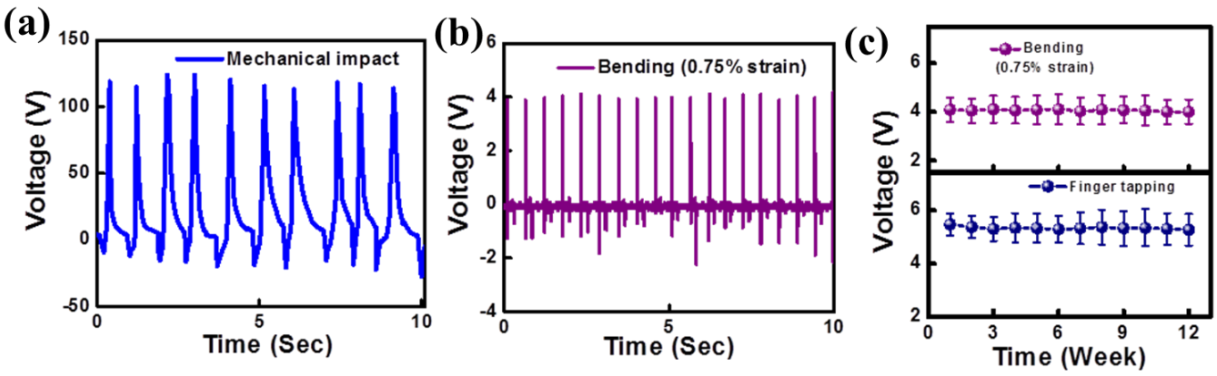

Figure 4.7 Open-circuit piezoelectric output voltage from PVDF-WS_2 PENG for 0.187% filler loading for repeated (a) Mechanical impact (~105 kPa) and (b) Bend/release action (c) Stability performance of the PVDF-WS_2 PENG in laboratory ambient for 12 weeks under repeated mechanical tapping and bending.

The fabricated PENG is also capable for generating piezoelectric output under repeated external bending and releasing at a low strain (~0.75%), which is depicted in Figure 4.7(b). The reproducibility of this PVDF-WS_2 device has been tested by measuring under the same external compressive force (application of finger tapping, 0.75% mechanical strain) in

weekly interval. In absence of any noticeable degradation in the output voltage over a prolonged period (of 12 weeks) confirms the stability of the fabricated device in ambient conditions and displayed in Figure 4.7(c).

The piezoelectric output voltage from this PVDF-WS_2 nanogenerator is found to be higher, ~44 times for finger tapping and 40 times in case for a mechanical impact (~11.33 kPa) than that of control PVDF device, as are depicted in Figure 4.8(a) & (b). This is attributed due to the interfacial or Maxwell-Wagner-Sillars polarization [49-51], which induces a change in the dielectric constant of the nanocomposite leading to enhancement of the piezoelectric output [13,52,53] from the PVDF-WS_2 nanogenerator device.

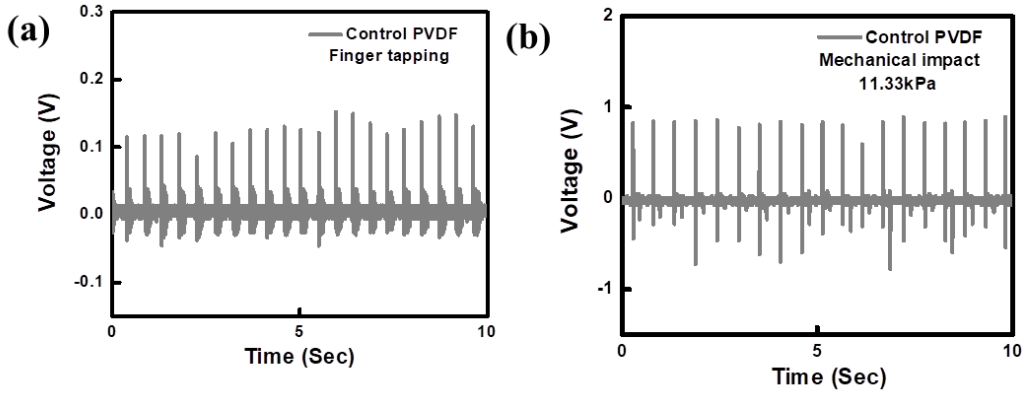

Figure 4.8 Open-circuit piezo-output voltages from control PVDF device under (a) Finger tapping and (b) Mechanical impact (11.33 kPa).

The PVDF-WS_2 based piezoelectric nanogenerator (PENG) device exhibits an excellent piezoelectric output performance without application any electrical poling, which is very important for practical applications. To investigate the driving capability of the PENG, a capacitor (~1.2 μF) can be charged up to ~21.8 V only within ~17 s, as presented in Figure 4.9(a). The cyclic charging and discharging behavior of the capacitor presents high energy drive capability and the reproducibility of the PENG. The stored energy in the capacitor has been used to drive commercial LEDs (four green, output power ~ 110 mW (max.) each at a forward current of ~ 25 mA (max.)) revealing the practical use of the PENG device (Figure 4.9(b)). Based on the charging capacity, we have estimated the stored energy across the capacitor using, $E_e = \frac{CV^2}{2}$, where C is the capacitance and V is the voltage in the steady state condition after a certain time. On the other hand, the mechanical strain energy E_s can be

estimated as, $E_s = \frac{YAL\sigma^2}{2}$, where A is the active area (~1.0 × 1.0 cm^2), L is the thickness of the composite device (~150 μm) including electrodes, σ is the applied strain (~0.75%) and Y is the Young's modulus of the nanocomposite, which has been estimated to be about ~2.66 GPa using the rule of mixtures [54,55]. The mechanical energy can also be estimated ~1.12×10^{-3} J and the generated output electrical energy is found to be~2.85×10^{-4} J, yielding the energy conversion efficiency, $\eta = \frac{E_e}{E_s}$ of this fabricated PENG to be ~25.6%. This calculated efficiency value is found to be the highest among the previously reported piezoelectric nanogenerators (PENG) [16,39,56] by using 2D and perovskite materials (Table-4.1). To demonstrate the energy harvesting performance of the PENG from routine activities (like writing on papers), acts as a source of mechanical stress, two ends of a PENG are connected to an oscilloscope. During drawing of lines and writing of different alphabets by using a simple pencil, piezoelectric output voltages of ~0.5-0.8V are generated as represented in Figure 4.9(c), demonstrating that the device can be used as a smart writing board also. Furthermore, when the PENG is attached with a computer mouse, an instantaneous piezo-voltage (~2.1 V) is generated (Figure 4.9(d)) for each click on the mouse. Thus the PVDF-WS_2 nanocomposite device is able to generate piezoelectric voltage by simple human activities (finger tapping, writing, mouse click etc.), making it a potential candidate for bio-mechanical energy harvesting. This PVDF-WS_2 composed PENG is also able produce output voltage due to impact of water droplet falling onto it, as depicted in Figure 4.9(e). An output voltage of~ 1.0 V for imparting water droplets (with a velocity ~0.92 m/s) reveals that the device can also be used as an energy harvester from rain water. In addition, the PVDF-WS_2 based PENG can be to produce output voltage under a minute strain produced due to the movement of different parts of human body with an average magnitude of ~17.0, 3.0 and 2.7 V for foot, elbow and wrist movements, respectively, as presented in Figure 4.9(f). Hence the fabricated nanogenerator is very much effective to harvest energy from regular biomechanical activities. The piezoelectric characteristics with record output piezoelectric voltage and superior energy conversion efficiency under application of mechanical stress as well as the biomechanical actions reveal the novelty of PVDF-WS_2 hybrid PENG compared to the other PENGs reported in the literature.

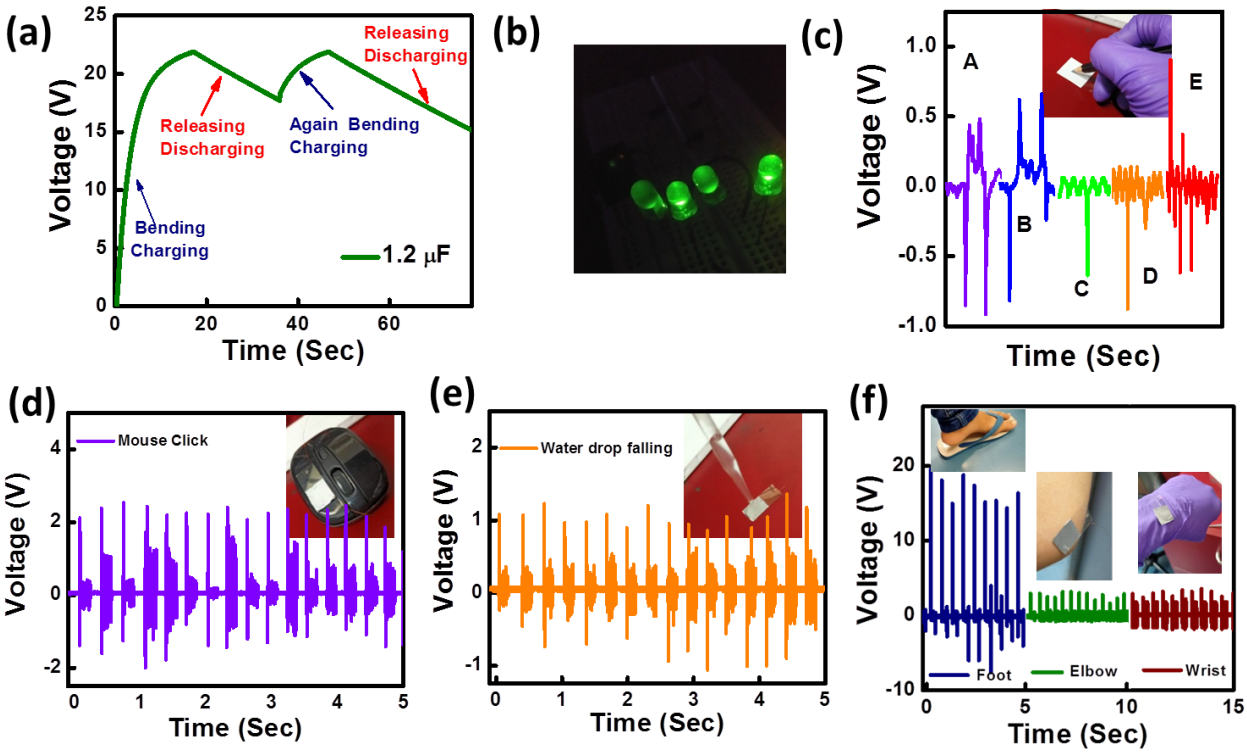

Figure 4.9 Charging-discharging behavior of a capacitor of 1.2 μF using the PENG device. (b) Glowing of four green commercial LEDs (I_{power} =110mW (max)) at a time. Output voltages from the PENG device due to (c) Writing on papers. (d) Clicking of a computer mouse. (e) Falling water drops and (f) Different human body movements and the images are shown in insets.

To study the piezo-phototronic characteristics of the PENG, the temporal response of the PVDF-WS_2 nanocomposite device has been studied under application of repetitive strain and release. The output currents of the control PVDF and PVDF-WS_2 PENG devices are monitored under an identical strain (~0.75%) condition and the relative increase (ΔI) in the output current is expressed as [57]

$$\frac{\Delta I}{I_o} = \frac{I_{strain} - I_o}{I_o} \qquad (4.2)$$

Where I_{strain} and I_o are the output currents in presence and in absence of external bending strain, respectively. It is observed that the ratio $\frac{\Delta I}{I_o}$ is ~22 (Figure 4.10(a)) for control PVDF. The absence of photocurrent in control PVDF PENG device even in the bent condition (Figure 4.10(b)), reveals that the photoresponse in PVDF-WS_2 PENG is attributed by semiconducting WS_2 nanosheets only.

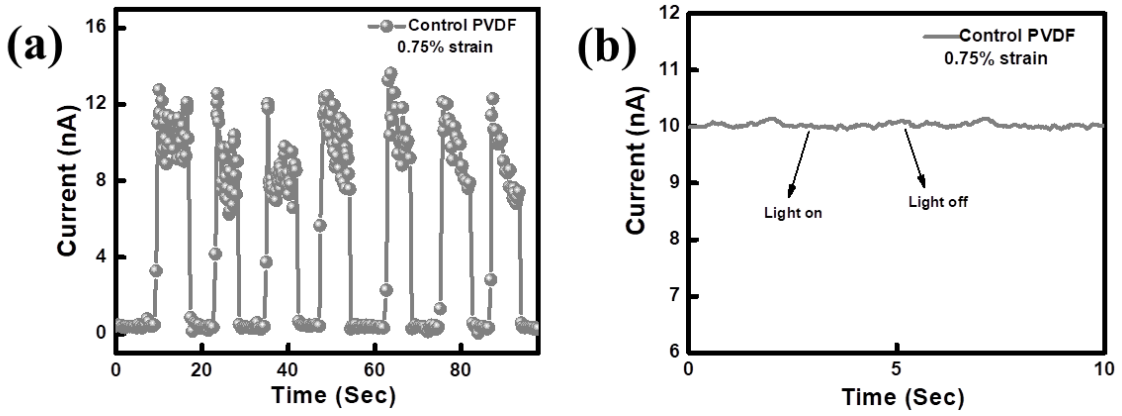

Figure 4.10 I-t characteristic from control PVDF PENG device (a) Under application of repeated bending and releasing at 0.75% stain. (b) Change of current for light on-off at 0.75% strain.

The ratio $\frac{\Delta I}{I_o}$ is enhanced to ~134 for PVDF-WS_2 PENG (at dark condition), as shown in Figure 4.11(a). This remarkable enhancement in piezoelectric response of PVDF-WS_2 nanocomposite PENG can be attributed to the higher density of piezo-charges within the nano-composite under an applied external mechanical stress. The interaction between semiconducting WS_2 nanosheets and PVDF dipoles induces polarization charges that enhances the electrical transport under an external stress even at a zero bias [15,34]. To confirm the piezo-phototronic effect of PVDF-WS_2 nanocomposite PENG, output currents have been measured by applying an identical external compressive stress under illumination (635 nm) and dark (Figure 4.11(a)) condition. From Figure 4.11(b) it is observed that there is enhancement of current under illuminated conditions than the dark, which indicates the enhanced photo-carrier density and reduced internal resistance of the PENG under light illumination than the dark condition. The stressed-to-relaxed current ratio (for ~0.75% strain) enhances under illumination, as compared to that in the dark condition (Figure 4.11(c)). The above ratio is found to be 519, 329 and 274 under violet (0.49 mW/cm^2), green (0.36

mW/cm^2) and red (0.4 mW/cm^2) illumination, respectively which are higher than the dark value ~134, due to strong optical absorption of WS_2 nanosheets.

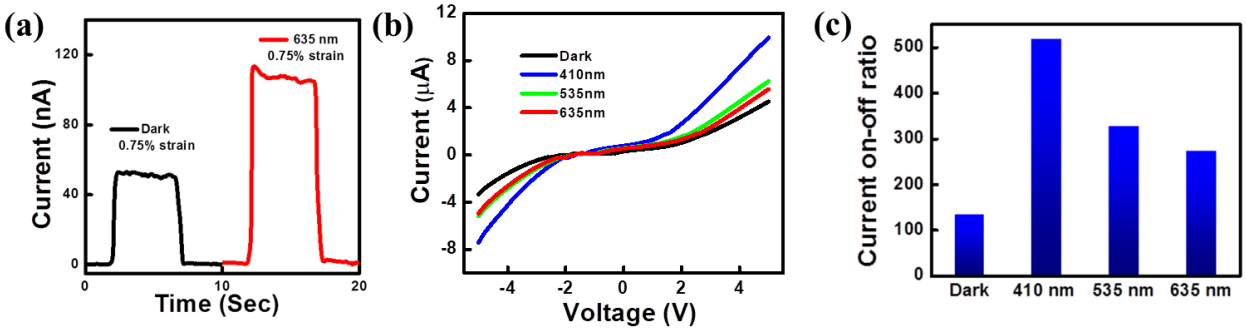

Figure 4.11 (a) I-t characteristics of PVDF-WS_2 PENG at zero bias with bending-releasing at dark and bending-releasing under 635 nm illumination. (b) I-V characteristic of the PENG under dark and illuminated conditions. (c) Bent-to-relaxed current on-off ratio for ~0.75% strain at dark and under illumination of different wavelengths.

Further measurements have been carried out to confirm the piezo-photoresponse of the PVDF-WS_2 nanocomposite PENG device, first by applying a compressive strain through mechanical bending followed by periodical illumination. Under an illumination at 635nm (0.4 mW/cm^2), a measurable photocurrent is observed and is depicted in Figure 4.12(a). Under the application of a compressive strain, piezo-polarization charges are generated within the nanocomposite, which assist an efficient transport of photogenerated e-h pairs by reducing the recombination probability of the charge carriers. The photogenerated e-h pairs are separated by the polarization induced built-in-field and an enhanced photocurrent is observed. The photocurrent response under each cycle is repeatable and consistent with no observable decay. Bending test has been carried out to explore the mechanical stability, which is very important for flexible photodetector application purposes. Here a good switching behavior of the current is observed (Figure 4.12(a)) under periodic illumination of light at zero bias with rise and decay time of 1.4 s and 5.4 s, respectively which are faster than the previously reported PVDF based photosensitive PENG [28,36,37]. The rise and decay times are defined as the time required for the photocurrent to increase from 10% to 90% and to decrease from 90% to 10% of its maximum value, respectively and most importantly this photocurrent remains almost invariable even after several bending cycles. In bent condition under self-powered mode, the current change depends on both the applied strain and the

optical illumination. To understand the effect of the external mechanical stress, this measurement has been performed under application of variable compressive strain. For a higher strain, the built-in electric field is stronger across the electrodes and under illumination the reduced recombination of photogenerated e-h pairs contributes to the increase in the current up to a strain magnitude of ~ 0.8%, which is depicted in Figure 4.12(b).

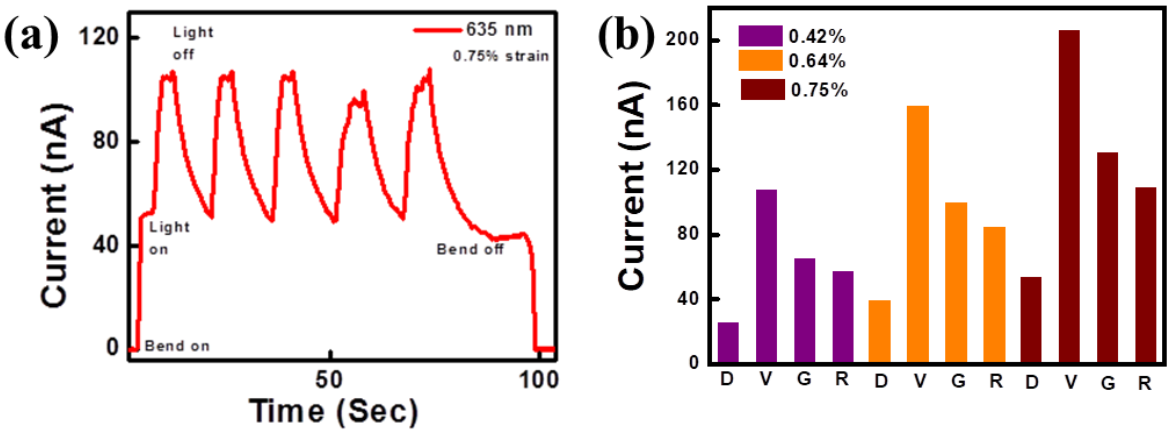

Figure 4.12 (a) I-t characteristics at zero bias with 0.75% strain and 635 nm illumination. (b) Variation of currents in dark and illuminated conditions under application for different strain. D, V, G and R representing dark, violet, green and red illuminations respectively.

We have estimated the relative change of photocurrent under strained condition [57] by using

$$\frac{\Delta I_p}{I_{p,o}} = \frac{I_{ps} - I_{p,o}}{I_{p,o}} \qquad (4.3)$$

where I_{ps}, $I_{p,o}$ are the photocurrent with and without external stress under light illumination, respectively. The photosensing behavior of PVDF-WS_2 nanocomposite PENG has been investigated without application of any external bias and external bending strain, which is presented in Figure 4.13(a). These results show that the values of $\frac{\Delta I_p}{I_{p,o}}$ under illuminated condition of 410 nm (~91), 535 nm (~72) and 635 nm (~65) are lower than the $\frac{\Delta I}{I_o}$ value in the dark condition (~134) for the same strain configuration (~0.75%) at zero bias. This difference is attributed to the piezoelectric screening effect from photogenerated carriers. Under irradiation, photogenerated carriers partially screen the piezo-polarization charges, the mechanism of which is schematically depicted in Figure 4.13(b). It can be observed that in the absence of any external stress, molecular dipoles within the nanocomposite are randomly

oriented, and therefore it does not possess any net field (Figure 4.13(b)i). Under application of an external stress, the piezoelectric dipolar charges are aligned along the stress induced direction leading to the generation of piezopotential across the electrodes (Figure 4.13(b)ii), and this resultant piezoelectric potential drives the electrons in the external circuit and develops a voltage pulse as well as also generates a piezo-current. When the illumination energy is comparable to the band-gap of semiconducting WS_2 nanosheet, light induced e-h pairs are produced inside the nanocomposite and they are separated by the built-in piezoelectric field. As the result the light induced photocarriers reduce the strain induced piezopotential. Thus the screening of piezo-charges by the photogenerated e-h pairs takes place and the redistributed piezoelectric charges appear across the opposite electrodes (Figure 4.13(b)iii). As indicated in the band diagram, the piezopotential may facilitate the charge carrier separation due to the reduction of barrier height. The screening of piezo-potential reduces the open circuit output voltage at illuminated condition than in the dark (Figure 4.13(c)).

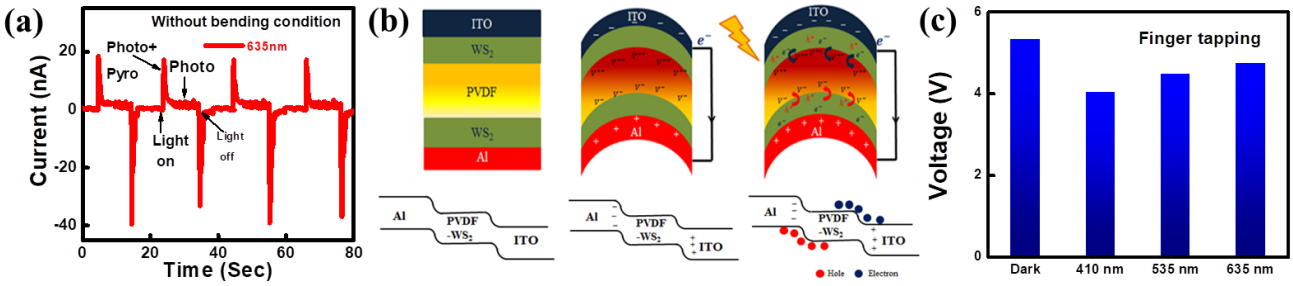

Figure 4.13 (a) I-t characteristic at zero bias without bending under 635 nm illumination. (b) Schematic working mechanism of piezo-photo coupled system. (c) Variation of open circuit voltage at dark and illuminated condition under finger tapping.

Thus, the piezo-polarization screening effect reduces the relative increase of the photocurrent (under a strained condition) as compared to the current without any illumination. The photo-responsivity (R_λ) and external quantum efficiency (EQE) of PVDF-WS_2 PENG at zero bias are calculated as, $R_\lambda = \frac{I_L - I_D}{P_L \times S}$ and $EQE = \frac{1240 R_\lambda}{\lambda}$, where I_L,I_D are the current at illuminated and dark conditions, respectively, P_L is the power of illuminated light and λ is the wavelength of incident illumination [36]. Both the responsivity and EQE are found to be higher in bent

condition than the relaxed state (Table: 4.2), which indicates that the applied strain has massive effect on controlling the performance of the photodetector. Both the photocurrent and the photoresponsivity of the device depend strongly upon the applied mechanical strain and this self-poled device exhibits a high photoresponsivity (6.98×10^{-3} A/W) and superior detectivity (8.61×10^{10}cm $H^{1/2}$ W^{-1}) under 0.75% strain at zero bias at 410 nm illumination. It is noticed that the photoresponsivity increases from 6.98×10^{-5} A/W (unstrained) to 6.98×10^{-3} A/W (for 0.75% strain), and higher values of responsivity and EQE are attributed to the strain induced piezopolarization charges, as they induce enhanced transport of photogenerated e-h pairs with reduced recombination of charge carriers [36]. In practice, the piezoelectrical power of the system depends on the external load resistance and therefore, performance of the device can be checked by measuring the output voltages across by varying the load resistances. The generated output voltage from the PENG across a load resistor gradually increases with increasing load resistance (Figure 4.14(a)) and reaches a saturation value at higher resistance which almost corresponds to the open circuit condition. The instantaneous piezoelectric power density can be estimated as $P = \frac{V_{out}^2}{A\times R_L}$, where A being the effective contact area and V_{out} is the effective output voltage considering the internal resistance (R_{int}) of the PENG and can be related as

$$V_{out} = \frac{R_L}{R_{int}+R_L}V = \frac{1}{1+\frac{R_{int}}{R_L}}V \qquad (4.4)$$

If $R_L << R_{int}$, then with increasing R_L, the enhancement of V_{out} is low. But whenever R_L is comparable to R_{int}, then V_{out} is increased monotonically with increasing R_L. Finally at $R_L >> R_{int}$, it provides almost an open circuit condition, in this regime with changing R, V_{out} does not change substantially. It is observed that the PENG attains a highest value (~ 30 μW/cm^2) under 2.0 MΩ load resistance at dark condition (Figure 4.14(a)). These results are comparable with the other piezoelectric devices based PVDF nanocomposites [52,56]. Under illuminated condition, photocarriers are generated within this PENG which enhance the conductivity and reduce the internal resistance of the PENG under illuminated condition as compared to the dark one (Figure 4.11(b)). It can be estimated that the internal resistance of the PENG is ~ 2.0 MΩ at dark condition and 0.76, 1.08 and 1.3 MΩ under illumination of 410 nm, 535 nm and 635 nm, respectively. As a result of photoactivity of PVDF-WS_2 nanocomposite, the piezoelectric output power density is observed to be higher under illumination and exhibits a maximum value ~ 48.5 μW/cm^2 under 410 nm illumination, as presented in Figure 4.14(b). The piezoelectric power density is higher under the violet light

(410 nm) than the green (535 nm) and red (635 nm) illuminations following the absorption pattern of WS_2 nanosheets. This result indicates that the fabricated PVDF-WS_2 composed PENG is able to generate enhanced piezoelectric output power density under illuminated condition and exhibits wavelength selectivity, with the highest energy harvesting ability at ~ 410 nm. Thus the fabricated 2D materials based PVDF-WS_2 composed nanogenerator can act as a high performance electrical power source as well as a self-powered flexible broadband visible light photodetector driven by novel piezo-phototronic effect, and is capable of harvesting enhanced energy under illumination with potential applications in future wearable and portable self-powered sensor systems.

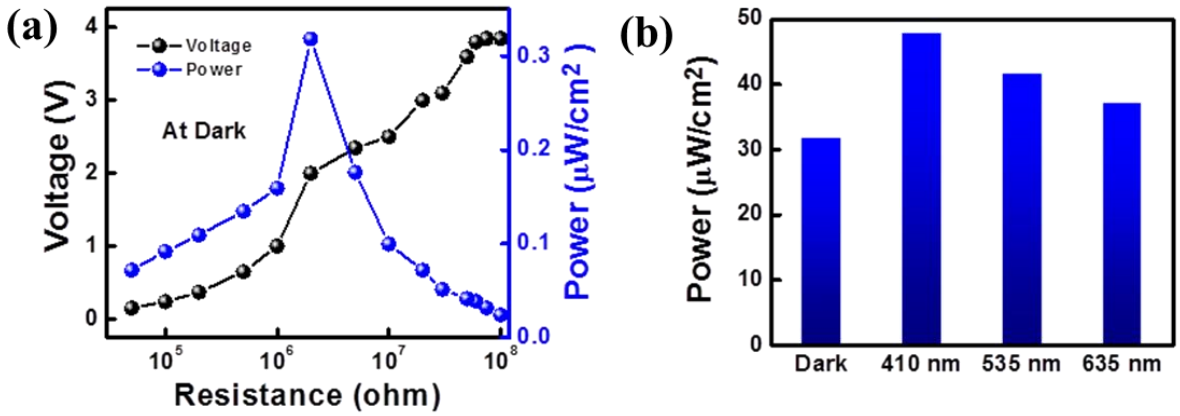

Figure 4.14 (a) Dependence of piezoelectric power-voltage with load resistance at dark and (b) Comparison of power at dark and illuminated condition under finger tapping.

Table-4.1

Comparison of piezoelectric performance of fabricated PVDF-WS_2 PENG with reported 2D and perovskite –PVDF based devices

Name of sample	Polling	Output Voltage	Power density & Efficiency	Photo-activity	Reference
PVDF-AlO/ rGO	Self-polled	36 V at 31.19 kPa	3.63 μW/ cm^2 12.47%	No	16
Ce3+ doped-Graphene/ PVDF	Electrospinning	11 V at 6.6 kPa	0.052 μW/cm^2	No	17
PVDF-Functionalized GO	Electrospinning	62 V at 40 kPa	48.3 μW/cm^2	No	27

PVDF-Graphene	Electromagnetic punch	18 V at 0.45N	----------	No	18
rGO-Ag/PVDF	external electric field of 148 kV cm^{-1}	18 V	14.72 $\mu W/cm^2$ 0.65 %	No	39
PVDF- graphene-Silver	Self-polled	0.1 V at 5.2 kPa	0.75nW/cm^2 15%	Yes	56
FAPbBr3/PVDF	Self-polled	26.2 V at 0.5 MPa	22.88 $\mu W/cm^2$	Yes	14
PVDF-MAPI	Self-polled	1.5 V at 2 kPa	2.5 $\mu W/cm^2$	Yes	29
hBN-PVDF NF	Electrospinning	68 V at 24.5 kPa	53.2 $\mu W/cm^2$	No	25
Graphene-BT NP-PVDF	electrospinning	11V under mechanical strain	0.656 $\mu W/cm^2$	No	10
PVDF NF-MoS_2	Electrospinning	9 V at 8.8 kPa	16 nW/cm^2	No	26
GO-PVDF NF	Electrospinning	7 V at 8.8 kPa	0.62 $\mu W/cm^2$	No	15
PVDF-WS_2	**Self -polled**	**116 V at 105 kPa**	**48.5 $\mu W/cm^2$ (3.1 kPa) 25.6%**	**Yes**	**This study**

Table-4.2

Variation of Responsivity and EQE with varying strain

	Without Strain		**Strain(0.50%)**		**Strain(0.64%)**		**Strain(0.75%)**	
	R_λ (A/W)	**EQE**	**R_λ (A/W)**	**EQE**	**R_λ (A/W)**	**EQE**	**R_λ (A/W)**	**EQE**
Violet(410nm)	6.98×10^{-5}	2.11×10^{-4}	3.584×10^{-3}	10.8×10^{-3}	5.316×10^{-3}	0.016	6.98×10^{-3}	0.0211
Green(535nm)	5.12×10^{-5}	1.186×10^{-4}	2.615×10^{-3}	6.049×10^{-3}	3.97×10^{-3}	9.2×10^{-3}	5.16×10^{-3}	0.0119
Red(635nm)	4.24×10^{-5}	8.345×10^{-5}	2.02×10^{-3}	3.975×10^{-3}	2.99×10^{-3}	5.885×10^{-3}	3.876×10^{-3}	7.636×10^{-3}

4.4 Summary:

Self-poled PVDF-WS_2 nanocomposites have been synthesized by using chemically exfoliated layered (two-dimensional) WS_2 nanosheets and PVDF polymers by using a simple, low cost, eco-friendly technique. The exfoliated WS_2 nanosheets with an optimized concentration of ~0.187% not only enhance the piezoelectric output voltage but also induce photo-activity in the nanocomposite devices over the pristine PVDF. A colossal piezoelectric voltage of ~ 116 V (for ~ 105 kPa) with a power density (~48.5 μW/cm^2 for ~3.1 kPa) and record energy (mechanical to electrical) conversion efficiency of ~ 25.6% among 2D materials based nanocomposites have been demonstrated. Apart from mechanical impacts, the hybrid PENG is also very sensitive to biomechanical movements and thus pave a promising way to drive IOT based portable devices. Furthermore, the piezo-coupled photocurrent ratio in mechanically stressed (strain ~0.75%) to relaxed configuration is enhanced by 287% under illumination (~410 nm), producing a high photoresponsivity (6.98×10^{-3} A/W) and detectivity (8.61×10^{10}cm $H^{1/2}$ W^{-1}). A high output power of ~ 48.5 μW/cm^2 generation under violet light irradiation makes the system promising for extracting power under illuminated condition. The excellent stability and capability of producing electrical power from surrounding environment and regular human activities make the PVDF-WS_2 system attractive for application in future wearable, stretchable and portable electronic devices.

4.5 References:

1. Z. L. Wang and J. Song, Science, 2006, **312**, 242-246.
2. G. Zhu, R. Yang, S. Wang and Z. L. Wang, Nano letters, 2010, **10**, 3151-3155.
3. J. H. Jung, M. Lee, J.-I. Hong, Y. Ding, C.-Y. Chen, L.-J. Chou and Z. L. Wang, ACS nano, 2011, **5**, 10041-10046.
4. B. K. Yun, Y. K. Park, M. Lee, N. Lee, W. Jo, S. Lee and J. H. Jung, Nanoscale research letters, 2014, **9**, 1-7.
5. E. J. Lee, T. Y. Kim, S.-W. Kim, S. Jeong, Y. Choi and S. Y. Lee, Energy & Environmental Science, 2018, **11**, 1425-1430.
6. Z.-H. Lin, Y. Yang, J. M. Wu, Y. Liu, F. Zhang and Z. L. Wang, The journal of physical chemistry letters, 2012, **3**, 3599-3604.

7. Y. Hu, Y. Zhang, C. Xu, G. Zhu and Z. L. Wang, Nano letters, 2010, **10**, 5025-5031.
8. C. H. Wang, W. S. Liao, Z. H. Lin, N. J. Ku, Y. C. Li, Y. C. Chen, Z. L. Wang and C. P. Liu, Advanced Energy Materials, 2014, **4**, 1400392.
9. W. Zeng, X.-M. Tao, S. Chen, S. Shang, H. L. W. Chan and S. H. Choy, Energy & Environmental Science, 2013, **6**, 2631-2638.
10. K. Shi, B. Sun, X. Huang and P. Jiang, Nano Energy, 2018, **52**, 153-162.
11. S. K. Ghosh and D. Mandal, Nano Energy, 2018, **53**, 245-257.
12. A. J. Lovinger, Science, 1983, **220**, 1115-1121.
13. S. K. Si, S. Paria, S. K. Karan, S. Ojha, A. K. Das, A. Maitra, A. Bera, L. Halder, A. De and B. B. Khatua, Nanoscale, 2020, **12**, 7214-7230.
14. R. Ding, X. Zhang, G. Chen, H. Wang, R. Kishor, J. Xiao, F. Gao, K. Zeng, X. Chen and X. W. Sun, Nano Energy, 2017, **37**, 126-135.
15. K. Roy, S. K. Ghosh, A. Sultana, S. Garain, M. Xie, C. R. Bowen, K. Henkel, D. Schmeiβer and D. Mandal, ACS Applied Nano Materials, 2019, **2**, 2013-2025.
16. S. K. Karan, R. Bera, S. Paria, A. K. Das, S. Maiti, A. Maitra and B. B. Khatua, Advanced Energy Materials, 2016, **6**, 1601016.
17. S. Garain, S. Jana, T. K. Sinha and D. Mandal, ACS applied materials & interfaces, 2016, **8**, 4532-4540.
18. T. Huang, S. Yang, P. He, J. Sun, S. Zhang, D. Li, Y. Meng, J. Zhou, H. Tang and J. Liang, ACS applied materials & interfaces, 2018, **10**, 30732-30740.
19. Y. Ye, Y. Jiang, Z. Wu and H. Zeng, Integrated Ferroelectrics, 2006, **80**, 245-251.
20. K. Matsushige, K. Nagata, S. Imada and T. Takemura, Polymer, 1980, **21**, 1391-1397.
21. K. Cai, X. Han, Y. Zhao, R. Zong, F. Zeng and D. Guo, ACS Sustainable Chemistry & Engineering, 2018, **6**, 5043-5052.
22. Y. Mao, P. Zhao, G. McConohy, H. Yang, Y. Tong and X. Wang, Advanced Energy Materials, 2014, **4**, 1301624.
23. C. Jin, N. Hao, Z. Xu, I. Trase, Y. Nie, L. Dong, A. Closson, Z. Chen and J. X. Zhang, Sensors and Actuators A: Physical, 2020, **305**, 111912.
24. D. Bhattacharya, S. Bayan, R. K. Mitra and S. K. Ray, ACS Applied Electronic Materials, 2020, **2**, 3327-3335.
25. P. Yadav, T. D. Raju and S. Badhulika, ACS Applied Electronic Materials, 2020, **2**, 1970-1980.

26. K. Maity, B. Mahanty, T. K. Sinha, S. Garain, A. Biswas, S. K. Ghosh, S. Manna, S. K. Ray and D. Mandal, Energy Technology, 2017, **5**, 234-243.
27. N. Scriven, Sustainable Energy & Fuels, 2021, **5**, 590-590.
28. Y. Ai, Z. Lou, S. Chen, D. Chen, Z. M. Wang, K. Jiang and G. Shen, Nano Energy, 2017, **35**, 121-127.
29. M. Kim, V. K. Kaliannagounder, A. R. Unnithan, C. H. Park, C. S. Kim and A. Ramachandra Kurup Sasikala, Applied Sciences, 2020, **10**, 3493.
30. A. Sultana, P. Sadhukhan, M. M. Alam, S. Das, T. R. Middya and D. Mandal, ACS applied materials & interfaces, 2018, **10**, 4121-4130.
31. L. Lv, F. Zhuge, F. Xie, X. Xiong, Q. Zhang, N. Zhang, Y. Huang and T. Zhai, Nature communications, 2019, **10**, 1-10.
32. R. Wang, F. Zhou, L. Lv, S. Zhou, Y. Yu, F. Zhuge, H. Li, L. Gan and T. Zhai, CCS Chemistry, 2019, **1**, 268-277.
33. L. Lv, J. Yu, M. Hu, S. Yin, F. Zhuge, Y. Ma and T. Zhai, Nanoscale, 2021, **13**, 6713-6751.
34. S. Mondal, T. Paul, S. Maiti, B. K. Das and K. K. Chattopadhyay, Nano Energy, 2020, **74**, 104870.
35. W. Han, L. Zhang, H. He, H. Liu, L. Xing and X. Xue, Nanotechnology, 2018, **29**, 255501.
36. Y. Purusothaman, N. R. Alluri, A. Chandrasekhar, V. Vivekananthan and S.-J. Kim, The Journal of Physical Chemistry C, 2018, **122**, 12177-12184.
37. S. Bayan, D. Bhattacharya, R. Mitra and S. Ray, Nanotechnology, 2020, **31**, 365401.
38. S. Sharma, S. Bhagat, J. Singh, R. C. Singh and S. Sharma, Journal of Materials Science, 2017, **52**, 11326-11336.
39. M. Pusty, L. Sinha and P. M. Shirage, New Journal of Chemistry, 2019, **43**, 284-294.
40. S. K. Karan, D. Mandal and B. B. Khatua, Nanoscale, 2015, **7**, 10655-10666.
41. A. Ghorai, A. Midya, R. Maiti and S. K. Ray, Dalton Transactions, 2016, **45**, 14979-14987.
42. A. Ghorai, A. Midya and S. K. Ray, New Journal of Chemistry, 2018, **42**, 3609-3613.
43. X. Cai, T. Lei, D. Sun and L. Lin, RSC advances, 2017, **7**, 15382-15389.
44. N. A. Hoque, P. Thakur, S. Roy, A. Kool, B. Bagchi, P. Biswas, M. M. Saikh, F. Khatun, S. Das and P. P. Ray, ACS applied materials & interfaces, 2017, **9**, 23048-23059.

45. P. Biswas, N. A. Hoque, P. Thakur, M. M. Saikh, S. Roy, F. Khatun, B. Bagchi and S. Das, ACS Sustainable Chemistry & Engineering, 2019, **7**, 4801-4813.
46. M. Fortunato, C. R. Chandraiahgari, G. De Bellis, P. Ballirano, F. Sarto, A. Tamburrano and M. S. Sarto, Nanomaterials, 2018, **8**, 743.
47. Y. Zhang, L. Ye, B. Zhang, Y. Chen, W. Zhao, G. Yang, J. Wang and H. Zhang, Journal of Membrane Science, 2019, **579**, 22-32.
48. C. Zhang, Y. Fan, H. Li, Y. Li, L. Zhang, S. Cao, S. Kuang, Y. Zhao, A. Chen and G. Zhu, ACS nano, 2018, **12**, 4803-4811.
49. G. Zhang, D. Brannum, D. Dong, L. Tang, E. Allahyarov, S. Tang, K. Kodweis, J.-K. Lee and L. Zhu, Chemistry of Materials, 2016, **28**, 4646-4660.
50. C. Chiang and R. Popielarz, Ferroelectrics, 2002, **275**, 1-9.
51. L. Zhu, The journal of physical chemistry letters, 2014, **5**, 3677-3687.
52. S. Ippili, V. Jella, J.-H. Eom, J. Kim, S. Hong, J.-S. Choi, V.-D. Tran, N. Van Hieu, Y.-J. Kim and H.-J. Kim, Nano Energy, 2019, **57**, 911-923.
53. V. Jella, S. Ippili, J.-H. Eom, J. Choi and S.-G. Yoon, Nano Energy, 2018, **53**, 46-56.
54. H. S. Kim, D. W. Lee, D. H. Kim, D. S. Kong, J. Choi, M. Lee, G. Murillo and J. H. Jung, Nanomaterials, 2018, **8**, 777.
55. K. Liu, Q. Yan, M. Chen, W. Fan, Y. Sun, J. Suh, D. Fu, S. Lee, J. Zhou and S. Tongay, Nano letters, 2014, **14**, 5097-5103.
56. T. K. Sinha, S. K. Ghosh, R. Maiti, S. Jana, B. Adhikari, D. Mandal and S. K. Ray, ACS applied materials & interfaces, 2016, **8**, 14986-14993.
57. S. Jeong, M. W. Kim, Y.-R. Jo, T.-Y. Kim, Y.-C. Leem, S.-W. Kim, B.-J. Kim and S.-J. Park, ACS applied materials & interfaces, 2018, **10**, 28736-28744.

Chapter: 5

Two-dimensional $Mo_xW_{1-x}S_2$ alloys for nanogenerators producing record piezo-output and coupled photodetectors for self-powered UV Sensor

In this work we propose a novel sustainable, self-driven UV photodetection system using ternary TMDC alloy ($Mo_xW_{1-x}S_2$) by coupling a photodetector as a light intensity sensor and a piezoelectric nanogenerator (PENG) as a power source. We have synthesized crystalline $Mo_xW_{1-x}S_2$ ternary alloy nanosheets via cost effective hydrothermal method to fabricate a UV (365 nm) photodetector with extraordinary high responsivity (~229 A/W). The microstructural, optical properties of different ternary alloy composition, along with their binary counterparts, have been studied. The optimized $Mo_{0.5}W_{0.5}S_2$ ternary alloy nanosheets are used as fillers in PVDF matrix to fabricate flexible self-polled PENGs, exhibiting piezoelectric open-circuit output ~50 V under finger tapping and a record high piezo-voltage ~187 V under impact of 12 kPa. By coupling the two devices, the output voltage of the PENG is tuned by the resistance of the photodetector, exhibiting superior voltage sensitivity (~ 0.75 V $\mu W^{-1} cm^{-2}$) with UV illumination. The impedance matching between the PENG and photodetector has been utilized to demonstrate self-powered UV sensors by monitoring the on/off states of LED directly. This self-powered, portable ternary TMD alloy device is attractive for future real-time monitoring of UV radiation and smart health sensors for IOT applications.

5.1 Introduction:

The recent advances in Internet of Things (IOTs), an important technology of significant interests towards rapidly growing smart sensors, have led to increasing demand for intelligent, multifunctional, cost-effective and compact sensors with very low power consumption. As one of the most important light-sensing devices, photodetectors have a wide range of applications in the field of security, ultra-violet (UV) radiation detection, infrared thermal imaging, remote sensing, astronomical detectors, communication system etc. Various traditional semiconductors (Si, Ge, ZnO, GaN, TiO_2 etc.) and recently two-dimensional materials, specially transition metal dichalcogenides (TMDCs) are attractive in photodetection application purposes due to their fascinating optoelectronic and electric properties. The wide applications of chemically exfoliated, large area TMDC nanosheets face significant challenges owing to the fact that chalcogen vacancies in such materials, lead to localized deep-level defect states (DLDs), which degrade their electronic and optoelectronics

performances. Composition modulation has been predicted to be a potential solution to suppress the DLDs [1,2], and theoretical calculations have predicted that ternary alloys of TMDCs are thermodynamically more favorable than their binary counterparts [3–5]. Although TMDC ternary alloys exhibit superior electrical, optoelectronic and catalytic properties than their binary counterparts [6–10], these advantages have not been exploited yet for device application purposes, mainly because of the complexity in growing these alloys by using either mechanical exfoliation or chemical vapor deposition.

Ultraviolet (UV) radiation is an important part of the solar spectrum, but overexpose of UV illumination can affect human health and also induces harmful effects on the environment [11,12]. In this regard, it is very much necessity to detect UV radiation, especially for exposure to human body at higher altitudes and signal detection purposes. Most of the existing and commercial UV photodetectors require an external input power supply for their operation, which in turn leads to configuration that not only increases the size of the sensor system, but also limits their portability and applications in real-time continuous monitoring. Therefore, it is extremely necessary to develop a self-powered UV photosensor system by circumventing the need of a traditional power supply. In this regard, mechanical energy harvesting through nanogenerators (viz., piezoelectric, triboelectric) have emerged as promising devices. Among them piezoelectric nanogenerators (PENG) are very attractive for energy harvesting as they possess high mechanical endurance and durability without any risk of continuous material abrasion which takes place in a triboelectric system. Various traditional piezoelectric materials [13–15] (PZT, $BaTiO_3$, ZnO etc.) along with piezoelectric polymers [16] have been studied rigorously. Recently two-dimensional materials [17–23] including TMDC nanosheets have drawn intense attention for use as fillers in polymer matrices [17,24–26], since they can strongly enhance the piezoelectric β-phase of the resulting nanocomposite. The fabricated piezoelectric nanogenerators with promising energy harvesting capabilities are attractive to design different self-powered, portable systems (such as chemical, thermal, pressure, photo sensors etc.) [27–32].

In this work, we have reported the characteristics of a self-powered real time UV photodetection system based on impedance matching between piezoelectric nanogenerator and photodetector by using ternary TMDC ($Mo_xW_{1-x}S_2$) alloys. The optimized $Mo_{0.5}W_{0.5}S_2$ ternary alloy nanosheets synthesized by using a simple hydrothermal method have been used to fabricate UV photodetectors, which exhibit outstanding photoresponsivity (229 A/W) and detectivity (6.95×10^{12} Jones) under 365 nm illumination. The piezoelectric nanogenerator

fabricated by using the ternary $Mo_{0.5}W_{0.5}S_2$ alloy nanosheets within PVDF matrix exhibits record performance (piezo-voltage ~ 50 V with areal piezo-power density ~1.18 mW/cm^2 under finger tapping, and ~187 V under a mechanical impact of 12 kPa). By coupling the above two individual devices (piezoelectric nanogenerator, photodetector) we have demonstrated a self-powered UV photodetection system, which produces a large voltage responsivity (R_v ~ 0.75 V $\mu W^{-1} cm^{-2}$) indicating the ability to detect UV radiation even at a very low intensity. The self-powered system is capable of real time UV radiation monitoring in human body and may stimulate its practical application in the next generation self-powered photodetection system in the sensor and wearable electronics based IOT devices.

5.2 Experimental section:

5.2.1 Materials:

Sodium molybdate dihydrate ($Na_2MoO_4 \cdot 2H_2O$), sodium tungstate dihydrate ($Na_2WO_4 \cdot 2H_2O$), and thiourea (CH_4N_2S) were purchased from Alpha Aser and Polyvenielidene-di-Fluoride (PVDF) was brought from Sigma Aldrich. All chemicals were and directly used without any further purification. Deionized water was purified using a Milli-Q system.

5.2.2 Synthesis of $Mo_xW_{1-x}S_2$ nanosheets:

$Mo_xW_{1-x}S_2$ nanosheets of different compositions (from x = 0 to 1) had been synthesized by hydrothermal reaction technique. To synthesize $Mo_xW_{1-x}S_2$ nanosheets $Na_2MoO_4 \cdot 2H_2O$ and $Na_2WO_4 \cdot 2H_2O$ are used as Mo and W sources, respectively, and thiourea was used as S source. The certain quantities of precursors were dissolved in 40 mL of pure water. The precursor solutions had to be subjected to stirring to get a homogeneous solution. The solution was then transferred to a Teflon-lined stainless autoclave, which was heated and then maintained at 190°C for ~26 hrs. before naturally cooling down to room temperature. The final dark solution was centrifuged several times and the precipitate was washed with distilled water and absolute ethanol and dried at 60°C for 12 hrs.

For synthesize MoS_2 (WS_2) nanosheets $Na_2MoO_4 \cdot 2H_2O$ ($Na_2WO_4 \cdot 2H_2O$) and thiourea were dissolved in water and after stirring the solution was transferred into 100-mL Teflon-lined stainless autoclave and was maintained at 190°C for 20 hrs. (28 hrs.) before naturally cooling down it to room temperature. The final dark solution was centrifuged several times, and the

precipitate was washed with distilled water and absolute ethanol and dried at 60 °C for 12 hrs. This obtained powder was bath sonicated for 6 hrs. (in IPA) to get the dispersion of nanosheets.

5.2.3 Fabrication of Photodetector:

In order to fabricate the photodetector, a Si/SiO_2 (285 nm) substrate was taken and cleaned in acetone and isopropyl alcohol through ultra-sonication bath. Then the electrodes were made by photolithography technique by using laser writer lithography (LW405-MICROTECH) followed by Ti/Au (5 nm/ 60 nm) deposition by e-beam deposition. The spacing between the electrodes was 10 µm (length) and 250 µm (width). Then 50 µl alloy samples (10 mg/ml, dispersed in IPA) were drop casted on the bare patterns to make the device. Finally the device was annealed at 80°C on a hot plate for 1 hr.

5.2.4 Fabrication of Piezoelectric Nanogenerator:

PVDF- $Mo_xW_{1-x}S_2$ nanocomposite is prepared by using 0.25 gm PVDF and 0.1 gm nanosheet power were firstly dispersed in 250 µl DMF solvent and then sonicated for 4 hrs. Then the nanocomposite solution was spin coated at 1000 rpm for 10 sec onto the PET side of ITO-PET substrate and ITO acts as an electrode here. The PI (kapton)-Al foil was attached on the top of the spin coated film such that the Al foil acts as another electrode. Thereafter, this device was kept for drying at 60^oC for 3 hrs. to obtain the device finally in Al-PI/ PVDF-$Mo_xW_{1-x}S_2$/ PET-ITO configuration.

5.2.5 Fabrication of self-powered photodetection system:

The fabricated photodetector and PENG were assembled together through relevant circuit to form a self-driven photodetector system. This circuit consists of constant resistors, zener diode and commercial LEDs.

5.2.6 Characterizations:

The morphology of hydrothermally synthesized $Mo_xW_{1-x}S_2$ nanosheets were investigated using a high-resolution transmission electron microscope (TEM) (FEI-TECNAI G2 20ST, energy 200 keV) and atomic force microscopy (AFM) (di INNOVA). Absorption spectrums were taken by using a UV-Vis spectrometer (Shimadzu -UV-Vis 2600 Spectrophotometer) and micro-raman and photoluminescence spectrums were recorded with a spectrometer

(LabRam HR Evolution; HORIBA France SAS-532 nm laser). The phase and crystallinity were investigated by X-ray diffraction (Rigaku (Smartlab)). Fourier transform infrared (FTIR) spectroscopy was carried out by using a JASCO FTIR-6300 spectrometer to estimate the piezoelectric active β-phase within the PVDF– $Mo_xW_{1-x}S_2$ nanocomposite. The surface profiles of all the nanocomposites and the chemical compositions were examined by using a field-emission scanning electron microscope (FESEM) equipped with an energy-dispersive X-ray (EDAX) spectrometer. The optoelectronic-characteristics of the photodetectors were measured by a probe station equipped with a Keithley 2450 source meter. Thorlab LED (365 nm) was employed for optical illumination source and to calibrate the illumination power spectrometer coupled with integrating sphere (Flame-Ocean optics) is used. The output voltages were recorded by using a digital oscilloscope (SMO702 (scientific)).

5.3 Results and Discussions:

5.3.1 Structural studies of $Mo_xW_{1-x}S_2$ ternary alloy nanosheets:

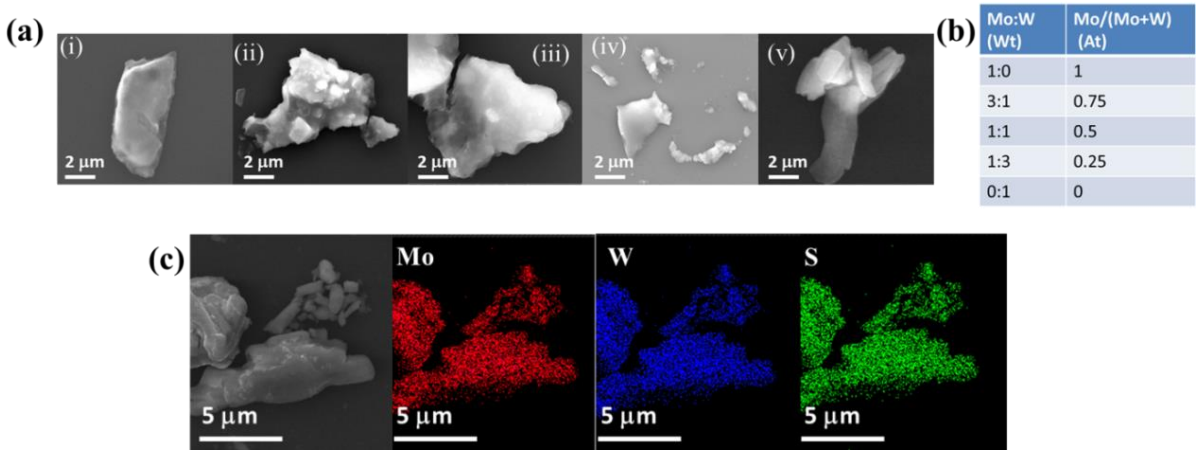

Mo:W (Wt)	Mo/(Mo+W) (At)
1:0	1
3:1	0.75
1:1	0.5
1:3	0.25
0:1	0

Figure 5.1 (a) SEM images for varying composition $Mo_xW_{1-x}S_2$ alloys for Mo fraction (x) of (i) 1.0, (ii) 0.75, (iii) 0.50, (iv) 0.25, (v) 0. (b) EDAX data of the samples in tabular form. (c) EDAX elemental (Mo, W, S) mapping of $Mo_{0.5}W_{0.5}S_2$ alloy nanosheets.

Morphology and chemical compositions of the synthesized $Mo_xW_{1-x}S_2$ ternary alloy nanosheets (x=0 to 1) are investigated by using diffraction and microscopy analyses. Elemental components are studied by using energy-dispersive X-ray (EDAX) analysis from scanning electron microscopies (SEM) and represented in Figure 5.1(a) & (b) respectively.

The EDAX mapping of different elements for typical $Mo_xW_{1-x}S_2$ (x=0.5) nanosheets are depicted in Figure 5.1(c), which show that Mo, W and S are uniformly distributed over the nanosheets.

TEM images are depicted in Figure 5.2(a) and AFM images are depicted in Figure 5.2(b) of the ternary alloy nanosheets (for all compositions, including the binary counterparts) reveal the formation of few layered alloy nanosheets.

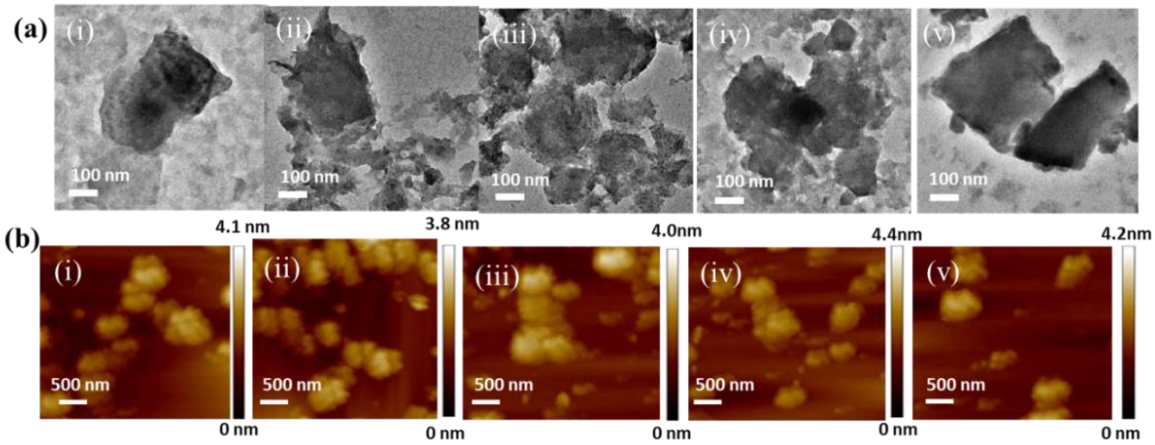

Figure 5.2 (a) TEM and (b) AFM images of ternary alloys for Mo fraction (x) of (i) 1.0, (ii) 0.75, (iii) 0.50, (iv) 0.25, (v) 0.

Typical high-resolution TEM (HRTEM) image of the ternary alloy nanosheets (x=0.5), shown in Figure 5.3(a), depicts the formation of a honeycomb like structure. The corresponding interlayer spacing from the lattice fringes (Figure 5.3(b)) are found to be 0.68 nm [33] and 0.27 nm [34] indicating the formation of (002) and (100) lattice planes of $Mo_{0.5}W_{0.5}S_2$, respectively. In selected area electron diffraction (SAED) pattern from the HRTEM image is shown in Figure.5.3(c), we observe multi-circular diffraction pattern, which reveals that the grown $Mo_{0.5}W_{0.5}S_2$ nanosheet is polycrystalline in nature and the TEM image of the corresponding nanosheet is shown in inset of Figure 5.3(c). The layer thickness (Figure 5.3(d)) can be estimated from the atomic force microscopy (AFM) image, revealing a typical nanosheet to be ~ 3 nm (~ 4/5 layers) thick. X-ray diffraction peaks (Figure 5.3(e)) of the ternary alloy nanosheets appearing at 32.6°, 58.8° depict the formation of (100), (106) planes of MoS_2, while those at 28.8° and 44.6° are the signatures of (004) and (006) planes of WS_2. A pronounced peak is observed at 14.3° owing to the formation of crystalline (002) plane [35] for both MoS_2 and WS_2. These results suggest that as-synthesized ternary alloy nanosheets are polycrystalline in nature [36,34] having hexagonal crystal structure [34].

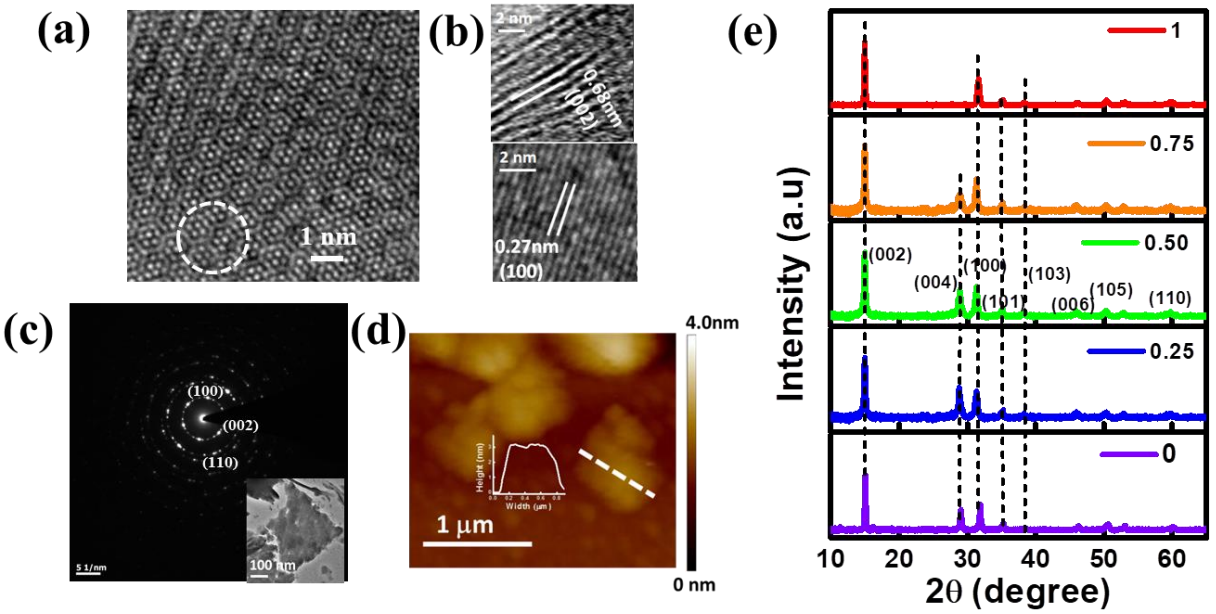

Figure 5.3 (a) Typical HRTEM image of $Mo_{0.5}W_{0.5}S_2$ alloy nanosheets. (b) Lattice fringes from the HRTEM image of the alloy with an interlayer spacing 0.68 nm and 0.27 nm indicating the formation of (002) and (100) planes, respectively. (c) Selected area electron diffraction pattern (SAED) showing the formation of crystalline alloy with the inset depicting the TEM image of the probed nanosheet. (d) Typical AFM micrograph showing the height profile of $Mo_{0.5}W_{0.5}S_2$ alloy nanosheets. (e) XRD diffraction patterns of $Mo_xW_{1-x}S_2$ TMDC alloys with different compositions including binary MoS_2 and WS_2 nanosheets.

5.3.2 Spectroscopic Studies $Mo_xW_{1-x}S_2$ ternary alloy nanosheets:

Raman spectroscopy has been carried out to characterize the composition dependent vibrational modes of as-synthesized $Mo_xW_{1-x}S_2$ alloy nanosheets (x=0 to 1), as displayed in Figure 5.4(a). Raman spectra of $Mo_xW_{1-x}S_2$ alloy nanosheets exhibit three prominent peaks (E^1_{2g} mode of WS_2, the E^1_{2g} mode of MoS_2 and a combined peak, the A_{1g} modes for both WS_2 and MoS_2), suggesting the successful synthesis of composition tunable $Mo_xW_{1-x}S_2$ ternary alloy nanosheets [8,37,38]. Pure MoS_2 exhibits two vibrational modes at 382 cm^{-1} (E^1_{2g}, in-plane) and 404 cm^{-1} (A_{1g}, out-of-plane). With increasing W content (0 to 1), the A_{1g} peak exhibits a prominent blue shift and the E^1_{2g} mode (S-Mo) shows a red shift accompanied by reduced intensity, which diminishes completely for pure WS_2. Also a new E^1_{2g} mode (S-W) emerges and undergoes a blue shift accompanied by increasing intensity [38]. The shift of out-of-plane (A_{1g}) mode can be explained by the difference of bond lengths for MoS_2 and WS_2

which varies due to the random replacement of Mo by W within ternary alloy nanosheets. Whereas the behavior of in-plane E^1_{2g} mode can be understood by the mass difference between the cations in the alloy nanosheets of different compositions [38]. UV-Vis absorbance spectroscopy is carried out to study the excitonic peak positions and their variation for different alloy compositions. All ternary nanosheets exhibit excitonic A and B peaks in the absorption spectrum arising from the spin-orbit split bands at K and K´ points of the Brillouin zone [38–40]. Excitonic A and B peaks for MoS_2 are observed at ~674 and ~614 nm, respectively. The transition energy of exciton-B increases monotonically with increasing tungsten content in the alloy compositions whereas that of exciton-A is first slightly red shifted followed by a blue shift (inset Figure 5.4(b)). It is shown in Figure 5.4(b) that for pure WS_2 the excitonic A and B peak appear at ~619 nm and ~555 nm, respectively. The separation of excitonic A and B peaks (E_B-E_A), originating from valance band splitting, increases monotonically from 0.15 eV (x=1) to 0.39 eV (x=0) with increasing tungsten content [41] in the alloy (inset Figure 5.4(b)). Micro-photoluminescence spectroscopy is one of the most effective method to estimate the optical band gap of semiconducting layered materials. An excitation by using 532 nm laser show (Figure 5.4(c)) sharp photoluminescence peaks at ~676 nm for MoS_2 and ~629 nm for WS_2 nanosheets, which correspond to their band-edge excitonic transitions [42]. We have observed the bowing phenomenon (nonlinearity factor due to the formation of alloy) in $Mo_xW_{1-x}S_2$ nanosheets (inset Figure 5.4(c)), which is previously reported for ternary TMDC alloy nanosheets [39,41,43]. This bowing effect is also observed in the photoluminescence spectrum with the lowest energy emission peak found for the ternary alloy composition with x=0.75 and shown in inset of Figure 5.4(c).

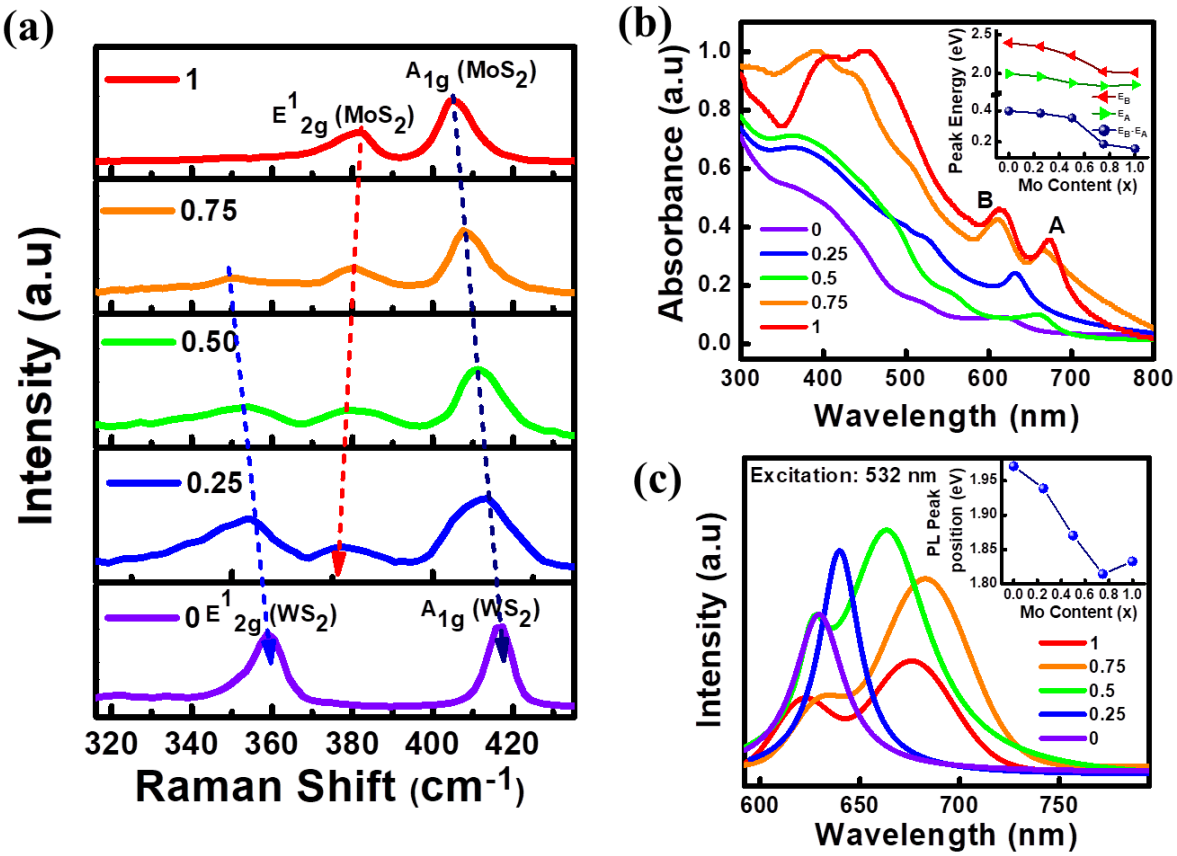

Figure 5.4 (a) Raman spectra of composition tunable $Mo_xW_{1-x}S_2$ alloy nanosheets. (b) Absorption spectra showing the excitonic peaks in the $Mo_xW_{1-x}S_2$ alloys. The inset presents the variation of excitonic A and B peaks and the difference of excitonic energy (E_B-E_A) with composition varying from Mo fraction (x) 0 to 1. (c) Photoluminescence spectra of alloy nanosheets with the inset showing the PL peak energy of different alloy composition with the Mo fraction (x) varying from 0 to 1.

5.3.3 Opto-electric Studies on $Mo_xW_{1-x}S_2$ ternary alloy nanosheets:

A schematic device structure of $Mo_xW_{1-x}S_2$ TMDC alloy-based photodetector is presented in Figure 5.5(a), and the optical image is displayed in inset of Figure 5.5(a). UV light (365 nm) photodetectors are fabricated by using the compositionally modulated $Mo_xW_{1-x}S_2$ ternary alloys (x=0.25, 0.5, 0.75) and also their binary counterparts (MoS_2 and WS_2). The optoelectronic performances of all the fabricated devices with same experimental conditions (365 nm, 10 μW/cm^2, 1 V bias) and identical geometry are evaluated. As depicted in Figure 5.5(b), the photocurrent of alloy devices is found to be higher than those obtained from their

binary counterpart, with the alloy having x=0.5 showing the highest photocurrent value. Both MoS_2 and WS_2 contain large number of sulfur vacancies (denoted as $V_{S\text{-}Mo}$ and $V_{S\text{-}W}$), which can generate to large density of defect states deep inside the band gap and can act as trap states and/or scattering centers which affect their optoelectronic performance. The formation energy of $V_{S\text{-}Mo}$ is larger than that of $V_{S\text{-}W}$ [10], and therefore the effect of $V_{S\text{-}W}$ dominates and act as shallow level traps within the bandgap of $Mo_{0.5}W_{0.5}S_2$ ternary alloy [10]. Photogenerated carriers, trapped by these shallow level defects ($V_{S\text{-}W}$) in $Mo_{0.5}W_{0.5}S_2$, are more likely to be brought back into the conduction band again to become free carriers, rather than getting recombined in the valance band, and thus increases the free carrier concentration in the conduction band and this phenomenon is schematically represented in Figure 5.5(c). Besides benefiting with the low defect concentration, only a small fraction of photogenerated carriers are captured by the defect states which is another reason[10] for a higher photocurrent generation from $Mo_{0.5}W_{0.5}S_2$ device.

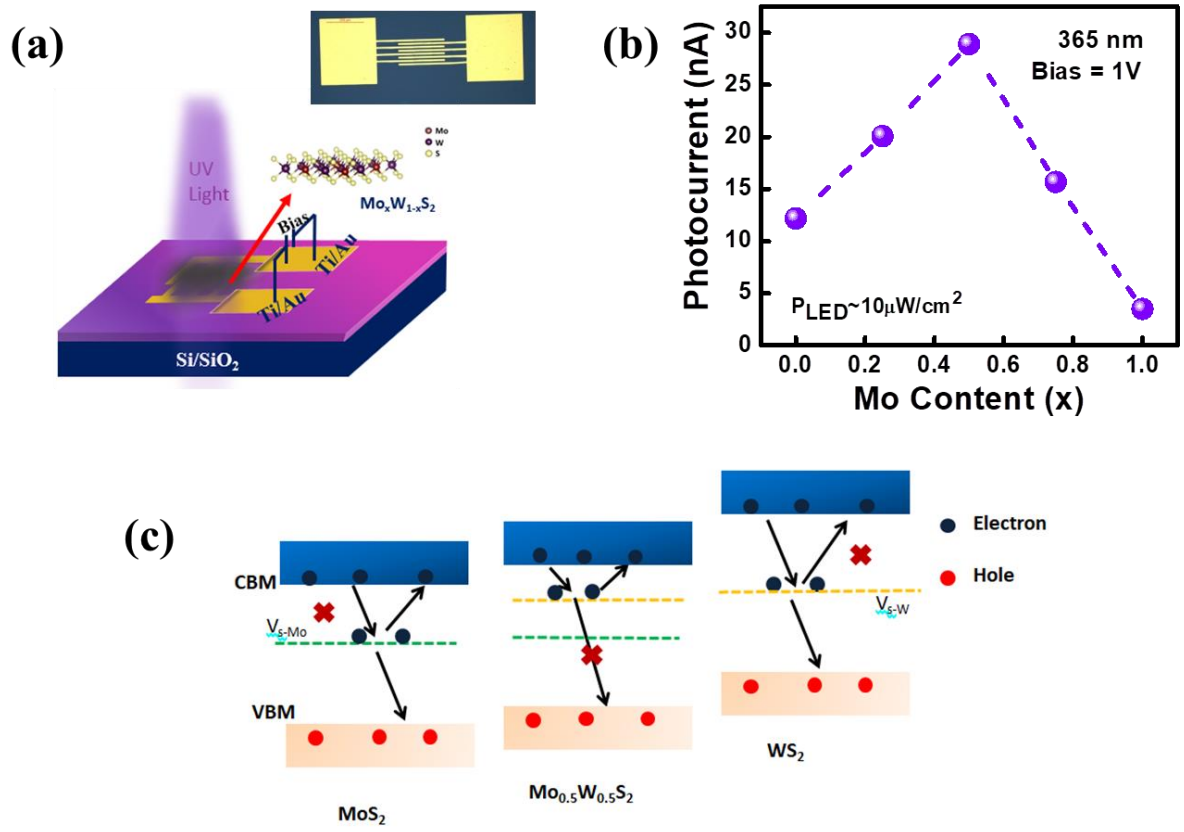

Figure 5.5 (a) Schematic of the photodetector device and the optical image of device in the inset. (b) Variation of photocurrent with Mo fraction (x) in the TMDC alloys with UV (365 nm) illumination. (c) Schematic band diagrams with localized defect states for MoS_2, $Mo_{0.5}W_{0.5}S_2$, and WS_2 to explain the photocurrent enhancement in ternary alloy.

From Figure 5.6(a) it is observed that the current from the device under 365 nm illumination increases monotonically with increasing illumination power (1.5 to 27.5 μW/cm^2). With increasing incident power, higher number of photogenerated carriers lead to the reduced internal resistance of the photodetector, as varies from ~ 11.78 MΩ (dark) to 6.22 MΩ under illumination of ~27.55 μW/cm^2 at a bias of 1 V and it is presented in Figure 5.6(b). This observed change in resistance with illumination intensity is advantageous for the fabrication of self-powered low intensity UV detection systems [44,45]. To further evaluate the performance of the fabricated photodetector, we have calculated the responsivity (R) and specific responsivity (D*) which can be estimated as $R = \frac{I_{ph}}{PS}$ and $D^* = R\sqrt{\left(\frac{S}{2qI_{dark}}\right)}$, respectively, where S stands for the effective illuminated area, I_{dark} is the dark current, and q is the absolute value of the charge (1.6×10^{-19} C) [11]. The maximum responsivity and specific detectivity of the $Mo_{0.5}W_{0.5}S_2$ device are estimated to be 229 A/W and 6.95×10^{12} Jones, respectively under an illumination (365 nm) intensity of ~1.5 μW/cm^2 at 1 V bias and it is depicted in Figure 5.6(c), indicating the low power detection ability of the fabricated photodetector. The dynamic behavior of this ternary alloy ($Mo_{0.5}W_{0.5}S_2$) UV sensor is characterized from the time-resolved photocurrent measurements by alternatively exposing the photodetector to UV light and dark. Figure 5.6(d) indicates that the photodetector device exhibits reproducible characteristics under multiple light on-off switching cycles with the response and recovery times ~ 2.1 s and 3.6 s (defined as the time between 10% and 90% of the maximum photocurrent and vice versa), respectively. The values of responsivity and detectivity with moderate response time of this $Mo_{0.5}W_{0.5}S_2$ alloy UV detector are superior to the previously reported photodetector devices [46,47]. The fabricated photodetector (x=0.5) exhibits an excellent stability, with the photocurrent under UV (365 nm, 27.55 μW/cm^2) illumination remaining almost unchanged even after six months from its fabrication and it is presented in Figure 5.6(e).

*Photodetector device fabrication credit: Shubhrasish Mukherjee

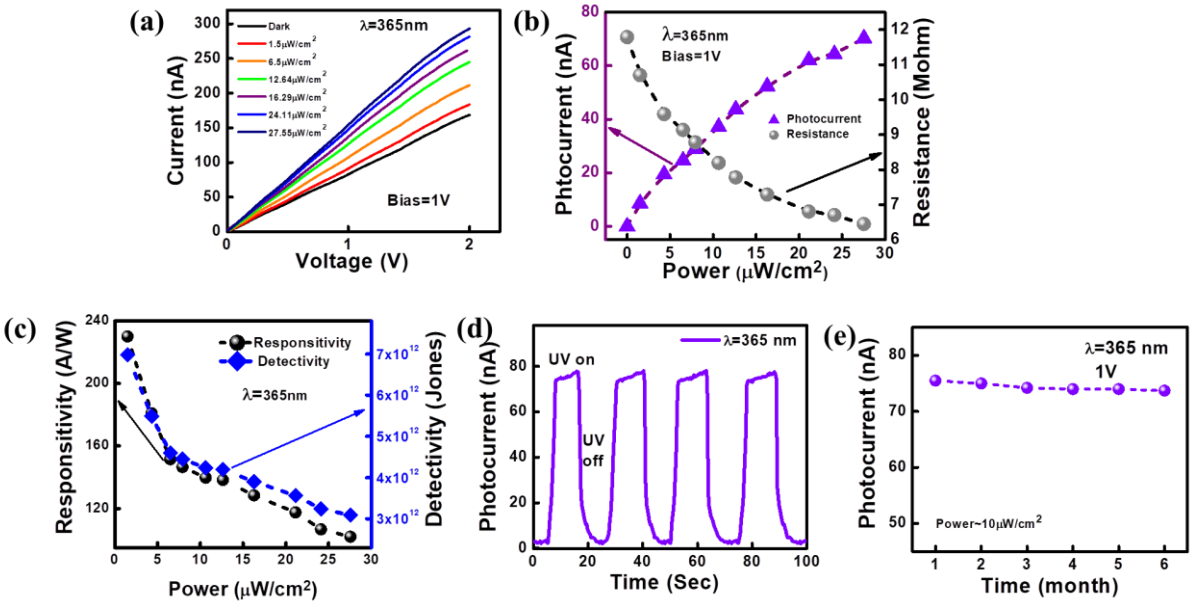

Figure 5.6 (a) Current-voltage characteristics of the $Mo_{0.5}W_{0.5}S_2$ alloy device with different intensity for 365 nm UV illumination. (b) Variation of photocurrent and resistance of the detector as a function of 365 nm illumination intensity for $Mo_{0.5}W_{0.5}S_2$ alloy device. (c) Variation of responsivity and detectivity with intensity under 365 nm illumination at 1 V bias for $Mo_{0.5}W_{0.5}S_2$ alloy photodetector. (d) Dynamic response of the device under 27.55 μW/cm^2 light intensity (365 nm). (e) Long duration (six month) stability of the $Mo_{0.5}W_{0.5}S_2$ photodetector measured under 365 nm, 27.55 μW/cm^2 illumination recorded at an interval of one month.

5.3.4 Piezoelectric Study:

In order to realize the operation of self-driven photodetection, PVDF-$Mo_{0.5}W_{0.5}S_2$ nanocomposite piezoelectric nanogenerator (PENG) has been utilized as the power source to drive the TMDC alloy-based photodetector and is schematically depicted in Figure 5.7(a) and the real image of the PENG device is presented in inset of the Figure 5.7(a). Under application of an external mechanical strain piezoelectric bound charges are induced within this PENG due to polarization, which eventually result in a potential drop at the two ends of the nanogenerator device. To neutralize this built-in-field, opposite free charges appear at the two electrodes of the PENG until the piezoelectric bound charges are balanced by the free charges and a positive piezo signal is produced. When the external stress is released, the piezoelectric potential diminishes and the free charges are accumulated at electrodes of the

PENG, gradually flow back in the opposite direction and consequently a negative signal is generated. Such repeated compress and release process produces a periodic alteration of positive and negative output voltage responses [19, 24,48], the mechanism is schematically presented in Figure 5.7(b). The switching of voltage polarity upon reversing the electrode connections is observed and depicted in Figure 5.7(c)), which concludes that the output voltage is truly piezoelectric in nature and does not arise from any instrumental artifacts. The mechanical energy harvesting ability of the self-polled PENG is tested under human finger tapping condition and the performance of the PENG is examined with changing the imparting frequency from 0.5 to 2.5 Hz. The open circuit piezo output voltage (V_{oc}) initially slightly increases with increasing impact frequency from 0.5 to 1.5 Hz and thereafter saturates and represented in Figure 5.7(d). This observation indicates that the frequency of mechanical impact can be ignored for the piezoelectric nanogenerator, making it suitable for practical PENG applications. This fabricated PENG device is able to produce ~50 V open circuit output piezo-voltage under finger tapping (1.5 Hz frequency). This PENG exhibits an areal power density of 1.18 mW/cm^2 across a ~0.9 MΩ resistance (Figure 5.7(e)) under simple finger tapping condition (~3 kPa at 1.5 Hz).

.

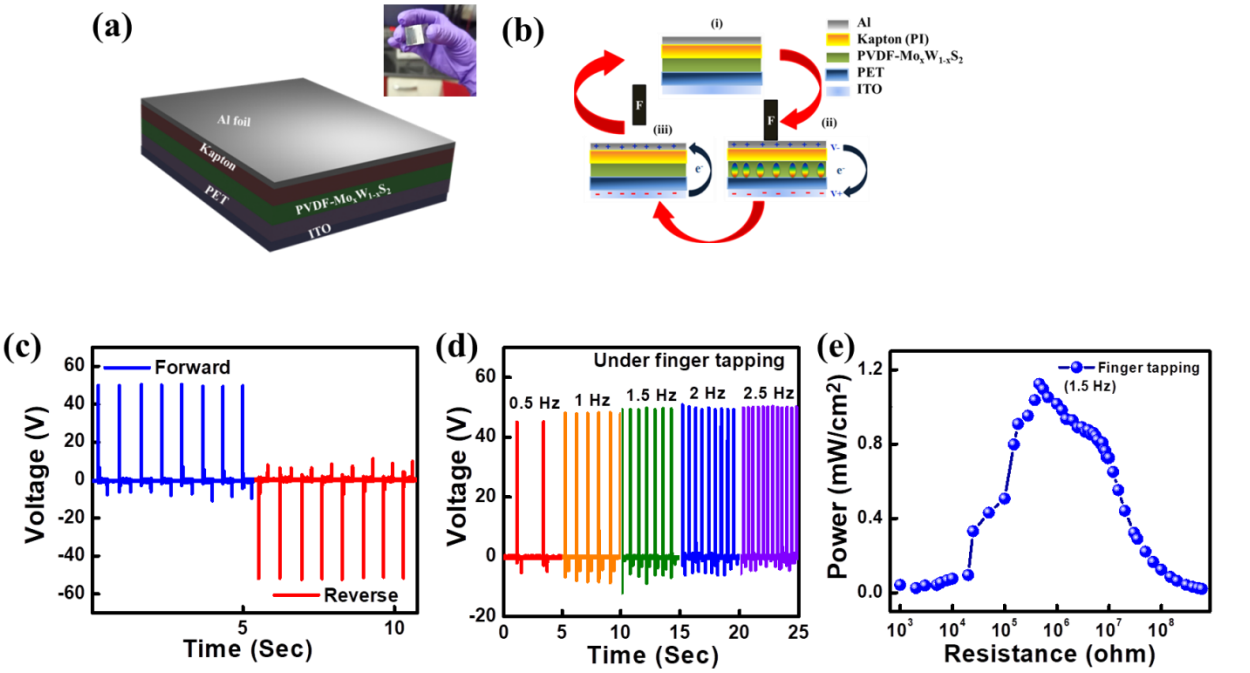

Figure 5.7 (a) Schematic of the fabricated nanogenerator device with its photograph shown in the inset. (b) Schematic working principle of the piezoelectric nanogenerator (PENG) device (i) without application of any impact, (ii) application of an external impact, (iii) removal of external impact. (c) Open circuit output voltage from $Mo_{0.5}W_{0.5}S_2$ PENG in forward and reverse connections under finger tapping. (d) Variation of open circuit output piezo-voltage from the PENG device with varying impact frequency under simple finger tapping condition. (e) Variation of piezoelectric power with varying load resistance for $Mo_{0.5}W_{0.5}S_2$ PENG under finger tapping condition.

On the other hand, it produces a piezo-voltage of ~187 V under 12 kPa mechanical impact (Figure 5.8(a)), making the fabricated PENG suitable for superior performance piezoelectric energy harvesting applications with a high stability (performance remains unaffected even after 6 months of the device fabrication) and is depicted in Figure 5.8(b)). As shown in Figure 5.8(c), the performance (piezo voltage per unit pressure) of fabricated self-poled PENG is superior to previously reported results on PVDF based PENG devices [49,50]. The finger tapping (at 1.5 Hz) has been performed throughout the study as a source of mechanical compression of the PENG device to drive the UV sensor, since this appears to be more practical than a high mechanical imparts for wearable sensor application purposes.

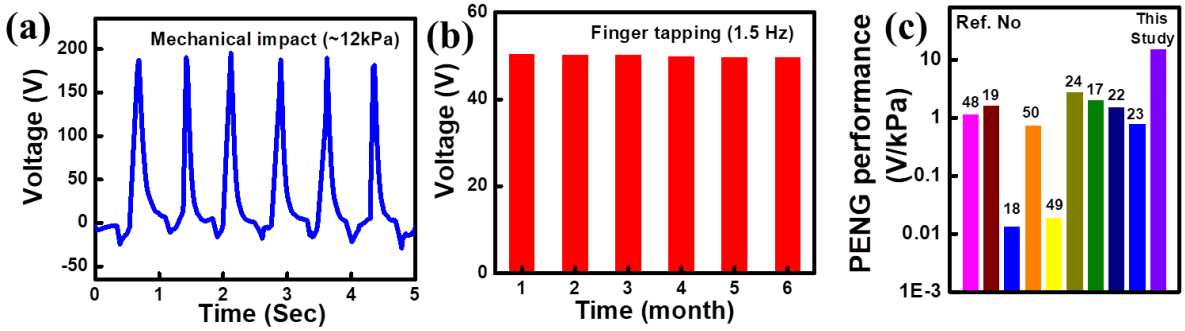

Figure 5.8 (a) Open circuit piezo voltage from the PENG device under a mechanical impact of ~12 kPa. (b) Stability (6 months) of $Mo_{0.5}W_{0.5}S_2$ PENG under finger tapping. (c) Comparison of piezoelectric performance (piezo voltage/ kPa) of the PENG device with reported results.

We have also measured the open circuit piezoelectric output voltages from other two composition (x=0.25, 0.75) of the ternary alloy and as well as the binary control samples under the same experimental conditions. We have observed that the PVDF-ternary nanocomposite alloy for x=0.5 offers the highest open circuit output voltage (Figure 5.9(a)). This observation is in agreement with FTIR and XRD results, which revealed that a highest fraction of piezoelectric β-phase for the PVDF-$Mo_{0.5}W_{0.5}S_2$ nanocomposite (Figure 5.9(b), (c), (d)).

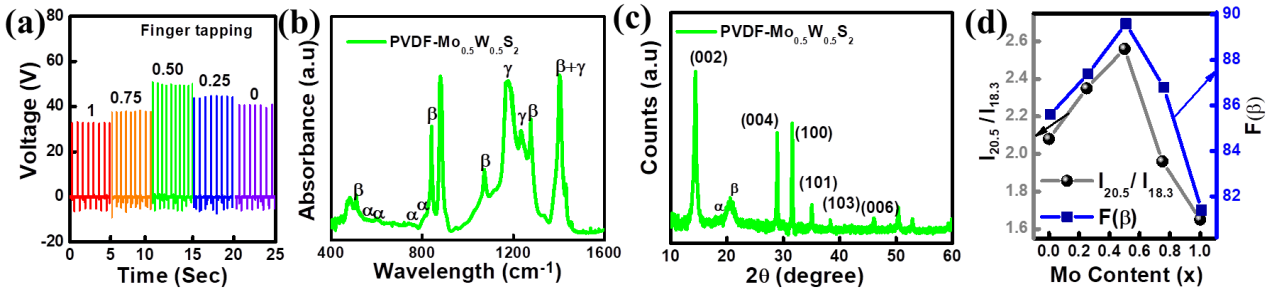

Figure 5.9 (a) Variation of piezoelectric output voltage for different Mo fraction (x: 0-1) of $Mo_xW_{1-x}S_2$ PENGs under finger tapping condition. (b) FTIR spectra. (c) XRD pattern of PVDF-$Mo_{0.5}W_{0.5}S_2$ nanocomposite. (d) Variation of the β-phase fraction F (β) and the $\frac{I_{20.5}}{I_{18.3}}$variation with different alloy compositions.

The piezoelectric output voltage of the PENG device can be varied by changing the external load resistance by following the relation [11]

$$V_R = \frac{Z_R}{Z_{in}+Z_R} V_{oc} = \frac{R}{\frac{1}{2\pi fc}+R} V_{oc} \qquad (5.1)$$

Where the impedance Z_R is the external load resistance R, C is related to the inherent capacitance of the PENG device, f the frequency of the mechanical impact onto the PENG and V_{oc} is the open circuit output voltage from the PENG. As shown in Figure 5.10, three typical working regions can be identified (i, ii, and iii) based on the impedance matching between the PENG and varying load resistance. For the load resistance in the range of ~ 1 to 500 kΩ, which is much lower than the inherent impedance, the output voltage is very small < 2V) (zone i). The output voltage rises sharply from 2 to 48.5 V with increasing load resistance from 0.5 to 100 MΩ (zone ii). For a load resistance higher than 100 MΩ (zone iii), which is much higher than the inherent impedance resembling almost an open-circuit condition, the output voltages no longer change with the load resistances. The key factor for the fabrication of a self-powered photodetector is the impedance matching between the PENG and the photodetector, which can be built up based on the coupling of piezoelectric effect and photoconductive effects [11,44,45,51]. The estimated resistance variation under the UV illumination matches well with the resistance dependent output characteristics in zone (ii) of the PENG device (under finger tapping).

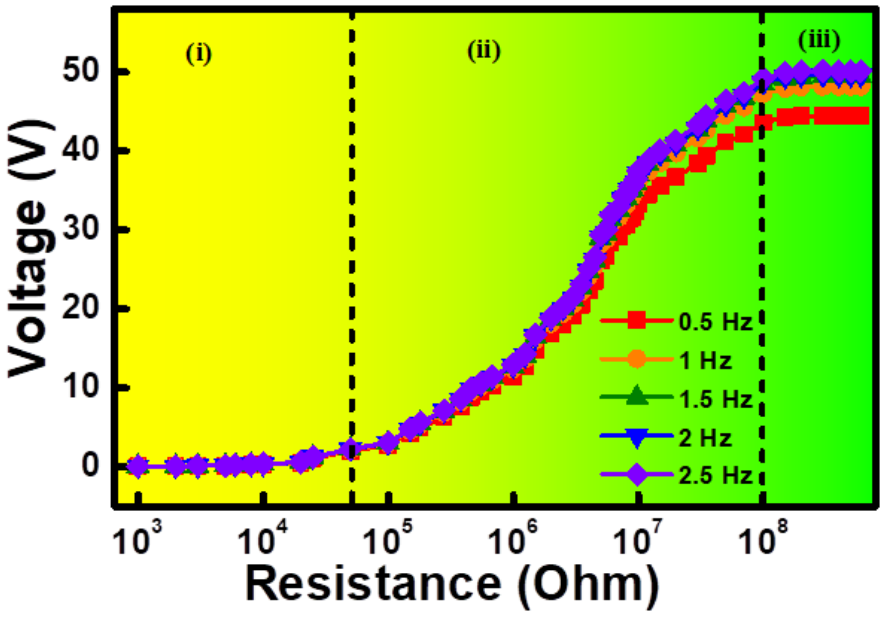

Figure 5.10 Output voltage of the PENG device across different load resistances under finger tapping at different frequencies.

5.3.5 Self powered UV sensor:

Therefore, by connecting the fabricated $Mo_xW_{1-x}S_2$ (x=0.5) UV detector in series with the self-powered PENG device (Figure 5.11(a)), a prototype of the self-powered UV detection can be preliminarily established. Figure 5.11(b) and Figure 5.11(c) show that with increasing UV illumination intensity, the output voltage across the photodetector decreases monotonically from ~11.9 V (dark) to ~5.9 V (27.55 μW/cm^2), owing to a decrease of internal resistance of the photodetector device. In order to evaluate the performance of the photodetector in voltage detection mode, we have estimated the sensitivity (S) and voltage responsivity (R_V), which are defined as [44,45]

$$S = \frac{|V_{dark} - V_{light}|}{V_{dark}} \times 100\% \qquad (5.2)$$

$$R_v = \frac{|V_{dark} - V_{light}|}{P_{light}} \qquad (5.3)$$

Figure 5.11(d) represents a sensitivity of ~ 50% (27.55 μW/cm^2) and a voltage responsivity of ~ 0.75 V $\mu W^{-1}cm^{-2}$ (at 1.5 μW/cm^2), demonstrating the superior performance of the PENG for self-powered UV photodetection [45,44]. Figure 5.11(e) shows the real-time continuous response and recovery performance, which are measured under a constant UV illumination (365 nm, 27.55 μW/cm^2). When the photodetector is exposed from dark to UV light (27.5 μW/cm^2), the output voltage drop across the photodetector decreases from ~11.9 to ~5.9 V with response and recovery time ~3 s and 5.4 s, respectively. In this case with the switching on UV illumination, the resistance of the photodetector decreases which eventually reduces the output voltage drop. If a light emitting diode (LED), is connected directly across the two ends of the fabricated photodetector, we have noticed that the LED is 'on' at dark (no illumination) and becomes 'off' in the presence of UV, demonstrating UV sensing.

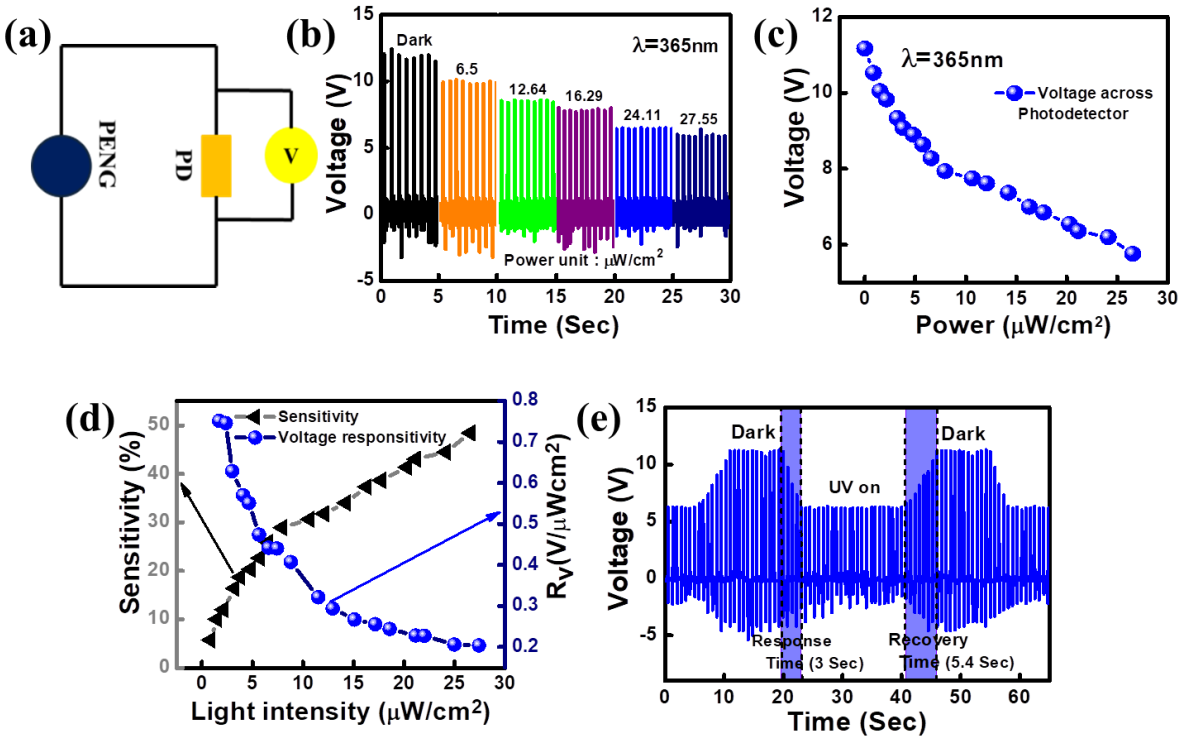

Figure 5.11 (a) Proposed circuit diagram to measure the responsivity of photodetector (PD) in self-powered mode. (b) Output voltage across the photodetector under different UV (365nm) illumination intensity. (c) Variation of voltage across the photodetector with varying UV illumination intensity. (d) Variation of sensitivity and voltage responsivity of the self-powered photodetector with changing UV illumination intensity. (e) Real time dynamic voltage response and recovery curve under 27.55 μW/cm^2 UV illumination.

But however, a direct correlation between the UV light intensity and output voltage is necessary for fabrication of practical UV sensing applications. Accordingly, a voltage divider circuit has been demonstrated by using several constant values of resistance and by connecting the LEDs directly across the resistors. The PENG device is connected in series with constant resistors and fabricated photodetector, with the output voltage of the PENG is regulated by using series of constant resistors and a commercial Zener diode (Figure 5.12(a)). This regulated output voltage is especially crucial for the UV sensing application because the detected voltage is solely dependent on the intensity of the incident light. The constant resistor (R_c) divides the output voltage (V_{RC}) of the PENG, which can be estimated as [11]

$$V_{Rc} = \frac{R_c}{\frac{1}{2\pi fc} + R_c + R_x} V_{oc} \qquad (5.4)$$

where R_x is the resistance of the photodetector. The voltage across the constant resistor is measured under different UV light intensities, as shown in Figure 5.12(b). It is noticed that the voltage across the constant resistor increases with increasing UV light intensity resulting in an enhanced current through the photodetector. It may be noted that no LED glows without any UV illumination. When the photodetector is illuminated with 16.3 μW/cm^2 intensity UV illumination, one LED is turned 'on' and two LEDs glow for an intensity of 27.55 μW/cm^2 (inset Figure 5.12(b)). Therefore, a higher UV light intensity can make more numbers of LEDs to lit because of the higher output voltage across the voltage divider and UV intensity can be estimated quantitatively by the variation of LED 'on'/'off' state.

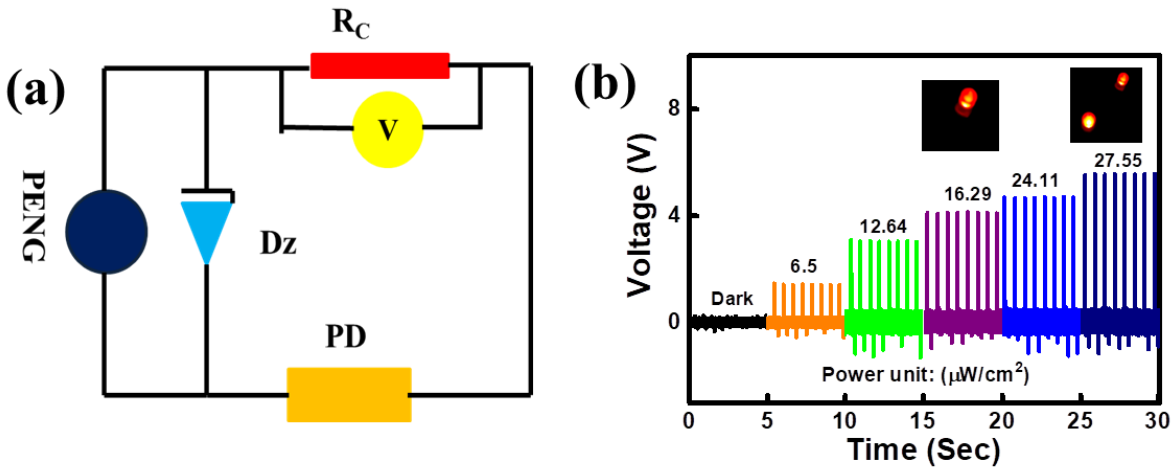

Figure 5.12 (a) Proposed circuit diagram of the self-powered UV photodetection system, where the piezoelectric nanogenerator, photodetector, constant resistor and Zener diode are denoted, respectively as PENG, PD, R_c and D_z. (b) Dynamic output voltage across a constant resistance under different UV illumination intensity, and LED glow indicating sensor for varying UV exposure (16.3 μW/cm^2 and 27.55 μW/cm^2 illumination intensity).

The fabricated self-powered UV detection system can be used in various practical applications especially in personal healthcare purposes. This self-powered UV sensing system can be placed at different parts of the human body (arm, wrist, skin etc.) which have chance to be exposed to UV radiation. In the absence of UV exposure, the LED sensor would be 'off', and as it is exposed to even a very weak (~16.3 μW/cm^2) UV radiation, the system would work immediately by glowing LEDs. The LEDs actually can act as an alarm or indicator of UV exposure and most importantly the LEDs can be turned on directly without

any need of a capacitor charge storing unit. The fabricated ternary TMDC alloy-based PENG device thus exhibits an outstanding capability to convert mechanical energy to electrical energy, which can be used as a self-powered UV sensor in wearable systems.

5.4 Summary:

In summary, we have presented a self-powered, portable UV photodetection system based on ternary 2D TMDC alloy ($Mo_{0.5}W_{0.5}S_2$) with impedance matching between a self-polled piezoelectric nanogenerator and a photodetector. Alloy engineering is found to be a proficient strategy to overcome the defect state related problems in binary TMDCs leading to the improved optical and electrical properties. The PENG device can harvest bio-mechanical energy by simple finger tapping and can convert into electrical energy to drive a UV photodetector. The self-polled PENG produces a superior piezoelectric output voltage ~50 V with a power density ~1.18 mW/cm^2 by simple finger tapping and ~187 V by a mechanical impact of 12 kPa, which are superior to the reported results using 2D TMDCs. The fabricated UV photodetector exhibits an exceptional photoresponsivity up to ~229 A/W and impressive detectivity of 6.95×10^{12} Jones for an illumination of 365 nm in the current detection mode, along with a large responsivity of ~0.75 V $\mu W^{-1}cm^{-2}$ in self-powered voltage detection mode. By connecting the PENG in series with a UV photodetector, the system works as a UV-light-intensity monitor, while the commercial constant chip resistors with parallel LEDs work as a UV sensitive alarm. Our results using novel ternary $Mo_{0.5}W_{0.5}S_2$ TMDC alloy pave the way for building highly efficient next generation mechanical energy harvesters for self-driven IOT devices.

5.5 References:

1. B. Huang, M. Yoon, B. G. Sumpter, S. H. Wei and F. Liu, Phys. Rev. Lett., 2015, **115**, 1–5.

2. X. Li, A. A. Puretzky, X. Sang, K. C. Santosh, M. Tian, F. Ceballos, M. Mahjouri-

Samani, K. Wang, R. R. Unocic, H. Zhao, G. Duscher, V. R. Cooper, C. M. Rouleau, D. B. Geohegan and K. Xiao, Adv. Funct. Mater., 2017, **27**, 1–10.

3. H. P. Komsa and A. V. Krasheninnikov, J. Phys. Chem. Lett., 2012, **3**, 3652–3656.
4. J. H. Yang and B. I. Yakobson, Chem. Mater., 2018, **30**, 1547–1555.
5. Y. Gao, J. Liu, X. Zhang and G. Lu, J.Phys.Chem.C, 2021, **125**, 774–781.
6. C. Zhen, B. Zhang, Y. Zhou, Y. Du and P. Xu, Inorg. Chem. Front., 2018, **5**, 1386–1390.
7. Q. Gong, L. Cheng, C. Liu, M. Zhang, Q. Feng, H. Ye, M. Zeng, L. Xie, Z. Liu and Y. Li, ACS Catal., 2015, **5**, 2213–2219.
8. X. Liu, J. Wu, W. Yu, L. Chen, Z. Huang, H. Jiang, J. He, Q. Liu, Y. Lu, D. Zhu, W. Liu, P. Cao, S. Han, X. Xiong, W. Xu, J. P. Ao, K. W. Ang and Z. He, Adv. Funct. Mater., 2017, **27**, 1–7.
9. Y. R. Lim, J. K. Han, Y. Yoon, J. B. Lee, C. Jeon, M. Choi, H. Chang, N. Park, J. H. Kim, Z. Lee, W. Song, S. Myung, S. S. Lee, K. S. An, J. H. Ahn and J. Lim, Adv. Mater., 2019, **31**, 1–14.
10. J. Yao, Z. Zheng and G. Yang, ACS Appl. Mater. Interfaces, 2016, **8**, 12915–12924.
11. Y. Zhang, M. Peng, Y. Liu, T. Zhang, Q. Zhu, H. Lei, S. Liu, Y. Tao, L. Li, Z. Wen and X. Sun, ACS Appl. Mater. Interfaces, 2020, **12**, 19384–19392.
12. Y. Zheng, L. Cheng, M. Yuan, Z. Wang and L. Zhang, Nanoscale, 2014, **6**, 7842–7846.
13. Z. H. Lin, Y. Yang, J. M. Wu, Y. Liu, F. Zhang and Z. L. Wang, J. Phys. Chem. Lett., 2012, **3**, 3599–3604.
14. G. Zhu, R. Yang, S. Wang and Z. L. Wang, Nano Lett., 2010, **10**, 3151–3155.
15. J. H. Jung, M. Lee, J. Il Hong, Y. Ding, C. Y. Chen, L. J. Chou and Z. L. Wang, ACS Nano, 2011, **5**, 10041–10046.
16. C. Chang, V. H. Tran, J. Wang, Y. K. Fuh and L. Lin, Nano Lett., 2010, **10**, 726–731.
17. D. Bhattacharya, S. Bayan, R. K. Mitra and S. K. Ray, ACS Appl. Electron. Mater., 2020, **2**, 3327–3335.

18. T. Huang, S. Yang, P. He, J. Sun, S. Zhang, D. Li, Y. Meng, J. Zhou, H. Tang, J. Liang, G. Ding and X. Xie, ACS Appl. Mater. Interfaces, 2018, **10**, 30732–30740.

19. S. Garain, S. Jana, T. K. Sinha and D. Mandal, ACS Appl. Mater. Interfaces, 2016, **8**, 4532–4540.

20. K. Shi, B. Sun, X. Huang and P. Jiang, Nano Energy, 2018, **52**, 153–162.

21. S. Siddiqui, H. B. Lee, D. Il Kim, L. T. Duy, A. Hanif and N. E. Lee, Adv. Energy Mater., 2018, **8**, 1–11.

22. S. Tiwari, A. Gaur, C. Kumar and P. Maiti, Sustain. Energy Fuels, 2020, **4**, 2469–2479.

23. K. Roy, S. K. Ghosh, A. Sultana, S. Garain, M. Xie, C. R. Bowen, K. Henkel, D. Schmeiβer and D. Mandal, ACS Appl. Nano Mater., 2019, **2**, 2013–2025.

24. P. Yadav, T. D. Raju and S. Badhulika, ACS Appl. Electron. Mater., 2020, **2**, 1970–1980.

25. K. Cai, X. Han, Y. Zhao, R. Zong, F. Zeng and D. Guo, ACS Sustain. Chem. Eng., 2018, **6**, 5043–5052.

26. D. Bhattacharya, S. Bayan, R. K. Mitra and S. K. Ray, Nanoscale, 2021, **13**, 15819–15829.

27. J. Meng, H. Li, L. Zhao, J. Lu, C. Pan, Y. Zhang and Z. Li, Nano Lett., 2020, **20**, 4968–4974.

28. Q. Shen, X. Xie, M. Peng, N. Sun, H. Shao and H. Zheng, Adv. Funct. Mater., 2018, **1703420**, 1–8.

29. Y. J. Y Su, M Yao, G Xie, H Yuan, MYang, H Tai, XDu, Appl. Phys. Lett., 2019, **073504**, 1–5.

30. X. Xie, Y. Zhang, C. Chen, X. Chen, T. Yao, M. Peng, X. Chen, B. Nie, Z. Wen and X. Sun, Nano Energy, 2019, **65**, 103984.

31. D. Zhang, Z. Yang, P. Li, M. Pang and Q. Xue, Nano Energy, 2019, **65**, 103974.

32. W. Liu, X. Wang, Y. Song, R. Cao, L. Wang, Z. Yan and G. Shan, Nano Energy, 2020, **73**, 104843.

33. Y. Lei, S. Pakhira, K. Fujisawa, X. Wang, O. O. Iyiola, N. Perea López, A. Laura Elías, L. Pulickal Rajukumar, C. Zhou, B. Kabius, N. Alem, M. Endo, R. Lv, J. L. Mendoza-Cortes and M. Terrones, ACS Nano, 2017, **11**, 5103–5112.

34. K. Yang, X. Wang, H. Li, B. Chen, X. Zhang, S. Li, N. Wang, H. Zhang, X. Huang and W. Huang, Nanoscale, 2017, **9**, 5102–5109.

35. W. Li, F. Li, Y. Liu, J. Li, H. Huo and R. Li, Int. J. Hydrogen Energy, 2017, **42**, 18774–18784.

36. D. G. Mohan, S. Gopi, V. Rajasekar, K. Krishnan, D. G. Mohan, Gopi S., L. Selvarajan, R. Rajavel, B. Prakash, D. G. Mohan, S. Gopi, A. A. Alloys, U. Taguchi, L. Selvarajan, R. Sasikumar, D. G. Mohan, P. Naveen Kumar and V. Muralidharan, Mater. Res. Express, 2019, **6**, 1–31.

37. Y. Chen, D. O. Dumcenco, Y. Zhu, X. Zhang, N. Mao, Q. Feng, M. Zhang, J. Zhang, P. H. Tan, Y. S. Huang and L. Xie, Nanoscale, 2014, **6**, 2833–2839.

38. D. C. H.Liu, K. K. Ansah Antwi, S.Chua, Nanoscale, 2014, **6**, 624–629.

39. N. Mutz, T. Meisel, H. Kirmse, S. Park, N. Severin, J. P. Rabe, E. List-Kratochvil, N. Koch, C. T. Koch, S. Blumstengel and S. Sadofev, Appl. Phys. Lett., 2019, **114**, 1–4.

40. A. F. Rigosi, H. M. Hill, K. T. Rim, G. W. Flynn and T. F. Heinz, Phys. Rev. B, 2016, **94**, 1–6.

41. V. Murugan, K. Meganathan, N. B. Shinde and S. K. Eswaran, Appl. Phys. Lett., 2021, **118**, 1–7.

42. J. Park, M. S. Kim, B. Park, S. H. Oh, S. Roy, J. Kim and W. Choi, ACS Nano, 2018, **12**, 6301–6309.

43. Y. Chen, J. Xi, D. O. Dumcenco, Z. Liu, K. Suenaga, D. Wang, Z. Shuai, Y. S. Huang and L. Xie, ACS Nano, 2013, **7**, 4610–4616.

44. H. Fang, Q. Li, J. Ding, N. Li, H. Tian, L. Zhang, T. Ren, J. Dai, L. Wang and Q. Yan, J. Mater. Chem. C, 2016, **4**, 630–636.

45. S. F. Leung, K. T. Ho, P. K. Kung, V. K. S. Hsiao, H. N. Alshareef, Z. L. Wang and J. H. He, Adv. Mater., 2018, **30**, 1–8.

46. Y. Wang, Z. He, J. Zhang, H. Liu, X. Lai, B. Liu, Y. Chen, F. Wang and L. Zhang, Nano Res., 2020, **13**, 358–365.

47. A. E. Yore, K. K. H. Smithe, S. Jha, K. Ray, E. Pop and A. K. M. Newaz, Appl. Phys. Lett., 2017, **111**, 1–6.

48. S. K. Karan, R. Bera, S. Paria, A. K. Das, S. Maiti, A. Maitra and B. B. Khatua, Adv. Energy Mater., 2016, **6**, 1–12.

49. T. K. Sinha, S. K. Ghosh, R. Maiti, S. Jana, B. Adhikari, D. Mandal and S. K. Ray, ACS Appl. Mater. Interfaces, 2016, **8**, 14986–14993.

50. M. Kim, V. K. Kaliannagounder, A. R. Unnithan, C. H. Park, C. S. Kim and A. R. K. Sasikala, Appl. Sci., 2020, **10**, 1–12.

51. L. Han, M. Peng, Z. Wen, Y. Liu, Y. Zhang, Q. Zhu, H. Lei, S. Liu, L. Zheng, X. Sun and H. Li, Nano Energy, 2019, **59**, 492–499.

Chapter: 6

Superior piezoelectric performance of chemically synthesized TMDC heterostructures for self-powered flexible piezoelectric nanogenerator

In addition to their superior electrical and optoelectronic attributes, two-dimensional layered transition metal dichalcogenides (TMDCs) have evoked considerable attention for their piezoelectric properties. In this study we report the piezoelectric characteristics of chemically exfoliated TMDCs and their heterostructures, as derived from piezoelectric force microscopy (PFM) measurements. It is observed that MoS_2-WSe_2 heterostructure exhibit higher piezoelectric coefficient than their individual counterparts due to a large band-offset induced by heterojunction formation. This allows the scalable fabrication of self-powered energy harvesting piezoelectric nanogenerators (PENG). The fabricated flexible MoS_2-WSe_2 heterostructure nanogenerator exhibits a piezoelectric output ~46 mV under a strain of ~0.66% strain yielding a power output ~12.3 nW and also reveals the ability of bio-mechanical energy harvesting. This cost effective MoS_2-WSe_2 heterostructure PENG fabricated in this work can be employed to develop flexible energy harvesting devices and may also be attractive as a self-powered sensor for bio-mechanical activities.

6.1 Introduction:

Today's growing demand for energy resources, environmental pollution from fossil fuels, and the inaccessibility of conventional fuels have made new challenges to discover unconventional forms of energy that are sustainable and environment friendly. In this regard, non-traditional natural abundant energy (solar, wind, thermal) and biomechanical energy resources attains immense research interest. Piezoelectricity [1] can be viewed as an alternative energy source that can generate electric charges due to deformation of a specific material under the action of external stress and these electric charges are responsible for conversion of mechanical to electric energy. Various piezoelectric materials based on inorganic [2,3] and polymer nanocomposite materials [4–7] have been reported previously, but suffer from the disadvantages like environmental toxicity, non-biodegradability, and complicated synthesis procedures. Two dimensional materials, specially transition metal dichalcogenides (TMDC) (like MoS_2, WS_2, etc.) are considered to be the emerging potential alternatives. Having non-symmetrical crystalline structure, TMDCs offer novel optoelectronic and electrical properties with high mechanical flexibility and stability, which are highly demanding for piezotronics [8] and photo piezotronics [9]. Each layer of TMDCs consists of transition metal atoms

sandwiched between two layers of chalcogen atoms and attached by weak out-of-plane van der Waals bonds and strong in-plane covalent bonds. It has been observed that the monolayer and odd layered TMDCs are non-centrosymmetric and exhibits piezoelectricity but piezoelectric effect disappears in even layered structure or in bulk counterpart, due to the opposite orientations of adjacent layers [10]. Wu et al. successfully fabricated a piezoelectric device using MoS_2 with an odd layer for energy conversion and piezoelectricity [10]. Han et al. used sulfur vacancy passivated MoS_2-based piezoelectric devices by reducing free charge carriers to efficiently prevent the screening effect [11]. The key point to achieving a high performance piezoelectric device is to explore a specific material with sufficiently high piezoelectric constant, facile fabrication process and good sensitivity under the external mechanical strain. Most of the demonstrations of piezoelectric devices using two dimensional materials have been made on mechanically exfoliated monolayer and odd layered nanosheets[12–16] , which pose several limitations for large scale applications. Ultrathin TMDC layers can be prepared by various well-known techniques such as liquid exfoliation [17,18], hydrothermal synthesis [19], chemical vapor deposition (CVD) [20,21], pulsed lased deposition (PLD) [22], atomic layer deposition (ALD) [23] etc. Sonochemical assisted hydrothermal technique is a promising way for cost effective scalable production of ultrathin TMDC layers for large area [20] electronic device fabrication. Recent studies have shown that piezoelectricity also exists in few layered two-dimensional materials [24–27] but with a low piezoelectric response, so improving the piezoelectric performance in TMDC laminates is still a challenge. The development of engineering on van der Waals heterostructure can be used to create novel physical phenomena that provide an effective approach to improve the piezoelectric properties of two-dimensional materials [28]. For atomic layer heterostructures, the spontaneous polarization of phosphorus-MoS_2, MoS_2-WS_2, In_2Se_3-MoS_2 [29], In_2Se_3-WS_2 [29], SnS_2-SnS [30] are previously reported, however the piezoelectric properties of the TMDC hybrid heterostructures are not still much explored.

In this study, we have synthesized ultrathin layered TMDCs and their heterostructures (MoS_2, WS_2, WSe_2, MoS_2-WS_2, WS_2-WSe_2, MoS_2-WSe_2) in sonochemical assisted hydrothermal synthesis technique and their piezoelectric characterizations are examined through piezoelectric force microscopy (PFM). It is observed that the MoS_2-WSe_2 heterostructure exhibits highest piezoelectric coefficient among all, due to the large band offset. This scalable, cost-effective piezoelectric device significantly increases the output voltage in comparison with previously reported two-dimensional material-based PENG devices [31–33]. In

this study, we have demonstrated for the first time chemically synthesized TMDC hybrid structures based piezoelectric devices which overcome the drawbacks of mechanically exfoliated low yield PENG devices. The strain sensitive piezoelectric properties and biomechanical energy harvesting abilities are also investigated. This self-powered, atomically thin, highly flexible and multi-functional PENG device may open up a new avenue for diverse research fields, particularly in biomechanical energy harvesting, human-machine interface control and sensor enabling technology.

6.2 Experimental Section:

6.2.1 Materials:

The synthesis of ultrathin TMDC and their heterostructure (MoS_2, WS_2, WSe_2, MoS_2-WS_2, WS_2-WSe_2, MoS_2-WSe_2) were carried out by sonochemical assisted hydrothermal synthesis technique. Sodium molybdate dihydrate ($Na_2MoO_4 \cdot 2H_2O$), sodium tungstate dihydrate ($Na_2WO_4 \cdot 2H_2O$), thiourea (CH_4N_2S) and Se powder were purchased from Alpha Aser and sodium borohydride ($NaBH_4$), isopropyl alcohol (IPA) were purchased from Sigma-aldrich. All these chemicals were directly used without further purification.

6.2.2 Synthesis

To synthesize MoS_2, WS_2 nanosheets $Na_2MoO_4 \cdot 2H_2O$ and $Na_2WO_4 \cdot 2H_2O$ were used as Mo and W sources, respectively and thiourea was used as the S source. $Na_2MoO_4 \cdot 2H_2O$ and $Na_2WO_4 \cdot 2H_2O$ and thiourea as precursors were dissolved in pure water. The precursor solutions had to be subjected to vigorous stirring (1200 rpm, 2hrs) to form a homogeneous solution. The solution was transferred to a 100- mL Teflon-lined stainless autoclave, which was heated for MoS_2 and WS_2 synthesis. The final dark solution was centrifuged three times at 6000 rpm for 15 min and the precipitate was washed with distilled water and IPA and dried at 60°C for 12 hrs. The resulting dried powder was dispersed in IPA and bath sonicated for 6 hrs followed by centrifugation at 8000 rpm for 15 mins to remove the bulk precipitate. In this typical procedure of WSe_2, $Na_2WO_4 \cdot 2H_2O$ and Se were used as precursors of W and Se respectively and $NaBH_4$ was used as reducing agent. For this synthesize procedure $Na_2WO_4 \cdot 2H_2O$ was dissolved in DI water, and Se powder was added to the above solution and then the resulting solution was homogenized by continuous magnetic stirring for 15 mins.

Then aqueous $NaBH_4$ was added dropwise into the above mixture till the colour of solution turned brown and thereafter the resulting solution was under magnetic stirring for 2.0 hrs to get complete homogeneous uniform mixture. This brown coloured solution was transferred into a 100 ml teflon-lined stainless autoclave and placed in an oven. After the reaction is over, the autoclave was naturally cooled to room temperature and the finally obtained black powder samples were collected by repeated washing and centrifugation (3 times at 8000 rpm) by D.I water and IPA. The cleaned wet powder sample was dried in an oven for 12 hr at 70°C. The resulting dried powder was dispersed in IPA and bath sonicated for 6 hrs followed by centrifugation at 8000 rpm for 15 mins to remove the bulk precipitate.

To synthesize TMDC heterostructures the constituent as-synthesized TMDCs were mixed in 1:1 weight ratio and grind continuously in a mortar and pestle for 30 min. This prepared black slurry was dispersed in binary mixture of IPA and DI water (7:3) and bath sonicated for 8 hrs. in bath sonication.

6.2.3 Characterizations:

The morphological and structural elemental analyses were carried out by using a field-emission scanning electron microscope (FESEM) equipped with an energy-dispersive X-ray (EDX) spectrometer. To further study the detailed morphology and surface profiles, high-resolution transmission electron microscopy (HRTEM) (FEI-TECNAI G2 20ST, energy 200 keV) had been utilized. The crystallinity of the as-synthesized nanosheets were investigated by X-ray diffraction (Rigaku (Smartlab)). Absorption spectrums were taken by using a UV-Vis spectrometer (Shimadzu-UV-Vis 2600 Spectrophotometer) and micro-raman and micro-photoluminescence spectrums were recorded with a spectrometer (LabRam HR Evolution; HORIBA France SAS-532nm laser). Piezoelectric characterizations were examined through a piezoelectric force microscope (PFM, Bruker), attached with an atomic force microscope (AFM, di-INOVA) set up. The substrate with samples was placed onto a metal plate disk and copper wires were used as the connector to realize the grounding of the substrate. The piezoelectric output voltages were measured by a Keithley 2450 source meter and the external mechanical strain had been employed through a linear stage.

6.2.4 Device fabrication:

The PENG devices were fabricated on flexible ITO-FET substrates. The electrodes were made by depositing Ti/Au (5/50 nm) by e-beam evaporation through a wire shadow mask. The separation between the electrodes was kept as 25 µm. Samples were drop casted within the channel gap. Finally, the electrical contacts were made by Ag paint in order to measure the device**.**

6.3 Results and discussions:

6.3.1 Structural studies:

The layered TMDC materials and their heterostructures have been synthesized by using chemical exfoliation methods are reported earlier [34,35] TEM characterizations (Figure 6.1(a-c)) along with HRTEM images (Figure 6.1(d-f)) reveal the morphology and crystal structures of WSe_2, WS_2, MoS_2 nanosheet. The interlayer spacing 0.28 nm, 0.27 nm and 0.27 nm indicate the formation of (100) plane of WSe_2, WS_2 and MoS_2, respectively [36].

* Piezoelectric device fabrication credit: Shubhrasish Mukherjee

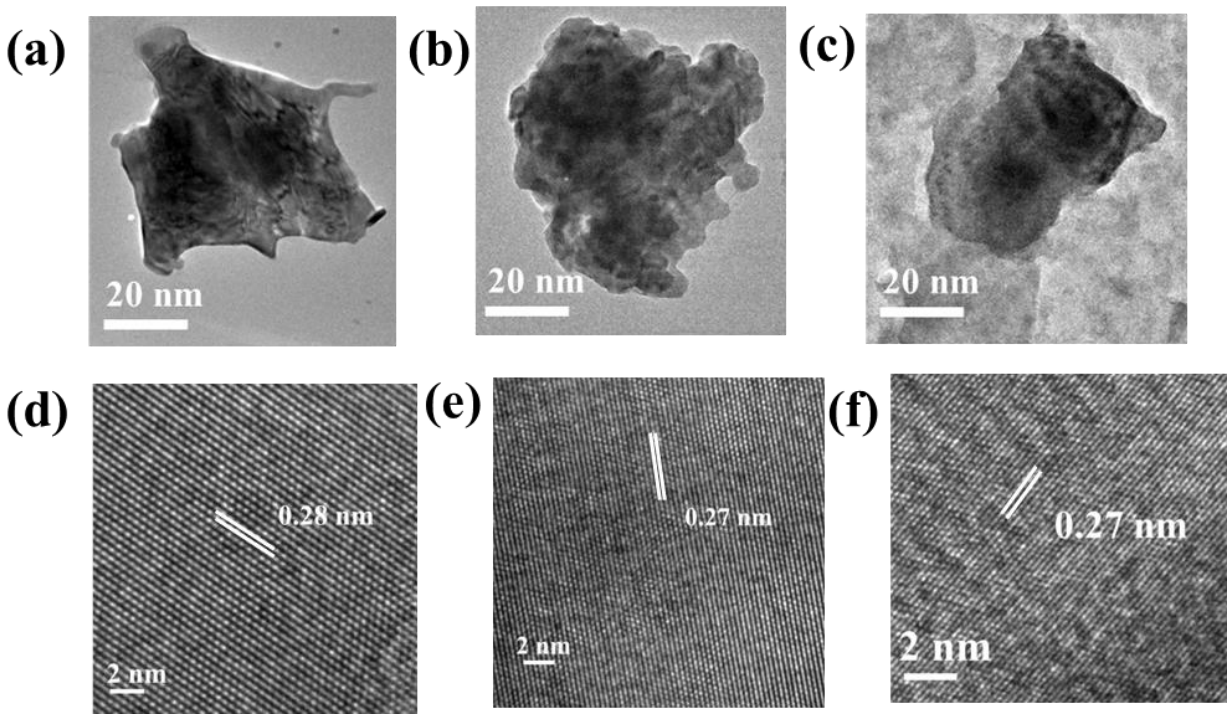

Figure 6.1 Plane-view TEM images of (a) WSe_2, (b) WS_2, (c) MoS_2 nanosheets and HRTEM images of (d) WSe_2, (e) WS_2, (f) MoS_2 nanosheets, indicating interlayer spacing

The sharp and distinguishable interfaces seen from the HRTEM images reveal the formation of the heterostructures (Figure 6.2(a-c)). Selected area electron diffraction (SAED) patterns of all heterostructure show two different sets of hexagonally arranged diffraction spots [36] (Figure 6.2(d-f)), which indicate the coexistence of individual layers [37].

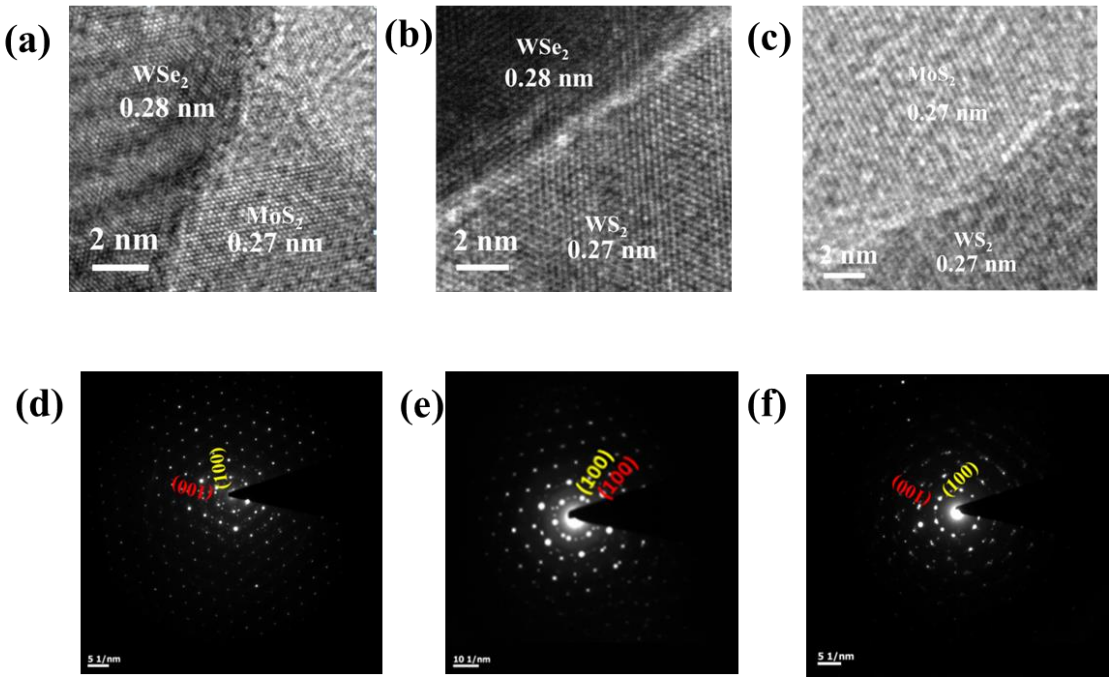

Figure 6.2 HRTEM interfacial images (a-c) and SAED pattern (d-f) of WSe_2 –MoS_2, WSe_2 – WS_2, MoS_2-WS_2 heterostructures, respectively.

The crystallinity and phase of all of those individual TMDC and their heterostructure (MoS_2, WS_2, WSe_2, MoS_2-WS_2, WS_2-WSe_2, MoS_2-WSe_2) are examined through XRD analysis. The diffraction peaks of exfoliated MoS_2, WS_2 and WSe_2 are found at distinctive positions which indicate the formation of desired phase and reveal the crystallinity of exfoliated nanosheets (Figure 6.3(a)). For example, in the MoS_2-WSe_2 heterostructure, the coexistence of diffraction peaks of MoS_2 and WSe_2 indicates that the MoS_2 nanosheets are successfully anchored with WSe_2 (Figure 6.3(b)). Similar observations are recorded for WS_2-WSe_2, MoS_2-WS_2 heterostructures, which also indicate the crystallinity and phases are maintained in all the heterostructures [38,39] (Figure 6.3(b)).

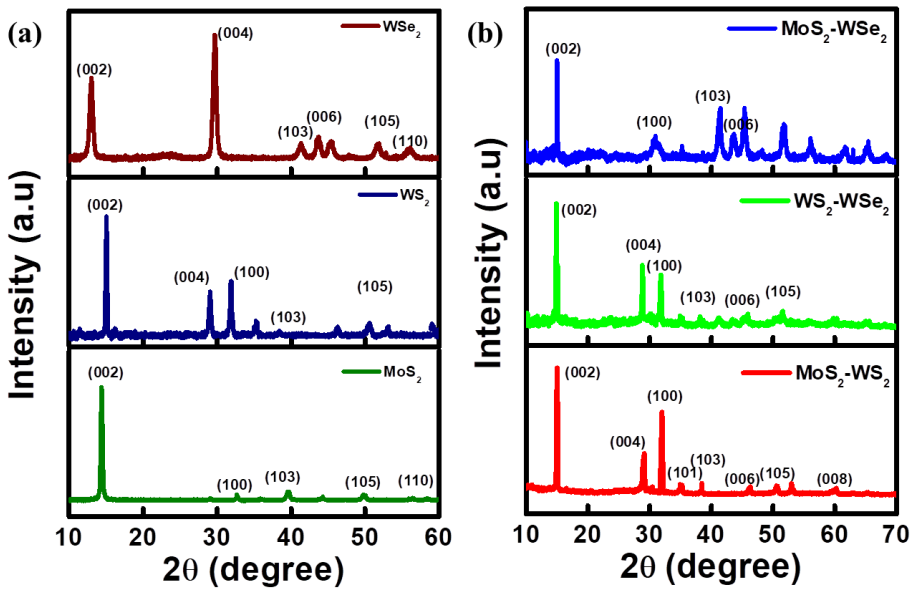

Figure 6.3 (a) XRD diffraction spectra of WSe_2, WS_2 and MoS_2 nanosheets. (b) WSe_2 – MoS_2, WSe_2 –WS_2 and MoS_2-WS_2 heterostructures.

6.3.2 Spectroscopic Studies:

Figure 6.4(a-c) represents the absorbance spectra of WSe_2–MoS_2, WSe_2–WS_2, MoS_2-WS_2 heterostructures. It is observed that the exciton A peak of WSe_2 is red shifted in MoS_2-WSe_2 heterostructure compared to bare WSe_2. The characteristic excitonic peaks in the absorbance spectrum are observed in the heterostructure, with their positions in consistent with the constituent TMDC components [40,41]. The shift in the excitonic absorbance peak in other heterostructures (MoS_2-WS_2, WS_2-WSe_2) indicates (Figure 6.4(b) & (c)) the charge transfer at the interface and the change of dielectric environment in the heterostructure. The steady state photoluminescence (PL with 532 nm) is studied to observe the emission at excitonic energies characteristic of MoS_2 (1.83 eV), WS_2 (1.98 eV) and WSe_2 (1.68 eV) in the adjacent TMDC layers [41–43]. In the MoS_2-WSe_2 heterostructure, the PL emission peak is red shifted with respect to the exciton-A of WSe_2 (Figure 6.4(d)), which corresponds to a Γ-K optical transition of MoS_2-WSe_2 heterostructure. PL emission peaks of all the heterostructures show a red shift with respect to the constituent TMDC layers. All the heterostructures also exhibit quenched emission as compared to the individual TMDC layers (Figure 6.4(d-f)), since the emission in the heterostructure region originates from the charge separation between the constituent TMDC layers forming type-II band alignments [43]. This PL quenching has been experimentally observed in type-II van der Waals heterostructure, which are attributed to the

interlayer charge transfer process [41-44]. Upon excitation interlayer e-h pairs are formed in individual TMDC layer separately, which are subsequently separated because of the type-II band alignment resulting in PL quenching [41–44].

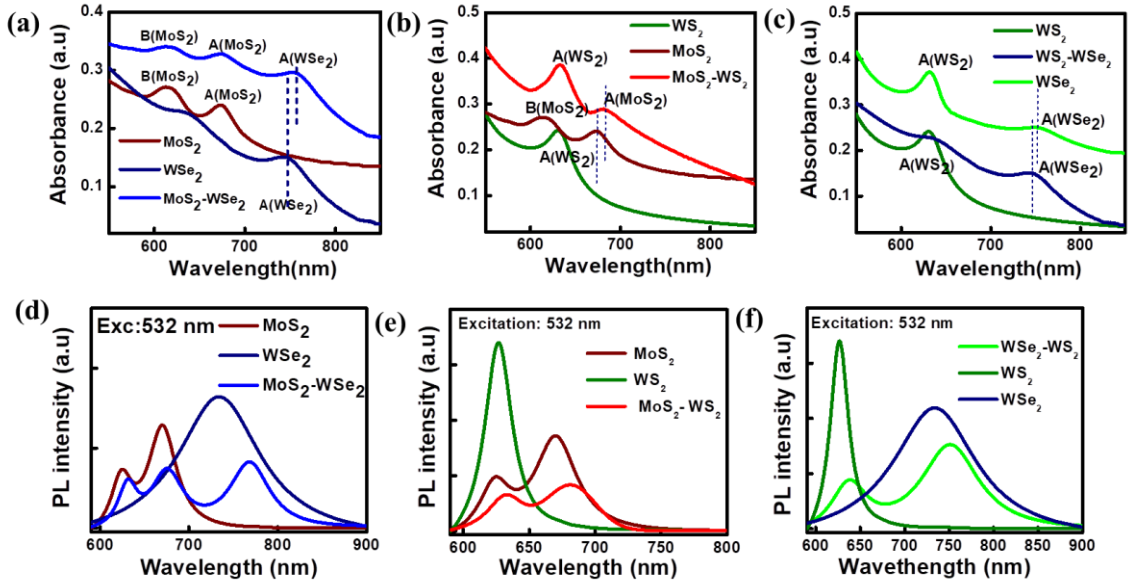

Figure 6.4 (a-c) Absorbance and (d-f) photoluminescence spectra of WSe_2 –MoS_2, MoS_2-WS_2 and WSe_2 –WS_2 heterostructures.

Raman spectra of WSe_2, WS_2 and MoS_2 nanosheets are shown in Figure 6.5(a). The spectrum of MoS_2-WSe_2 heterostructure exhibits the characteristic Raman modes of both MoS_2 (E^1_{2g} and A_{1g}) and WSe_2 (degenerate E^1_{2g} & A_{1g}), indicating the presence of both in the heterostructure (Figure 6.5(b)). Raman spectra of MoS_2-WS_2 and WS_2-WSe_2 heterostructures are also depicted in Figure 6.5(b). The absorbance, Raman and photoluminescence spectra indicate the interlayer coupling and charge transfer at the hetero-interfaces [45,46].

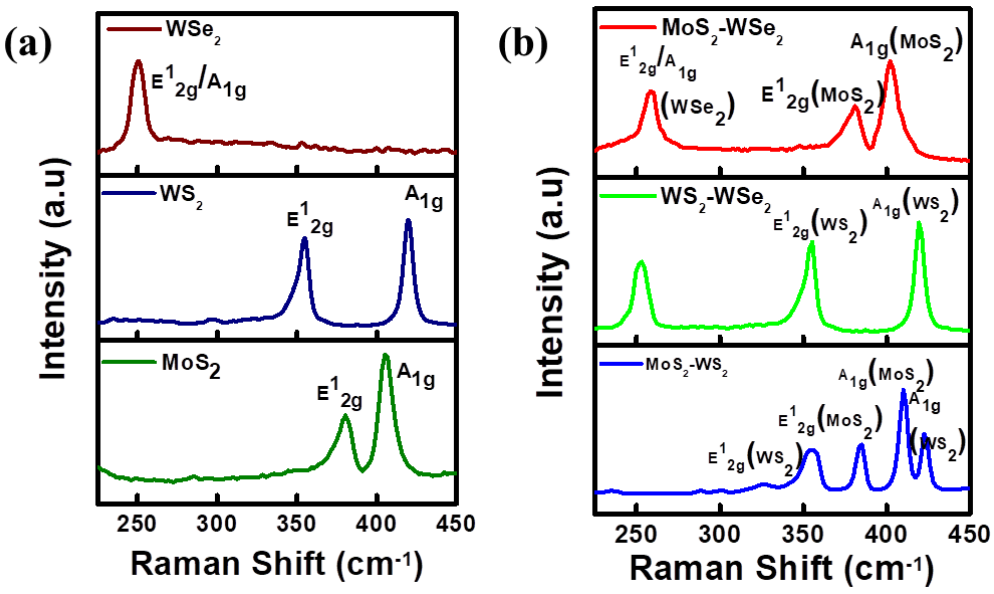

Figure 6.5 Raman spectra of (a) of WSe_2, WS_2 and MoS_2 nanosheets. (b) WSe_2 –MoS_2, WSe_2 –WS_2 and MoS_2-WS_2 heterostructures.

For piezoelectric material, electric charges are developed on material surfaces under an external mechanical stress. Piezoelectric properties of individual TMDC and their heterostructures are investigated by piezoelectric force microscopy (PFM), where the tip deflections are measured upon the application of vertical electrical field to the samples [47,48] (Scheme:6.1).

6.3.3 Piezoelectric force microscopy Studies:

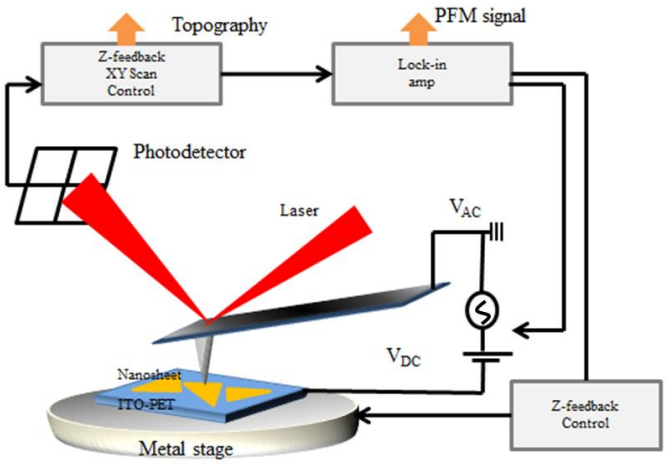

Scheme: 6.1 Schematic of Piezoelectric Force Microscopy (PFM) measurements.

Figure 6.6(a-c) display the local PFM images of MoS_2, WSe_2 and MoS_2-WSe_2 heterostructures, respectively (keeping all parameters identical for all the samples). Among all the samples, MoS_2-WSe_2 heterostructure exhibits the largest piezoelectric amplitude than the others, which indicating strong piezoelectricity of this heterostructure. Using these measured PFM amplitudes along with the deflection sensitivity (nm/V) and applied bias through the conductive tip, the piezoelectric coefficients are estimated as $d = \frac{A.S}{F.V}$, where A is the amplitude (in Voltage), S is deflection sensitivity, F is the facility parameter (resonance quality factor) and V is the externally applied AC voltage [30,49]. The calculated piezoelectric coefficients are found to be ~3.23, 1.96, 2.46, 5.06, 6.04 and 7.66 pm/V for MoS_2, WS_2, WSe_2, MoS_2-WS_2, WS_2-WSe_2 and MoS_2-WSe_2, respectively. The values are presented in Figure 6.6(d). It is observed that the MoS_2-WSe_2 heterostructure produces highest piezoelectric coefficient. For all the 2H-TMDCs, the application of a vertical electric field (through PFM tip) yields a net electric dipole, producing piezo response [50]. The van der Waals heterostructure of TMDC atomic layers with different work functions and band gaps form a type-II staggered band alignment [44,51–53]. The band offset of conduction band minima (CBM) and valance band maxima (VBM) between two different layered materials is the key point to induce electric polarization and piezoelectricity [28]. The highest piezoelectric coefficient is obtained in the MoS_2-WSe_2 heterostructure, is attributed to larger band offset as compared to other heterostructures (MoS_2-WS_2, WS_2-WSe_2) [54,55], which is schematically depicted in Figure 6.6(e).

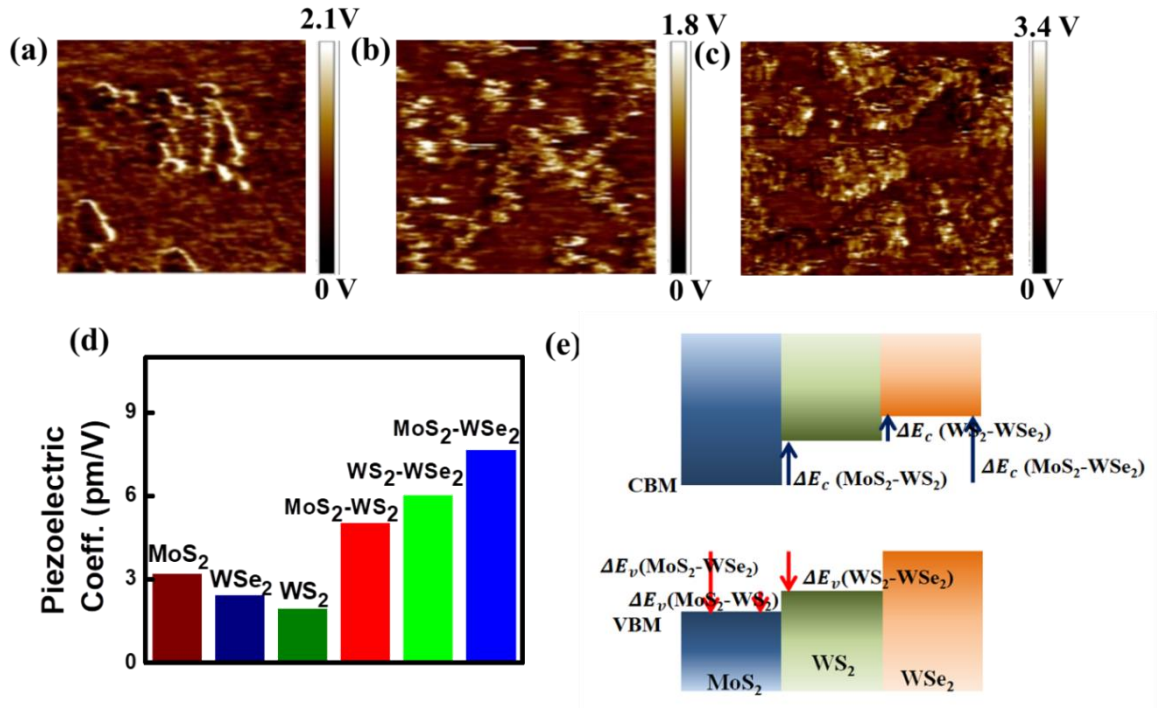

Figure 6.6 Piezo-response amplitude images from (a) MoS_2, (b) WSe_2 and (c) MoS_2-WSe_2 nanosheets. (d) Estimated piezoelectric coefficient (pm/V) from the TMDC nanosheets and the heterostructures. (e) Schematic band alignment of TMDC nanosheets and band offset estimation of band offsets for heterostructures

The PFM study of bare ITO-PET substrate does not show any significant piezo response. The topography of ITO-PET substrate along with PFM amplitude and phase are depicted in Figure 6.7(a-c), indicating that the originated piezoresponse solely coming from TMDC nanosheets.

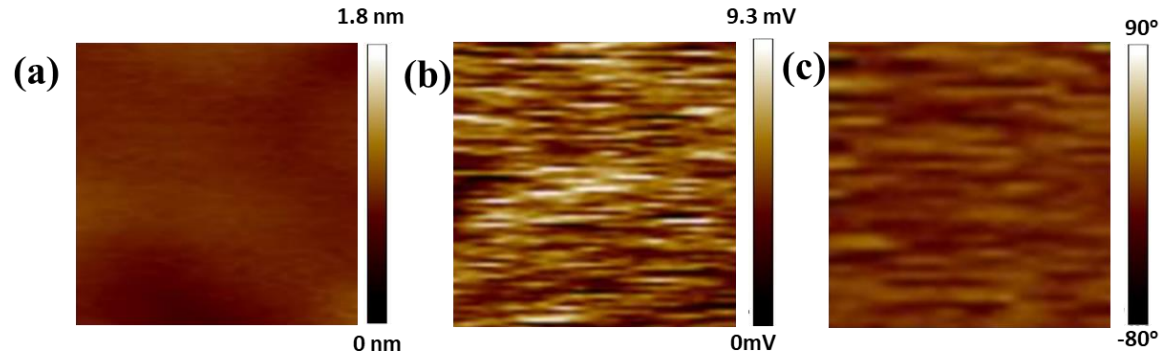

Figure 6.7 (a) Amplitude topography, (b) piezo- amplitude and (c) piezoelectric phase image from control ITO-PET substrate.

To study the response of MoS_2-WSe_2 heterostructure in more detail, the piezoelectric topography (both amplitude and phase) on the ITO-PET substrate is further carried out (Figure 6.8(a-c)). Butterfly shaped loop in amplitude response curve is observed with varying bias voltage and an increased in the piezoelectric displacement with the applied voltage is observed (Figure 6.8(d)). The phase response as a function of the bias presents a rectangular hysteresis loop, indicating the ability of switching the direction of polarization (Figure 6.8(e)). The phase component provides information about the local polarization orientation under the applied electric field. So by combining the topography, amplitude and phase mapping the nanoscale piezoelectric phenomenon can be visualized.

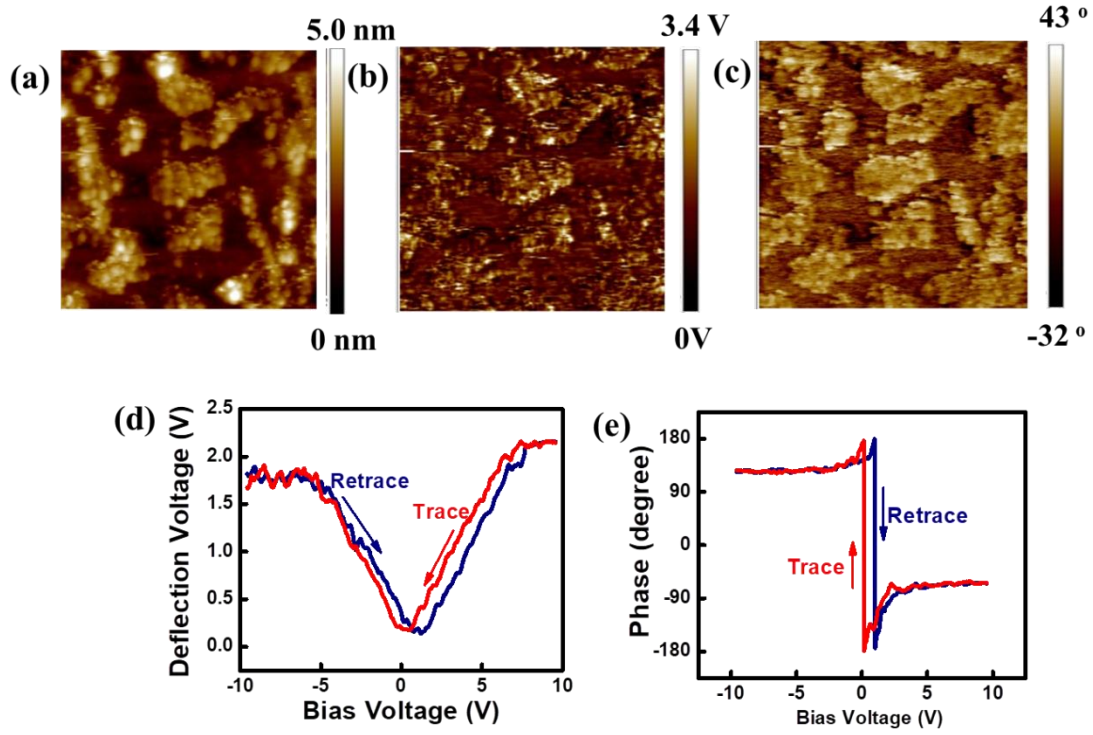

Figure 6.8 (a) Amplitude topography, (b) piezo-amplitude and (c) piezoelectric phase images from MoS_2-WSe_2 heterostructure nanosheets. PFM hysteresis loop with bias voltage showing the (d) amplitude and (e) phase response of MoS_2-WSe_2 heterostructure nanosheets.

6.3.4 Piezoelectric Nanogenerator device Study:

Based on the PFM study, the temporal piezoelectric measurements are performed in MoS_2-WSe_2 type II heterostructure in two-electrode configuration (optical image inset in Figure 6.9(a)) by applying external stress via bending (Figure 6.9(a)). The compressing and

releasing deformations (both forward and reverse bias) of the MoS_2-WSe_2 PENG device are depicted in Figure 6.9(b) in which the total process can be divided into 3 steps. In the initial state, there is no piezoelectric potential between the two electrodes and no signal is observed. When the device is bent, the nanosheet undergoes a uniaxial strain then dipole moments are aligned along the strain induced direction and piezo polarization charges are consequently generated at the edges of the nanosheets. This generates a piezo potential between the two electrodes, resulting in a positive piezoelectric signal peak. When the device is released, the external strain decreases and the piezo potential drops, causing a reverse charge flow which leads to a voltage peak with opposite sign (Figure 6.9(b)) [32,31]. The polarity switching tests in accordance with the proposed piezo-charge generation process confirm that the measured piezoelectric signals are not measurement artifacts. The periodic bending-releasing (~0.66% strain) at zero bias has led to repetitive piezoelectric output voltage signals. The cycling test demonstrates that the output signal of the PENG is stable over a long period of time, which indicates the durability required for energy conservation. It may be noted that no piezoelectric output signal can be detected for the PENG device without any channel material (Figure 6.9(c)).

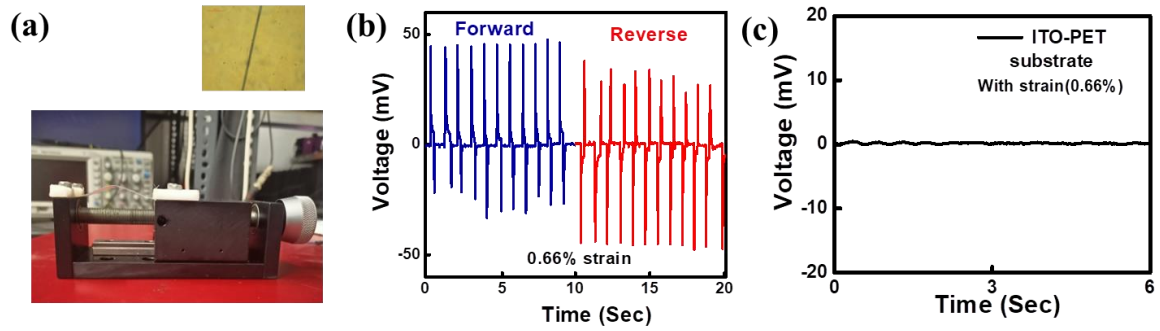

Figure 6.9 (a) Flexible bending set up of linear stage and the optical image of the device in the inset. (b) Open circuit piezo voltage from MoS_2-WSe_2 heterostructure PENG at forward and reverse bias condition at 0.66% strain. (c) The absence of piezoelectric output voltage due to bending of control ITO-PET substrate.

To evaluate the effect of an applied stress on the fabricated PENG device, the piezoelectric responses are examined under variable strain conditions, with the generated strain defined as

56

$$\varepsilon = \frac{3a}{2l}\frac{D_{max}}{l}\left(1 - \frac{z_o}{l}\right) \qquad (6.1)$$

where a and l depict the thickness and the length of the PET substrate, z_o represents the distance between the fixed end and nanosheet edge, D_{max} is the lateral shift of the free end of the substrate. It is noticed that the piezoelectric output performance of this PENG is strain sensitive, the output performance of this PENG device is enhanced (9.8 mV to 45.7 mV) with increasing strain (0.16% to 0.66%) (Figure 6.10(a)). Compared with other fabricated two dimensional materials based PENG, our fabricated MoS_2-WSe_2 hybrid heterostructure device exhibits higher or comparable piezoelectric response[16,24,30,49,57,58]. Figure 6.10(b) displays the piezoelectric output voltages as a function of external load resistance under 0.66% strain, the output voltage increases monotonically with increasing load resistance upto 200 MΩ and negligible voltage fluctuation is observed for the load resistance higher than ~ 200 MΩ. This fabricated MoS_2-WSe_2 PENG is able to produce 12.3 nw power for ~100 MΩ resistance. To compare the piezoelectric outputs of all devices (MoS_2, WS_2, WSe_2, MoS_2-WS_2, WS_2-WSe_2, MoS_2-WSe_2), measurements are done under the same bending condition by using a linear stage. From Figure 6.10(c) it is observed that the other PENG devices exhibit lower piezoelectric performance than the MoS_2-WSe_2 heterostructure based one. The larger band-offset leads a stronger polarization which leads to higher piezoelectric response in the MoS_2-WSe_2 hybrid heterostructure. This heterostructure of this TMDC atomic layers with different work function forms a type-II staggered gap alignment and the Fermi level is located near the VBM of WSe_2 and CBM of MoS_2, which indicates that high density of holes accrues at WSe_2 atomic layer while high density of free electrons at MoS_2 layer. This causes a built-in electric field induced polarization between WSe_2 and MoS_2 atomic layers in the MoS_2-WSe_2 hybrid heterostructure. It is observed that for another heterostructure with narrower band offset, the electric potential is attenuated which results in the decreased piezoelectric performance [28,54]. The performance of the fabricated self-poled, flexible MoS_2-WSe_2 heterostructure PENG is superior to the previously reported results on two dimensional materials based PENG device and depicted in Table-6.1.

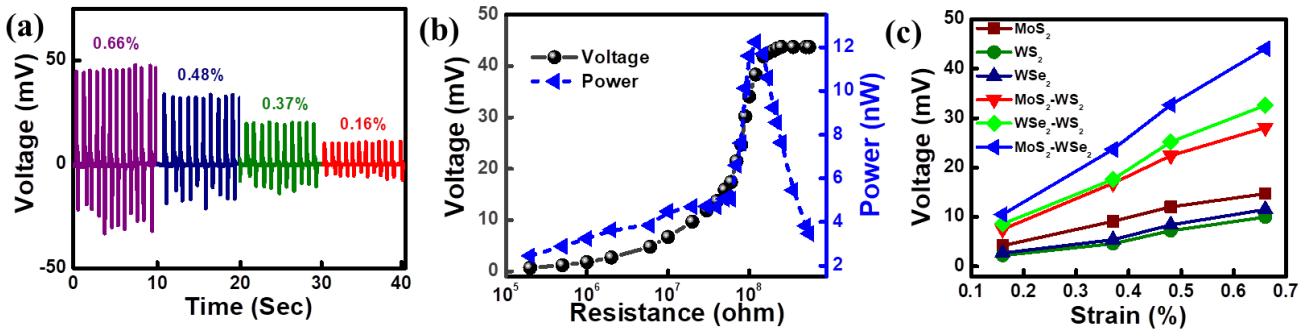

Figure 6.10 (a) Variation of piezo-voltage with varying strain. (b) Dependence of output voltage and power on the externally connected load resistances from MoS_2-WSe_2 heterostructure PENG. (c) Variation of open circuit piezo voltage from all the PENG devices with varying strain.

To explore the energy harvesting ability of the self-powered MoS_2-WSe_2 PENG from regular human activity, this device is attached on different parts of human body and the piezoelectric output voltages on movement of body parts are measured. The device is attached with finger and wrist joint, and piezoelectric output voltages are generated for finger and wrist bending (Figure 6.11(a-b)). The bending of wrist (~7.7 mV) produces much higher piezo voltage than that of finger bending (~2 mV). By the application of a pressure with fingertip, the piezoelectric output voltages (~1.5 mV) are produced (Figure 6.11(c)). This PENG is able to harvest energy from human vocal vibration also. It is observed that different piezoelectric signals are obtained by pronouncing different word, but identical piezoelectric signals are obtained by pronouncing the same word (Figure 6.11(d)), indicating that this PENG can be used for voice recognition purpose. As this PENG can harvest energy from body movements, it has an enormous potential for applications in self-powered wearable devices. These demonstrated results indicate that the strain sensing and self-powered functionalities can be used as human-robot interaction platform to synchronize human-robot motion.

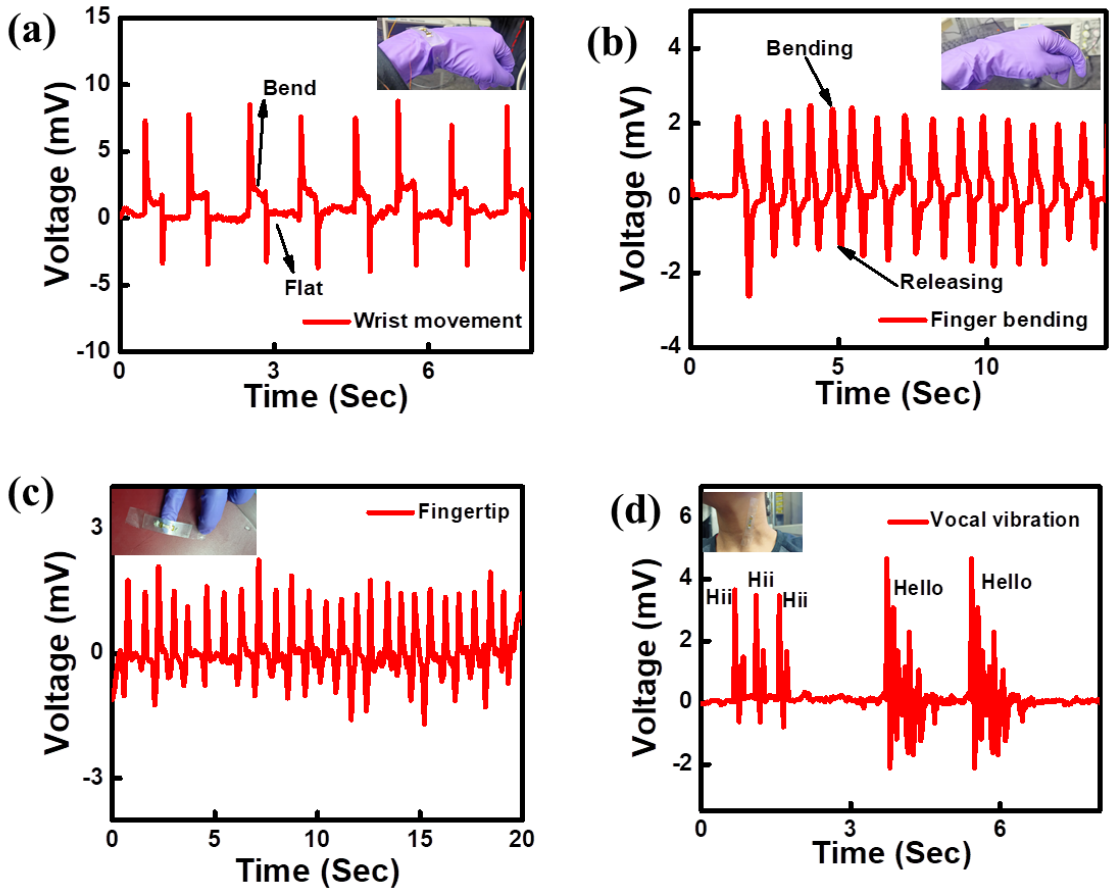

Figure 6.11 Output voltages from MoS_2-WSe_2 heterostructure PENG when attached with (a) wrist and (b) finger, exhibiting piezo voltages due to the movement of wrist and finger. (c) Piezo-voltage generation due to the pressure of fingertip. (d) Output voltage of the PENG when attached with vocal cords for different trace words with excellent repeatability, indicating its potential application as wearable sensors.

Table:6.1 Performance of the PENG in this work compared with reported results

SL. No	Sample Name	Applied Strain	Voltage and Power	Reference
1.	Monolayer CVD MoS_2	0.60%	34 mV 62.72 pW	32
2.	Monolayer CVD $MoSe_2$	0.6%	35 mV 42 mW m^{-2}	33
3.	Monolayer CVD $MoSe_2$	0.6%	60mV	31
4.	CVD monolayer MoS_2	0.48%	12 mV 73 μW m^{-2}	11
5.	Mechanically exfoliated monolayer MoS_2	0.53%	15 mV 2mWm^{-2}	10
6.	CVD grown SnS_2	0.6%	6 mV 12 pW	49
7.	**Chemically exfoliated MoS_2-WSe_2 heterostructure**	**0.66%**	**45.7 mV** **12.3 nW**	**This Study**

6.4 Summary:

In summary, different TMDC heterostructure structures are fabricated using the layered nanosheets (MoS_2, WS_2, WSe_2) synthesized by sonochemical assisted hydrothermal technique. To the best of our knowledge, the intrinsic piezoelectric properties of such chemically exfoliated TMDC heterostructures are reported for the first time (from best of our knowledge). Piezoelectric properties of these as-synthesized nanosheets are examined through piezoelectric force microscopy (PFM). The piezoelectric coefficient of the MoS_2-WSe_2 hybrid heterostructure is found to be higher than the individual TMDC layers and other two hybrid heterostructure combinations, revealing the key role of the band offset. PENG devices are fabricated by using heterostructures, in order to demonstrate the real-life device applications for transforming mechanical energy to electricity. In support with PFM measurements, the enhanced piezoelectric output performance is obtained for MoS_2-WSe_2 heterostructure device than the other PENG devices. The optimized device is able to produce an open circuit voltage ~45.7 mV under ~0.66% strain and generates an instantaneous power 12.3 nw for ~200 MΩ load resistance. Besides the energy harvesting ability of this PENG, it can be used as a sensor and bio-mechanical energy harvester producing piezoelectric output voltage for simple human activities. Thus, the MoS_2-WSe_2 PENG can be adopted as practical wearable energy-harvesting devices as well as self-powered sensors. The fabrication of large-area, lithography-free, cost effective thin-film PENG ensures that the reproducible output

performance could also be used for other purposes. Our approach provides a simple route to realize large-area 2D material-based PENGs and wearable smart sensors.

6.5 References:

1. Z. L. Wang, *Adv. Mater.*, 2012, 24, 4632–4646.
2. G. Zhu, R. Yang, S. Wang and Z. L. Wang, *Nano Lett.*, 2010, **10**, 3151–3155.
3. K. Il Park, S. Xu, Y. Liu, G. T. Hwang, S. J. L. Kang, Z. L. Wang and K. J. Lee, *Nano Lett.*, 2010, **10**, 4939–4943.
4. D. Bhattacharya, S. Bayan, R. K. Mitra and S. K. Ray, *ACS Appl. Electron. Mater.*, 2020, **2**, 3327–3335.
5. D. Bhattacharya, S. Bayan, R. K. Mitra and S. K. Ray, *Nanoscale*, 2021, **13**, 15819–15829.
6. F. Cao, W. Tian, L. Meng, M. Wang and L. Li, *Adv. Funct. Mater.*, 2019, **1808415**, 1–8.
7. W. Zeng, X. M. Tao, S. Chen, S. Shang, H. L. W. Chan and S. H. Choy, *Energy Environ. Sci.*, 2013, **6**, 2631–2638.
8. M. N. Blonsky, H. L. Zhuang, A. K. Singh and R. G. Hennig, *ACS Nano*, 2015, **9**, 9885–9891.
9. S. Pak, J. Lee, A. R. Jang, S. Kim, K. H. Park, J. I. Sohn and S. N. Cha, *Adv. Funct. Mater.*, 2020, **30**, 1–7.
10. W. Wu, L. Wang, Y. Li, F. Zhang, L. Lin, S. Niu, D. Chenet, X. Zhang, Y. Hao, T. F. Heinz, J. Hone and Z. L. Wang, *Nature*, 2014, **514**, 470–474.
11. S. A. Han, T. H. Kim, S. K. Kim, K. H. Lee, H. J. Park, J. H. Lee and S. W. Kim, *Adv. Mater.*, 2018, **30**, 1–7.
12. E. Nasr Esfahani, T. Li, B. Huang, X. Xu and J. Li, *Nano Energy*, 2018, **52**, 117–122.
13. M. Dai, W. Zheng, X. Zhang, S. Wang, J. Lin, K. Li, Y. Hu, E. Sun, J. Zhang, Y. Qiu, Y. Fu, W. Cao and P. A. Hu, *Nano Lett.*, 2020, **20**, 201–207.
14. C. J. Brennan, R. Ghosh, K. Koul, S. K. Banerjee, N. Lu and E. T. Yu, *Nano Lett.*, 2017, **17**, 5464–5471.
15. A. Sohn, S. Choi, S. A. Han, T. H. Kim, J. H. Kim, Y. Kim and S. W. Kim, *Nano Energy*, 2019, **58**, 811–816.

16. Jiang S. J., Wan S. M., Luo W., et al., *J. Mater. Chem*, 2020, **1**, 3777.
17. D. Bhattacharya, S. Mukherjee and R. K. Mitra, *Nanotechnology*, 2020, **31**, 1–9.
18. S. Mukherjee, D. Bhattacharya, S. Patra, S. Paul, R. K. Mitra, P. Mahadevan, A. N. Pal and S. K. Ray, *ACS Appl. Mater. Interfaces*, 2022, **14**, 5775–5784.
19. K. Hou, Z. Huang, S. Liu, G. Liao, H. Qiao, H. Li and X. Qi, *Nanoscale Adv.*, 2020, **2**, 2185–2191.
20. S. K. Kim, R. Bhatia, T. H. Kim, D. Seol, J. H. Kim, H. Kim, W. Seung, Y. Kim, Y. H. Lee and S. W. Kim, *Nano Energy*, 2016, **22**, 483–489.
21. A. Y. Lu, H. Zhu, J. Xiao, C. P. Chuu, Y. Han, M. H. Chiu, C. C. Cheng, C. W. Yang, K. H. Wei, Y. Yang, Y. Wang, D. Sokaras, D. Nordlund, P. Yang, D. A. Muller, M. Y. Chou, X. Zhang and L. J. Li, *Nat. Nanotechnol.*, 2017, **12**, 744–749.
22. J. Yao, Z. Zheng and G. Yang, *ACS Appl. Mater. Interfaces*, 2016, **8**, 12915–12924.
23. J. G. Song, G. H. Ryu, S. J. Lee, S. Sim, C. W. Lee, T. Choi, H. Jung, Y. Kim, Z. Lee, J. M. Myoung, C. Dussarrat, C. Lansalot-Matras, J. Park, H. Choi and H. Kim, *Nat. Commun.*, 2015, **6**, 1–10.
24. W. Ma, J. Lu, B. Wan, D. Peng, Q. Xu, G. Hu, Y. Peng, C. Pan and Z. L. Wang, *Adv. Mater.*, 2020, **32**, 1–9.
25. J. Shakya, H. N. Gayathri and A. Ghosh, *Nanotechnology*, 2022, **33**, 1–7.
26. J. M. Wu, W. E. Chang, Y. T. Chang and C. K. Chang, *Adv. Mater.*, 2016, **28**, 3718–3725.
27. S. Li, Z. Zhao, D. Yu, J. Z. Zhao, Y. Su, Y. Liu, Y. Lin, W. Liu, H. Xu and Z. Zhang, *Nano Energy*, 2019, **66**, 1–10.
28. S. Yu, Q. Rice, B. Tabibi, Q. Li and F. J. Seo, *Nanoscale*, 2018, **10**, 12472–12479.
29. S. Yuan, W. F. Io, J. Mao, Y. Chen, X. Luo and J. Hao, *ACS Appl. Nano Mater.*, 2020, **3**, 11979–11986.
30. V. A. Cao, M. Kim, W. Hu, S. Lee, S. Youn, J. Chang, H. S. Chang and J. Nah, *ACS Nano*, 2021, **15**, 10428–10436.
31. P. Li and Z. Zhang, *ACS Appl. Mater. Interfaces*, 2020, **12**, 58132–58139.
32. D. Zhang, Z. Yang, P. Li, M. Pang and Q. Xue, *Nano Energy*, 2019, **65**, 1–8.
33. D. Wang, D. Zhang, P. Li, Z. Yang, Q. Mi and L. Yu, *Nano-Micro Lett.*, 2021, **13**, 1–13.
34. A. B. Patel, H. K. Machhi, P. Chauhan, S. Narayan, V. Dixit, S. S. Soni, P. K. Jha, G. K. Solanki, K. D. Patel and V. M. Pathak, *ACS Appl. Mater. Interfaces*, 2019, **11**, 4093–4102.

35. G. J. Lai, L. M. Lyu, Y. S. Huang, G. C. Lee, M. P. Lu, T. P. Perng, M. Y. Lu and L. J. Chen, *Nano Energy*, 2021, **81**, 105608.
36. X. Duan, C. Wang, J. C. Shaw, R. Cheng, Y. Chen, H. Li, X. Wu, Y. Tang, Q. Zhang, A. Pan, J. Jiang, R. Yu, Y. Huang and X. Duan, *Nat. Nanotechnol.*, 2014, **9**, 1024–1030.
37. H. Fang, C. Battaglia, C. Carraro, S. Nemsak, B. Ozdol, J. S. Kang, H. A. Bechtel, S. B. Desai, F. Kronast, A. A. Unal, G. Conti, C. Conlon, G. K. Palsson, M. C. Martin, A. M. Minor, C. S. Fadley, E. Yablonovitch, R. Maboudian and A. Javey, *Proc. Natl. Acad. Sci. U. S. A.*, 2014, **111**, 6198–6202.
38. J. Yang, J. Zhu, J. Xu, C. Zhang and T. Liu, *ACS Appl. Mater. Interfaces*, 2017, **9**, 44550–44559.
39. K. Si, J. Ma, C. Lu, Y. Zhou, C. He, D. Yang, X. Wang and X. Xu, *Appl. Surf. Sci.*, 2020, **507**, 1–11.
40. W. Yang, H. Kawai, M. Bosman, B. Tang, J. Chai, W. Le Tay, J. Yang, H. L. Seng, H. Zhu, H. Gong, H. Liu, K. E. J. Goh, S. Wang and D. Chi, *Nanoscale*, 2018, **10**, 22927–22936.
41. K. Wang, B. Huang, M. Tian, F. Ceballos, M. W. Lin, M. Mahjouri-Samani, A. Boulesbaa, A. A. Puretzky, C. M. Rouleau, M. Yoon, H. Zhao, K. Xiao, G. Duscher and D. B. Geohegan, *ACS Nano*, 2016, **10**, 6612–6622.
42. X. Hong, J. Kim, S. F. Shi, Y. Zhang, C. Jin, Y. Sun, S. Tongay, J. Wu, Y. Zhang and F. Wang, *Nat. Nanotechnol.*, 2014, **9**, 682–686.
43. M. H. Doan, Y. Jin, S. Adhikari, S. Lee, J. Zhao, S. C. Lim and Y. H. Lee, *ACS Nano*, 2017, **11**, 3832–3840.
44. V. Zatko, S. M. M. Dubois, F. Godel, C. Carrétéro, A. Sander, S. Collin, M. Galbiati, J. Peiro, F. Panciera, G. Patriarche, P. Brus, B. Servet, J. C. Charlier, M. B. Martin, B. Dlubak and P. Seneor, *ACS Nano*, 2021, **15**, 7279–7289.
45. H. Seok, Y. T. Megra, C. K. Kanade, J. Cho, V. K. Kanade, M. Kim, I. Lee, P. J. Yoo, H. U. Kim, J. W. Suk and T. Kim, *ACS Nano*, 2021, **15**, 707–718.
46. L. L. Chiu M, Li M, Zhang W, Hsu W, Chang W, Terrones M, Terrones H, *ACS Nano*, 2014, **8**, 9649–9656.
47. A. Apte, K. Mozaffari, F. S. Samghabadi, J. A. Hachtel, L. Chang, S. Susarla, J. C. Idrobo, D. C. Moore, N. R. Glavin, D. Litvinov, P. Sharma, A. B. Puthirath and P. M. Ajayan, *Adv. Mater.*, 2020, **32**, 2–9.
48. H. J. Jin, W. Y. Yoon and W. Jo, *ACS Appl. Mater. Interfaces*, 2018, **10**, 1334–1339.

49. P. K. Yang, S. A. Chou, C. H. Hsu, R. J. Mathew, K. H. Chiang, J. Y. Yang and Y. T. Chen, *Nano Energy*, 2020, **75**, 104879.
50. Y. Wang, L. M. Vu, T. Lu, C. Xu, Y. Liu, J. Z. Ou and Y. Li, *ACS Appl. Mater. Interfaces*, 2020, **12**, 51662–51668.
51. M. H. Chiu, C. Zhang, H. W. Shiu, C. P. Chuu, C. H. Chen, C. Y. S. Chang, C. H. Chen, M. Y. Chou, C. K. Shih and L. J. Li, *Nat. Commun.*, 2015, **6**, 1–6.
52. M. A. Khan, S. Rathi, C. Lee, D. Lim, Y. Kim, S. J. Yun, D. H. Youn and G. H. Kim, *ACS Appl. Mater. Interfaces*, 2018, **10**, 23961–23967.
53. H. M. Hill, A. F. Rigosi, K. T. Rim, G. W. Flynn and T. F. Heinz, *Nano Lett.*, 2016, **16**, 4831–4837.
54. J. Kang, S. Tongay, J. Zhou, J. Li and J. Wu, *Appl. Phys. Lett.*, 2013, **102**, 1–4.
55. Z. Cao, M. Harb, S. Lardhi and L. Cavallo, *J. Phys. Chem. Lett.*, 2017, **8**, 1664–1669.
56. F. Xue, J. Zhang, W. Hu, W. T. Hsu, A. Han, S. F. Leung, J. K. Huang, Y. Wan, S. Liu, J. Zhang, J. H. He, W. H. Chang, Z. L. Wang, X. Zhang and L. J. Li, *ACS Nano*, 2018, **12**, 4976–4983.
57. P. Li, Z. Zhang, W. Shen, C. Hu, W. Shen and D. Zhang, *J. Mater. Chem. A*, 2021, **9**, 4716–4723.
58. D. Tan, C. Jiang, N. Sun, J. Huang, Z. Zhang, Q. Zhang, J. Bu, S. Bi, Q. Guo and J. Song, *Nano Energy*, 2021, **90**, 106528.

Chapter: 7

Size dependent optical properties of MoS_2 nanoparticles and their photo-catalytic applications

While two dimensional layered MoS_2 nanosheets have been extensively studied owing to their fascinating optoelectronic properties, less attention has been paid on the corresponding zero-dimensional nano-crystals. In this contribution, we report the efficacy of MoS_2 nanocrystals for their size tunable properties for optical and photocatalytic applications. We have synthesized different sized (10-70 nm), crystalline, hexagonal 2H-MoS_2 nanoparticles (NPs) dispersed in DMF solvent using a simple exfoliation technique. Synthesized NPs are found to exhibit size dependent optical properties and excitation dependent fluorescence characteristics in the visible region, which are not observed in bulk or 2D MoS_2 layers. Size tunable band gap and broad absorbance and emission spectrum covering the visible range could be exploited in the fabrication of various opto-electronic devices. Charge carrier emission dynamics of different sized MoS_2 NPs are investigated using time correlated single photon counting (TCSPC) spectroscopic technique. We found two time components, one in the order of several hundreds of ps, which arises due to the radiative recombination of charge carriers, while the other one is of the order of a few ns, which emanates from the defect states of MoS_2 NPs. The average time constants are found to decrease with increase in particle size. A noticeable photocatalytic activity of the synthesized MoS_2 NPs under visible light illumination for the degradation of Brilliant Green dye is also demonstrated for the first time and the effect of size variation of NPs in the dye degradation process is reported.

7.1 Introduction:

Layered two dimensional (2D) materials have gained immense research interests for applications in electronics, photonics, catalysis and energy conversion/storage, portable, wearable, smart devices [1-3] during the last decade [4-6] due to their exceptional mechanical, electrical, chemical, optoelectronic and spectroscopic properties [7]. In spite of various extraordinary electrical properties, graphene, the most extensively studied 2D material, but is unsuitable for optoelectronic and photocatalytic applications due to its zero bandgap nature. On the contrary, 2D transition metal dichalcogenides (TMDs), a vertically stacked layered materials bonded by weak van-der-Waals (vdW) interaction in out-of-plane direction, possess a finite energy gap, which can be found useful for optoelectronic applications and spectroscopic studies. Molybdenum disulphide (MoS_2) is one of the most widely studied

TMDCs due to its abundance in nature and attractive semiconducting, electrical, spectroscopic, optoelectronic, catalytic properties. Depending on the stacking orders and the coordination of S atoms with the central Mo atom they can be categorized into three phases, i.e., 1T, 2H and 3R where, T, H, R denote tetragonal (T), hexagonal (H) and rhombohedral (R) types crystal symmetry of MoS_2 respectively. It is reported that MoS_2 exhibits layer dependent tunable band gap in such a way that bulk MoS_2 is an indirect band gap semiconductor (~1.2 eV) while for a single layer it exhibits direct gap transition (~1.9 eV) [4,8,9] with strong photoluminescence intensity. Such indirect-to-direct transformation occurs due to the local shifts of valance band maxima and conduction band valleys in the Brillouin zone [10].

Layered MoS_2 is mostly synthesized by micromechanical exfoliation [11], liquid phase exfoliation (LPE) [12,13], chemical vapor deposition (CVD) [14] and hydrothermal/ solvothermal [15] synthesis techniques. While mechanical exfoliation produces extremely low surface coverage with less control over monolayer thickness, CVD grown MoS_2 yields large area growth but needs specific condition for growth and exhibits inferior optical and electronic properties. Moreover, both these synthesis techniques produce highly saturated inactive basal planes which are difficult to functionalize. On the other hand, chemically exfoliated nanosheets offer an active basal plane [16,17] and can be easily deposited to various substrates with maintaining a good interfacial properties. This is an easy, low cost, reproducible method to synthesize single to few-layered 2D TMDC at large scale. Moreover, a colloidal dispersion of TMDC materials provide an additional degree of freedom to fabricate large area wafer scale devices on any kind of substrate including flexible ones, just by simple spin or dip coating technique [18,19]. On the other hand, colloidal zero dimensional (0D) MoS_2 nanoparticles (NPs) possess very high surface to volume ratio with enhanced electrical, opto-electric, spectroscopic, chemical, physio-chemical activities due to larger fraction of edge terminated, unsaturated chalcogen atoms compared to its 2D layered counterpart [20]. Size variable MoS_2 NPs can easily be prepared by chemical exfoliation (LPE) followed by gradual centrifugation technique with tunable optical, electronic and spectroscopic properties, which provide additional advantages over 2D layered MoS_2 sheets [12,21]. Size tunable optical properties of TMDC nanoparticles (NPs) lead to the possibility of various optoelectronic devices viz., selective and multi-color photo-detection (photodiode, phototransistor), wavelength selective emitters, modulators and absorbing layers for solar cells, light emitting diode etc.

Chapter: 7

In the present study, we have demonstrated liquid phase exfoliation (LPE) technique to synthesize highly luminescent, sized tunable MoS_2 NPs by using a combined sonication-centrifugation technique. Size dependent optical properties of synthesized MoS_2 NPs have been studied using UV-Vis absorption, photoluminescence (PL), Raman scattering and time resolved emission spectroscopy (TCSPC) techniques. Chemically exfoliated MoS_2 NPs have broad absorption spectrum with three distinct excitonic absorption peaks. This size tunable absorption feature is found to be much useful for various photonic and spectroscopic applications. The emission wavelength of synthesized MoS_2 NPs is found to be tunable with varying excitation wavelength, which is very useful for various excitation dependent optical and biological applications. The photoluminescence (PL) intensity and relative quantum yield (Q.Y.) can be controlled by tuning the size of NPs, which is a direct evidence of quantum confinement effect. The time resolved emission spectroscopy studies provide an idea about the charge carrier lifetime and variation of carrier lifetimes with the NP sizes. Finally, photocatalytic activity of the synthesized MoS_2 NPs is investigated by using the degradation of a model dye molecule (brilliant-green (BG) (ammonium, 4- (p-diethylamino)-alpha-(pheylbenzylidene), $C_{27}H_{34}N_2O_4S$), which is carcinogenic but is extensively used in textile dying and paper printing technology and is found abundantly in industrial waste water [22]. The broad absorption spectra of MoS_2 NPs enable them to absorb light in the visible wavelength region and consequently generation of photo-carriers, can eventually degrade organic dyes. Importantly bulk MoS_2 does not show any such photocatalytic activity and its efficiency gets enhanced with reducing MoS_2 NPs size. Conventional semiconductors (such as TiO_2, ZnS, CdS, ZnO, Cu_2O etc.) can act as strong catalysts, which can degrade pollute molecules under natural sunlight as well as under UV irradiation. However, the report on the degradation of organic dyes by using MoS_2 NP as a unary photo-catalyst in presence of visible light is sparse in the literature. Our present study systematically demonstrates that the different sized semiconducting MoS_2 NPs are promising candidate for fabrication of optoelectronic devices with a strong potential for the degradation of harmful chemicals in waste water under visible light irradiation.

7.2 Experimental Section:

7.2.1 Materials:

All the chemicals (MoS_2 powder, DMF solvent, Brillant Green dye) were purchased from Sigma-Aldrich and used without any further purification.

7.2.2 Synthesize of MoS_2 Nanoparticles (NPs):

MoS_2 nanoparticles (NPs) were prepared by a generic solvent assisted sono-chemical exfoliation technique starting from bulk MoS_2 powder (purchased from Sigma). Initially the bulk MoS_2 powder was dissolved in N, N-dimethylformamide (DMF) solvent at a concentration of 1mg/ml and the mixture was kept in bath sonication for 8 hrs. In the beginning of the sonication process, the weak interlayer van-der-Waals) interaction was overcome and gradually exfoliated few-layers MoS_2 from its bulk counterparts. Prolonged sonication was used to break 2D MoS_2 layers into variable sized NPs. Thereafter, the suspension was centrifuged at 1000 rpm for 15 mins to separate out the un-exfoliated large flakes and the supernatant was used for further processing. The supernatant was then centrifuged from 2000 rpm to 12000 rpm with 2000 rpm incremental steps successively for 20 minutes each and the precipitate was collected after each step. A change in colour of MoS_2 NPs from black to greenish yellow to light yellow was observed with increasing rpm vis-à-vis reduction of NPs size.

7.2.3 Characterizations:

The synthesized samples were structurally characterized by using X-ray diffraction (XRD) (PANalytical X-PERT PRO), field-emission scanning electron microscopy (FESEM) (Quanta FEG 250) and high resolution transmission electron microscopy (HRTEM) (FEI Technai S-Twin instrument with 200 kV acceleration voltage, the selected area diffraction pattern was done in a normal mode). The optical properties of as-synthesized MoS_2 NPs were studied using optical absorption, photoluminescence (PL) and Raman spectroscopy techniques. Absorption spectra were recorded by Shimadzu UV-2600 spectrometer in the UV-visible spectral range. PL measurements were carried out using a He-Cd laser with 325 nm excitation source, a monochromator [TRIAX-320] and a PMT detector [Hamamatsu R928].

Raman spectra were recorded in the backscattering configuration using a 514 nm excitation source and an optical microscope with 50x objective lens (Jobin Yvon Horiba T64000). Steady state fluorescence spectra were recorded in Jobin-Yvon Fluorolog fluorimeter. Picosecond time resolved fluorescence transients were recorded using a time correlated single photon counting (TCSPC) setup of Edinburgh Instruments with a pulsed diode laser of wavelength 375 nm as the excitation source with instrument response function (IRF) of ~80 ps.

7.3 Results and Discussions:

7.3.1 Structural Studies:

Typical TEM images of as-synthesized MoS_2 NPs are shown in Figure 7.1(a-c), which are collected following centrifugation at a speed of 12000, 10000 and 8000 rpm respectively. The corresponding inset histograms depict the size distribution of as synthesized MoS_2 NPs ,which the average size has been estimated to be ~11 nm (±2.0 nm), ~17 nm (±2.0 nm) and ~26 nm (±1.8 nm), respectively. The TEM images indicate that the synthesized NPs are found to be nearly mono-dispersed and spherical in nature (Figure 7.1(d)). The inter-planar lattice fringe spacing of a typical MoS_2 NP (radius~ 11 nm) is found to be ~0.26 nm (Figure 7.1(e)) which is attributed due to the formation of (100) crystalline lattice plane [12,13,21]. The selected area electron diffraction (SADE) pattern in Figure 7.1(f) indicates that MoS_2 NPs remain in hexagonal crystal structure even after exfoliation and size reduction.

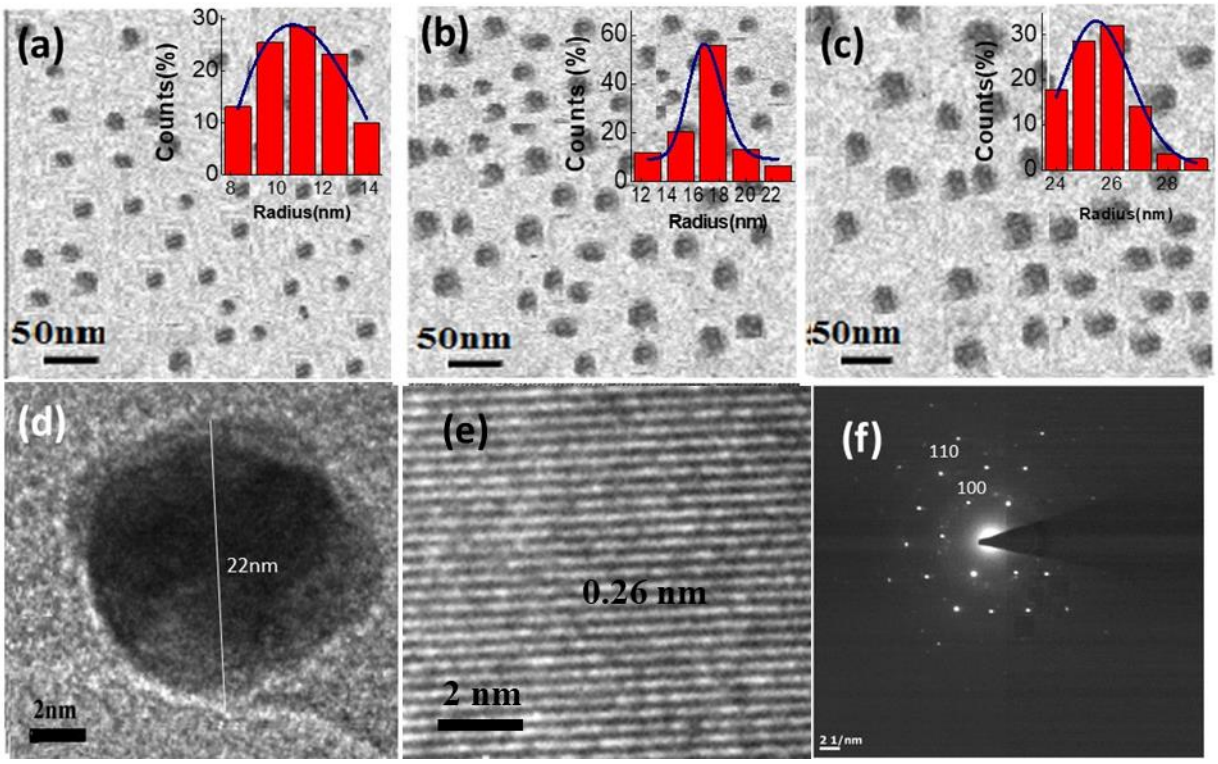

Figure 7.1 TEM images of MoS_2 NPs of different average size: (a) 11 nm, (b) 17 nm and (c) 26 nm. The corresponding insets show the distribution of NP size. (d) Magnified HRTEM image of a typical MoS_2 NP (radius ~11 nm). (e) Lattice fringes of MoS_2 (100) plane and (f) Selected area diffraction pattern of MoS_2 NPs (radius ~11 nm).

X-ray diffraction (XRD) patterns of the different sized MoS_2 NPs are displayed in Figure 7.2(a). An intense peak is noticed at 14.4^0 which is attributed to the formation of crystalline (002) plane of MoS_2. The intensity of a weaker peak at 44.5^0 corresponding to the (006) plane of MoS_2 does not change appreciably with reduction of nanoparticle dimension. So it can be claimed that the XRD pattern is in well agreement with the TEM results. Raman spectroscopy measurements with varying NPs size have been carried out under 514 nm excitation and a typical raman spectrum is depicted in the inset of Figure 7.2(b). Two prominent peaks at 382.5 cm^{-1} and 407 cm^{-1} are attributed due to the in-plane (E^1_{2g}) and out of plane (A_{1g}) vibrational modes of S-Mo-S layers, respectively [12,23]. The location and spacing between characteristic Raman peaks (~24.5 cm^{-1}) remain almost unchanged with varying NP sizes. However, the intensities of both the peaks as well as the ratio of peaks (E^1_{2g}/A_{1g}) are found to decrease with reducing nanoparticle size (Figure 7.2(b)). Reduced crystalline quality (as evident from the XRD measurements) of smaller sized NPs might be the reason behind the weaker Raman intensity. On the other hand, surface reconstruction due

to NP formation increases the surface-to-volume ratio and also the ratio between the number of surface to the total number of bonds in the nanocrystals [24]. Additionally, interlayer separation between the planes is affected [24]. A combination of both the above factors lead to the observation is represented in the inset of Figure 7.2(b). A shift in the E^1_{2g} and A_{1g} peak positions as well as the spacing between the peaks have earlier been reported, which change with variation of the number of layers [24]. In this study for MoS_2 NPs, however, the peak separation remains unchanged, while the peak intensities and their ratio are observed to decrease with decreasing nanoparticle size.

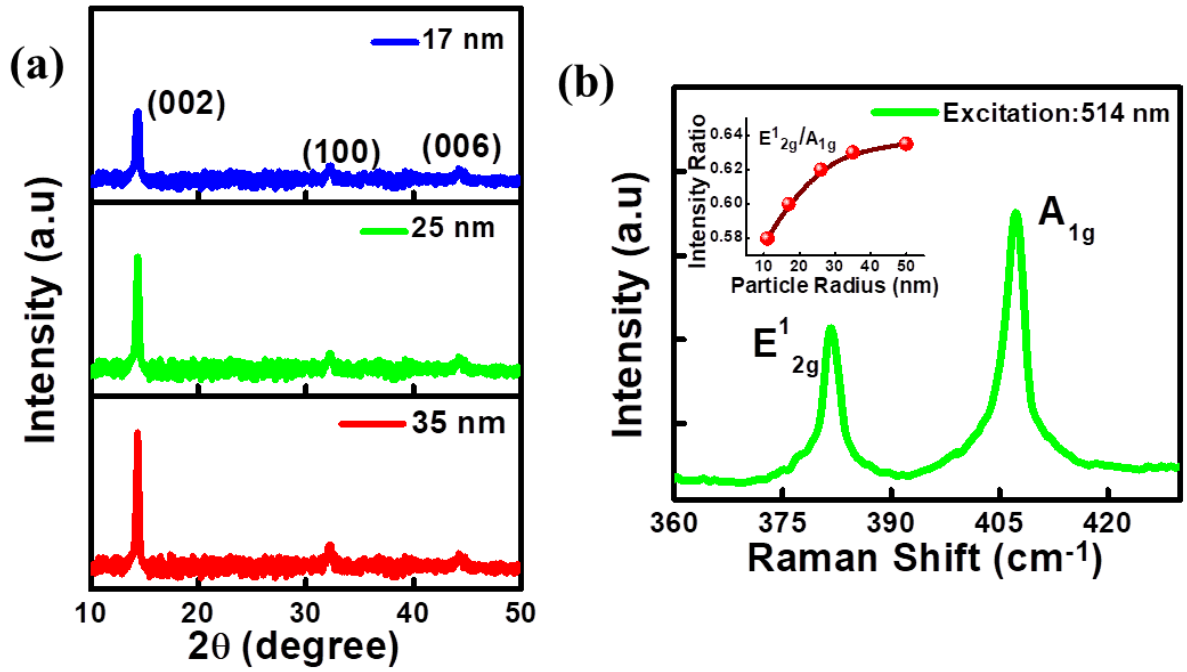

Figure 7.2 (a) XRD diffraction pattern of MoS_2 NPs of different sizes. (b) Raman spectrum of MoS_2 NPs of average size ~17 nm and the inset shows the variation of the ratio of characteristic Raman peak intensity with particle size.

7.3.2 Spectroscopic Studies:

The quantum size effect of MoS_2 NPs has been studied by UV-Vis optical absorption and photoluminescence (PL) spectroscopy. In a typical absorption spectrum (Figure 7.3(a)) of MoS_2 NPs, two prominent excitonic peaks at ~680 and ~618 nm are observed, which have their respective origin due to the transition between spin-orbit coupled split valance bands and conduction band edges. The absorption peak at 680 nm is defined as the excitonic-A peak while that at 618 nm is the excitonic-B peak. Another absorption feature is observed in the lower wavelength range (300-480 nm) with excitonic peak centered at ~460 nm (peak-C)

along with a weak shoulder at ~395 nm (peak-D). This absorption feature can be correlated to the band nesting phenomenon as commonly observed in this type of TMDC materials. In band nesting region, conduction and valance bands lie parallel with each other in the momentum space [25]. Upon the absorption of photons electrons and holes pairs are generated and propagate with equal velocity but in opposite directions. Strong Van-Hove singularities (VHS) facilitate the band nesting phenomenon, resulting in a divergence in joint density of states (JDOS), and correspondingly a higher transition energy gap [25]. The C-excitonic peak shows a prominent blue shift with decreasing NPs size which can be explained on the basis of increased band gap with reduction in size due to quantum confinement effect. Emission spectra of three different sized MoS_2 NPs have been measured by 325 nm excitation and are represented in Figure 7.3(b). From the emission spectra it is noticed that the smallest sized NPs exhibit the most intense emission and the emission intensity decreases gradually with increasing NP size. This photoluminescence (PL) spectrum can be deconvoluted into two overlapping Gaussian peaks: one is centered at ~420 nm while the other one at ~500 nm (Figure 7.3(c)). The lower energy PL emission can be ascribed due to the transition between quantized energy levels [13] and the other peak may be considered due to defect state mediated transition [26]. The ratio of integrated PL intensity between two peaks (direct-to-defect) increases with increasing particle size and is depicted in Figure 7.3(d). With decreasing nanoparticle size, the surface- to-volume ratio of nanoparticle increases, which may lead to an enhanced surface defect state contribution in the PL emission.

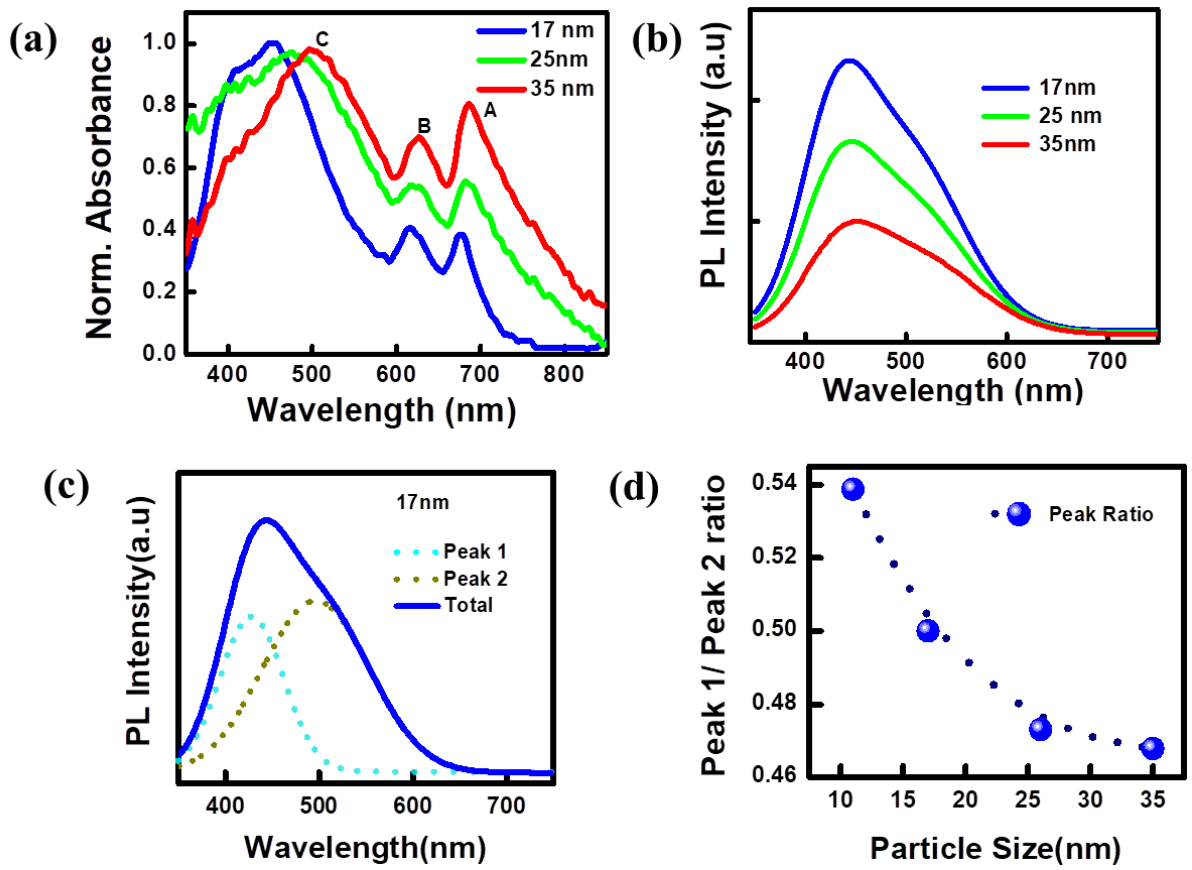

Figure 7.3 (a) Absorption spectrum of different size MoS_2 NPs, exhibiting different peaks. (b) PL spectrum of different sized NPs (excitation: 325 nm). (c) Deconvolution of the PL spectrum of ~17 nm NP radius into two Gaussian curves. (d) Variation of intensity ratio of the two PL peaks with particle size.

Interestingly the excitation dependent fluorescence is observed for all the synthesized NPs, the representative emission spectra are depicted for ~17 nm NPs in Figure 7.4(a). The emission peak has been found to be red-shifted almost linearly with the variation of excitation wavelength (Figure 7.4(b)). The broadband absorption profile (Figure 7.3(a)) manifests a distribution of ground state valance band energy as a consequence of size distribution of MoS_2 NPs, resulting in excitation dependent transitions between various band energy states. Such wavelength dependency has also been observed reported previously in other TMDC materials as well as in graphene QDs [27-29]. We have observed a gradual red shift of the emission peak with increasing excitation wavelength. The integrated intensity of the peaks is found to be decreased with increasing excitation wavelength.

We have estimated the relative quantum yield (Q.Y.) of the emission as:

$$QY_{sample} = QY_{ref}\left(\frac{I_{sample}}{I_{ref}}\right)\left(\frac{A_{ref}}{A_{sample}}\right)\left(\frac{n_{ref}^2}{n_{sample}^2}\right) \qquad (7.1)$$

where *I* is the corresponding area under the emission curve, *A* is the value of absorbance and *n* is the refractive index of nanoparticles and the reference samples. We have used C153 as a reference dye with known Q.Y. of 54% in ethanol [30]. This is noticed that the estimated relative QY (following equation 7.1) is a manifestation of the emissive power, which is directly related to the recombination rate of the charge carriers [30]. It is observed that the estimated relative Q.Y. gradually decreases with increasing NP size, as represented in Figure 7.4(c). The increase of the Q.Y. with size reduction unambiguously points out towards the increase in the radiative recombination rate, which is further supported by the time-resolved emission measurements (see later).

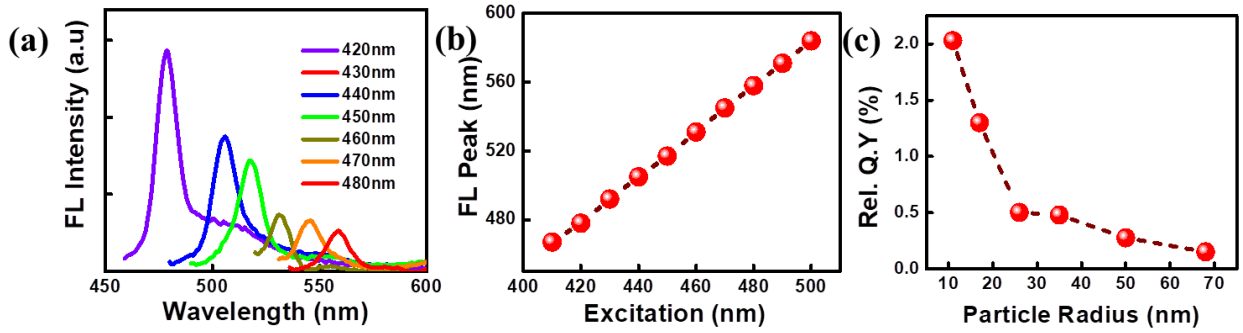

Figure 7.4 (a) Excitation dependent fluorescent spectrum of ~17 nm MoS_2 NPs. (b) Variation of emission peak position with excitation wavelength. (c) Variation of the relative quantum yield with nanoparticle size.

Time resolved photoluminescence decays have been recorded at 450 nm under 375 nm excitation for all synthesized MoS_2 NPs (Figure 7.5(a)) and the average lifetimes are estimated and its variation with nanoparticle size is depicted in Figure 7.5(b) and the variation of decay rate with varying the nanoparticle size is shown in Figure 7.5(c).

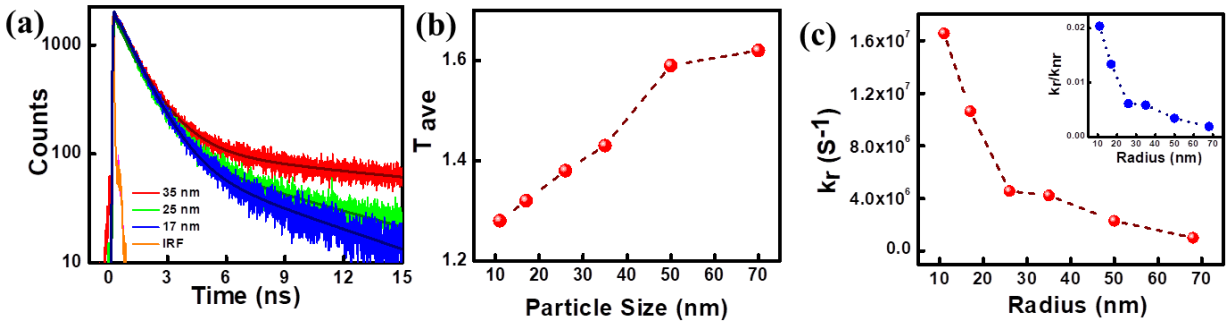

Figure 7.5 (a) Emission lifetime study of different size MoS_2 NP. (b) Variation of lifetime with varying size. (c) Variation of radiative decay rate with varying NPs size.

The decay transients are fitted with a bi-exponential function:

$$I(t) = Aexp\left(-\frac{t}{\tau_1}\right) + Bexp\left(-\frac{t}{\tau_2}\right) \qquad (7.2)$$

where I(t) is the intensity of the decay, the pre-exponential factors A and B are the amplitudes of decays corresponding to the decay time constants τ_1 and τ_2, respectively. The fitting parameters are presented in table-7.1

Table-7.1 Variation of nanoparticle lifetime with variation of nanoparticle size:

Particle size (nm)	**τ_1 (ns)**	**τ_2 (ns)**	**$<\tau>$ (ns)**
11	0.71 (72%)	3.4 (28%)	1.28
17	0.76 (74%)	3.4 (26%)	1.32
26	0.85 (77%)	3.45 (23%)	1.38
35	0.95 (78%)	3.5 (22%)	1.43
50	1.19 (80%)	3.5 (20%)	1.59
70	1.22 (84%)	3.6 (16%)	1.62

The fitting of experimental data with equation: 7.2 indicates the presence of two different relaxation processes responsible for the emission decay. The faster lifetime component (τ_1), contributing to the lager share in the decay process, changes from 0.71 ns (72%) (for 11 nm NPs) to 1.22 ns (84%) (for 70 nm NPs), while the slower one (τ_2) remains almost constant with the NP size and this variation is depicted in Figure 7.6.

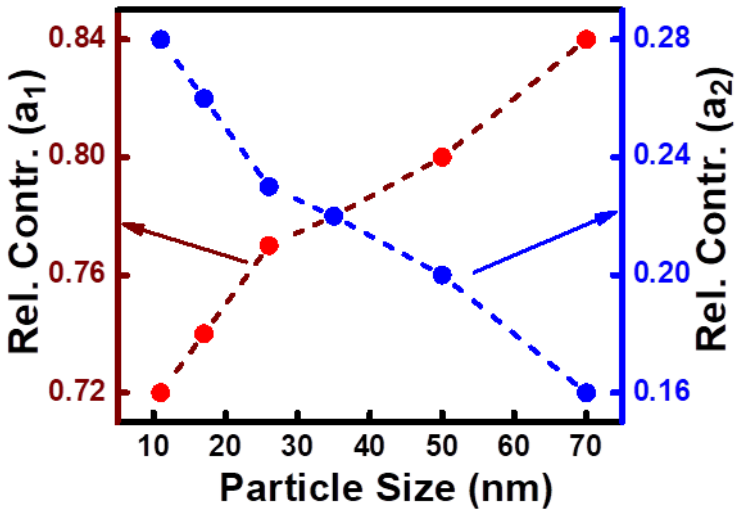

Figure 7.6 Variation of relative contribution of the decay time constants as a function of particle size.

Such bi-exponential decay behavior has previously been also reported for NPs of other direct bandgap semiconductor such as ZnO [31]. For layered TMDC materials [32] including MoS_2 [24], a tri-exponential decay pattern is more frequently observed, however, such studies are yet not to be reported for TMDC NPs. In this present study, the faster decay time component can be correlated with the direct radiative transition of the free charge carriers, while the slower one originates due to the recombination of localized charge carriers at the surface, which in turn is governed by the presence of both radiative and non-radiative traps due to the presence of defect states [31]. It is observed that the contribution of the slower lifetime component (τ_2) increases (16% to 28%) with decreasing nanoparticle size. This result corroborates with the steady state PL result, which concludes that there is increase in the contribution of the defect state with decrease in the nanoparticle size. In case of τ_1, with the increase of NP size the coupling between the exciton and the surface state is reduced, which results in an increased lifetime [31,33]. The average lifetime of the NP increases monotonically with increasing NP size.

The radiative (k_r) and the non-radiative (k_{nr}) decay constants for the relaxation process can be expressed in terms of the relative QY (which is estimated from steady-state measurements) (equation 7.3):

$$Q.Y. = \frac{k_r}{k_r + k_{nr}} = k_r < \tau_{av} > \qquad (7.3)$$

We have obtained the average lifetime, $<\tau_{av}>$ from the time resolved TCSPC measurements and have estimated k_r and k_{nr} values for the MoS_2 NPs. The k_{nr} is found to be order(s) of magnitude higher than the k_r, resulting due to the overall low Q.Y. of the NPs. It is also found that k_{nr} does not change appreciably (7.81×10^8 to 6.17×10^8 s^{-1}) with variation of NPs size, whereas the magnitude of k_r is decreased (1.6×10^7 to 1.15×10^6 s^{-1}) with the increase of NP size from 11 to 70 nm. The ratio of k_r/k_{nr} decreases with increasing NP size, however, the change is not linear, it first decreases sharply up to a size corresponding to the Bohr radius value and beyond this dimension the change is moderate (Figure 7.5(c)). As the quantum confinement in MoS_2 structure is prominent below the excitonic Bohr radius, strong spatial overlap of electron and hole wave functions leads to an increase in the radiative decay rate [33], which is evident in the present case. Analytically k_r is related to the square of overlap integral in the following way: $k_r \sim |V_{ab}(R)|^2 \sim e^{-2R/a_0}$, where V_{ab} is the exchange overlap integral, a_0 is the Bohr radius (23.5 nm for MoS_2) and R is the separation distance between an electron and a hole. On plotting $ln(k_r)$ as a function of $(-2R/a_0)$, we have obtained two distinct slopes. For $R<a_0$, the slope is ~ 1.01 while it is found to be ~ 0.44 for $R>a_0$. This sharp change in the slope around the Bohr radius signifies an enhanced overlap of the wave functions leading to quantum confinement.

7.3.3 Photocatalysis study:

Photocatalytic performance of MoS_2 NPs under visible irradiation is studied by monitoring the degradation rates of brilliant green (BG) dye in aqueous solution. The amount of MoS_2 NPs is varied in aqueous BG solution (10 μM) to optimize the maximum degradation rate. The dye and MoS_2 NP solution is kept stirring for 30 minutes in dark before visible light illumination. Thereafter fixed amount of solution is taken from this mixture at certain time intervals and the concentration of the dye in the solution as a function of time is estimated by recoding absorption spectrum in a UV-Vis spectrometer.

We have explored the photocatalytic property of the synthesized MoS_2 NPs on brilliant green (BG) dye and representative results for ~17 nm are depicted in Figure 7.7(a). MoS_2 NPs are added to aqueous BG solution, which is kept under visible light irradiation. Absorbance of the solution is then monitored and it is observed that the peak intensity of BG at 624 nm decreases with time (Figure 7.7(a)), which unambiguously shows the photocatalytic activity

of synthesized MoS_2 NPs. The change in colour of the dye solution following visible light irradiation for 180 mins is presented in inset of Figure 7.7(a). Assuming a first order decay kinetics of BG degradation, we have plotted (c_0/c) against time, as shown in Figure 7.7(b). For 0.18 mg ml^{-1} MoS_2 solution, the rate constant of BG degradation is estimatted to be 2×10^{-2} min^{-1}. Size dependency of MoS_2 NP is presented in Figure 7.7(c). It is found that the activity increases monotonically with decreasing the size of NPs. The catalytic activity does not change much on further decrease of NP size below ~ 17.0 nm.

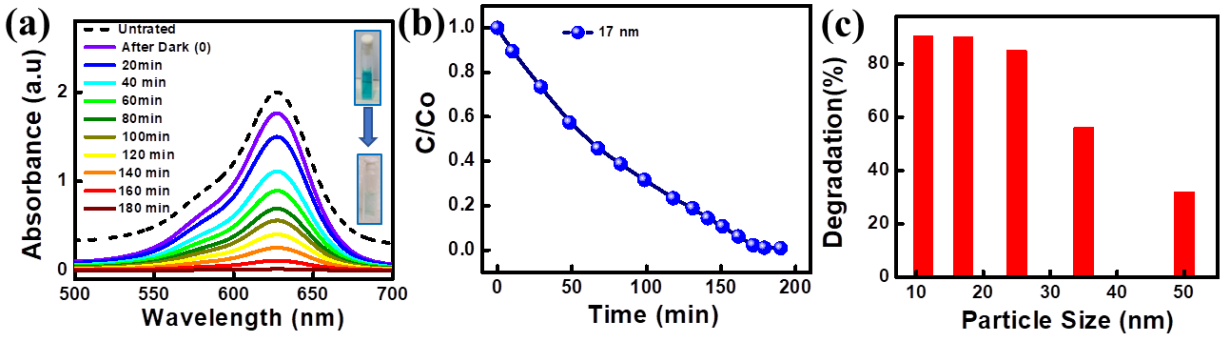

Figure 7.7 (a) Absorption spectrum for Brilliant Green dye degradation and the change of the colour of the solution depicts in inset. (b) Variation of photocatalytic decay rate with time. (c) Variation of degradation of BG dye with varying particle size (180 min) under visible illumination.

Mechanism of photocatalytic dye degradation is presented schematically in scheme: 7.1. It can be noted here that bulk 2H-semiconductor MoS_2 has an indirect band gap of 1.2 eV and does not show any photocatalytic activity. In case of chemically exfoliated MoS_2 NPs we have observed three distinct absorption peaks (excitonic A ~1.85 eV, B ~1.95 eV and C ~2.5 eV) peaks. Overall the NPs produce a broad absorption spectrum (350-800 nm) covering the almost entire visible range, which helps to absorb illuminations of different wavelengths. As the dimension of NP is reduced, the quantum confinement becomes prominent, moreover due to surface modification and the formation of surface defect and trap states, various optical transitions evolve. The formation of such a broad absorption spectrum in the visible range and the enhanced effective surface area lead to the generation of a larger density of photo-generated carriers.

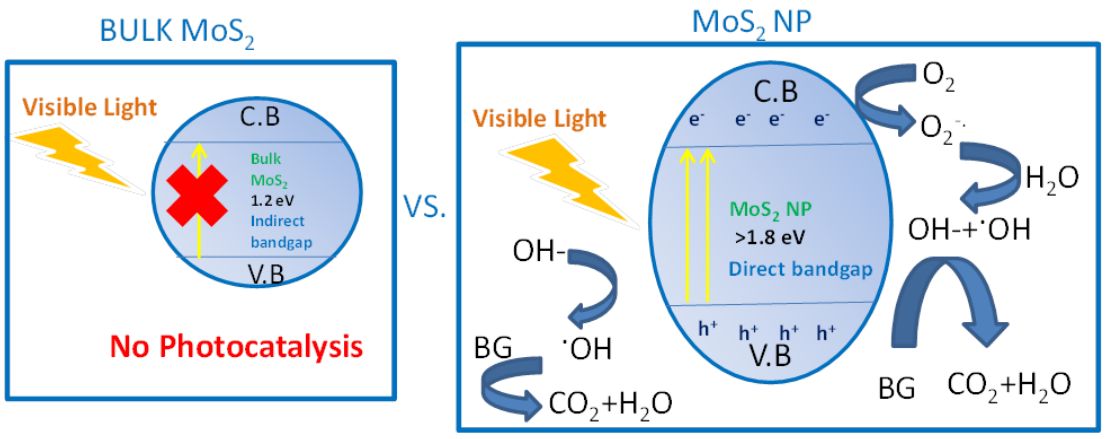

Scheme: 7.1. Schematic representation of photo-catalysis of BG with MoS_2 NPs. Bulk MoS_2 having an indirect band gap of 1.2 eV does not absorb visible light and is, therefore, photo-catalytically inactive. MoS_2 NPs, on the other hand, has a direct band gap of >1.8 eV along with a wide absorption band resulting in enhanced absorption of visible light and degradation of BG dye.

The generated photo carriers, before recombination, react with oxygen and water molecules to produce super oxide and hydroxyl radicals, which can degrade the dye molecules. Thus the irradiation of MoS_2 NPs produce *electron* and *hole* pairs, which led to the dissociation of BG to generate H_2O and CO_2 [34] in the following way: the holes react with the surface absorbed BG to produce highly reactive hydroxyl radicals ($\dot{OH}^-$), while electrons on reaction with molecular oxygen produces superoxide radicals ($\dot{O_2^-}$) The hydroxyl radical being highly active leads to the degradation of BG. The estimated value of decay rate 2×10^{-2} min^{-1} is comparable to the best results reported in the literature for SnO_2 and Zn capped SnO_2 NPs [35], TiO_2 and TiO_2/SnO_2 nanocomposite [36], TiO_2 and TiO_2-Zn and TiO_2-Cu nanocomposites [37]. We have compared the photocatalytic degradation efficiency of the present system with some previously reported MoS_2 nano-structures [38-40], which is presented in Table 7.2. We have observed that the rate constants obtained in those studies are either smaller or comparable to the present investigation.

Table: 7.2 Comparison of photocatalytic activity of MoS_2 NP with previous reports

Dye type	**Catalyst**	**Illumination condition**	**Time / Rate**	**Reference**
Rhodamine B and Methylene blue	3D flower-like MoS_2 hemispheres	450 nm, 5W	90% in 120 min	38
Methylene blue	Porous MoS_2	Visible, 100 W Xe-lamp	89.2% in 150 min, 0.0148 min^{-1}	39
Methyl Orange	MoS_2 nanosheets	Visible, 300 W incandescent lamp	98% in 120 min (pH=2)	40
Brilliant green	**MoS_2 nanoparticles, size ~ 17nm**	**Visible light**	**~99% in 180 min 2.0×10^{-2} min^{-1}**	**Present work**

7.4 Summary:

In this study variable sized (11-70 nm) MoS_2 NPs are synthesized through a simple chemical exfoliation technique. The NPs are found to be stable exhibiting good crystallinity, as explored using XRD and Raman spectroscopy techniques. It is observed that the size tunable optical properties of NPs as a consequence of quantum confinement, which are otherwise not observed in layered MoS_2. MoS_2 NPs also display excitation dependent emission profile, which makes them useful for specific applications. Emission lifetime of the dispersed NPs is found to be dependent on their size with the radiative and non-radiative dynamics mediated by relaxation between bands as well as the defect and trap states of the NPs. The average lifetime is decreased with the reduction of size indicating the influence of carrier recombination dynamics and the role of surface defect states in defining the emission profile. We have observed a non-linear increase in the relative Q.Y of the NPs as the size decreases below the Bohr radius. The synthesized MoS_2 NPs show good photocatalytic activity for degradation of brilliant green dye in visible light which can be used for textile and dye removal treatment applications.

7.5 References:

1. B. C. Tran Khac, K.-J. Jeon, S. T. Choi, Y. S. Kim, F. W. DelRio and K.-H. Chung, ACS appl. Mat & inter., 2016, **8**, 2974-2984.
2. Y. H. Lee, X. Q. Zhang, W. Zhang, M. T. Chang, C. T. Lin, K. D. Chang, Y. C. Yu, J. T. W. Wang, C. S. Chang and L. J. Li, Adv. Mat., 2012, **24**, 2320-2325.
3. H. Li, Y. Shi, M.-H. Chiu and L.-J. Li, Nano Energy, 2015, **18**, 293-305.
4. Q. H. Wang, K. Kalantar-Zadeh, A. Kis, J. N. Coleman and M. S. Strano, Nat. Nanotech., 2012, **7**, 699.
5. R. Ganatra and Q. Zhang, ACS Nano, 2014, **8**, 4074-4099.
6. H. Zhang, ACS Nano, 2015, **9**, 9451-9469.
7. A. Gupta, T. Sakthivel and S. Seal, Prog. Mat. Sci., 2015, **73**, 44-126.
8. K. F. Mak, C. Lee, J. Hone, J. Shan and T. F. Heinz, Phys. Rev. Lett., 2010, **105**, 136805.
9. X. Fan, P. Xu, D. Zhou, Y. Sun, Y. C. Li, M. A. T. Nguyen, M. Terrones and T. E. Mallouk, Nano Lett., 2015, **15**, 5956-5960.
10. A. Splendiani, L. Sun, Y. Zhang, T. Li, J. Kim, C.-Y. Chim, G. Galli and F. Wang, Nano Lett, 2010, **10**, 1271-1275.
11. G. Z. Magda, J. Pető, G. Dobrik, C. Hwang, L. P. Biró and L. Tapasztó, Sci. Rep., 2015, **5**, 14714.
12. S. Mukherjee, R. Maiti, A. Midya, S. Das and S. K. Ray, ACS Photonics, 2015, **2**, 760-768.
13. S. Mukherjee, R. Maiti, A. K. Katiyar, S. Das and S. K. Ray, Sci. Rep., 2016, **6**, 29016.
14. J. Jeon, S. K. Jang, S. M. Jeon, G. Yoo, Y. H. Jang, J.-H. Park and S. Lee, Nanoscale, 2015, **7**, 1688-1695.
15. A. Midya, A. Ghorai, S. Mukherjee, R. Maiti and S. K. Ray, J. Mat. Chem. A., 2016, **4**, 4534-4543.
16. X.-L. Fan, Y. Yang, P. Xiao and W.-M. Lau, J. Phys. Chem. C, 2014, **2**, 20545-20551.
17. H. Li, C. Tsai, A. L. Koh, L. Cai, A. W. Contryman, A. H. Fragapane, J. Zhao, H. S. Han, H. C. Manoharan and F. Abild-Pedersen, Nat. Mat., 2016, **15**, 48.
18. V. Nicolosi, M. Chhowalla, M. G. Kanatzidis, M. S. Strano and J. N. Coleman, Science, 2013, **340**, 1226419.

19. S. Mukherjee, S. Jana, T. K. Sinha, S. Das and S. K. Ray, Nanoscale Adv., 2019, **1**, 3279-3287.
20. M. Nasilowski, B. Mahler, E. Lhuillier, S. Ithurria and B. Dubertret, Chem Rev, 2016, **116**, 10934-10982.
21. T. P. Nguyen, W. Sohn, J. H. Oh, H. W. Jang and S. Y. Kim, J. Phys. Chem. C, 2016, **120**, 10078-10085.
22. V. L. Gole, A. Priya and S. P. Danao, App. Wat. Sci, 2017, **7**, 4237-4245.
23. C. Lee, H. Yan, L. E. Brus, T. F. Heinz, J. Hone and S. Ryu, ACS nano, 2010, **4**, 2695-2700.
24. T. Guo, S. Sampat, K. Zhang, J. A. Robinson, S. M. Rupich, Y. J. Chabal, Y. N. Gartstein and A. V. Malko, Sci. Rep., 2017, **7**, 41967.
25. L. Wang, Z. Wang, H.-Y. Wang, G. Grinblat, Y.-L. Huang, D. Wang, X.-H. Ye, X.-B. Li, Q. Bao and A.-S. Wee, Nat. Commun., 2017, **8**, 13906.
26. P. K. Chow, R. B. Jacobs-Gedrim, J. Gao, T.-M. Lu, B. Yu, H. Terrones and N. Koratkar, ACS Nano, 2015, **9**, 1520-1527.
27. T. P. Nguyen, W. Sohn, J. H. Oh, H. W. Jang and S. Y. Kim, J. Phys. Chem. C, 2016, **120**, 10078-10085.
28. S. Sharma, S. Bhagat, J. Singh, R. C. Singh and S. Sharma, J. Mat. Sci, 2017, **52**, 11326-11336.
29. A. Sharma, T. Gadly, A. Gupta, A. Ballal, S. K. Ghosh and M. Kumbhakar, J. Phys. Chem. Lett., 2016, **7**, 3695-3702.
30. M. Grabolle, M. Spieles, V. Lesnyak, N. Gaponik, A. Eychmüller and U. Resch-Genger, Anal. Chem., 2009, **81**, 6285-6294.
31. A. Layek, B. Manna and A. Chowdhury, Chem. Phys. Lett., 2012, **539**, 133-138.
32. L. Yuan and L. Huang, Nanoscale, 2015, **7**, 7402-7408.
33. N. Chestnoy, T. Harris, R. Hull and L. Brus, SPIE MILESTONE SERIES MS, 1998, **150**, 574-580.
34. Z. Cai, Y. Sun, W. Liu, F. Pan, P. Sun and J. Fu, Env. Sci. Poll. Rev., 2017, **24**, 15882-15904.
35. N. Shanmugam, T. Sathya, G. Viruthagiri, C. Kalyanasundaram, R. Gobi and S. Ragupathy, Appl. Surf. Sci., 2016, **360**, 283-290.
36. S. Hassan and M. A. Mannaa, Int. J. Nano & Matl. Sci, 2016, **5**, 9-19.

37. S. Munusamy, R. sai laxmi Aparna and R. gunneswara subramanya vara Prasad, Sust. Chem. Proc., 2013, **1**, 4.

38. X. Zhang, H. Suo, R. Zhang, S. Niu, X.-q. Zhao, J. Zheng and C. Guo, Mat. Res. Bulletin, 2018, **100**, 249-253.

39. Z. Zhou, Y. Lin, p. Zhang, E. Ashalley, M. Shafa, H. Li, J. Wu and Z. Wang, Mat. Lett., 2014, **131**, 122-124.

40. W. Liu, Q. Hu, F. Mo, J. Hu, Y. Feng, H. Tang, H. Ye and S. Miao, J. Mat. Chem. A, 2014 **395**, 322-328.

Chapter: 8

Conclusions and Future Scope of Study

8.1 Conclusions:

Chemically TMDC nanosheets attain immense research interest for developing next generation self-powered piezoelectric devices. Alloy engineering and heterostructure formation improve it's optoelectric and electric properties. Nanocomposite formation of the TMDC nanosheets with piezoelectric polymer develops new way for fabrication of self-powered piezoelectric nanogenerator. Besides that the broadband absorbance band, emissive properties are the key parameters to the study the interesting optoelectronic properties of TMDCs and also helpful for fabricating self-powered photosensitive nanogenerators and optical sensors. TMDCs are eco-friendly, easy to synthesis, highly stable, flexible, possess high mechanical strength which necessary to build up low cost, highly stable, strain sensitive piezoelectric nanogenerator. In this dissertation self-powered, flexible piezoelectric nanogenerators are fabricated (based on TMDC nanosheets) and various piezoelectric properties are studied, the major outcomes are summarized below:

Mechanically flexible, self-poled PVDF-MoS_2 nanocomposites have been synthesized with chemically exfoliated two-dimensional MoS_2 nanosheets and PVDF polymers. Fabricated PVDF-MoS_2 nanogenerator exhibits a record piezoelectric output (~ 2.07 V/kPa) and superior power density (~88.5 $\mu W/cm^2$), it can also generate piezoelectric output under a very low mechanical strain and exhibits high sensitivity towards human finger touch, which paves a promising application energy harvesting exploiting everyday biomechanical activities. The energy conversion efficiency of the nanogenerator is ~ 17.8% and the experimental evidence of charging of a capacitor and the glowing of light sources led us to assume that the appropriate design of this PENG can explore its application to power up different electronic gadgets, which are used in our everyday life.

Self-poled PVDF-WS_2 nanocomposites have been synthesized by using chemically exfoliated two-dimensional WS_2 nanosheets and PVDF polymers by following a low cost, eco-friendly technique. The exfoliated WS_2 nanosheets not only enhance the piezoelectric output voltage but also induce photo-activity in the nanocomposite devices over the pristine PVDF. Colossal piezoelectric voltage of ~ 116 V (for ~ 105 kPa) and record energy conversion efficiency of ~ 25.6% are obtained from the PVDF-WS_2 PENG. Further, the piezo-coupled photocurrent

ratio in mechanically stressed to relaxed configuration is enhanced by 287% under illumination, producing a high photoresponsivity, detectivity. A high output power generation under illumination than dark makes the system promising for extracting power under light illuminated condition. The excellent stability and capability of producing electrical power from surrounding environment and routine activities make the PVDF-WS_2 system attractive for application in future wearable, stretchable and portable electronic devices.

A self-powered, portable UV photodetection system based on ternary 2D TMDC alloy ($Mo_{0.5}W_{0.5}S_2$) with impedance matching between a self-polled piezoelectric nanogenerator and a photodetector is demonstrated. Alloy engineering is found to be a proficient strategy to overcome the defect state related problems in binary TMDCs, leads to the improved optoelectronic properties. The TMDC alloy based PENG produces a superior piezoelectric output voltage (~50 V) by simple finger tapping. The fabricated UV photodetector exhibits an exceptional photoresponsivity, impressive detectivity for an illumination of UV (365 nm). The PENG device can harvest bio-mechanical energy by simple finger tapping and can convert into electrical energy to drive a UV photodetector and the coupled device exhibits a large responsivity of ~0.75 V $\mu W^{-1}cm^{-2}$ in self-powered voltage detection mode. By connecting the PENG in series with a UV photodetector, the system works as a UV-light-intensity monitor, while the commercial constant chip resistors with parallel LEDs work as a UV sensitive alarm. Our results using novel ternary $Mo_{0.5}W_{0.5}S_2$ TMDC alloy pave the way for building highly efficient next generation mechanical energy harvesters for self-driven IOT devices.

Intrinsic piezoelectric properties of such chemically exfoliated TMDC heterostructures are studied for first time (from best of our knowledge). Inverse piezoelectric properties of these as-synthesized nanosheets are examined through piezoelectric force microscopy (PFM). In support with PFM measurements, the enhanced piezoelectric output performance is obtained from MoS_2-WSe_2 heterostructure PENG devices than the other PENG devices. Besides the energy harvesting ability of this PENG, it can be used as senor and bio-mechanical energy harvester also, producing piezoelectric output voltage from simple human activities. Thus, the MoS_2-WSe_2 PENG can be adopted as a practical wearable energy-harvesting device as well as self-powered sensors. In addition, large-area, lithography free, cost effective thin-film PENG ensures that the reproducible output performance and also used for other the

applications purposes also. Our approach provides a simple route to realize large-area 2D material-based PENGs and wearable smart sensors.

Variable sized MoS_2 nanoparticles (NPs) are synthesized through a simple chemical exfoliation technique. Highly stable, crystalline NPs exhibit strong size dependency in their spectroscopic properties as the consequence of quantum confinement effect. The synthesized MoS_2 NPs show good photocatalytic activity for degradation of brilliant green dye in visible light which can be used for textile and dye removal treatment applications.

8.2 Future scope of study:

Although details study on TMDC based piezoelectric devices are carried out and the optoelectric properties of TMDC alloy and piezoelectric properties of TMDC heterostructures has been reported, but several important sites cannot be covered in the present work, which requires further investigations. Some of the important studies are presented below:

- Detailed spectroscopic properties (photoluminescence, raman) of TMDC ternary alloy nanosheets.
- Piezo-phototronics, flexible photodetector study with the ternary alloy and heterostructure of TMDC nanosheets.
- Ultrafast charge carrier dynamics studies of TMDC alloy and heterostructure nanosheets.
- Size dependent spectroscopic and electric studies on TMDC nanocrystals.
- Piezotronics study on single TMDC nanosheet and fabrication of flexible TMDC devices by using e-beam/ ion-beam lithography.